

# 学位論文

**Measurement of the tau Michel parameters**

**$\bar{\eta}$  and  $\xi\kappa$  in the radiative leptonic decay**

$$\tau \rightarrow \ell\nu\bar{\nu}\gamma$$

(輻射レプトニック崩壊 $\tau \rightarrow \ell\nu\bar{\nu}\gamma$ を用いた  
タウ粒子のミシェルパラメータ $\bar{\eta}$ と $\xi\kappa$ の測定)

平成 28 年 12 月博士 (理学) 申請

東京大学大学院理学系研究科

物理学専攻 清水 信宏

## Abstract

We present the measurement of the Michel parameters of  $\tau$  lepton  $\bar{\eta}$  and  $\xi\kappa$  in the radiative leptonic decay  $\tau^- \rightarrow \ell^- \nu \bar{\nu} \gamma$  using  $703 \text{ fb}^{-1}$  of collision data collected with the Belle detector at the KEKB  $e^+e^-$  collider. The Michel parameter is a fundamental property of unstable charged leptons and characterizes the dynamics of leptonic decays. The experimental values of  $\bar{\eta}$  and  $\xi\kappa$  parameters may reveal the presence of new physics beyond the Standard Model.

The Michel parameters are measured by an unbinned maximum likelihood method where  $\bar{\eta}$  and  $\xi\kappa$  are fitted to the kinematic distribution of  $e^+e^- \rightarrow \tau^+\tau^- \rightarrow (\pi^+\pi^0\bar{\nu})(\ell^- \nu \bar{\nu} \gamma)$  ( $\ell = e$  or  $\mu$ ). Using the muon mode,  $\bar{\eta}$  and  $\xi\kappa$  are simultaneously fitted to the spectra to be  $\bar{\eta}^\mu = -1.3 \pm 1.5 \pm 0.8$  and  $(\xi\kappa)^\mu = 0.8 \pm 0.5 \pm 0.3$ . In the electron mode, taking into account the suppression of  $\bar{\eta}$  sensitivity from the small mass of daughter electron, we extract  $(\xi\kappa)^e$  by fixing  $\bar{\eta}$  value to the Standard Model prediction of  $\bar{\eta}_{\text{SM}} = 0$ . The measured value is  $(\xi\kappa)^e = -0.4 \pm 0.8 \pm 0.9$ . The first error is statistical and the second is systematic. This is the first measurement of these parameters. These results are consistent with the Standard Model predictions within their uncertainties and give a constraint on the coupling coefficient of the generalized weak interaction.

We also measured the branching ratio of the radiative leptonic decays under the photon energy threshold of  $E_\gamma^* > 10 \text{ MeV}$  in the  $\tau$  rest frame to be  $\mathcal{B}(\tau^\pm \rightarrow e^\pm \nu \bar{\nu} \gamma) = (1.82 \pm 0.02 \pm 0.10) \times 10^{-2}$  and  $\mathcal{B}(\tau^\pm \rightarrow \mu^\pm \nu \bar{\nu} \gamma) = (3.68 \pm 0.02 \pm 0.15) \times 10^{-3}$ . These results are consistent with the leading order Standard Model prediction. In the next-leading order, there are effects from multiple photon emission, which is not implemented in the current event generator. An improvement of generator is required to make comparison at the next-leading order.

# Contents

<b>1</b>	<b>Introduction</b>	<b>5</b>
1.1	The Standard Model . . . . .	5
1.1.1	Search for physics beyond the Standard Model . . . . .	6
1.2	Search for physics beyond the Standard Model in charged leptons . . . . .	6
1.3	Michel Parameters . . . . .	7
1.3.1	History of test of the charged current . . . . .	8
1.3.2	Michel formalism . . . . .	8
1.4	Further tests of the $V - A$ interaction in $\tau$ decays . . . . .	9
1.5	Physics motivation . . . . .	10
1.6	Production of $\tau$ leptons . . . . .	11
<b>2</b>	<b>Radiative leptonic decay <math>\tau^- \rightarrow \ell^- \nu \bar{\nu} \gamma</math></b>	<b>13</b>
2.1	Definition of the radiative decay and its distribution . . . . .	13
2.2	Spin-spin correlation of $\tau^+ \tau^-$ and two-body decay $\tau^+ \rightarrow \rho^+ \bar{\nu} \rightarrow \pi^+ \pi^0 \bar{\nu}$ . . . . .	15
2.3	Branching ratio of $\tau^- \rightarrow \ell^- \nu \bar{\nu} \gamma$ decays . . . . .	17
2.4	Effect of the Michel parameter on the distribution . . . . .	18
2.5	Determination of $\tau$ direction . . . . .	19
<b>3</b>	<b>Experimental Apparatus</b>	<b>23</b>
3.1	The KEKB accelerator . . . . .	23
3.1.1	Definition of frame . . . . .	25
3.2	The Belle detector . . . . .	26
3.2.1	Silicon Vertex Detector (SVD) . . . . .	28
3.2.2	Central Drift Chamber (CDC) . . . . .	28
3.2.3	Electromagnetic Calorimeter (ECL) . . . . .	31
3.2.4	Aerogel Cerenkov Counter (ACC) . . . . .	32
3.2.5	Time-Of-Flight counter (TOF) . . . . .	34
3.2.6	$K_L$ and muon detector (KLM) . . . . .	36
3.2.7	Trigger . . . . .	37
3.2.8	Data acquisition system (DAQ) . . . . .	37
3.2.9	Particle identifications . . . . .	40
3.3	Operation of Belle data taking . . . . .	44
3.4	Monte Carlo simulation . . . . .	44
<b>4</b>	<b>Event selection</b>	<b>46</b>
4.1	Preselection . . . . .	46
4.2	Second selection . . . . .	46
4.3	Final selection . . . . .	48
4.4	Background components for the selected candidates . . . . .	59
4.4.1	$\tau^+ \tau^- \rightarrow (\pi^+ \pi^0 \bar{\nu})(e^- \nu \bar{\nu} \gamma)$ decay candidates . . . . .	59

4.4.2	$\tau^+\tau^- \rightarrow (\pi^+\pi^0\nu)(\mu^-\nu\bar{\nu}\gamma)$ decay candidates	64
4.5	Total efficiency	70
<b>5</b>	<b>Method of the measurement of the Michel parameters</b>	<b>71</b>
5.1	Notations and conventions	71
5.2	Unbinned maximum likelihood method	71
5.3	Average efficiency and normalization	72
5.4	Implementation of probability density functions	73
5.4.1	Description of the signal PDF	73
5.4.2	Description of the major background PDFs	78
5.4.3	Description of other background modes	80
5.4.4	Implementation of the effect of collinear ISR	85
5.4.5	Implementation of the effect of detector resolution	86
5.5	Fitting	87
5.6	Validation of fitter	87
5.6.1	Linearity of fitter	87
5.6.2	Dependence of sensitivity on selection criteria	87
5.6.3	Fitting Michel parameters with background PDFs	92
<b>6</b>	<b>Analysis of the experimental data</b>	<b>97</b>
6.1	Trigger efficiency corrections *	97
6.2	Particle selection efficiency corrections	98
6.2.1	$\pi^0$ ID and $\gamma$ ID efficiency corrections	102
6.3	Reconstruction efficiency corrections	105
6.4	Binning of correction factors	109
6.5	Confirmation of the correction $R$	110
<b>7</b>	<b>Evaluation of uncertainties</b>	<b>115</b>
7.1	Statistical uncertainties	115
7.2	Systematic errors	115
7.2.1	Systematic uncertainty from branching ratios	115
7.2.2	Uncertainty from the relative normalization	115
7.2.3	Uncertainty from the absolute normalization	119
7.2.4	Uncertainties from correction factors and inefficiencies	119
7.2.5	Uncertainty due to imperfect formulation of PDFs	121
7.2.6	Uncertainty from the simulation of overlap in the ECL clusters	122
7.2.7	Uncertainty from the detector resolution	123
7.2.8	Uncertainty from the beam Energy spread	123
7.2.9	Uncertainty from $E_\gamma$ distribution	123
<b>8</b>	<b>Results and discussion</b>	<b>125</b>
8.1	Fit result	125
8.2	Goodness of fit	125
8.3	Upper limits on couplings $g_{ij}^N$	129
8.4	Couplings with right-handed lepton	131
8.5	Relationship with the right-left symmetric model	133

<b>9</b>	<b>Measurement of the branching ratio <math>\mathcal{B}(\tau^- \rightarrow \ell^- \nu \bar{\nu} \gamma)</math></b>	<b>134</b>
9.1	Event selection . . . . .	134
9.2	Method . . . . .	138
9.3	Evaluation of systematic uncertainties . . . . .	139
9.4	Result . . . . .	140
9.4.1	Ratio of branching ratio $Q = \mathcal{B}(\tau^- \rightarrow e^- \nu \bar{\nu} \gamma) / \mathcal{B}(\tau^- \rightarrow \mu^- \nu \bar{\nu} \gamma)$ . . . . .	140
9.5	Discussion . . . . .	143
9.5.1	Treatment of double photons . . . . .	143
9.5.2	Anomalous four-point interaction . . . . .	144
<b>10</b>	<b>Future prospects and conclusion</b>	<b>146</b>
10.1	Future experiment and expected improvements . . . . .	146
10.2	Conclusion . . . . .	148
<b>A</b>	<b>Measurement of the branching ratio <math>\mathcal{B}(\tau^- \rightarrow \ell^- \nu \bar{\nu} \gamma)</math> (validation)</b>	<b>157</b>
A.1	Method and evaluation of systematic uncertainties . . . . .	157
A.2	Result . . . . .	157
A.3	Discussion and conclusions . . . . .	157
A.3.1	$E_{\text{extray}}^{\text{LAB}}$ dependence . . . . .	157
A.3.2	Conclusions . . . . .	158
<b>B</b>	<b>Description of background PDFs</b>	<b>160</b>
B.1	Ordinary leptonic decay + beam background . . . . .	160
B.2	Description of PDF for $3\pi$ events . . . . .	161
B.2.1	Extraction of the inefficiencies . . . . .	164
B.3	Description of $\rho\rho$ background . . . . .	164
B.3.1	Extraction of inefficiency . . . . .	168
B.4	Description of ISR photon + ordinary leptonic decay events . . . . .	168
B.5	Description of $3\pi-2\pi$ decay events . . . . .	170
B.5.1	extraction of inefficiency . . . . .	171
B.6	Description of an ordinary leptonic decay + bremsstrahlung events . . . . .	173
<b>C</b>	<b>Calculation of Jacobians</b>	<b>176</b>
C.1	Jacobian for Lorentz-transformation . . . . .	176
C.2	2-body decay . . . . .	176
C.2.1	$\left  \frac{\partial(P_{\pi_0}, \Omega_{\pi_0}, \Omega_{\gamma}^{**})}{\partial(P_{\gamma}, \Omega_{\gamma}, \Omega_{\gamma'})} \right $ . . . . .	177
C.3	$\left  \frac{\partial(P_{a_1}, \Omega_{a_1}, m_{a_1}^2, \hat{\Omega}_p)}{\partial(P_{\pi_{\text{lost}}^0}, \Omega_{\pi_{\text{lost}}^0}, P_{\rho}, \Omega_{\rho})} \right $ . . . . .	178
C.4	$\left  \frac{\partial(\Omega_{\rho_1}^*, \Omega_{\rho_2}^*, \Omega_{\tau})}{\partial(P_{\rho_1}, \Omega_{\rho_1}, P_{\rho_2}, \Omega_{\rho_2})} \right $ . . . . .	179
C.4.1	$\left  \frac{\partial(\Omega_{\rho}^*, \Omega_{\tau})}{\partial(P_{\rho}, \Omega_{\rho}, \Phi_{\tau})} \right $ . . . . .	179
C.5	$\left  \frac{\partial(P_{\gamma}, \Omega_{\gamma})}{\partial(\tilde{\Omega}_{\gamma}, \beta)} \right $ . . . . .	180
C.6	Recursive relation of the Lorentz-invariant phase space . . . . .	182
<b>D</b>	<b>Doubly radiative leptonic decay <math>\tau^- \rightarrow \ell^- \nu \bar{\nu} \gamma \gamma</math></b>	<b>183</b>

<b>E</b>	<b>Detector resolution</b>	<b>186</b>
E.1	description of energy response . . . . .	186
<b>F</b>	<b>The right-left symmetric model</b>	<b>188</b>

# Chapter 1

## Introduction

### 1.1 The Standard Model

Everything in our universe is believed to be made from fundamental particles. Their interactions or forces are described by an exchange of other particles. Such *particles* are described so as not to have their sizes as well as internal structures thereby they are called *elementary* particles. The quantum field theory (QFT) is a physical framework which treats an entity of such a particle as an excitation of field in the space-time, relying on both the quantum mechanics and the special relativity—most successful theories of physics in the twentieth century.

In principle, in the framework of QFT, people can freely build new theories: arbitrary types of particles and rules of interactions can form one theory. However, there are few theories which can reasonably predict real behaviors of known particles. The Standard Model (SM) is known to be the strongest predictable theories of QFT, in which twelve types of fermions (corresponding to matters) are governed by three types of forces. The forces are mediated by corresponding bosons. The masses of these particles are uniquely determined by strengths of each coupling to the field of Higgs boson. Below we give a summary of the SM.

#### Types of elementary particles

- Higgs boson is a spin-0 particle to give other particles masses.
- There are three types of forces: electromagnetic interaction, charged and neutral weak interactions and strong interaction. These forces are mediated by spin-1 particles and play roles in cancellations of position-dependent phases. The invariance under the phase transformation is called gauge invariance, hence these particles are also called gauge bosons. These gauge bosons are named photon  $\gamma$  for the electromagnetic,  $W^\pm$  and  $Z$  bosons for the charged and neutral weak interactions and gluon  $g$  for the strong force.
- Matters are made from spin- $\frac{1}{2}$  particles which are categorized into two groups: six types of quarks and six types of leptons. The quark has charges of all forces above and is able to participate in all interactions. Whereas the lepton does not have a charge of strong force but has a weak charge, accordingly it participates in the weak interactions. The three quarks have  $+2/3$  electromagnetic charges and other three have  $-1/3$ . Three leptons which have electromagnetic charges  $+1$  are called charged leptons and are able to interact via electromagnetic force while the other three do not and are called neutrinos. The three types are also called *flavors*.
- Except the neutral particles  $\gamma$ ,  $Z$  and  $g$ , all particles have their corresponding anti-particles, which have opposite quantum numbers.

## Important characteristics

- Particles have a property called chirality, whose eigenvalue is 1 or -1. In the massless limit, it is well known that the chirality equals to helicity that is defined as  $h = \hat{\mathbf{S}} \cdot \mathbf{n}$ , where  $\hat{\mathbf{S}}$  is a normalized vector of spin and  $\mathbf{n}$  is a unity vector of the particle movement. The positive and negative helicities are called right-handed and left-handed, respectively.
- Of all forces, only charged weak interaction can change the flavor of particle. Moreover, it violates the symmetry of chirality, *i.e.*, only negative-chirality particles and anti-particles are active in the charged weak interaction.
- Strong forces have a potential proportional to distance  $V(r) \propto kr$ : in other words, the strength of coupling becomes large in low energy or weak in high energy, so called *asymptotic freedom*. This means that a system which has two free distant quarks is unstable, hence, in terms of energy, it is more beneficial to create  $q\bar{q}$  pair ( $q$  represent a quark) from vacuum to form two  $q\bar{q}$  binding states (or mesons). For this reason, neither the free quark nor its fractional charge has not been discovered yet (*quark confinement*).
- In addition, because of the asymptotic freedom, theoretical calculations using perturbation technique are less accurate for low energy behaviors of strong interaction. In such energy scale, therefore, a precise comparison between a value observed by experiment and theoretical prediction is difficult.

### 1.1.1 Search for physics beyond the Standard Model

In 2012, at Conseil Européen pour la Recherche Nucléaire (CERN), Higgs boson was discovered by experiments at the large hadron collider (LHC) from proton-proton collision data [1, 2]. The existence of the Higgs boson, though many researcher had believed in it, made a validity of the SM decisive. The SM can explain almost all of particle phenomena that occur in our universe. Various quantum behaviors of particles are within a prediction of this framework. Many physicist, however, believe that the SM to be neither complete nor ultimate theory which describes nature because there are several strong facts that are inconsistent with the SM. The observation of nonzero mass of neutrinos discovered by the neutrino oscillation [3, 4], the unknown source of the gravitational potential (*dark matter*), the asymmetry of amounts between matter and antimatter and the unnaturally small mass of Higgs boson (so called *hierarchy problem*) [5], all of them are not well explained in the framework of the SM.

For the reason noted above, physicists are trying to find an inconsistency of the SM or physics beyond the SM (BSM). At least from existing observations, the effect from physics BSM in various behaviors of particles appears to be small. This may imply that a new particle, which is responsible for phenomena BSM, has a very large mass. In fact, using the LHC, people achieved very high-energetic environment of 10 TeV or  $10^{14}$  K by accelerating and colliding protons and are attempting to directly unveil the appearance BSM. Another approach is to precisely measure the properties of already known phenomena. Based on observations of a huge number of interactions of particles at relatively low energy, possible effects from the physics BSM are precisely verified.

## 1.2 Search for physics beyond the Standard Model in charged leptons

In the SM, there are three flavors of charged leptons:  $e, \mu$  and  $\tau$ . The electron  $e$  has the smallest mass in all particles that have electromagnetic charges, hence the charge conservation does not allow



electrons to decay. The stability of electrons opens various experimental possibilities to measure their properties. The muon  $\mu$  and tau  $\tau$  have masses  $(105.65837545 \pm 0.0000024) \text{ MeV}/c^2$  and  $(1776.86 \pm 0.12) \text{ MeV}/c^2$ , respectively [7], and can decay into lighter particles. The tests of these decays also give us additional information from the physics BSM.

In terms of search BSM based on the precision measurement of particle properties, experiments using the charged leptons turn out to offer beautiful laboratories. The inactivity of charged leptons to the strong interaction enables us to pursue excellent precision in the theoretical calculation. Various properties of these decays, described by the electroweak sector of the SM, are precisely calculated, therefore, experimental results can be definitely compared with theoretical predictions. Moreover, unlike quarks, the charged leptons can exist in *bare* states and we are able to directly test the nature of elementary particles. Though neutrinos also share this nature, it is difficult to do similar measurement due to the small reaction rate.

## The $\mu$ particle

There have been varieties of experiments to measure  $\mu$  properties. Most notably, at Brookhaven National Laboratory (BNL), the E821 experiment measured an anomalous magnetic moment of the  $\mu$  using polarized beam with amazing precision (0.7 ppm!) [6] and as a result exhibited a significant deviation from the SM prediction by  $3\sigma$  level. Not only the anomalous magnetic moment but a variety of properties of  $\mu$  have been measured for more than one century. Its relatively long lifetime ( $\sim 2 \mu\text{s}$ ) and availability of thereby large number of pure  $\mu$  (moreover sometimes polarized) sample enables us to perform excellent precision experiments for  $\mu$ : it may not be overstate that we understand the muon very well.

## The $\tau$ particle

On the other hand, in spite of its equally interesting characteristics, various properties of  $\tau$  lepton are not so precisely measured, particularly due to its technical difficulties of experiment. Theoretical treatment of  $\tau$  is as simple as that of  $\mu$  case, but the short lifetime of  $\tau$  ( $\sim 0.3 \text{ ps}$ ) does not allow competitive measurement in terms of absolute precision.

Nevertheless, measurements of the  $\tau$  decay is one of the most sensitive probes to the effects BSM. The large mass of the  $\tau$  allows us to expect an enhancement of the sensitivity on the BSM. For instance, the two Higgs doublet model (2HDM), one of the branches of the supersymmetric models, predicts an existence of the charged Higgs and the magnitude of their couplings is proportional to mass of a lepton. As a result, in comparison with  $\mu$  decays, we can expect the gain of sensitivity by a factor of  $(m_\tau/m_\mu)^2 \sim 300$ .

The large mass of the  $\tau$  makes it possible to decay into both leptons and hadrons. The former one is called *leptonic* decay and accounts for approximately 35% of all tau decays. The rest decays of the  $\tau$  contain hadrons in the final state and are called *hadronic* decay.

Taking into account the sensitivities to the effects from physics BSM, we chose the  $\tau$  lepton for the theme of study. In this thesis, we describe the method in detail.

## 1.3 Michel Parameters

The measurement of *Michel parameters* is one of the most established strategies for the verification of the decay of charged leptons. The formalism was developed in the course of the clarification of the (weak) charged interaction.

Since the discovery of weak force, physicist have been trying to unveil its unique dynamic nature spending long time. Before moving to main topic, we review the history.

### 1.3.1 History of test of the charged current

The weak interaction was first proposed by Fermi [8, 9] to explain the beta decay of the nucleus. He incorporated an idea of the neutrino, which had been suggested by Pauli, and succeeded to explain the continuous momentum spectrum of the daughter electron. In 1957, C. S. Wu found that the weak force did not respect the symmetry of the parity in the beta decay from  $^{60}\text{Co}$  [10]. The angular distribution of the electron from the polarized cobalt nuclei suggested the maximal violation of parity in the couplings, *i.e.*, the interaction results in the asymmetric couplings between left-handed and right-handed particles. The structure of the coupling contains the vector and axial-vector contributions almost in the same magnitudes with opposite signs, so it is called  $V - A$  interaction.

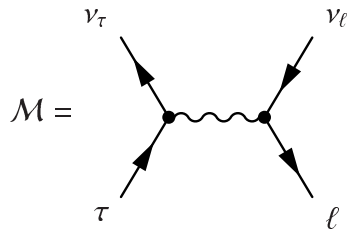
Because of its unique properties, over more than one century there have been various attempts to reveal the nature of the weak interaction. In 1949, Ruderman and Finkelstein predicted that a ratio of decay rates  $\mathcal{B}(\pi^+ \rightarrow e^+ \nu)/\mathcal{B}(\pi^+ \rightarrow \mu^+ \nu)$  was suppressed by four order of magnitude if the weak interaction occurs through the  $V - A$  structure [11]. The  $V - A$  type current permits only negative-helicity particles to participate in the weak interaction, which results in the violation of angular momentum conservation in  $\pi^+ \rightarrow \ell^+ \nu$  in the massless limit  $m_\ell \rightarrow 0$  ( $\ell = e$ , or  $\mu$ ). This well known mechanism is often called *helicity suppression*. In 1958, the electron decay of pion  $\pi^+ \rightarrow e^+ \nu$  was first observed [12] and then a recent experimental value using stopped  $\pi^+$ ,  $\mathcal{B}(\pi^+ \rightarrow e^+ \nu)/\mathcal{B}(\pi^+ \rightarrow \mu^+ \nu) = (1.2346 \pm 0.0035 \pm 0.0036) \times 10^{-4}$  [13] well supports its theoretical prediction  $(1.233 \pm 0.004) \times 10^{-4}$  [14].

More general tests of the Lorentz structure of the weak interaction have been performed in the decay of  $\mu^- \rightarrow e^- \nu \bar{\nu}$  and  $\tau^- \rightarrow \ell^- \nu \bar{\nu}$  by the measurement of Michel parameters.

### 1.3.2 Michel formalism

The most general Lorentz-invariant derivative-free matrix element of leptonic  $\tau$  decay\*  $\tau^- \rightarrow \ell^- \nu \bar{\nu}^\dagger$  is represented as [17]

$\mathcal{M} =$



$$= \frac{4G_F}{\sqrt{2}} \sum_{\substack{N=S,V,T \\ i,j=L,R}} g_{ij}^N [\bar{u}_i(\ell) \Gamma^N v_n(\nu_\ell)] [\bar{u}_m(\nu_\tau) \Gamma_N u_j(\tau)], \quad (1.1)$$

where  $G_F$  is the Fermi constant,  $i$  and  $j$  are the chirality indices for the charged leptons,  $n$  and  $m$  are the chirality indices of the neutrinos,  $\ell$  is  $e$  or  $\mu$ ,  $\Gamma^S = 1$ ,  $\Gamma^V = \gamma^\mu$  and  $\Gamma^T = i(\gamma^\mu \gamma^\nu - \gamma^\nu \gamma^\mu)/2\sqrt{2}$  are, respectively, the scalar, vector and tensor Lorentz structures in terms of the Dirac matrices  $\gamma^\mu$ , and  $g_{ij}^N$  are the corresponding dimensionless couplings. The chirality indices  $n$  and  $m$  are not summed in Eq. (1.1) because they are uniquely fixed for given  $i$ ,  $j$  and the interaction type. In the SM,  $\tau^-$  decays into  $\ell^-$  exclusively via the  $W^-$  vector boson with the  $V - A$  Lorentz structure, *i.e.*, the only non-zero coupling is  $g_{LL}^V = 1$ . Experimentally, only the squared matrix element is observable and so bilinear combinations of the  $g_{ij}^N$  are accessible. Of all such combinations, four Michel parameters— $\eta$ ,  $\rho$ ,  $\delta$  and  $\xi$ —can be measured by the leptonic decay of the  $\tau$  when the final state neutrinos are not

\*The discussion here holds also for  $\mu$  when the daughter lepton  $\ell$  is changed to  $e$ .

†Unless otherwise stated, use of charge-conjugate modes is implied throughout the thesis.

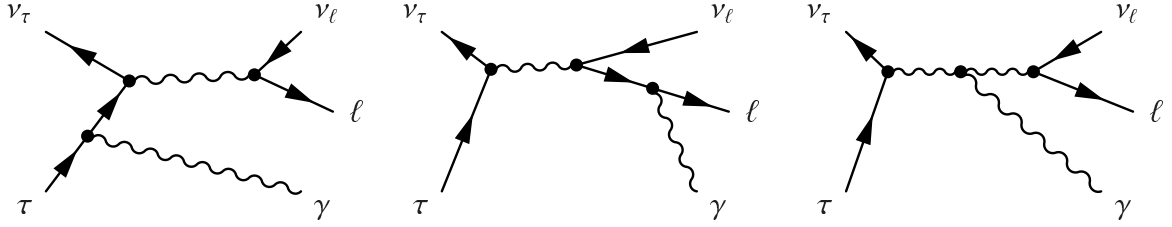


Figure 1.1: Radiative decay. The last diagram arises from the radiation from  $W$  boson but this is suppressed by the very small factor of  $(m_\tau/m_W)^2 \sim 5 \times 10^{-4}$ .

observed [18]:

$$\rho = \frac{3}{4} - \frac{3}{4} \left( |g_{LR}^V|^2 + |g_{RL}^V|^2 + 2|g_{LR}^T|^2 + 2|g_{RL}^T|^2 + \Re(g_{LR}^S g_{LR}^{T*} + g_{RL}^S g_{RL}^{T*}) \right), \quad (1.2)$$

$$\eta = \frac{1}{2} \Re \left( 6g_{RL}^V g_{LR}^{T*} + 6g_{LR}^V g_{RL}^{T*} + g_{RR}^S g_{LL}^{V*} + g_{RL}^S g_{LR}^{V*} + g_{LR}^S g_{RL}^{V*} + g_{LL}^S g_{RR}^{V*} \right), \quad (1.3)$$

$$\begin{aligned} \xi = & 4\Re(g_{LR}^S g_{LR}^{T*} - g_{RL}^S g_{RL}^{T*}) + |g_{LL}^V|^2 + 3|g_{LR}^V|^2 - 3|g_{RL}^V|^2 - |g_{RR}^V|^2 \\ & + 5|g_{LR}^T|^2 - 5|g_{RL}^T|^2 + \frac{1}{4} \left( |g_{LL}^S|^2 - |g_{LR}^S|^2 + |g_{RL}^S|^2 - |g_{RR}^S|^2 \right), \end{aligned} \quad (1.4)$$

$$\begin{aligned} \xi\delta = & \frac{3}{16} \left( |g_{LL}^S|^2 - |g_{LR}^S|^2 + |g_{RL}^S|^2 - |g_{RR}^S|^2 \right) \\ & - \frac{3}{4} \left( |g_{LR}^T|^2 - |g_{RL}^T|^2 - |g_{LL}^V|^2 + |g_{RR}^V|^2 - \Re(g_{LR}^S g_{LR}^{T*} + g_{RL}^S g_{RL}^{T*}) \right). \end{aligned} \quad (1.5)$$

Parametrized by these values, the differential decay width of  $\tau^- \rightarrow \ell^- \nu \bar{\nu}$  is explicitly given by

$$\begin{aligned} \frac{d\Gamma(\tau^- \rightarrow \ell^- \nu \bar{\nu})}{dE_\ell^* d\Omega_\ell^*} = & \frac{4G_F^2 m_\tau E_{\max}^3}{(2\pi)^4} \sqrt{x^2 - x_0^2} \left[ x(1-x) + \frac{2\rho}{9}(4x^2 - 3x - x_0^2) \right. \\ & \left. + \eta x_0(1-x) - \xi \frac{\mathbf{n}_\ell^* \cdot \mathbf{S}_\tau^*}{3} \sqrt{x^2 - x_0^2} \left( 1-x + \frac{2\delta}{3}(4x - 4 + \sqrt{1-x_0^2}) \right) \right], \end{aligned} \quad (1.6)$$

where  $E_{\max} = (m_\tau^2 + m_\ell^2)/2m_\tau$  is the maximum energy of lepton in the tau rest frame,  $x = E_\ell^*/E_{\max}$  is a normalized lepton energy,  $x_0 = m_\ell/E_{\max}$ , and  $\mathbf{n}_\ell^* \cdot \mathbf{S}_\tau^*$  is the cosine of angle between the tau spin and lepton direction. Thus the Michel parameters characterize spectra of lepton momentum and direction. Moreover, as Eq. (1.6) shows  $\xi$  and  $\xi\delta$  appear with  $\mathbf{n}_\ell^* \cdot \mathbf{S}_\tau^*$ , it is thus these two variables determine the lepton angular dependence vs tau-spin direction.

## 1.4 Further tests of the $V - A$ interaction in $\tau$ decays

The Feynman diagrams describing the radiative leptonic decay of the  $\tau$  are presented in Fig 1.1. The last amplitude turned out to be suppressed by the very small factor of  $(m_\tau/m_W)^2 \sim 5 \times 10^{-4}$  [26] and can be neglected. Then, as shown in Refs. [27, 28, 29], the presence of a radiative photon in the final state (or sometimes called *inner bremsstrahlung*) exposes three more Michel parameters,  $\bar{\eta}$ ,  $\eta''$  and  $\xi\kappa$ , which are explicitly given by

$$\bar{\eta} = |g_{RL}^V|^2 + |g_{LR}^V|^2 + \frac{1}{8} \left( |g_{RL}^S + 2g_{RL}^T|^2 + |g_{LR}^S + 2g_{LR}^T|^2 \right) + 2 \left( |g_{RL}^T|^2 + |g_{LR}^T|^2 \right), \quad (1.7)$$

$$\eta'' = \Re \left\{ 24g_{RL}^V (g_{LR}^{S*} + 6g_{LR}^{T*}) + 24g_{LR}^V (g_{RL}^{S*} + 6g_{RL}^{T*}) - 8(g_{RR}^V g_{LL}^{S*} + g_{LL}^V g_{RR}^{S*}) \right\}, \quad (1.8)$$

$$\xi\kappa = |g_{RL}^V|^2 - |g_{LR}^V|^2 + \frac{1}{8} \left( |g_{RL}^S + 2g_{RL}^T|^2 - |g_{LR}^S + 2g_{LR}^T|^2 \right) + 2 \left( |g_{RL}^T|^2 - |g_{LR}^T|^2 \right). \quad (1.9)$$

Table 1.1: Michel parameters of the  $\mu$  lepton

Name	SM value	Spin correlation	Experimental result <sup>†</sup> [7]	Comments and Ref.
$\eta$	0	no	$0.057 \pm 0.034$	[19]
$\rho$	3/4	no	$0.74979 \pm 0.00026$	[20]
$\xi$	1	yes	$1.0009^{+0.0016}_{-0.0007}$	[21]
$\delta$	3/4	yes	$0.75047 \pm 0.00034$	[20]
$\bar{\eta}$	0	no	$0.02 \pm 0.08$	[22]
$\xi\kappa$	0	yes	$0.00 \pm 0.01$	calc. from $\xi'$ value [23]

<sup>†</sup> Experimental results represent average values obtained by the particle data group (PDG) [7]. The most precise results are referenced here.

The formula of differential decay width for the radiative decay, which corresponds to Eq. (1.6) in  $\tau^- \rightarrow \ell^- \nu \bar{\nu}$  case, becomes more complicated and we postpone its description until Chapter 5. Nevertheless, these new Michel parameters also affect the spectra of daughter particles.

Similarly to  $\rho$  and  $\eta$ , both  $\bar{\eta}$  and  $\eta''$  appear as spin-independent terms in the differential decay width. Since all terms in Eq. (1.7) are non-negative, the upper limit on  $\bar{\eta}$  provides a constraint on each coupling constant. The value of  $\eta''$  is suppressed by a factor of  $m_\ell/m_\tau \sim 0.03\%$  for an electron daughter and  $\sim 6\%$  for a muon daughter and so difficult to measure with the statistics available so far. In this study, we use the SM value  $\eta'' = 0$ .

To measure  $\xi\kappa$ , which appears in the spin-dependent part of the differential decay width, we must determine the spin direction of the  $\tau$ . This spin dependence is extracted using the spin-spin correlation with the partner  $\tau$  in the event (it is explained in detail in the next chapter).

The information on Michel parameters is summarized in Tables 1.1 and 1.2 for muon and tau, respectively.  $\bar{\eta}$  and  $\xi\kappa$  parameters have been already measured in  $\mu^-$  decay (note that  $\xi\kappa$  parameter is induced from  $\xi'$  parameter). Using the statistically abundant data set of ordinary leptonic decays, previous measurements had determined the Michel parameters  $\eta$ ,  $\rho$ ,  $\delta$  and  $\xi$  to an accuracy of a few percent and in agreement with the SM prediction. Taking into account this measured agreement, the smaller data set of the radiative decay and its limited sensitivity, we focus in this analysis only on the extraction of  $\bar{\eta}$  and  $\xi\kappa$  by fixing  $\eta$ ,  $\rho$ ,  $\delta$  and  $\xi$  to the SM values. This represents the first measurement of the  $\bar{\eta}$  and  $\xi\kappa$  parameters of the  $\tau$  lepton.

## 1.5 Physics motivation

As introduced in Sec. 1.3, the relationships between the coupling constants  $g_{ij}^N$  and the Michel parameters intricately intertwine each other. Consequently, an intuitive understanding of the connection to a specific model BSM is a room for discussion. For example, it is known that  $\eta$  is directly associated with the charged Higgs model. In the SM, only  $g_{LL}^V = 1$  is nonzero and other  $g_{ij}^N$  being zero, hence from Eq. (1.3) we obtain  $\eta \sim 0.5 \cdot \Re\{g_{RR}^S\}$ . Since the charged Higgs mediates the radiative leptonic decay of the  $\tau$  as a scalar-type interaction, the measurement of  $\eta$  is regarded as the verification of the coupling of Higgs to the right-handed  $\tau$ . The same analogy holds for  $\eta''$ :  $\eta'' \sim 8 \cdot \Re\{g_{RR}^S\}$ . On the contrary, other Michel parameters appear as the complex combinations of many contributions BSM.

Nevertheless, there are a few comments for the new Michel parameters,  $\bar{\eta}$  and  $\xi\kappa$ . First, the ordinary Michel parameters ( $\eta$ ,  $\rho$ ,  $\delta$  and  $\xi$ ) can be measured blindly to the polarization of outgoing lepton. Conversely, the measurement of the new parameters  $\bar{\eta}$  and  $\xi\kappa$  in the  $\tau^- \rightarrow \ell^- \nu \bar{\nu} \gamma$  is equivalent

Table 1.2: Michel parameters of the  $\tau$  lepton

Name	SM value	Spin correlation	Experimental result <sup>†</sup> [7]	Comments and Ref.
$\eta$	0	no	$0.013 \pm 0.020$	[24]
$\rho$	3/4	no	$0.745 \pm 0.008$	[25]
$\xi$	1	yes	$0.995 \pm 0.007$	measured in hadronic decays [24]
$\xi\delta$	3/4	yes	$0.746 \pm 0.021$	[25]
$\bar{\eta}$	0	no	not measured	from radiative decay (RD)
$\xi\kappa$	0	yes	not measured	from RD
$\eta''$	0	no	not measured	from RD, suppressed by $m_\ell/m_\tau$

<sup>†</sup> Experimental results represent average values obtained by the particle data group (PDG) [7]. The most precise results are referenced here.

to the verification of the couplings of each chirality of the daughter lepton. The angular distribution of the photon vs the movement of the daughter lepton provides the information of the polarization of the lepton. In fact, according to Ref. [30], the  $\xi\kappa$  is related to another Michel-like parameter  $\xi' = -\xi - 4\xi\kappa + 8\xi\delta/3$ . Because the probability that the  $\tau^-$  decays into the right-handed charged daughter lepton  $Q_{\ell_R}^\tau$  is given by  $Q_{\ell_R}^\tau = (1 - \xi')/2$  [31], the measurement of  $\xi\kappa$  provides a further constraint on the  $V-A$  structure of the weak current.<sup>†</sup> It is known that verification of the asymmetric nature of the chirality has a strong impact on the theory BSM like right-left symmetric model [32, 33].

Second, as is mentioned before, the  $\bar{\eta}$  is a sum of non-negative terms, hence the upper limit of the  $\bar{\eta}$  constrains the value of each component. As summarized in  *$\tau$ -Lepton decay parameters* in Ref. [7], some of the  $g_{ij}^N$  included in Eq. (1.7) are not well measured for the  $\tau$  decay:

$$|g_{RL}^V| < 0.52 \quad (95\% \text{ C.L.}), \quad (1.10)$$

$$|g_{RL}^T| < 0.51 \quad (95\% \text{ C.L.}), \quad (1.11)$$

$$|g_{RL}^S| < 2.01 \quad (95\% \text{ C.L.}), \quad (1.12)$$

$$|g_{LR}^S| < 0.95 \quad (95\% \text{ C.L.}). \quad (1.13)$$

The measurement of the  $\bar{\eta}$  is very powerful way to constrain these couplings. Moreover,  $\bar{\eta}$  is also related to another Michel-like parameter  $\xi'' = 16\rho/3 - 4\bar{\eta} - 3$ , which represents the angular dependence of the longitude spin of the daughter lepton (see *e.g.* Ref [34]). Although  $\xi''$  has been already measured for  $\mu$  decay, that of  $\tau$  is not yet known.

Finally, these six Michel parameters deliver independent information. Figure 1.2 summarizes the matrix of the correlation coefficients of these Michel parameters calculated by fitting the parameters to the spectra of Monte Carlo events for  $\tau^- \rightarrow e^- \nu \bar{\nu} \gamma$  (the detailed method of this evaluation is explained in Chapter 5). The correlations of the Michel parameters between the ordinary and radiative ones, *i.e.*,  $\eta, \rho, \delta, \xi$  and  $\bar{\eta}, \xi\kappa$  are sufficiently small and this implies a potential impact on the constraint of  $g_{ij}^N$  in terms of the construction of theories.

## 1.6 Production of $\tau$ leptons

In Table 1.3, information of possible  $\tau$  decay data collected by various experiments is listed. To precisely measure the properties of the  $\tau$  lepton, there are two requirements: the observation of large

<sup>†</sup> Similarly, the probability that the right handed  $\tau$  couples the daughter lepton is given by  $Q_R^\tau = [1 + (3\xi - 16\xi\delta)/9]/2$ .

	$\bar{\eta}$	$\eta''$	$\xi\kappa$	$\rho$	$\eta$	$\xi$	$\xi\delta$
$\bar{\eta}$	—	$-2 \times 10^{-4}$	0.06	-0.11	$7 \times 10^{-4}$	$-5 \times 10^{-3}$	$-2 \times 10^{-3}$
$\eta''$	—	—	$-6 \times 10^{-5}$	$1 \times 10^{-4}$	$1 \times 10^{-5}$	$-9 \times 10^{-5}$	$-8 \times 10^{-5}$
$\xi\kappa$	—	—	—	$2 \times 10^{-3}$	$1 \times 10^{-4}$	-0.11	-0.05
$\rho$	—	—	—	—	$-3 \times 10^{-3}$	0.08	0.19
$\eta$	—	—	—	—	—	$-4 \times 10^{-5}$	$-6 \times 10^{-4}$
$\xi$	—	—	—	—	—	—	0.16

Figure 1.2: Correlation coefficients between the Michel parameters.

Table 1.3: List of available  $\tau$  data

Experiment	Integrated luminosity ( $\text{fb}^{-1}$ )	Beam energies
ARGUS	0.5	$E_{ee} = 9.4\text{-}10.6$ GeV
CLEO-II	4.7	$E_{ee} = 10.6$ GeV
CLEO-c	0.8	$E_{ee} = 3.8$ GeV
Babar	467	$E_{ee} = 10.0\text{-}10.6$ GeV
Belle	980	$E_{ee} = 9.5\text{-}10.9$ GeV
LHCb	$> 2.0$	$E_{pp} = 13$ TeV (2015-2016)

number of  $\tau$  decays and clean environment in the detection of daughter particles. Accounting for not only number of events but also clean environment of lepton collider, the Belle experiment possesses the best  $\tau$  data for its precision measurement.

The Belle experiment, which was operated for more than ten years from 1999 to 2010 at Tsukuba Ibaraki Japan, is a project using an electron-positron collider KEKB and Belle detector. The project was originally organized to aim for an observation of the source of CP violation in the decays of  $B$  mesons based on huge number of events. Indeed, Belle succeeded to uncover the mechanism of the CP asymmetry in the context of the SM. At the same time, however, the Belle experiment collected data from huge number of  $\tau$  decays produced by  $e^+e^- \rightarrow \tau^+\tau^-$  process. We use this excellent environment to reveal the fundamental nature of  $\tau$  lepton.

# Chapter 2

## Radiative leptonic decay $\tau^- \rightarrow \ell^- \nu \bar{\nu} \gamma$

In order to measure the Michel parameters,  $\bar{\eta}$  and  $\xi\kappa$ , the probability density function (PDF) is fitted to the decay spectra of  $\tau^- \rightarrow \ell^- \nu \bar{\nu} \gamma$  decay ( $\ell = e$  or  $\mu$ ). Using  $\tau^+ \rightarrow \pi^+ \pi^0 \bar{\nu}$  decay as a spin analyzer for the partner side of  $\tau^+$  in  $e^+ e^- \rightarrow \tau^+ \tau^-$  production, information of polarization is extracted. In this section, we review the characteristics of the signal decay. Detailed method about the fit procedure is explained in Chapter 5.

### 2.1 Definition of the radiative decay and its distribution

Two kinetic parameters characterize the radiative leptonic decay  $\tau^- \rightarrow \ell^- \nu \bar{\nu} \gamma$ . First one is an energy of the radiative photon  $E_\gamma$ . Figure 2.1 shows the  $E_\gamma$  distribution simulated by KKMC and TAUOLA generators.\* Here, the  $E_\gamma$  is defined in the center of mass system (CMS) of  $e^+ e^-$  beam.† As the histograms show, the distribution of the photon energy diverges in the limit  $E_\gamma \rightarrow 0$ . This comes from the fact that the  $d\Gamma/dE_\gamma^*$  has a singularity at  $E_\gamma^* \rightarrow 0$ , where  $E_\gamma^*$  represents the photon energy in the  $\tau$  rest frame.

For the reason noted above, the ordinary leptonic decay (no photon) and the radiative decay cannot be naturally distinguished. That is to say, the energy threshold is conceptually required: if  $E_\gamma^*$  exceeds a certain threshold, the event is regarded as the *radiative* decay. A conventional choice  $E_\gamma^* = 10$  MeV is determined in such a way that  $\gamma$  is realistically measured by experiment and at the same time branching ratio becomes reasonable fraction. In addition, if we apply typical photon energy threshold  $\sim 100$  MeV in the laboratory frame (such veto is necessary to exclude variety of backgrounds), a soft radiative events whose photon energy is less than  $E_\gamma^* < 10$  MeV is rarely selected (order of 1%). We use this specific value in the whole analysis to define efficiency of our radiative decay.‡ The energy threshold of  $E_\gamma^* = 10$  is also used to define the branching ratio of radiative decay, which is explained in next subsection.

In reality, it is also required to determine lower threshold to generate the radiative decays by MC simulation. The TAUOLA generator adopts the generating-energy threshold  $E_{\gamma\text{gen}}^* = m_\tau/1000$ , which should obviously satisfy  $E_{\gamma\text{gen}}^* < E_\gamma^*$ . Figure 2.2 shows the fraction of the radiative process out of total amounts of generated leptonic decays as a function of  $E_\gamma^*$  threshold. These plots tell that the fraction of radiative events (used to determine efficiency) are 10.6% and 2.6% for electron and muon modes, respectively.

A cosine of angle between the outgoing lepton and photon  $\cos\theta_{\ell\gamma}$  is another important variable in this analysis. Because the decay amplitude is approximately expressed as a sum of  $[\theta_{\ell\gamma}^2 + m_l^2/E_l^2]^{-n}$

---

\*These generators are explained in Sec. 3.4.

†Otherwise stated, variables without any labels always mean those of the CMS.

‡From theoretical point of view, to justify the precision of perturbation technique, the choice of smaller value less than 10 MeV is not reasonable.

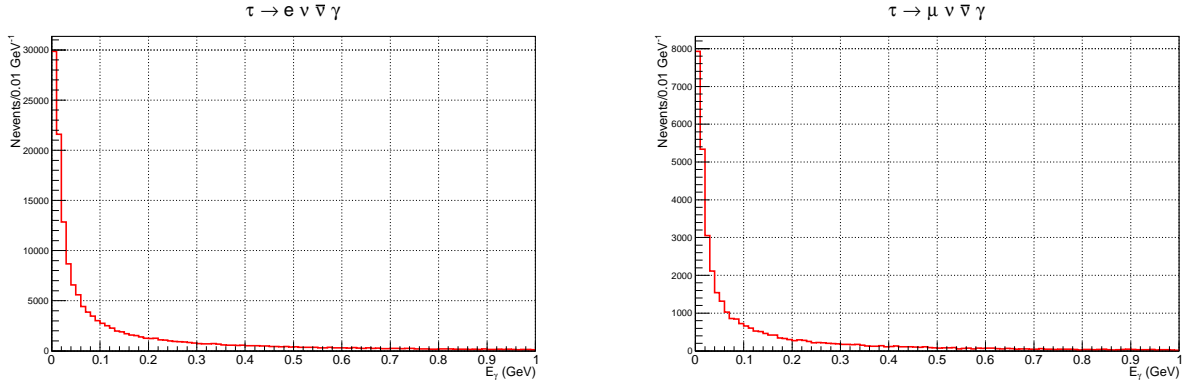


Figure 2.1: Energy distribution of the radiative photon on the CMS generated by KKMC.

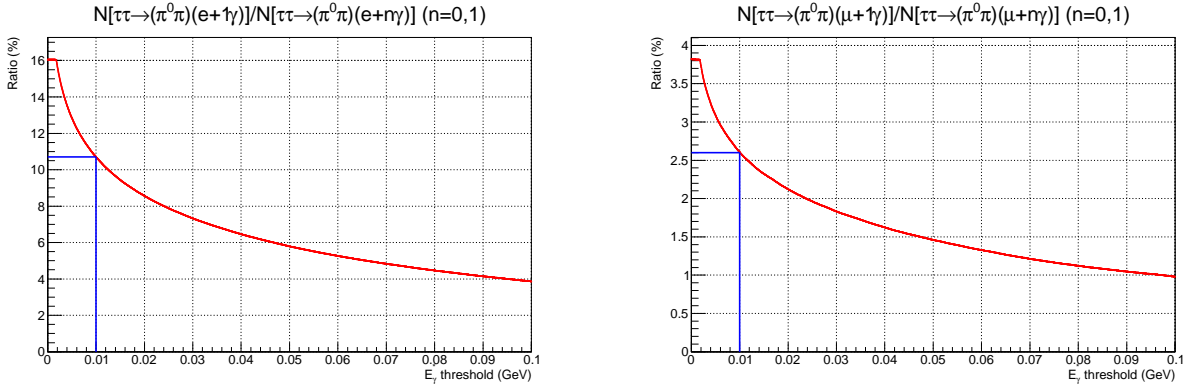


Figure 2.2: Fraction of event having a photon energy above threshold (out of generated leptonic decays): (left)  $\tau^- \rightarrow e^- \nu \bar{\nu} \gamma$  and (right)  $\tau^- \rightarrow \mu^- \nu \bar{\nu} \gamma$ . The horizontal axis represents photon energy threshold on the  $\tau$ -rest frame and the vertical axis indicates the ratio. If conventional definition,  $E_\gamma^* = 10$  MeV, is used, the fractions are 10.6% and 2.6% for the electron and muon modes, respectively. The flat shape of small-energy region comes from the generating-energy threshold  $E_{\gamma\text{gen}}^* = m_\tau/1000$ .



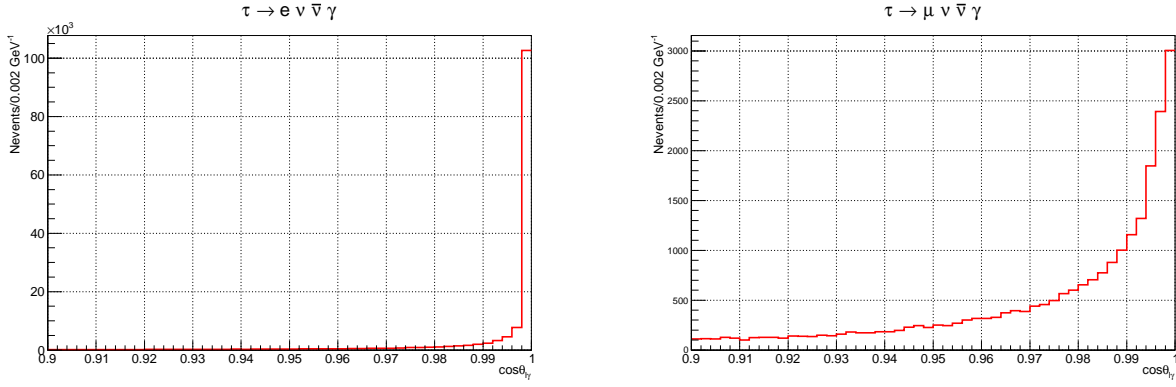


Figure 2.3: Distribution of an angle between lepton and photon: (left)  $\tau^- \rightarrow e^- \nu \bar{\nu} \gamma$  and (right)  $\tau^- \rightarrow \mu^- \nu \bar{\nu} \gamma$ . The horizontal is  $\cos\theta_{l\gamma}$ .

for an integer  $n$ , the heavier mass of muon exhibits a broad distribution as can be seen in Fig. 2.3. The requirement of maximum-allowed angle between lepton and photon is used to discriminate signal from background contamination.

## 2.2 Spin-spin correlation of $\tau^+ \tau^-$ and two-body decay $\tau^+ \rightarrow \rho^+ \bar{\nu} \rightarrow \pi^+ \pi^0 \bar{\nu}$

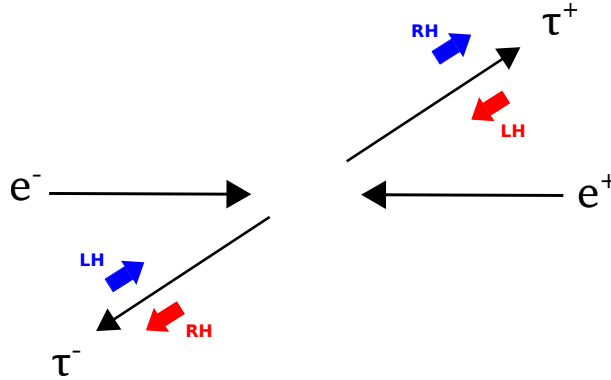


Figure 2.4: Spin-spin correlation in  $e^+e^- \rightarrow \tau^+\tau^-$  process. The helicities of  $\tau^+\tau^-$  pair are preferably anti-correlated each other. Same color indicates same combination.

As mentioned in Sec. 1.3, the measurement of the  $\xi\kappa$  requires the information of the spin of mother  $\tau$ . This is extracted through the correlation of the  $\tau$  and its partner  $\tau$  in  $e^+e^- \rightarrow \tau^+\tau^-$  production. As drawn in Fig. 2.4, the helicities of  $\tau^+\tau^-$  pair are anti-correlated (against) each other. Since this process occurs through an exchange of  $\gamma$  (spin-1 particle), the angular conservation permits only either  $\tau_R^+\tau_L^-$  or  $\tau_L^+\tau_R^-$  states in the high energy limit  $E_\tau \rightarrow \infty$ , where  $L$  and  $R$  denote the helicities of taus. In case of beam energy of KEKB accelerator (approximately  $E_\tau \sim 5$  GeV), 95% of  $\tau^+\tau^-$  pairs are anti-correlated while 5% are correlated.

In the other side of  $\tau$ , or sometimes called *tag-side*, we use  $\tau^+ \rightarrow \pi^+ \pi^0 \bar{\nu}$  decay. In general, the hadronic decay of the  $\tau$  with two pseudo-scalar mesons have a quantum number  $J^P$  of either  $0^+$  or  $1^-$ . The conserved vector current (CVC) theorem allows only the latter choice, hence the spin-1 excited state of  $\rho(770)$  as well as its radial excitations  $\rho(1450)$ ,  $\rho(1700)$ ... are believed to dominate this process. Figure 2.5 shows the invariant mass distribution of the two-pion system for  $\tau^+ \rightarrow \pi^+ \pi^0 \bar{\nu}$  process simulated by the KKMC and TAUOLA generators.

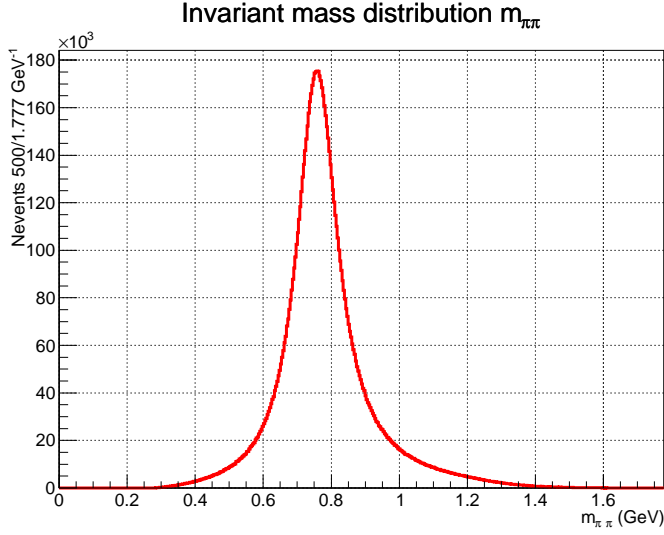


Figure 2.5: Invariant mass distribution for the two-pion system generated by KKMC and TAUOLA.

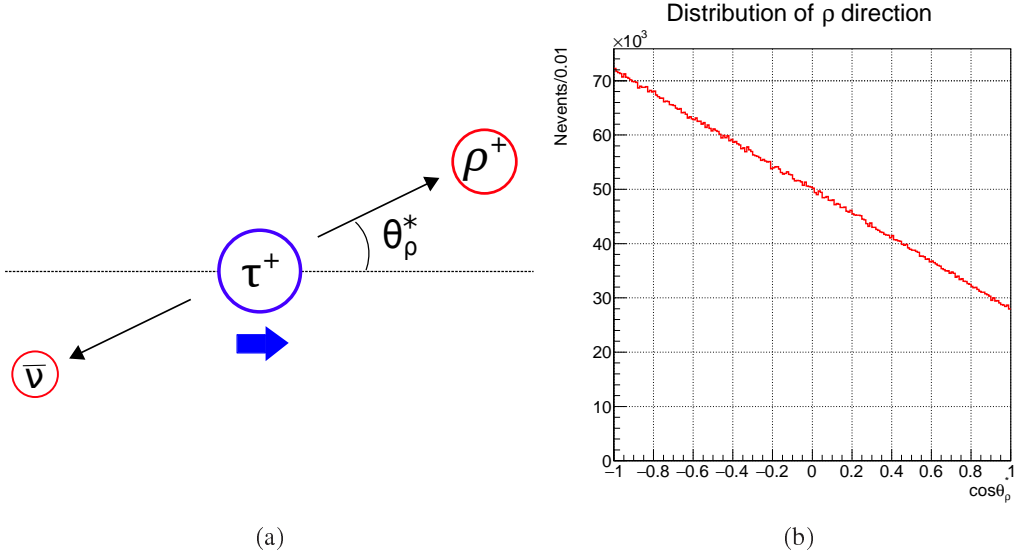


Figure 2.6: Angular dependence of  $\rho^+$  movement in  $\tau^+ \rightarrow \rho^+ \bar{\nu}$  decay: (a)  $\theta_\rho^*$  is the angle between spin direction of tau and  $\rho^+$  in the  $\tau^+$  rest frame (b) distribution of  $\cos\theta_\rho^*$ . The blue arrow represents spin of  $\tau^+$ .

The spin direction of  $\tau^+$  affects the angular distribution of  $\rho^+$  particle. As Fig. 2.6 shows, the  $\rho^+$  are preferably generated into the opposite direction of the tau spin. This situation can be explained by a superposition of two amplitudes of  $a$  and  $b$ :

$$|a\rangle = |0\rangle \otimes \left| \frac{1}{2} \right\rangle \quad : \quad \mathcal{A}_a = \langle a|+\rangle, \quad (2.1)$$

$$|b\rangle = |1\rangle \otimes \left| \frac{1}{2} \right\rangle \quad : \quad \mathcal{A}_b = \langle b|+\rangle, \quad (2.2)$$

where the brackets in the right hand side represent helicities of  $\rho^+$  meson and  $\bar{\nu}$ ,  $|+\rangle$  represents the initial state of  $\tau^+$  polarized in  $+z$  direction, and  $\mathcal{A}_a$  and  $\mathcal{A}_b$  are the corresponding amplitudes of each channel whose maximums have a relation given by  $|\mathcal{A}_a^{\max}/\mathcal{A}_b^{\max}| = \sqrt{2}m_\rho/m_\tau$  [35]. As illustrated in Fig. 2.7, the amplitudes of  $a$  and  $b$  become maximum (minimum) at  $\theta_\rho^* = \pi$  (0) and  $\theta_\rho^* = 0$  ( $\pi$ ),

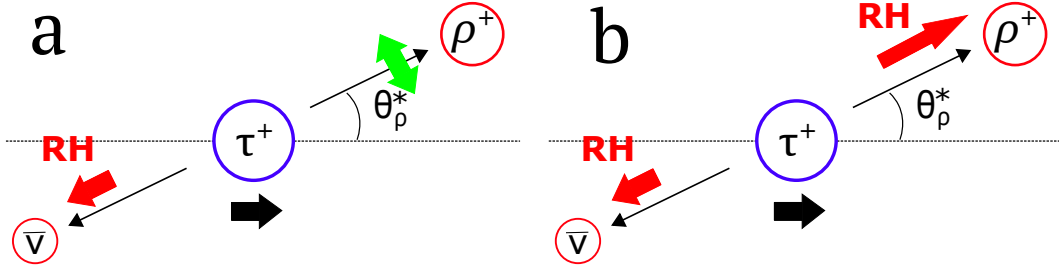


Figure 2.7: Two spin configurations of  $\rho^+$  and  $\bar{\nu}$ : (a) the angular momentum perfectly conserves when  $\theta_{\rho^*} = \pi$  while violates when  $\theta_{\rho^*} = 0$ : (b) the situation becomes opposite. As a result, (a) and (b) have angular dependences of  $\sin \theta_{\rho^*}/2$  and  $\cos \theta_{\rho^*}/2$ , respectively.

respectively, and in fact it is known that the angular dependences are given by  $\sin \theta_{\rho^*}/2$  and  $\cos \theta_{\rho^*}/2$ . Observed probability is thus calculated to be

$$P(\theta) \propto 1 - \frac{|\mathcal{A}_a^{\max}|^2 - |\mathcal{A}_b^{\max}|^2}{|\mathcal{A}_a^{\max}|^2 + |\mathcal{A}_b^{\max}|^2} \cos \theta_{\rho^*} = 1 - \frac{m_{\tau}^2 - 2m_{\rho}^2}{m_{\tau}^2 + 2m_{\rho}^2} \cos \theta_{\rho^*} \sim 1 - 0.43 \cos \theta_{\rho^*}. \quad (2.3)$$

This linear dependence on  $\cos \theta_{\rho^*}$  is seen in the figure.

This *rho decay* is chosen because of its large branching fraction  $\mathcal{B}(\tau^+ \rightarrow \pi^+ \pi^0 \bar{\nu}) = (25.52 \pm 0.09)\%$  [7] and relatively simple form-factor, which results in an easy implementation of the PDF. As a matter of fact, taking into account the magnitude of polarizations and branching fractions, Ref. [35] reports that  $\tau^+ \rightarrow \pi^+ \pi^0 \bar{\nu}$  exhibits the largest sensitivities of all  $\tau$  decays on the polarization measurement.

As explained above, through the spin-spin correlation in  $e^+e^- \rightarrow \tau^+\tau^-$  production and the angular distribution of pions from *rho decay*, information of  $\tau^-$  spin is indirectly extracted only to measure the  $\xi\kappa$  parameter.

## 2.3 Branching ratio of $\tau^- \rightarrow \ell^- \nu \bar{\nu} \gamma$ decays

Before starting this project to measure the Michel parameters, the most accurate experimental values of the branching ratio of  $\tau^- \rightarrow \ell^- \nu \bar{\nu} \gamma$  decay were the measurement by the CLEO experiment [36]. Using  $4.68 \text{ fb}^{-1}$  of  $e^+e^-$  annihilation data, the CLEO obtained

$$\mathcal{B}_{\text{CLEO}}^{\text{EX.}}(\tau^- \rightarrow e^- \nu \bar{\nu} \gamma)_{E_{\gamma}^* > 10 \text{ MeV}} = (1.75 \pm 0.06 \pm 0.017) \times 10^{-2}, \quad (2.4)$$

$$\mathcal{B}_{\text{CLEO}}^{\text{EX.}}(\tau^- \rightarrow \mu^- \nu \bar{\nu} \gamma)_{E_{\gamma}^* > 10 \text{ MeV}} = (3.61 \pm 0.16 \pm 0.35) \times 10^{-3}, \quad (2.5)$$

where the first uncertainty is statistical and second is systematic. This measurement was renewed in 2015 by BaBar experiment using much more abundant statistics of  $431 \text{ fb}^{-1}$   $e^+e^-$  collision data to give [37],

$$\mathcal{B}_{\text{BaBar}}^{\text{EX.}}(\tau^- \rightarrow e^- \nu \bar{\nu} \gamma)_{E_{\gamma}^* > 10 \text{ MeV}} = (1.847 \pm 0.015 \pm 0.052) \times 10^{-2}, \quad (2.6)$$

$$\mathcal{B}_{\text{BaBar}}^{\text{EX.}}(\tau^- \rightarrow \mu^- \nu \bar{\nu} \gamma)_{E_{\gamma}^* > 10 \text{ MeV}} = (3.69 \pm 0.03 \pm 0.10) \times 10^{-3}. \quad (2.7)$$

These measurements are in good agreement with the theoretical calculations, which rely on the formula given by [38, 39].

On the other side, as reported by Ref. [40] in 2015, the renewal of theory found a deviation between these experimental values and the up-to-date theoretical prediction. In this update, the next leading order quantum electrodynamics (QED) correction was newly taken into account, where up to order- $\alpha^2$  effects were included. The additional  $\alpha$ -correction gives not only the loop correction, but

also another infrared divergence in the final result. Therefore, the conceptual treatment of photon differs from that of single emission: a combination of one visible photon and one invisible photon ( $\gamma_{\text{soft}}, \gamma_{\text{vis.}}$ ) is categorized as an *exclusive* mode while a combination where at least one visible photon exists ( $\gamma_{\text{vis.}}, \gamma_{\text{vis.}}$ ) + ( $\gamma_{\text{soft}}, \gamma_{\text{vis.}}$ ), is categorized as an *inclusive* mode (both visible mode ( $\gamma_{\text{vis.}}, \gamma_{\text{vis.}}$ ) is also distinguished as a *doubly decay*). Interestingly, the measurement of mentioned branching ratios for  $\tau^- \rightarrow e^- \nu \bar{\nu} \gamma$  decay, which is in fact approximately the exclusive mode, deviates from the exclusive SM prediction by  $3.5\sigma$ . According to the reference, the leading order (LO) calculation predicts

$$\mathcal{B}_{\text{LO}}^{\text{Th}}(\tau^- \rightarrow e^- \nu \bar{\nu} \gamma)_{E_{\gamma}^* > 10 \text{ MeV}} = 1.834 \times 10^{-2}, \quad (2.8)$$

$$\mathcal{B}_{\text{LO}}^{\text{Th}}(\tau^- \rightarrow \mu^- \nu \bar{\nu} \gamma)_{E_{\gamma}^* > 10 \text{ MeV}} = 3.663 \times 10^{-3}, \quad (2.9)$$

whereas the next-leading order (NLO) predicts

$$d\mathcal{B}_{\text{NLO}}^{\text{Th}}(\tau^- \rightarrow e^- \nu \bar{\nu} \gamma)_{E_{\gamma}^* > 10 \text{ MeV}} = 1.645(19) \times 10^{-2}, \quad (2.10)$$

$$\mathcal{B}_{\text{NLO}}^{\text{Th}}(\tau^- \rightarrow \mu^- \nu \bar{\nu} \gamma)_{E_{\gamma}^* > 10 \text{ MeV}} = 3.572(3) \times 10^{-3}. \quad (2.11)$$

Herein, the errors for the NLO calculation arise from a next-next-leading order effects, numerical calculation and an experimental value of the lifetime of the  $\tau$ .

As a byproduct of this analysis, we also measure the branching ratio. The procedures are described in detail in Chapter 9.

## 2.4 Effect of the Michel parameter on the distribution

In this section, we demonstrate the effect of the Michel parameter on the spectra of daughter particles. As we shall explain, every event of signal  $\tau^+ \tau^- \rightarrow (\pi^+ \pi^0 \bar{\nu})(\ell^- \nu \bar{\nu} \gamma)$  is represented as a corresponding point in the twelve-dimension phase space. Due to its large dimension, it is difficult to intuitively observe the change of distribution. However, we can glimpse the dependence of spectra of the lepton and photon variables on the Michel parameter by observing distributions projected on 1D-axis.

The dependence on  $\xi\kappa$  disappears when we integrate isotropically in the phase space because  $\xi\kappa$  is included in the spin-dependent term of the differential decay width as:

$$\frac{d\Gamma(\tau \rightarrow \ell \nu \bar{\nu} \gamma)}{d\text{PS}} \supset \mathcal{S}_{\tau}^* \cdot \mathbf{V}^* \xi\kappa, \quad (2.12)$$

where  $\mathbf{V}^*$  is a vector function, which does not depend on  $\mathcal{S}_{\tau}^*$  and is written as a linear combination of the direction of lepton  $\mathbf{n}_{\ell}^*$  and photon  $\mathbf{n}_{\gamma}^*$ . Integrations over the directions of lepton and photon ( $\mathbf{n}_{\ell}^*$  and  $\mathbf{n}_{\gamma}^*$ ) give a net contribution of zero. Thus it is required to adopt some asymmetric manipulation to visualize  $\xi\kappa$  effects. To separate the overall phase space, we use a helicity sensitive parameter  $\omega_h$ , which represents polarization of the  $\tau$  and is calculated only from observables. By construction,  $\omega_h$  varies in an open interval:  $\omega_h \in (-1, 1)$ . The positive value of  $\omega_h$  implies it is probable that the spin of the  $\tau^+$  ( $\rightarrow \pi^+ \pi^0 \bar{\nu}$ ) is pointing to the same (opposite when  $\tau^-$  decays to  $\pi^- \pi^0 \nu$ ) direction as that of  $\tau^+$  movement. The detailed definition of  $\omega_h$  is introduced in Sec. 6.1. To observe the asymmetric effect, we integrate the differential decay width in the phase space only where  $\omega_h$  becomes positive.

Figures 2.8 and 2.9 show the dependence of the shape of momenta of lepton and photon on the Michel parameters. Each distribution is calculated for a certain value of the Michel parameter by the integration of the differential decay widths with other variables. For demonstration purpose, the range of variation of the Michel parameters are chosen to be larger than physically-realistic values.

As explained above, only  $\omega_h > 0$  events are used for the integration to draw Fig. 2.9. We observe that the magnitude of the momentum of lepton is more strongly affected by the Michel parameters than other variables. Furthermore, the dependence of Michel parameter on  $\tau^- \rightarrow \mu^- \nu \bar{\nu} \gamma$  decay is

larger than that of  $\tau^- \rightarrow e^- \nu \bar{\nu} \gamma$  decay. This comes from the fact that the contribution from physics BSM is enhanced by a factor proportional to  $m_\ell/m_\tau$  as the explicit formula is introduced in Sec. 5.4.1.

Here, we show the variation of distribution assuming very large Michel parameters, the real possible values are, however, of order of 1 and this implies that measurement of these Michel parameters requires the precise verification of the small variation of spectrum shape. That is why we need to observe large number of events.

## 2.5 Determination of $\tau$ direction

Due to the short lifetime of  $\tau$ , it is difficult to directly measure the decay direction. Nevertheless, in the  $\tau^+ \tau^-$  rest frame, we can constrain their direction assuming the masses of neutrinos to be zero. When the leptonic decay occurs, two neutrinos appear in the final state. Because the two-body system of  $\nu \bar{\nu}$  must not have a negative invariant mass, an inequality holds:

$$\begin{aligned} 0 &\leq M_{\nu\bar{\nu}}^2 = p_{\nu\bar{\nu}}^2 = (p_\tau - p_\ell)^2 \\ \Leftrightarrow \cos \theta_{\tau\ell} &\geq \frac{2E_\tau E_\ell - M_\tau^2 - M_\ell^2}{2P_\tau P_\ell}, \end{aligned} \quad (2.13)$$

which means that the  $\tau$  decays in the region enclosed by a cone around lepton direction. On the other hand, if the  $\tau$  decays hadronically, one neutrino is produced and gives an equality:<sup>§</sup>

$$\begin{aligned} 0 &= M_\nu^2 = p_\nu^2 = (p_\tau - p_h)^2 \\ \Leftrightarrow \cos \theta_{\tau h} &= \frac{2E_\tau E_h - M_\tau^2 - M_h^2}{2P_\tau P_h}, \end{aligned} \quad (2.14)$$

where  $p_h$  is a sum of four vectors for the hadronic daughters and  $M_h$  is its invariant mass. This means that the  $\tau$  decays inside the surface of a cone determined from the direction of hadron momentum. Depending on the conditions, through which type two taus decay, we can divide the situation into three categories:  $(h, h)$ ,  $(\ell, h)$  and  $(\ell, \ell)$ , where  $(a, b)$  with  $a, b = l, h$  means two tau decay leptonically ( $l$ ) or hadronically ( $h$ ). As Fig 2.10 shows,  $(h, h)$  decay enables us to fix the direction of the tau into two candidates. If either of the  $\tau$  decays leptonically, the direction is no more fixed and becomes a region:  $(\ell, h)$  constrains on a line and  $(\ell, \ell)$  constrains on a region. In the case of signal of this analysis— $\tau^- \rightarrow \ell^- \nu \bar{\nu} \gamma$  and  $\tau^+ \rightarrow \pi^+ \pi^0 \bar{\nu}$ —the candidate becomes a line. Therefore, we parametrize the direction using one parameter  $\Phi \in [\Phi_1, \Phi_2]$ . As described later, this determination of  $\tau$  direction is used to describe a probability density function (PDF).

---

<sup>§</sup>Current upper limit of the mass of tau neutrino  $m_{\nu_\tau} \leq 18.2$  MeV [41] is practically sufficient to justify this equation.

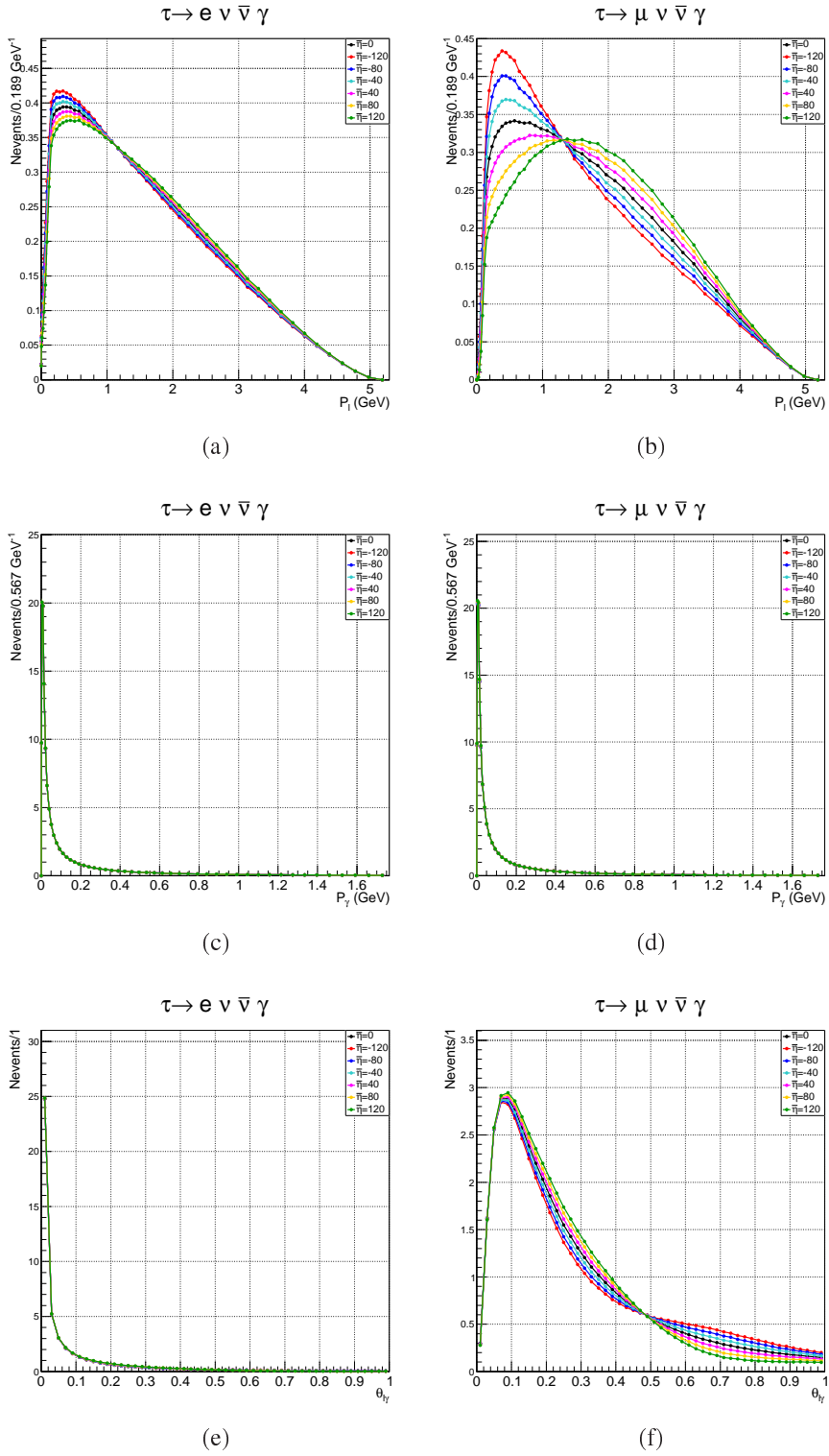


Figure 2.8: Dependence of momenta and angles on  $\bar{\eta}$ : left figures (a)(c)(d) represent dependence of the shape of  $P_l$ ,  $P_\gamma$  and  $\theta_{l\gamma}$  spectra on  $\bar{\eta}$  for  $\tau \rightarrow e\nu\bar{\nu}\gamma$  decay and right figures (b)(d)(f) represent those for  $\tau \rightarrow \mu\nu\bar{\nu}\gamma$  decay.

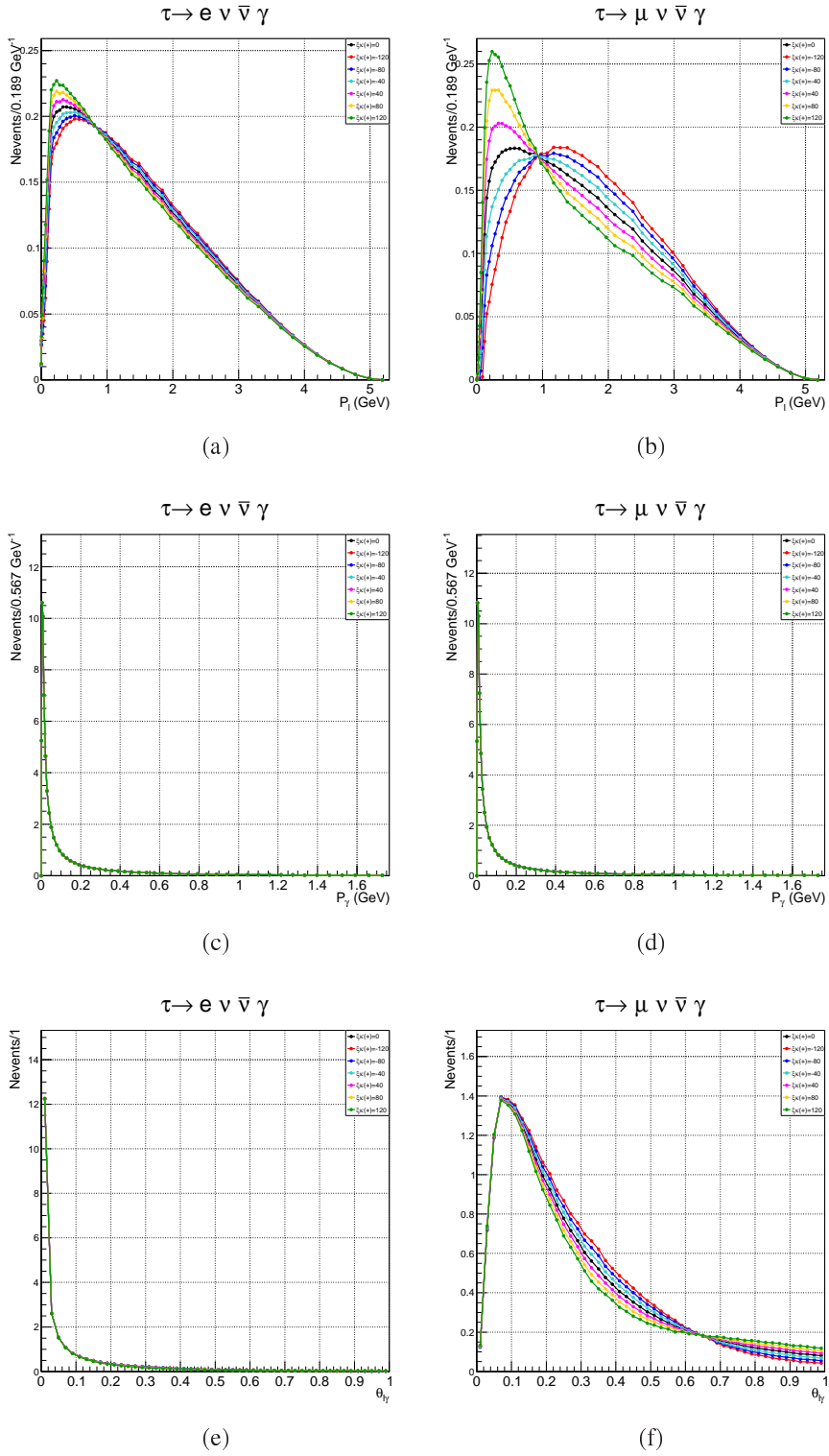


Figure 2.9: Dependence of momenta and angles on  $\xi_\kappa$ : left figures (a)(c)(d) represent dependence of the shape of  $P_\ell$ ,  $P_\gamma$  and  $\theta_{\ell\gamma}$  spectra on  $\xi_\kappa$  for  $\tau \rightarrow e\nu\bar{\nu}\gamma$  decay and right figures (b)(d)(f) represent those for  $\tau \rightarrow \mu\nu\bar{\nu}\gamma$  decay.

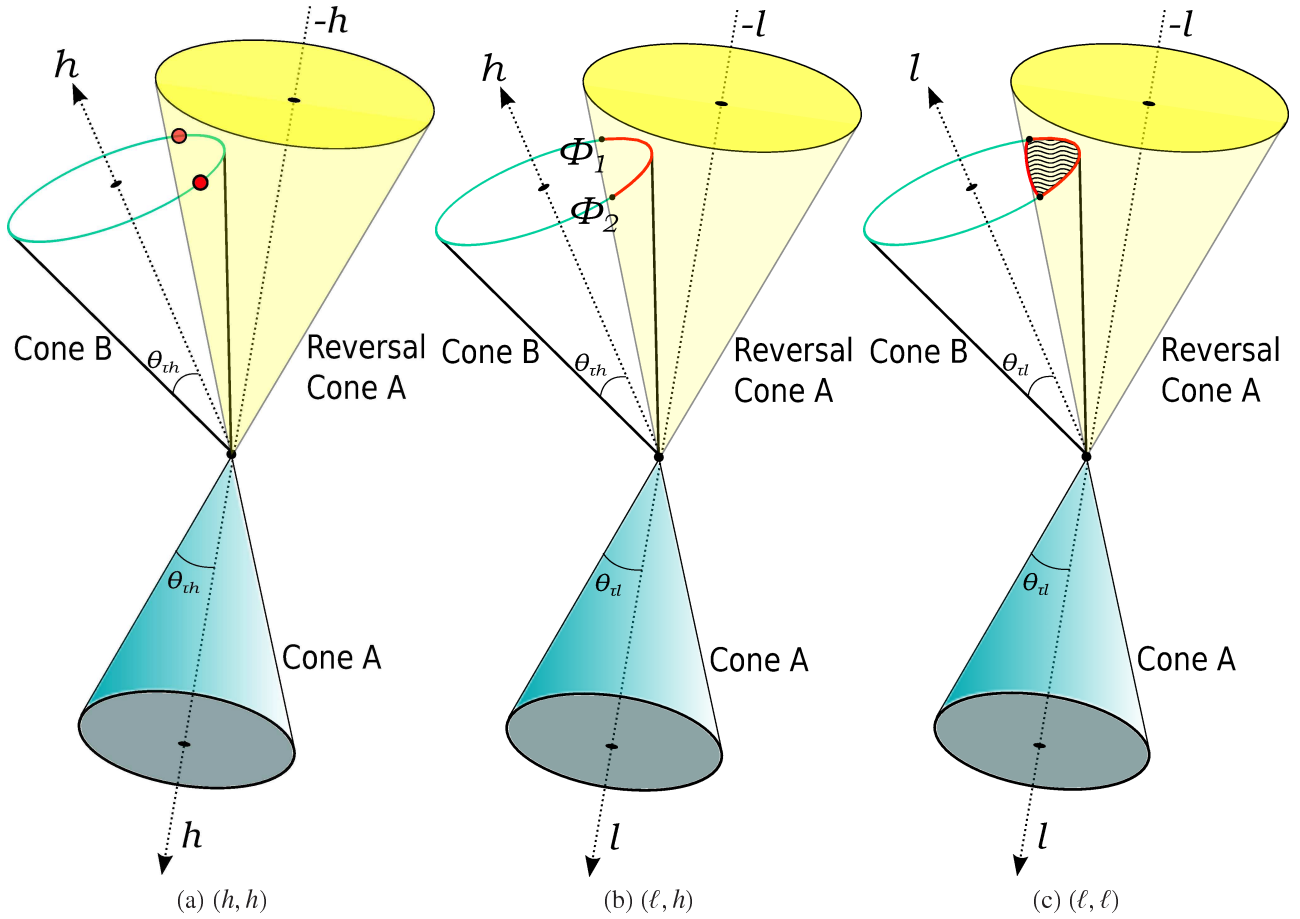


Figure 2.10: Kinematics of  $\tau\tau$  decay for (a)  $(h, h)$ , (b)  $(\ell, h)$  and (c)  $(\ell, \ell)$ . Cones A and B are surfaces which satisfy condition:  $p_{\text{miss}}^2 = 0$ . In the case of  $(h, h)$  decay, the candidate of the  $\tau$  direction becomes generally two points determined by crossed points of the reversal cone A and cone B. Similarly in  $(\ell, h)$  case, the candidate becomes line as colored by red and  $(\ell, \ell)$  constrains onto a region enclosed by red curve. In the case of signal decay,  $\tau^+\tau^- \rightarrow (\pi^+\pi^0\bar{\nu})(\ell^-\nu\bar{\nu}\gamma)$ , the candidate is line (b).



# Chapter 3

## Experimental Apparatus

We describe the experimental apparatus which realizes the measurement of the Michel parameters,  $\bar{\eta}$  and  $\xi\kappa$ , using  $e^+e^- \rightarrow \tau^+\tau^- \rightarrow (\pi^+\pi^0\nu)(\ell^-\nu\bar{\nu}\gamma)$  process. Events are produced by the KEKB accelerator and observed/recorded by the Belle detector.

### 3.1 The KEKB accelerator

The KEKB accelerator is an asymmetric energy collider of  $e^+$  and  $e^-$ . The beam energies of  $E_{e^-} = 8.0$  GeV and  $E_{e^+} = 3.5$  GeV are chosen such that the center of mass energy coincides with a mass of resonance state of  $\Upsilon(4S)$ :  $\sqrt{s} = 10.58$  GeV where  $s$  is the Mandelstam variable. The  $\Upsilon(4S)$  state, which consists of  $b\bar{b}$  quark pair, successively decays into  $B\bar{B}$  pairs. Meanwhile, via a virtual  $\gamma$  interchange, the  $e^+$  and  $e^-$  pair also annihilates into  $\tau^+\tau^-$  and  $c\bar{c}$  pairs, etc. The asymmetry of beam,  $\beta\gamma = 0.425$ , is intended to enlarge the decay lengths of  $B$  mesons in the laboratory frame to gain an effective time resolution for the measurement of their decay rates.

A key goal of KEKB accelerator is to produce  $B$  and  $\tau$  particles of interest as many as possible. In fact, KEKB achieved the maximum instantaneous luminosity  $L = 2.11 \times 10^{34}$  cm<sup>-2</sup>s<sup>-1</sup>, which is the world-largest instantaneous luminosity at the time of writing.\* For this reason, KEKB accelerator is called *B-factory* or  *$\tau$ -factory*. To realize the precise measurement of  $\tau^- \rightarrow \ell^-\nu\bar{\nu}\gamma$  decay (order  $\alpha$ -suppressed relative to the ordinary leptonic decay  $\tau^- \rightarrow \ell^-\nu\bar{\nu}$ ), the large number of taus thanks to the  $\tau$ -factory are necessary.

Not only did the KEKB accumulated  $e^+e^-$  annihilation data at  $\Upsilon(4S)$  energy, but it also collected data at different energy settings such as mass resonances of  $\Upsilon(1S)$  (9.46 GeV/ $c^2$ ),  $\Upsilon(2S)$  (10.02 GeV/ $c^2$ ) and  $\Upsilon(5S)$  (10.86 GeV/ $c^2$ ). At these energies, the  $e^+e^- \rightarrow \tau^+\tau^-$  process still occurs, however, the situations of event selection and trigger are not necessarily same as that of  $\Upsilon(4S)$ , and moreover the different beam energies make the description of PDF (which is explained later) complex. For this reason, we use only  $\Upsilon(4S)$  resonance data, which amounts to 703fb<sup>-1</sup> and corresponds to 70% of all data.

Figure 3.1 shows an overall view of the KEKB accelerator. The electrons are generated from a thermal electron while positrons are obtained by colliding 4 GeV  $e^-$  beam into a high-Z material (tungsten) in which a gamma conversion  $\gamma \rightarrow e^+e^-$  generates the positrons. Both  $e^+$  and  $e^-$  are accelerated by a linear accelerator (LINAC) and injected into a low energy ring (LER) and a high energy ring (HER), respectively. At Tsukuba area, the  $e^+$  and  $e^-$  collide at interaction point (IP) with a crossing angle of 22 mrad enclosed by the Belle detector. In table 3.1, the machine parameters of KEKB accelerator are summarized.

---

\*The upgrade project of the Belle experiment, Belle II, is planning to start physics data taking from 2017 using the Super KEKB accelerator and Belle II detector, where further increase of the luminosity by a factor of fifty is expected. In Chapter 10, we explain the prospect of this analysis using data from the next-generation experiment.

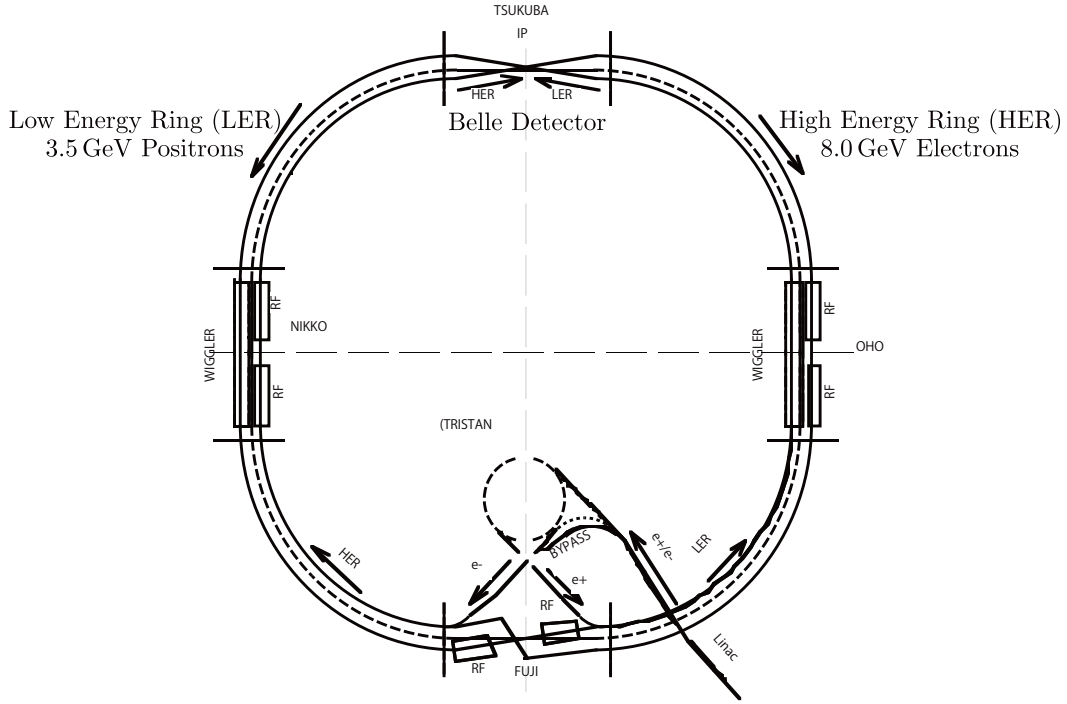


Figure 3.1: A drawing of KEKB accelerator. Electrons and positrons circulate the high and low energy rings in clockwise and anti-clockwise, respectively. The Belle detector is located at the Tsukuba hall [42].

Table 3.1: KEKB accelerator machine parameter

Item	HER ( $e^-$ )	LER ( $e^+$ )
Circumference (m)	3016	
Beam energy (GeV)	8.0	3.5
Beam current (A)	1.6	1.2
Beam-beam parameter $\xi_y$ (mm) †	0.09	0.129
Beta function at IP $\beta_y^*$ (mm) †	5.9	
Beam size at IP $\sigma_x/\sigma_y$ ( $\mu\text{m}/\mu\text{m}$ )	1.9/77	1.9/77
Number in bunches †	1584	
Crossing angle (mrad)	22	

† Achieved values

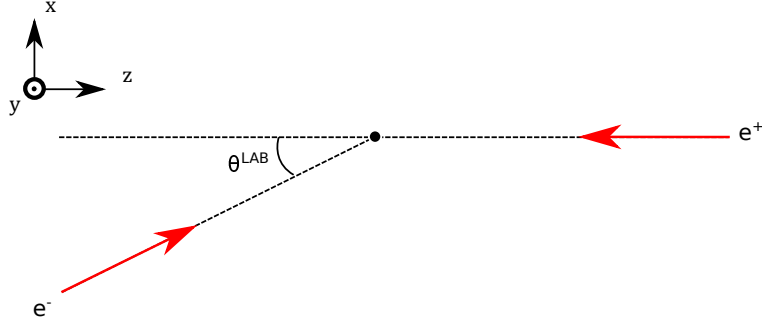


Figure 3.2: Definition of axis in the laboratory frame. The direction of  $z$ -axis is defined as reversal way of positron beam. The electron and positron movement forms  $xz$  plane.

### 3.1.1 Definition of frame

The directions of the electron and positron beams are not precisely back-to-back in the laboratory frame: the tilt angle is  $\theta_{\text{LAB}} = 22$  mrad. This situation is shown in Fig. 3.2.  $xyz$ -axis in the laboratory frame are defined by using beam direction: the positron direction is defined as a reversal way of  $+z$ , the plane, in which both electron and positron settle, is  $xz$ -plane. Therefore, the four vectors of the electron and positron are parametrized in the laboratory frame as:

$$p_{e^-}^{\text{LAB}} = (E_{e^-}^{\text{LAB}}, P_{e^-}^{\text{LAB}} \sin\theta^{\text{LAB}}, 0, P_{e^-}^{\text{LAB}} \cos\theta^{\text{LAB}}) \quad (3.1)$$

and

$$p_{e^+}^{\text{LAB}} = (E_{e^+}^{\text{LAB}}, 0, 0, -P_{e^+}^{\text{LAB}}). \quad (3.2)$$

The sum of these momenta  $p_{\text{CMS}}^{\text{LAB}}$  is that of the CMS in the laboratory frame and the velocity  $\beta_{\text{CMS}}^{\text{LAB}} = p_{\text{CMS}}^{\text{LAB}}/E_{\text{CMS}}^{\text{LAB}}$  allows us to convert four vectors in both frames each other. When the beam momenta are boosted to the CMS with this  $\beta_{\text{CMS}}^{\text{LAB}}$ , the direction of  $z$ -axis does not coincide with that of electron. For this reason, we rotate frame around  $y$ -axis by  $\theta$  such that both beams become collinear along  $z$ -axis, where  $\theta$  is approximately 13.24 mrad. The rotated frame is the definition of our CMS frame.

Here, we summarize the definition of the coordinate system and notations.

- Directions of  $z$  in both the laboratory and CMS frames are defined using  $e^+$  beam which points  $-z$  direction.
- Direction of  $x$  in both the laboratory and CMS frames are determined by rotating aforementioned  $z$  direction by  $90^\circ$  in the plane formed by the laboratory movements of electron and positron ( $\Pi$ -plane).
- Direction of  $x$  in CMS frame is determined by rotating the defined  $z$  direction by  $90^\circ$  in the  $\Pi$ -plane.
- Direction of  $y$  is defined by the cross product of vectors  $e_y = e_z \times e_x$ , where  $e_i$  ( $i$  is  $x$ ,  $y$  or  $z$ ) stands for the unit vector of  $i$  direction.
- $\theta$  stands for the polar angle from  $+z$  direction
- $\phi$  stands for the azimuthal angle around  $z$  axis
- $r$  stands for the transverse distance calculated as  $r = \sqrt{x^2 + y^2}$ .
- Transverse momentum of  $p$  is notated as  $p_t$  and defined as the  $r$  of  $p$ , i.e.,  $p_t = \sqrt{p_x^2 + p_y^2}$ .

Table 3.2: Information of sub-detectors of the Belle detectors [43]

Detector	Type	Configuration	Performance
SVD-1	Double sided Si-strip 3-layers Strip pitch 25(p)/42(n) $\mu\text{m}$	$r = 30.0, 45.5, 60.5 \text{ mm}$ $23^\circ < \theta < 139^\circ$	$\sigma_z = 42 \oplus 44/p\beta \sin^{5/2} \theta \mu\text{m}$ [44] $\sigma_{r\phi} = 19 \oplus 54/p\beta \sin^{3/2} \theta \mu\text{m}$ ( $p$ in GeV/ $c$ )
SVD-2	Double sided Si-strip 4-layers Strip pitch 50(p)/75(n) $\mu\text{m}$ (lay.1-3) 65(p)/73(n) $\mu\text{m}$ (lay.4)	$r = 20.0, 43.5, 70.0, 88.0 \text{ mm}$ $17^\circ < \theta < 150^\circ$	$\sigma_z = 26 \oplus 33/p\beta \sin^{5/2} \theta \mu\text{m}$ [44] $\sigma_{r\phi} = 17 \oplus 34/p\beta \sin^{3/2} \theta \mu\text{m}$ ( $p$ in GeV/ $c$ )
CDC	Wire drift chamber Anode: 50 layers Cathode: 3 layers	$r = 8.3\text{-}87.4 \text{ cm}$ (SVD1), $10.4\text{-}87.4 \text{ cm}$ (SVD2) $-77 < z < 160 \text{ cm}$ $17^\circ < \theta < 150^\circ$	$\sigma_{r\phi} = 130 \mu\text{m}$ $\sigma_z = 200 - 1400 \mu\text{m}$ $\sigma_{p_t}/p_t = 0.2\% p_t \oplus 0.3\%/\beta$ $\sigma_{dE/dx} = 6\%$
ECL	CsI Scintillator # crystals in barrel 6624 # crystals in endcap 2112	Barrel: $r = 125\text{-}162 \text{ cm}$ , $32.2^\circ < \theta < 128.7^\circ$ Endcap: $z = -102 \text{ cm}$ , $130.7^\circ < \theta < 155.1^\circ$ : $z = 196 \text{ cm}$ , $12.4^\circ < \theta < 31.4^\circ$	$\sigma_E/E = 1.3\%/\sqrt{E}$ $\sigma_{\text{pos}} = 0.5 \text{ cm}/\sqrt{E}$ ( $E$ in GeV)
ACC	Silica aerogel # aerogel in barrel 960 # aerogel in endcap 228	Barrel: $r = 89\text{-}117 \text{ cm}$ Endcap: $z = 1660 \text{ cm}$	$P(\pi K) < 10\%$ , $P(K K) > 80\%$ for $1.2 \text{ GeV}/c < P < 3.5 \text{ GeV}/c$
TOF	Plastic Scintillator 128 $\phi$ segmentation	$r = 120 \text{ cm}$	$2\sigma$ $K/\pi$ separation for $P < 1.2 \text{ GeV}/c$ $\sigma_t = 100 \text{ ps}$
KLM	Resistive plate counter 14 layers	Endcap: $20^\circ < \theta < 45^\circ$ : $125^\circ < \theta < 155^\circ$ Barrel: $45^\circ < \theta < 125^\circ$	$\Delta\phi = \Delta\theta = 30 \text{ mrad}$ .

## 3.2 The Belle detector

The Belle detector is a general-purpose measurement system which is composed of several sub-detectors. The detector is configured by 1.5 T superconducting solenoid and encloses the IP of the  $e^+e^-$  beam.

Figure 3.3 shows the overall view of the Belle detector. The decay vertices are measured by the silicon vertex detector (SVD) located just outside of a cylindrical beam pipe. Tracking of the charged particles are performed by the central drift chamber (CDC). Energy of electromagnetic shower is measured by the electromagnetic calorimeter (ECL). Particle identification is provided by the information of  $dE/dx$  measurements by the CDC, a shape of shower in the clusters and  $E/p$  measurement in the ECL, an aerogel Cherenkov counter (ACC) and a time-of-flight counter (TOF). The  $K_L$  and muons are identified by arrays of the resistive plate counters and iron plates located at the outermost part of the Belle detector named  $K_L$  and muons detector (KLM). All of these information is processed and recorded by a data acquisition (DAQ) system when events are selected by a trigger. The general information and performances of the sub-detectors are summarized in Table 3.2. In this section, we describe functions and principles of the sub-detectors.

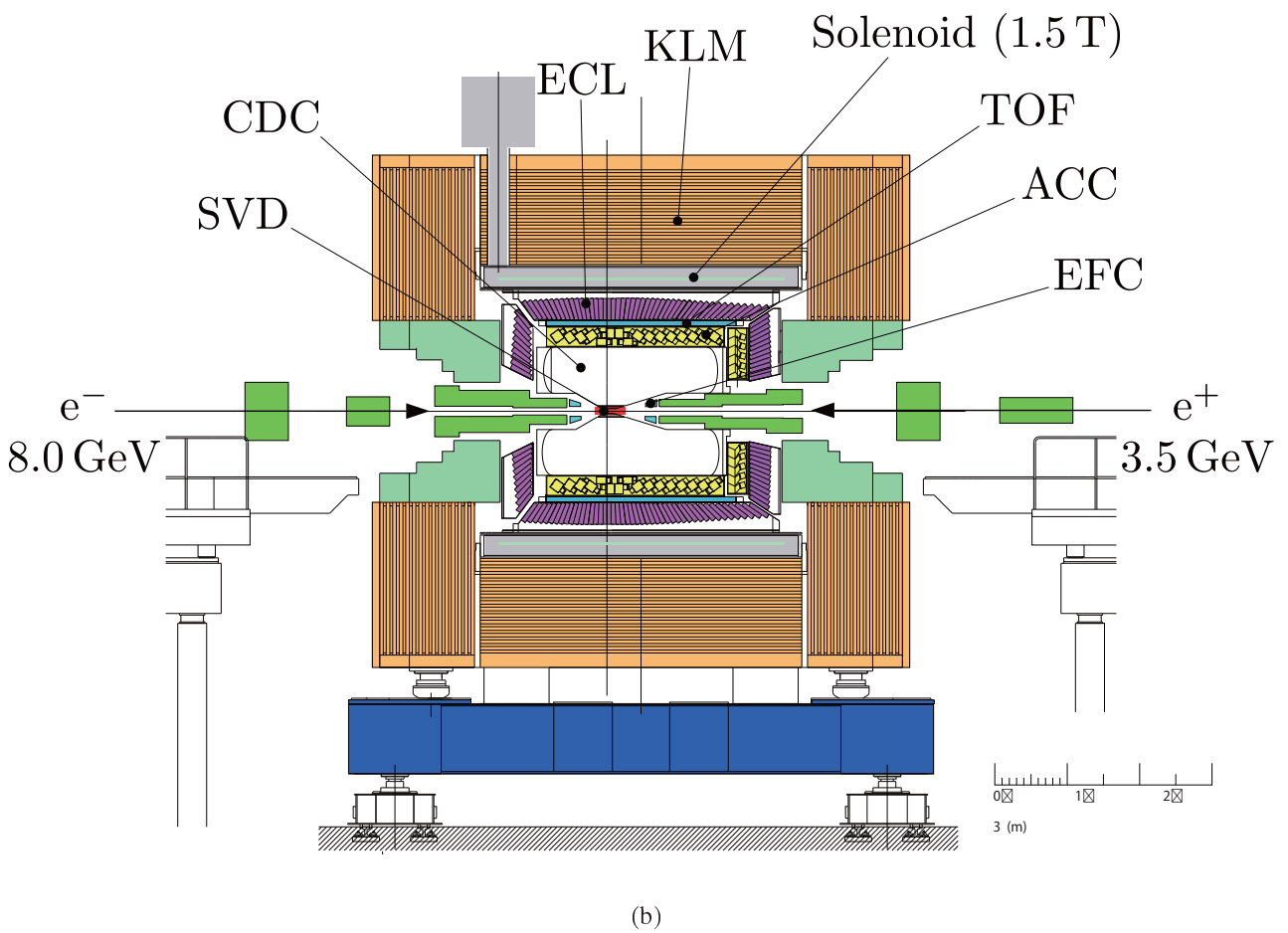
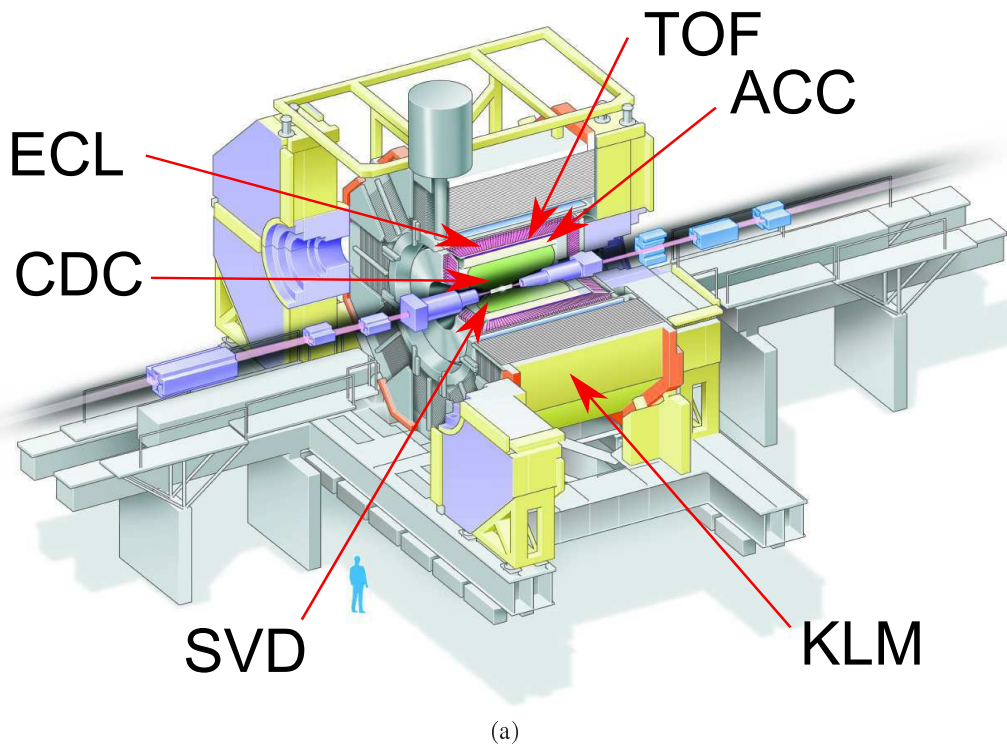


Figure 3.3: Drawings of the Belle detector: (a) the overall view and (b) the cross section [43].

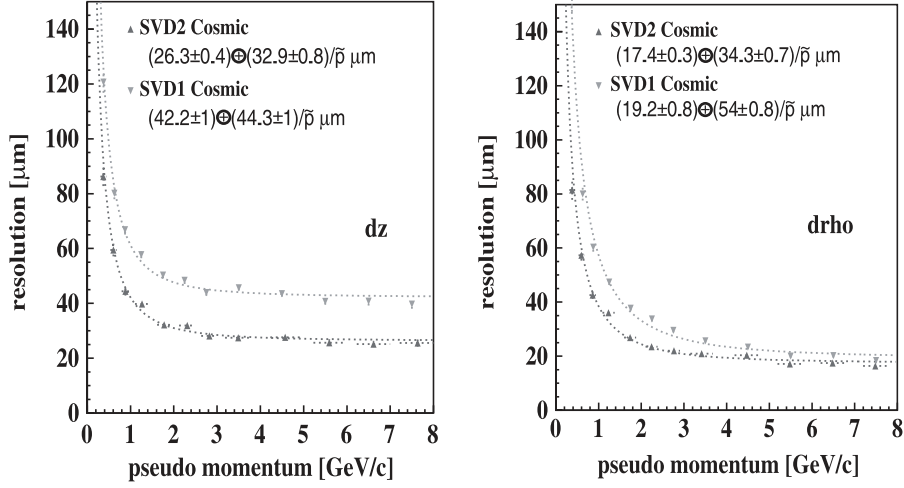


Figure 3.4: Impact parameter resolution of the SVD as a function of pseudo-momentum: (a)  $\sigma_z$  and (b)  $\sigma_{r\phi}$  [44].

### 3.2.1 Silicon Vertex Detector (SVD)

The main goal of the Belle experiment is to verify the mechanism of the CP violation in  $B$  decays, where the violation of the CP appears as a time dependent asymmetry of the decay rate between  $\Gamma_{B \rightarrow f_{CP}}(t)$  and  $\Gamma_{\bar{B} \rightarrow f_{CP}}(t)$  ( $f_{CP}$  stands for a CP eigenstate). Since the difference of the decay rate of  $B/\bar{B}$  mesons is measured as that of the flight length, the precise measurement of the vertex position is crucial. The SVD plays a role in locating the vertex position of  $B$  mesons. Furthermore, a low momentum track, which does not reach the CDC inner wall, is reconstructed only by the SVD. In this analysis, the SVD helps the CDC in the charged track reconstruction.

There are two types of SVDs. The first version is called SVD1 and worked until 2003. Because of a problem in the front-end chip, the SVD1 was upgraded to SVD2. The SVD1 (SVD2) is composed of three (four) layers located at radii  $r = 30.0, 45.5, 60.5 \text{ mm}$  ( $r = 20.0, 43.5, 70.0, 88.0 \text{ mm}$ ) and covers  $23^\circ < \theta < 139^\circ$  ( $17^\circ < \theta < 150^\circ$ ), which is constructed from 8, 10, 14 (6, 12, 18, 18) ladder structures, respectively. Each layer is made of double-sided Si-strip detectors (DSSD). The DSSD has crossed linear effective areas (strip) on top and bottom sides, which are orthogonally segmented along  $r\phi$  and  $z$  directions, respectively, and each strip is made by a p-type or n-type semiconductor.

When a charged particle passes through the p-n junction, the ionized electron-hole pair is separated by an applied high bias voltage and read out separately from p and n-side strips of the detector. The front-end circuit named VA1 chip provides an amplification of the current and a shaping of the signal. Figure 3.4 shows the achieved impact parameter resolution of the SVD1 and SVD2 as a function of pseudo-momentum, which takes into account the effective increase of the pass length inside material and defined by  $\tilde{p} = p\beta \sin^{5/2} \theta$  and  $\tilde{p} = p\beta \sin^{3/2} \theta$  for  $z$  and  $r\phi$  directions, respectively. The information of the SVD1 and SVD2 is summarized in Table 3.3.

### 3.2.2 Central Drift Chamber (CDC)

The CDC plays a role in the tracking of charged particle and a precise determination of the momentum. Since the Belle detector is in the magnetic field of  $B = 1.5 \text{ T}$ , the momentum of charged particle is determined according to  $p = 0.3B\rho$ , where  $p$  is a momentum of charged track in  $\text{GeV}/c$  and  $\rho$  is the observed curvature in meter. The trajectory of the charged track is parametrized by five free parameters (also known as a helix parameter) and fitted to a map of detected energy deposition. The helix parameter contains information of not only the magnitude of curvature but also the impact

Table 3.3: Information of SVDs

Item	SVD1	SVD2
# layers	3	4
$r$ (mm)	30.0, 45.5, 60.5	20.0, 43.5, 70.0, 88.0
coverage	$23^\circ < \theta < 139^\circ$	$17^\circ < \theta < 150^\circ$
# DSSD $\times$ # ladders		
layer1:	$2 \times 8$	$2 \times 6$
layer2:	$3 \times 10$	$3 \times 12$
layer3:	$4 \times 14$	$5 \times 18$
layer4:	-	$6 \times 18$
DSSD n-strips	$42 \mu\text{m} \times 640$	$50 \mu\text{m} \times 512$ (layer 1-3) $65 \mu\text{m} \times 512$ (layer 4)
DSSD p-strips	$25 \mu\text{m} \times 640$	$75 \mu\text{m} \times 1024$ (layer 1-3) $73 \mu\text{m} \times 1024$ (layer 4)
DSSD Thickness	$300 \mu\text{m}$	$300 \mu\text{m}$
Total number of channel	81920	110592

parameter, which is the distance of the closest approach to the interaction point and denoted as  $dr$  and  $dz$  in transverse and beam directions, respectively. The impact parameters are useful to reduce backgrounds such as secondary particles from beam and cosmic rays. Moreover, the CDC also provides information of the particle identification based on  $dE/dx$  and reliable trigger signals.

As the structure of CDC is shown in Fig. 3.5, the CDC is a cylindrical wire drift chamber which lies in the region  $83 \text{ mm} < r < 880 \text{ mm}$  for SVD1 term and  $104 \text{ mm} < r < 880 \text{ mm}$  for SVD2 term, respectively, and covers  $17^\circ < \theta < 150^\circ$  angle. The asymmetrical structure in  $z$ -direction is optimized for the boost of beam. The chamber has 8400 drift cells, all of which are grouped as axial or stereo super-layers. The stereo wires are tilted and allow us to determine  $z$ -position. A gas mixture of 50% He and 50%  $\text{C}_2\text{H}_6$  was chosen because of its small low- $Z$  so as to reduce the multiple scattering for low momentum tracks.

The readout signals from the chamber are amplified by Radeka-type pre-amplifier [46] and sent to the shaper and discriminator. The data are finally processed by a charge-to-time converter with retaining the information of the drift time and pulse height. With an aid of SVD, the combined charged-track momentum resolution is given by:

$$\frac{\sigma_{p_T}}{p_T} = \left( 0.19 p_T \oplus \frac{0.30}{\beta} \right) \%, \quad (3.3)$$

where  $p_T$  is in  $\text{GeV}/c$  and the tracking efficiency of charged pion is approximately 90% for 1  $\text{GeV}/c$  track.

Figure 3.6 shows a scatter plot of  $dE/dx$  vs momentum for various particle types. It can be understood that the particle types are well separated according to each expected curve. The resolution of  $dE/dx$  is 7% and utilized to discriminate particle types of charged tracks.

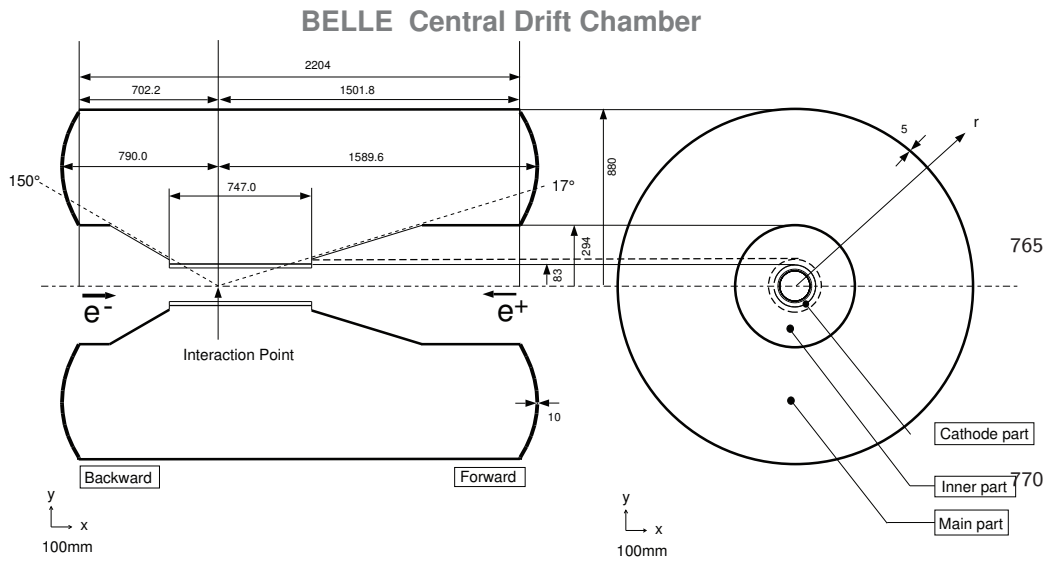


Figure 3.5: Dimension of the CDC [45] for SVD1 configuration. The inner wall was extended from 83 mm to 104 mm when SVD2 was installed.

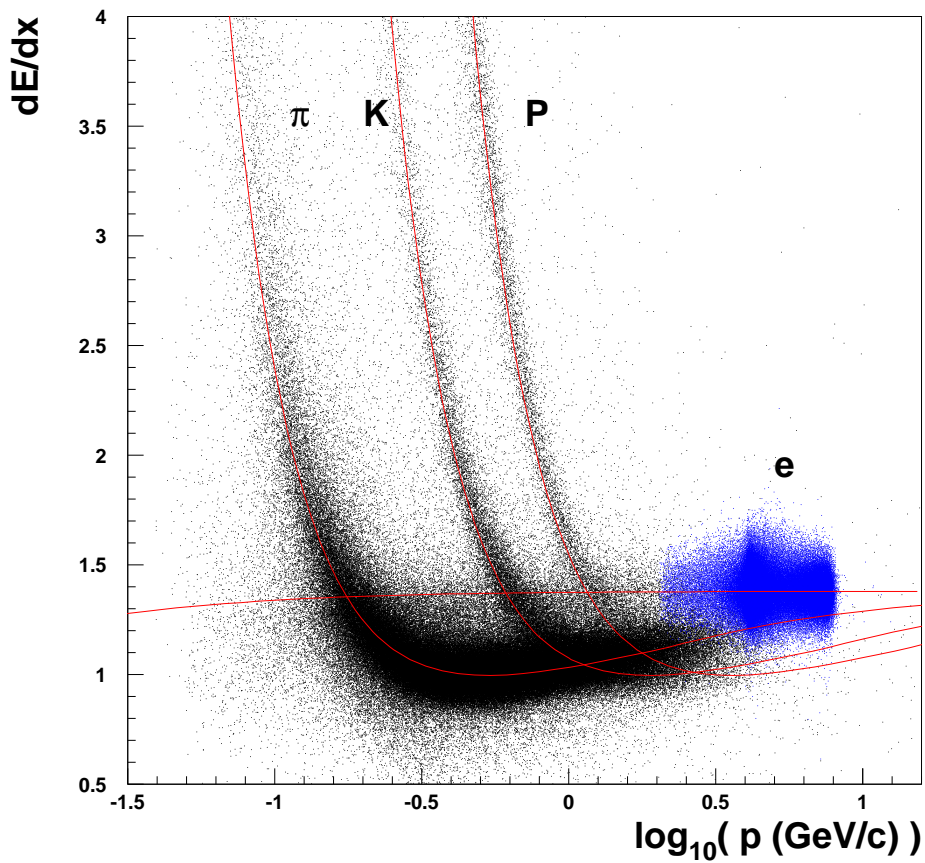
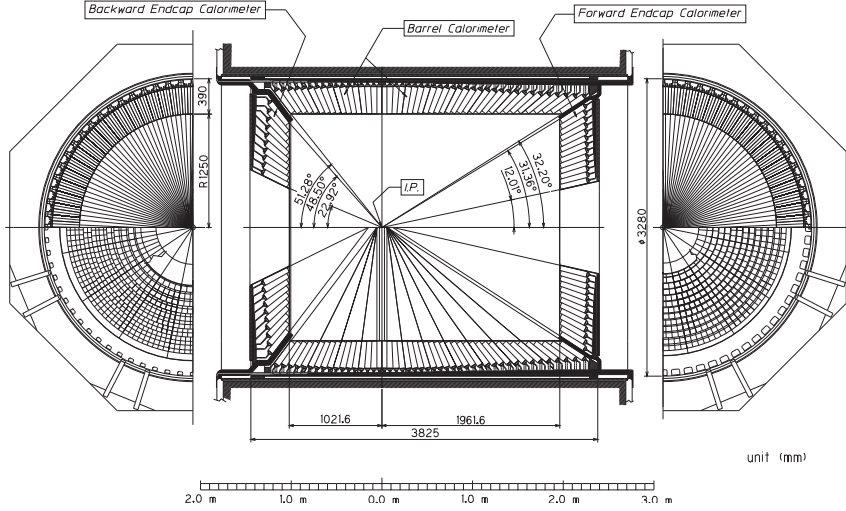


Figure 3.6: Scatter plot of  $\frac{dE}{dx}$  vs momentum. The red curves are expected energy loss values for  $\pi$ ,  $K$  and proton [43] and blue region corresponds to electron.



## BELLE CsI ELECTROMAGNETIC CALORIMETER



(a)

Figure 3.7: Geometry of the ECL [47].

### 3.2.3 Electromagnetic Calorimeter (ECL)

The main purpose of the Belle ECL is to measure an energy of photon which is often generated by cascade decays of  $B$  meson as well as the  $\tau$  leptons. Because the energy of photons generated by daughter of the  $\Upsilon(4S)$  tend to be relatively small ( $\sim 1$  GeV), it is required to provide a good energy and position resolutions for such photons. On the other hand, the ECL is also designed to accommodate high energy photons ( $\sim 4$  GeV) produced from low-multiplicity processes like forbidden  $\tau$  decay  $\tau \rightarrow \ell\gamma$ . Furthermore, the ECL plays an important role in the electron identification based on the shower shape inside crystals and  $E/p$  value.

The Belle ECL is composed of three sections—backward and forward endcaps and a barrel region—which separately cover  $12.4^\circ < \theta < 31.4^\circ$ ,  $130.7^\circ < \theta < 155.1^\circ$  and  $32.2^\circ < \theta < 128.7^\circ$ , respectively. Figure 3.7 shows the configuration of the ECL. All regions consist of CsI (TI) arrays and amount to 8736 crystals in total. Each crystal has a trapezoidal shape and points to the interaction region. The typical dimension of the crystal is  $55 \times 55$  mm<sup>2</sup> (front face),  $65 \times 65$  mm<sup>2</sup> (rear face) and 30 cm long (*i.e.*, 16.2 radiation length) but slightly varies depending on its location. The scintillation photons are detected by two PIN photo-diodes, whose active area are 10 cm $\times$ 20 cm, glued on the end surface of a crystal. The pulse from the PIN photo-diodes is amplified by a pre-amplifier attached nearby and sent to a shaping circuit. The separate two shaped signals are summed and processed by a charge-to-time converter. The energy and position resolution of the ECL are

$$\frac{\sigma_E}{E} = \left( 1.34 \oplus \frac{0.066}{E} \oplus \frac{0.81}{E^{1/4}} \right) \%, \quad (3.4)$$

$$\sigma_{\text{pos}} = \left( 0.27 \oplus \frac{3.4}{\sqrt{E}} \oplus \frac{1.8}{E^{1/4}} \right) \text{ mm}, \quad (3.5)$$

where  $E$  is in GeV.

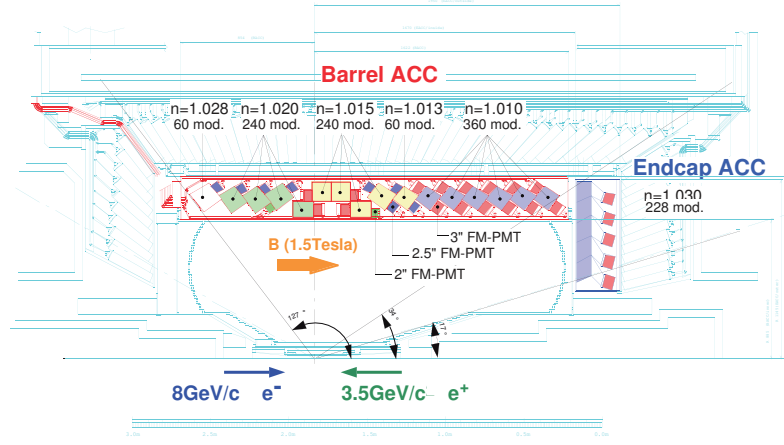


Figure 3.8: Configuration of the ACC [48].

### 3.2.4 Aerogel Cerenkov Counter (ACC)

The ACC provides the Belle with information of particle identification. In particular,  $K/\pi$  separation in high momentum region  $1.2 \text{ GeV}/c < p < 3.5 \text{ GeV}/c$ , which is in fact a key of the analysis of  $B$  physics, mainly depends on the information from ACC. To generate a Cerenkov light inside a medium, it is required to satisfy the formula

$$n > \frac{1}{\beta} = \sqrt{1 + \frac{m^2}{p^2}}, \quad (3.6)$$

where  $n$  is a refractive index of material and  $m$  is a mass of particle in question. As a result, for fixed values of  $n$  and  $m$ , there is a lower threshold of momentum  $p > m/\sqrt{n^2 - 1}$  and the emission of Cerenkov light enables us to identify the type of incoming particle.

Figures 3.8 and 3.9 show the configuration of the ACC in the Belle detector and the drawing of one module. The ACC is composed of the 960 counter modules which are segmented into 60 divisions in  $\phi$  directions. Silica aerogels, which have low refractive indexes, were specially developed and adopted as its medium. Aerogels with  $n = 1.030$  are used for the forward endcap region, while  $n = 1.020, 1.015, 1.013, 1.010$  are used for the barrel region from forward to backward order. These refractive indexes are chosen to take into account the asymmetry of the beam energy. The produced photons are detected by the attached fine-mesh photomultiplier tubes (FM-PMTs) which are chosen because of their high gain and the relatively strong tolerance to the high magnetic field environment. The signals from FM-PMTs are amplified by a pre-amplifier and processed by a charge-to-time converter.

The number of photo-electron generated by  $\pi^+$  and  $K^+$  candidates from  $D^*$  decays, both of which are selected based on the information of TOF and  $dE/dx$  measurements, is shown in Fig. 3.10. The heavier  $K$  does not emit Cerenkov light and this allows us to separate  $K$  and  $\pi$ . Up to approximately  $4 \text{ GeV}/c$  in the momentum of particle,  $P(K|K) > 0.8$  and  $P(\pi|K) < 0.1$  are achieved when  $\mathcal{P}_K = P_K/(P_K + P_\pi) > 0.6$  is applied, where  $P_a$  ( $a = K$  or  $\pi$ ) is a likelihood that the particle type is  $a$ , which are calculated by combined information of the CDC, ACC, TOF and ECL.

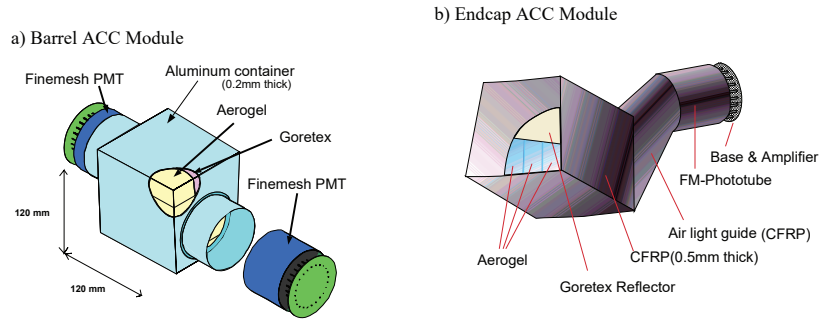


Figure 3.9: Modules of ACC. The left module is Barrel ACC, while right one is that of the forward endcap. The cube structure of Silica aerogel (approximately  $12 \times 12 \times 12 \text{ cm}^3$ ) is enclosed by a Goretex reflector and produced photons are detected by the attached PMTs [49].

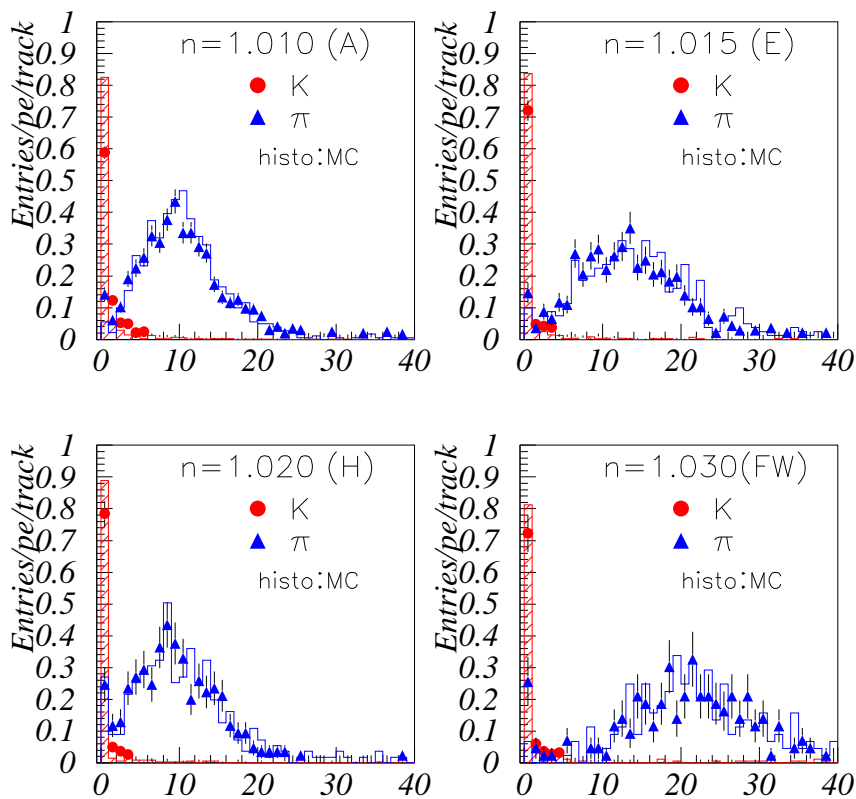


Figure 3.10: Distribution of the number of photo electron generated from  $K^+$  and  $\pi^+$  tracks for various refractive index values. The red and blue dots indicate experimental distribution of  $K^+$  and  $\pi^+$ , respectively and histograms represent that of MC simulation [43].

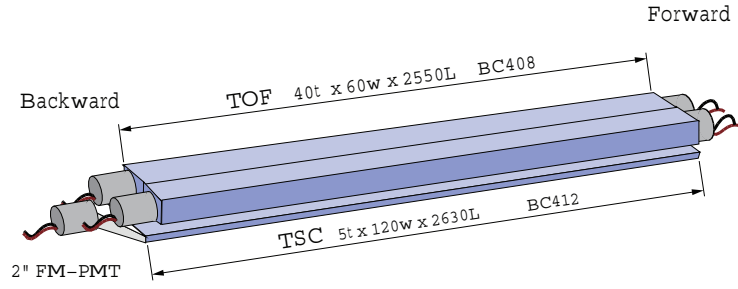


Figure 3.11: TOF/TSC module.

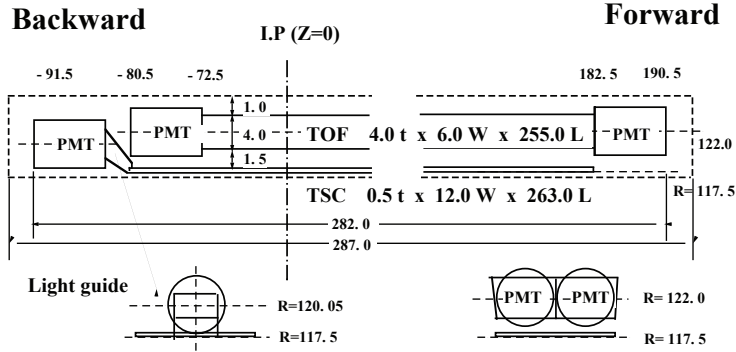


Figure 3.12: Configuration of the TOF/TSC [50].

### 3.2.5 Time-Of-Flight counter (TOF)

Particle identification of a low momentum charged track up to 1.2 GeV/c is mainly performed by the TOF counter. The time-of-flight of a particle is given by:

$$T = \frac{L}{c\beta} = L \left[ 1 + \frac{m^2}{p^2} \right]^{-1/2}, \quad (3.7)$$

where  $L$  is the flight length of the particle. Thus the particle type can be determined using observed  $T$  value by combining the momentum information from CDC.

Figure 3.11 shows the drawing of the TOF module. The module is composed of two plastic scintillators and one thin trigger scintillation counter (TSC) to all of which FM-PMTs are attached at both ends. The configuration of the TOF module is shown in Fig. 3.12. The module is located at  $r = 1.2$  m just inside the ECL barrel and covers  $33^\circ < \theta < 121^\circ$  range with 64 modules in total. The signal from FM-PMT is split into two streams: one is used for a charge measurement and the other generates timing information and a source of trigger.

The mass distribution calculated based on Eq. (3.7) is shown in Fig. 3.13. We can see a good agreement between the experiment and MC simulation. The timing resolution of the TOF is approximately 100 ps and the separation power of  $K^+$  and  $\pi^+$  is  $2\sigma$  for a particle momentum up to 1.2 GeV/c.

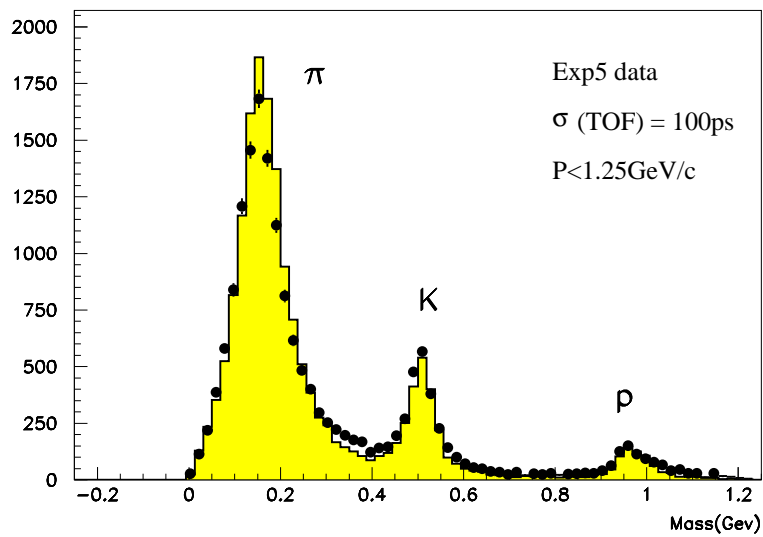


Figure 3.13: Distribution of masses of  $\pi$ ,  $K$  and proton with momenta less than 1.25 GeV/c. Dots indicate the experimental distribution and histogram is that of MC simulation [50].

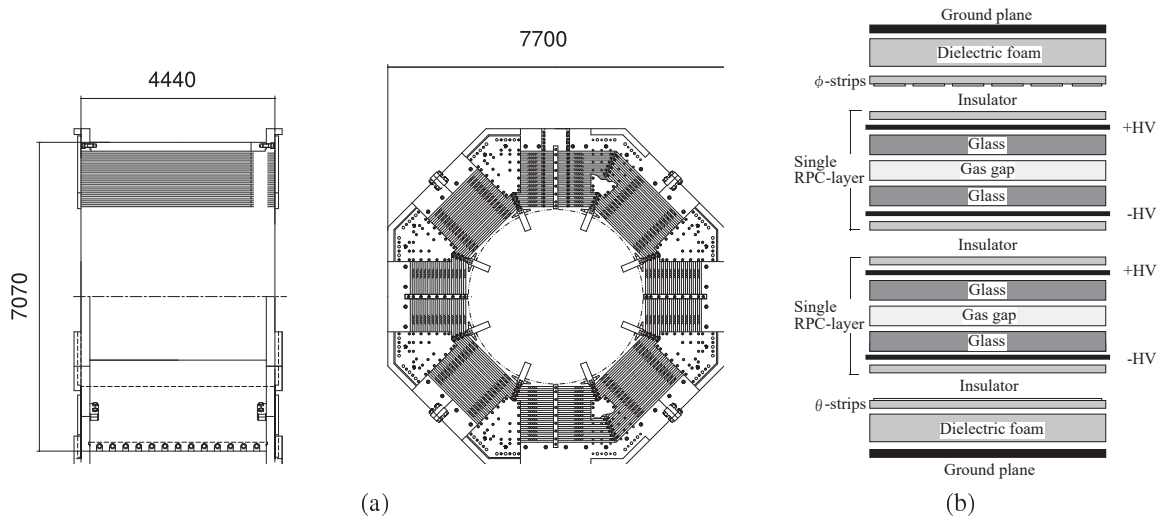


Figure 3.14: (a) Geometry of the barrel KLM [43]. (b) Cross section of the KLM layers [51]

### 3.2.6 $K_L$ and muon detector (KLM)

The main purpose of the KLM system is to identify  $K_L$  and muons with high efficiency by judging whether a hadronic shower is observed or not. The momentum target of the muons is  $p > 600 \text{ MeV}/c$  because the magnetic field  $B = 1.5 \text{ T}$  traps low energy tracks before reaching the KLM. Moreover, the KLM provides an angular information of the  $K_L$  meson.

As shown in Figs 3.14a and 3.3, the KLM is configured to enclose all sub-detectors explained above. The system consists of forward and backward endcaps and a barrel part, which separately cover  $20^\circ < \theta < 45^\circ$ ,  $45^\circ < \theta < 125^\circ$  and  $125^\circ < \theta < 155^\circ$ , respectively. Figure 3.14b shows the cross section of the KLM layers. The KLM barrel (endcap) has a sandwich structure of fourteen 4.7-cm-thick iron plates and fifteen (fourteen) grass-resistive plate counters (RPCs). The RPC is a type of the gas chamber, in which thin gap filled with gas is sandwiched by high resistive glass plates on both sides. An electric field is applied by two electrodes (typically  $\sim 8 \text{ kV}$  is applied) attached on the external side of the glass plates. In the streamer mode, when a charged particle traverses the gap, ionized electron-hail pair is gas-amplified by the cascade generation of the avalanche effect, which results in the local polarization of the glass plates. The variation of the local voltage is read out as a current from the outermost electrodes arranged orthogonally in  $\theta$  and  $\phi$  directions and enables us to record the location and timing. Thanks to the relatively large pulse from RPC, the signal is directly processed with discriminator followed by a multiplexer.

A hadronic cluster observed in the ECL, which is not associated with any extrapolated charged tracks, is identified as  $K_L$ . The comparison of the measured range of track vs its expected range for muon hypothesis is used to determine the likelihood of muon.

### 3.2.7 Trigger

The event of interest— $B\bar{B}$ ,  $\mu^+\mu^-$ ,  $\tau^+\tau^-$ , two-photon processes, etc—are selected by a trigger system with appropriate scale factors so as to accommodate a limited DAQ bandwidth and storage capabilities.

The Belle trigger system consists of hardware and software triggers also known as level 1 and level 3 (L1 and L3) triggers, respectively. As Fig. 3.15 shows the schematic view of the L1 trigger, the trigger signal is generated by a global decision logic (GDL) which makes a logical determination of correlated information from sub-detectors. For example, the CDC and TOF generate trigger signals from charged tracks while the ECL provides a signal according to the total energy deposit with a veto on the Bhabha processes  $e^+e^- \rightarrow e^+e^-(\gamma)$ . The KLM yields supplementary information of the muons. The decision by GDL finishes with fixed time 2.2  $\mu\text{s}$  latency after the event occurrence. There are 64 or 75 kinds of trigger sources depending on the version of SVDs, and the information of the GDL is stored in several bytes format. Each bit of the GDL output corresponds to a certain trigger source.

Although the efficiency of the L1 trigger is sufficiently high (>96%) for typical  $B$  decays, the low multiplicity event like  $e^+e^- \rightarrow \tau^+\tau^- \rightarrow (1\text{-prong})(1\text{-prong})^\dagger$  processes are suffered from the notable decrease of the efficiency due to the similar structure to the Bhabha events. This turns out to give a systematic effect on the measurement of the Michel parameters (not only main target of this analysis  $\bar{\eta}$  and  $\xi\kappa$  but also  $\rho, \eta, \xi, \xi\delta$  measurements) as well as the branching ratio of such processes. In a typical running condition, the average trigger rate is 200-400 Hz.

As explained later in Sec. 6.1, to determine trigger efficiency, we require the selected signal candidates to be fired by following specific GDL output bits:

- *clst4*: this bit is set when the number of isolated ECL clusters exceeds three after cosmic ray veto.
- *hie*: this bit is set when the energy deposit in the ECL is larger than 1 GeV after the Bhabha and cosmic ray vetos.
- *ffs\_zt2* (SVD1 only): this bit is set when a number of short transverse tracks is more than or equal to 1, at least one full track exists, hits in TSC exceed two and there is more than or equal to one longitudinal track. Here, the short transverse track means that it is reconstructed using only  $r$  and  $\phi$  information from the three innermost layers of the CDC. Similarly, the longitudinal track is reconstructed using only  $r$  and  $z$  information from the CDC.
- *klm\_opn*: this bit is set when the maximum opening angle exceeds  $135^\circ$  and there is at least one hit in the KLM.
- *klm\_b2b*: this bit is set when there is a back-to-back track with 64 segmented  $r$ - $\phi$  region in the CDC and there is at least one hit in the KLM.

The first two bits are categorized as a neutral trigger which uses ECL information while the others are categorized as a charged trigger determined mainly by the CDC, TOF and KLM. It turns out to be important that the neutral and charged triggers base on physically independent sources.

### 3.2.8 Data acquisition system (DAQ)

The DAQ system receives the data from sub-detectors when the L1 fired the trigger signal for an event, packs the fragmented detector-by-detector information into an event-by-event format, selects events with more intelligent decision with fast reconstructed data and stores the event.

---

<sup>†</sup> 1-prong means a decay with one charged track.

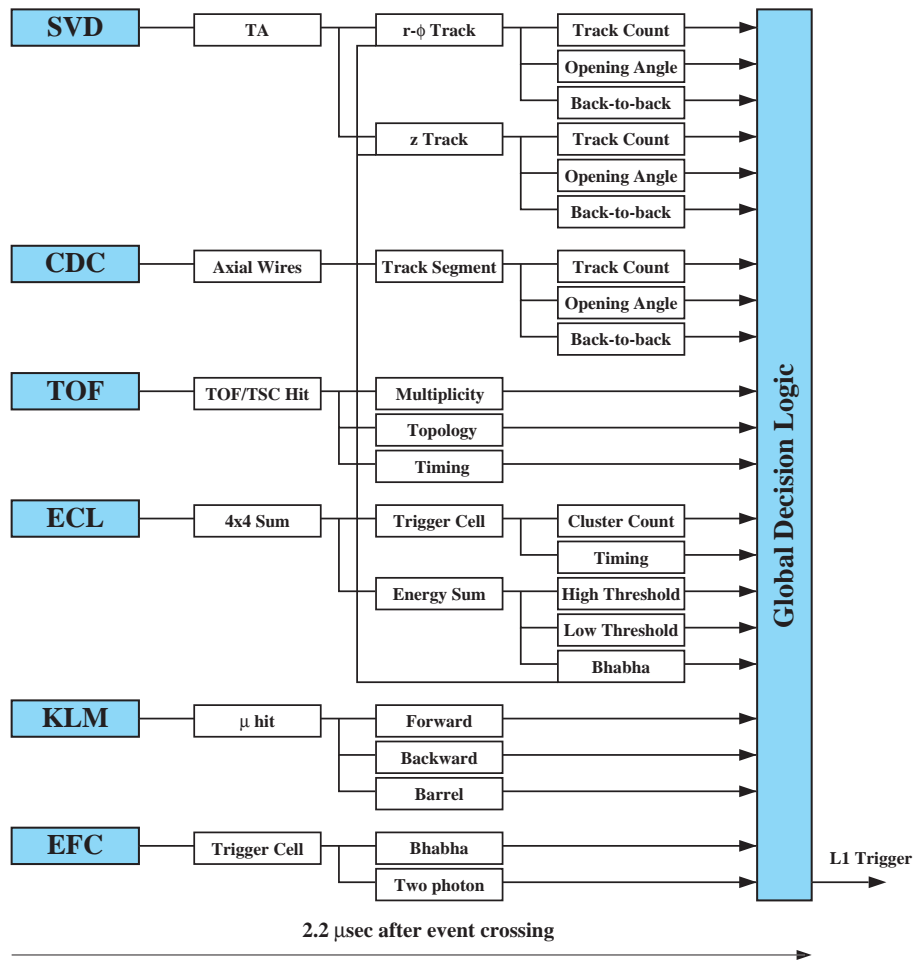


Figure 3.15: Schematic view of the Belle trigger system (L1) [52].



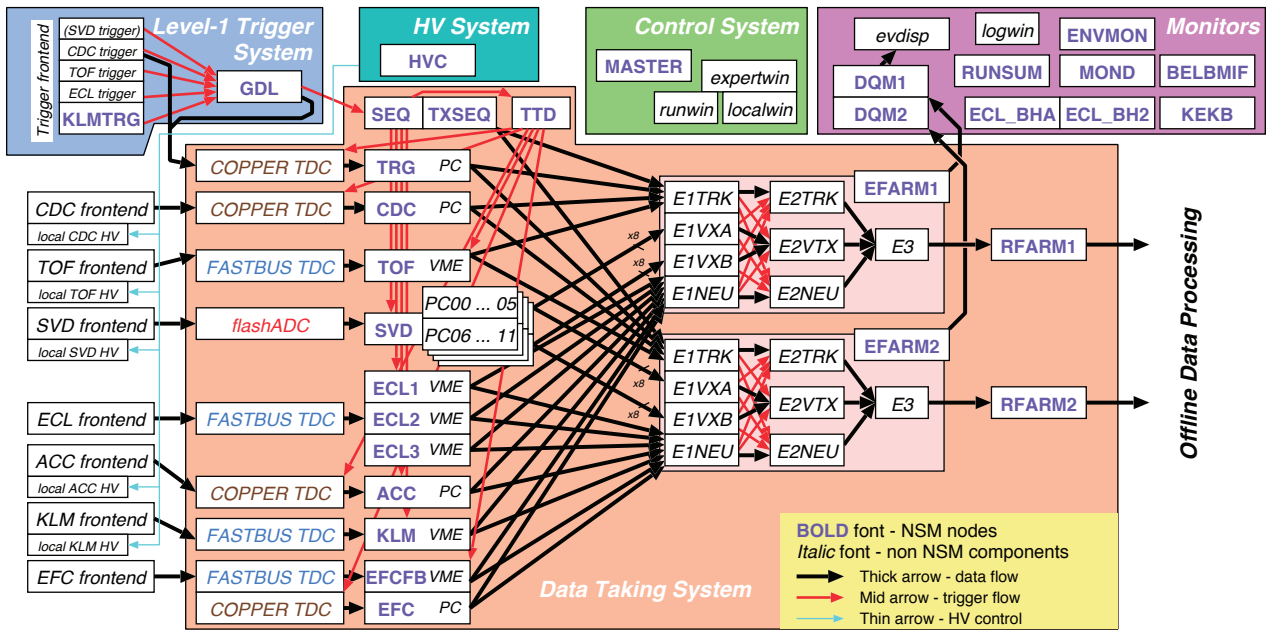


Figure 3.16: Schematic view of the Belle DAQ system. The individual signals from all sub-detectors are integrated by the GDL to generate a L1 trigger [53].

Figure 3.16 shows a schematic view of the DAQ system. Data from all sub-detectors except the SVD are sent with Q-to-T-converted format and digitized by a common time-to-digital converter (TDC) module. At the beginning of Belle project, TDC was performed by VME processor called FASTBUS but it was replaced to pipelined system named COPPER. Because of the large number of channels in the SVD, the data from front-end chip of the SVD are separately digitized by analog-to-digital converter (ADC) with a reduction of the amount of data size.

The L3 trigger signal initiates the event-building in which digitized data from sub-detectors are collected to an event-by-event format on the online computer farm with linux PC servers (EFARM). The real time reconstruction farm (RFARM) is responsible for the fast reconstruction of the charged tracks. To reduce a beam background, in which bremsstrahlung from beam generates secondary particles far away from the IP, at least one charged track originating around IP with  $dr < 1$  cm,  $|dz| < 4$  cm and  $P_t > 0.3$  GeV/c, is required. The event which satisfies L3 is stored in a storage system.

Table 3.4: Relationship between various particle identifications and sub-detectors

Type	SVD	CDC	ECL	ACC	TOF	KLM
$e$	tracking	tracking $dE/dx$	$E/p$ shower shape	Cerenkov light -	time-of-flight -	- -
$\mu$	tracking	tracking	energy deposit	- -	time-of-flight -	range -
$K$	tracking	tracking	-	Cerenkov light -	time-of-flight -	- -
$\pi$	$\pi$ identification is determined by a complementary condition of $K$ identification					
$p$	tracking	tracking $dE/dx$	-	Cerenkov light -	time-of-flight -	- -
$K_L$	excluding tracks		-	- -	- -	hadron cluster -
$\gamma$			EM cluster	-	-	-

### 3.2.9 Particle identifications

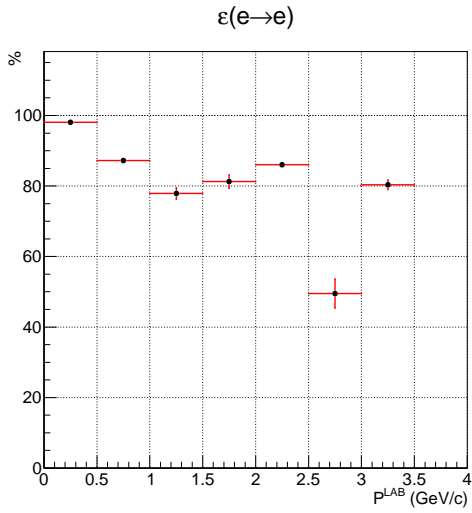
In this section, we summarize information of various particle identifications using the sub-detectors explained above.

Electron is identified using the ratio of energy deposited in the ECL out of track momentum measured by the CDC ( $E/p$ ), the transverse shape of the ECL cluster,  $dE/dx$  value measured in the CDC, light yield in the ACC and time-of-flight measured by the TOF. Based on these values, likelihood values for electron and non-electron hypotheses,  $L_e$  and  $L_x$ , are determined. The selection of electron candidate uses likelihood ratio values  $\mathcal{P}_e = L_e/(L_e + L_x)$ . For more detail, see Ref. [54]. Figure 3.17 shows an efficiency of electron and a ratio pion-misidentification efficiency when  $\mathcal{P}_e > 0.9$  is applied.

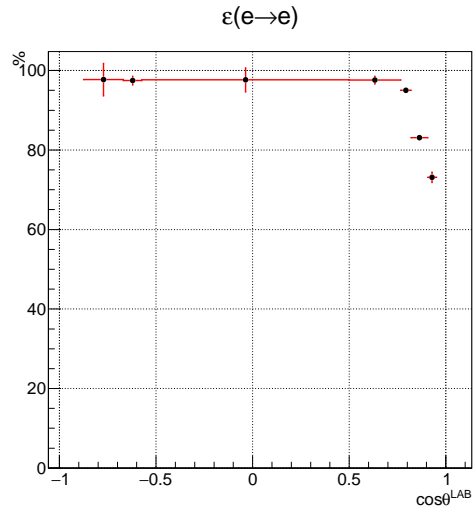
Muon is identified using an observed range inside the KLM for a charged track reconstructed by the SVD and CDC. The charged track is extrapolated to the KLM and candidate of a cluster is associated. The range is determined by the outermost layer of the KLM and the charged track position. The likelihood values of  $\mu^+$ ,  $\pi^+$ ,  $K^+$  and  $p$ — $L_\mu$ ,  $L_\pi$ ,  $L_K$  and  $L_p$ , respectively—are determined by the measured range vs predicted range and the selection of muon uses likelihood ratio values  $\mathcal{P}_\mu = L_\mu/(L_\mu + L_\pi + L_K)$ . For more detail, see Ref. [55]. Figure 3.18 shows an efficiency of muon and a ratio of pion-misidentification efficiency when  $\mathcal{P}_\mu > 0.9$  is applied.

Kaon and pion are identified using  $dE/dx$  value measured in the CDC, light yield in the ACC and time-of-flight measured by the TOF. ACC and TOF provide good discrimination capabilities of  $K/\pi$  for high ( $> 1.2 \text{ GeV}/c$ ) and low momentum ( $< 1.2 \text{ GeV}/c$ ) region, respectively. The likelihood values of  $K^+$  and  $\pi^+$  ( $L_K$  and  $L_\pi$ ), are determined based on information above and the selections use the likelihood ratios  $\mathcal{P}_\pi = L_\pi/(L_\pi + L_K)$  and  $\mathcal{P}_K = L_K/(L_\pi + L_K)$ . Figure 3.19 shows efficiencies of muon when  $\mathcal{P}_\pi > 0.4$  is applied.

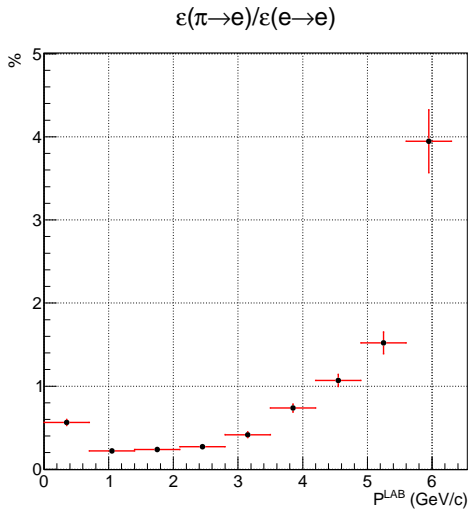
Photon is identified from the candidates of the ECL clusters without any matched charged tracks. Above information is summarized in Table 3.4.



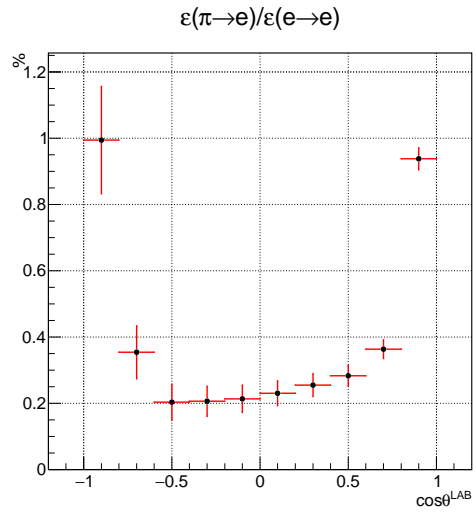
(a)  $\varepsilon(e \rightarrow e)$  momentum



(b)  $\varepsilon(e \rightarrow e)$  polar angle

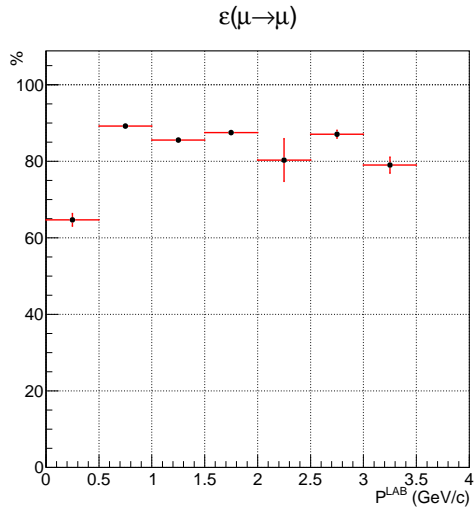


(c)  $\frac{\varepsilon(\pi \rightarrow e)}{\varepsilon(e \rightarrow e)}$  momentum

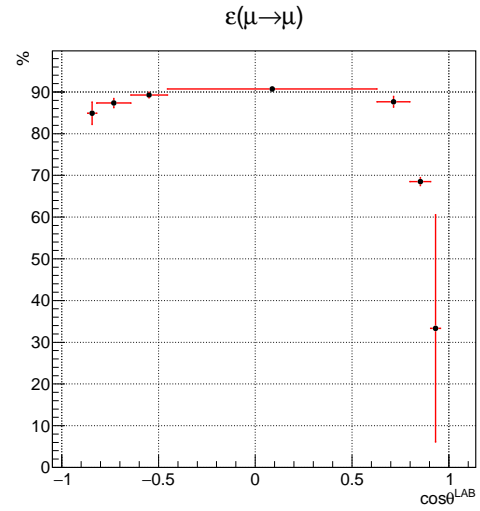


(d)  $\frac{\varepsilon(\pi \rightarrow e)}{\varepsilon(e \rightarrow e)}$  polar angle

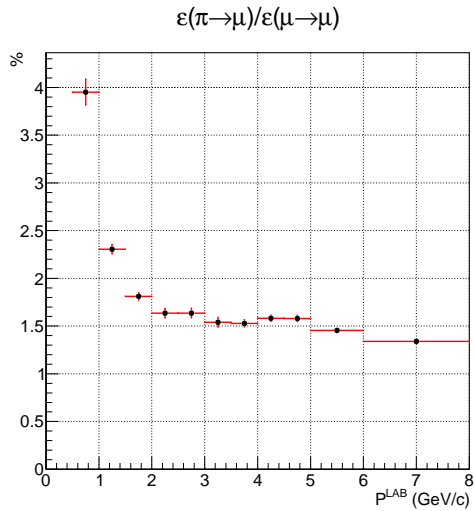
Figure 3.17: Efficiency of electron and ratio of pion misidentification efficiency for  $\mathcal{P}_e > 0.9$ :  $\varepsilon$  as functions of (a)(c) momentum (b)(d) angle.



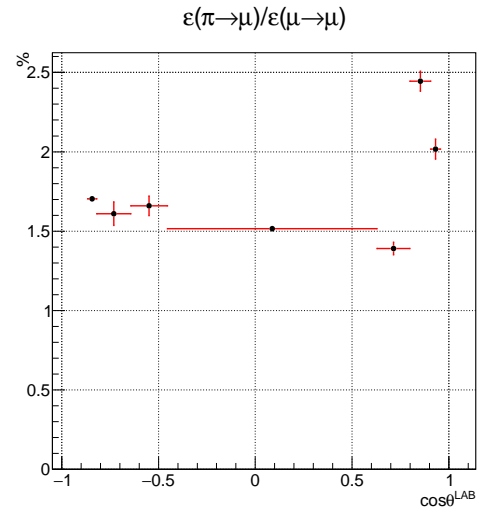
(a)  $\varepsilon(\mu \rightarrow \mu)$  momentum



(b)  $\varepsilon(\mu \rightarrow \mu)$  polar angle



(c)  $\frac{\varepsilon(\pi \rightarrow \mu)}{\varepsilon(\mu \rightarrow \mu)}$  momentum



(d)  $\frac{\varepsilon(\pi \rightarrow \mu)}{\varepsilon(\mu \rightarrow \mu)}$  polar angle

Figure 3.18: Efficiency of muon and ratio of pion misidentification efficiency for  $\mathcal{P}_\mu > 0.9$ :  $\varepsilon$  as functions of (a)(c) momentum (b)(d) angle.

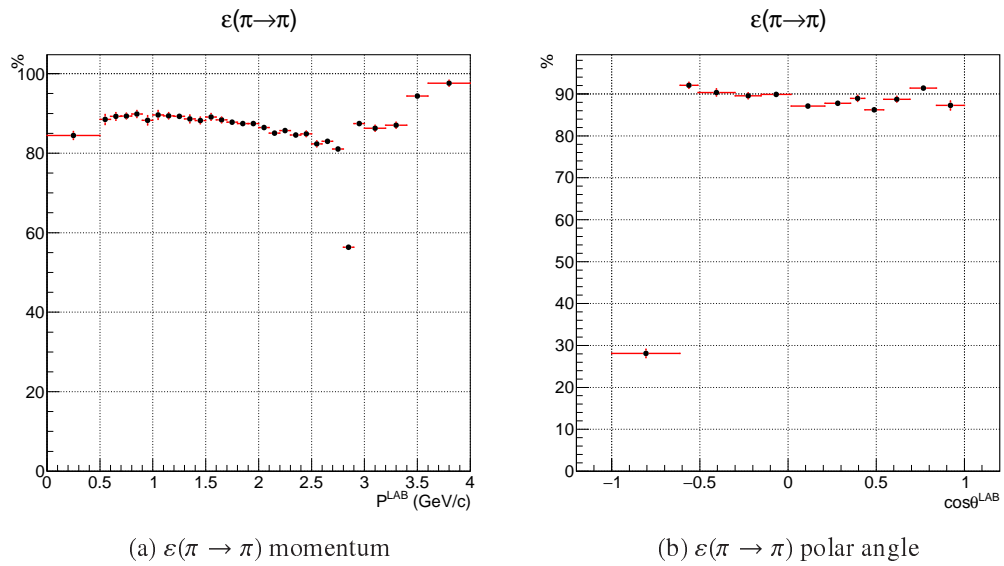


Figure 3.19: Efficiencies of pion for  $\mathcal{P}_\pi > 0.4$ :  $\varepsilon$  as a function of (a) momentum (b) angle.

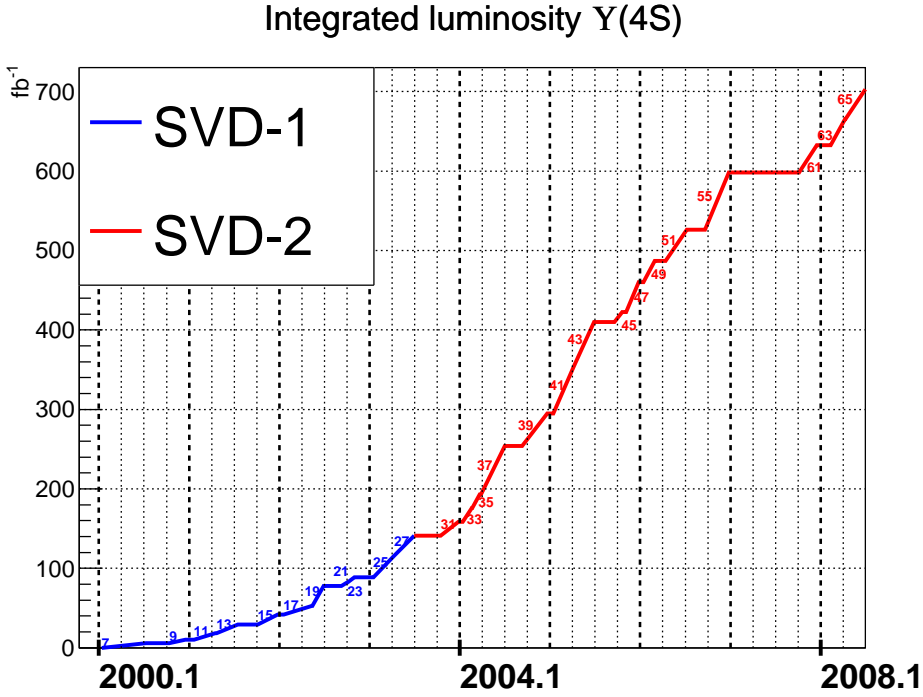


Figure 3.20: Integrated luminosity with  $\Upsilon(4S)$  resonance energy. Blue and red lines indicate SVD1 and SVD2 terms, respectively. The numbers represent the identification number.

### 3.3 Operation of Belle data taking

The Belle experiment was managed with identification numbers of runs. The odd numbers are intended for the increase of data, *i.e.*, *luminosity run*, while the even numbers are for calibrations. The overall numbers vary from 7 to 27 for the SVD1 term and from 31 to 73 for the SVD2 term. Since the numbers 67, 69, 71 and 73 were operated with different beam energies, the  $\Upsilon(4S)$  operation ranges only from 7 to 65. Between the run number of 55 and 61, a minor update of the DAQ system was performed, thereby the detection efficiency of event was slightly improved. Figure 3.20 shows a record of an increase of the integrated luminosity. Continuing the operation of the experiment, we collected  $703 \text{ fb}^{-1}$  available data with the  $\Upsilon(4S)$  resonance beam energy.

### 3.4 Monte Carlo simulation

The physics processes of  $e^+e^- \rightarrow \tau^+\tau^-$  are simulated by KKMC [56] generator. The QED radiative corrections from initial and final state radiations are simulated up to second order and electroweak corrections are included up to its first order. Moreover, correlations among  $\tau^+\tau^-$  spin polarizations, which are of crucial importance in this analysis, are fully taken into account.

The successive decay of the  $\tau$  is simulated by TAUOLA [57, 58, 59] generator incorporated in the KKMC library. The TAUOLA provides final state of tau leptons with a resonant distributions from intermediate hadrons and a complete spin structure. The radiative leptonic decay  $\tau^- \rightarrow \ell^- \nu \bar{\nu} \gamma$  are also simulated by this generator. Other internal QED bremsstrahlung processes from various hadronic  $\tau$  decays are simulated by PHOTOS [60] generator. These corrections base on a process-independent formalism, where probabilities of a soft photon emission and a collinear production of photon with a charged particle are factorized as an original matrix element and the bremsstrahlung kernel function.

Although only small fraction of events turn out to be finally selected ( $< 0.1\%$ ), two photon

processes  $e^+e^- \rightarrow e^+e^-\Gamma$  ( $\Gamma$  is a state generated by  $\gamma\gamma$  interaction) are simulated by TREPS generator [61]. The overall process of  $\gamma$  emissions and their interaction are implemented by the *double equivalent photon approximation*, therein a radiation of photon is interpreted as a flux of photons.

The detector effects are simulated based on the GEANT3 package [62]. The GEANT is a toolkit to simulate passage of elementary particles through matters, where reaction of particles such as energy deposit, cascade generation of electromagnetic daughters and decay in flight, are calculated at every step-by-step path evolution of the particle. Simulated detector responses are processed by the same chain as the real experiment and results are recorded in the same format.

# Chapter 4

## Event selection

In this chapter, selection criteria are explained in detail. The reduction process is composed of three stages: preselection of  $\tau^+\tau^-$  pairs, second and final selections.

### 4.1 Preselection

First of all, the decay of the  $\tau^+\tau^-$  is preselected from  $e^+e^-$  collision data. The definition of the criteria is summarized in Table 4.1. With this selection, backgrounds are efficiently rejected while retaining the efficiency of  $\tau^+\tau^-$  process by approximately 70%. In case of signal, approximately 50% of events pass this stage including the trigger selection. The information of the efficiency is summarized in Table 4.2.

The basic strategy of the preselection is to select events which show strong directivity and large energy loss. Compared to other physics processes,  $e^+e^- \rightarrow \tau^+\tau^-$  decays produce small number of large momentum particles (so called *low multiplicity*) and show large missing energies escaped by (at least) two neutrinos. This selection criteria are common for other  $\tau$  analyses at Belle using the  $e^+e^- \rightarrow \tau^+\tau^-$  annihilation process.

### 4.2 Second selection

After the preselection, we select events coarsely to further reduce the number of background events. Processes such as Bhabha  $e^+e^- \rightarrow e^+e^-(\gamma)$ ,  $\mu^+\mu^-$  pair production, and two photon events  $e^+e^- \rightarrow \ell^+\ell^-e^+e^-$  are additionally suppressed only to be less than 0.01% out of rest events. Figure 4.1 shows 2D-plot of the missing angle  $\theta_{\text{miss}}^{\text{CMS}}$  and mass  $M_{\text{miss}}$ , which provide an essential discrimination capability. Note that, at this stage, the correspondence of signal particle candidates and observed ones are decided. With this selection, the number of selected events becomes approximately 0.1% out of the total number of  $\tau^+\tau^-$  pair productions including other tau decays.

- Missing four momentum is defined by  $p_{\text{miss}} = p_{\text{beam}} - p_{\text{obs}}$ , where  $p_{\text{beam}}$  is a sum of beam electron and positron momenta and  $p_{\text{obs}}$  is sum of observed momenta. Missing angle  $\theta_{\text{miss}}^{\text{CMS}}$  is a polar angle of  $p_{\text{miss}}$  in the CMS frame and missing mass  $M_{\text{miss}}$  is defined as  $p_{\text{miss}}^2 = M_{\text{miss}}^2$ . To calculate CMS momenta of charged tracks, we use a pion hypothesis for the mass of corresponding particles. These variables must satisfy  $30^\circ \leq \theta_{\text{miss}}^{\text{CMS}} \leq 150^\circ$  and  $1 \text{ GeV}/c^2 \leq M_{\text{miss}} \leq 7 \text{ GeV}/c^2$ , which essentially select events having large missing energy (and resulting off-balance of transverse momentum) from neutrinos. The corresponding efficiency for signal events is 69%.



Table 4.1: Preselection criteria

<b>Definitions</b>	
Good charged track	$P_i^{\text{LAB}} \geq 0.1 \text{ GeV}/c$ and $dr < 2 \text{ cm}$ , $ dz  < 5 \text{ cm}$ .
ECL cluster and photon	$E_{\text{ECL}}^{\text{LAB}} > 0.1 \text{ GeV}$ .
Missing four momentum	$p_{\text{miss}} = p_{\text{beam}} - p_{\text{obs}}$ , where $p_{\text{beam}}$ is momenta of sum of beam and $p_{\text{obs}}$ is sum of observed momenta. Accordingly, $M_{\text{miss}}^2 = p_{\text{miss}}^2$ and $\theta_{\text{miss}}^{\text{CMS}}$ is its polar angle in the CMS frame.
$E(\text{ECL})^{\text{LAB}}$	Total energy deposit in ECL in the laboratory frame.
$E(\text{ECL})^{\text{CMS}}$	Total energy deposit in ECL in the CMS frame.
$E_{\text{rec}}^{\text{CMS}}$	Sum of momenta of good charged tracks + sum of energy of photons both in CMS.
$P_{i \text{ MAX}}^{\text{LAB}}$	Maximum $P_i$ of good charged track in laboratory frame.
$E_{\text{tot}}^{\text{CMS}}$	$E_{\text{rec}}^{\text{CMS}} + P_{\text{miss}}^{\text{CMS}}$ (massless particles are boosted to CMS).
$N_{\text{barrel}}$	Number of good charged track within barrel region.
$\theta_{\text{opn MAX}}^{\text{LAB}}$	Maximum opening angle of charged tracks in the laboratory frame.
$E^{\text{CMS}}(\text{photon})$	Total energy of photon clusters in ECL in the CMS frame.
$E(\text{ECL})_{\text{trk}}^{\text{CMS}}$	$E(\text{ECL})^{\text{LAB}} - E^{\text{CMS}}(\text{photon})$ .
<b>Criteria</b>	
	$2 \leq \text{number of good track} \leq 8$ .
	$ \text{sum of charge}  \leq 2$ .
	$P_{i \text{ MAX}}^{\text{LAB}} > 0.5 \text{ GeV}/c$ .
	Event vertex $dr < 1 \text{ cm}$ , $ dz  < 3 \text{ cm}$ .
	$E_{\text{rec}}^{\text{CMS}} > 3 \text{ GeV}$ or $P_{i \text{ MAX}}^{\text{LAB}} > 1.0 \text{ GeV}/c$ .
	Two-track events must satisfy that $E(\text{ECL})^{\text{LAB}} < 11 \text{ GeV}$ and $5^\circ < \theta_{\text{miss}}^{\text{CMS}} < 175^\circ$ .
	2-4 charged track events must satisfy ① and ②
	① $E_{\text{tot}}^{\text{CMS}} < 9 \text{ GeV}$ or $\theta_{\text{opn MAX}}^{\text{LAB}} < 175^\circ$ or $2 \text{ GeV} < E(\text{ECL})^{\text{LAB}} < 10 \text{ GeV}$ .
	② $N_{\text{barrel}} \geq 2$ or $E(\text{ECL})_{\text{trk}}^{\text{CMS}} < 5.3 \text{ GeV}$ .

Table 4.2: Efficiency of preselection

Process	Cross section (nb)	Efficiency (%)	Effective cross section (nb)
$\tau^+ \tau^-$	0.92	70.2	0.65
$\mu^+ \mu^-$	1.05	5.7	0.06
$e^+ e^- (\gamma)$	1249	0.0011	0.014
$e^+ e^- e^+ e^-$ (2-photon)	40.85	0.24	0.098
$e^+ e^- u^+ u^-$ (2-photon)	11.7	0.56	0.065
<b>Signal</b>			
Electron mode	$1.67 \times 10^{-2}$	46.6	$7.85 \times 10^{-3}$
Muon mode	$3.37 \times 10^{-3}$	49.1	$1.65 \times 10^{-3}$

- There must be exactly two oppositely charged tracks in the event. To reject tracks not originating from  $e^+e^-$  collision, the impact parameters of these tracks (relative to the IP) are required to be within  $\pm 2.5$  cm along the beam axis and  $\pm 0.5$  cm in the transverse plane. Both transverse momenta must exceed  $0.1$  GeV/ $c$  in the laboratory frame and the larger one must have more than  $0.5$  GeV/ $c$ . The corresponding efficiency for signal events is 92%.
- Number of hard photons  $\leq 5$ , where hard photon is defined by  $E_\gamma^{\text{CMS}} > 0.08$  GeV. The corresponding efficiency for signal events is 99%.
- Total energy deposit in ECL must not exceed 9 GeV in the laboratory frame, which results in the suppression of Bhabha process  $e^+e^- \rightarrow e^+e^-(\gamma)$ . This criteria do not essentially reduce the efficiency for signal events.
- One of the charged tracks must have lepton likelihood ratio  $\mathcal{P}_\ell > 0.7$  ( $\ell = e$  or  $\mu$ ). The other track must have a pion-likelihood ratio  $\mathcal{P}_\pi > 0.4$ . The corresponding efficiency for signal events is 87% and 73% for electron and muon modes, respectively.
- A  $\pi^0$  candidate is formed from two photon candidates, each of whose energies satisfies  $E_\gamma > 80$  MeV, with an invariant mass of  $115 \text{ MeV}/c^2 < M_{\gamma\gamma} < 150 \text{ MeV}/c^2$ . The corresponding efficiency for signal events is 51%.
- The  $\rho$  candidate is formed from a  $\pi^\pm$  and a  $\pi^0$  candidates, with an invariant mass of  $m_{\pi^\pm\pi^0} < 3.0$  GeV/ $c^2$ . The corresponding efficiency for signal events is 96%.
- Signal photon candidate is chosen with  $\cos\theta_{\ell\gamma} > 0.9$  in the CMS frame. If more than or equal to two candidates satisfy this condition, the event is rejected. The chosen photon candidate must have an energy more than 80 MeV for the barrel region ( $31.4^\circ < \theta_\gamma^{\text{LAB}} < 131.5^\circ$ ) and 100 MeV for the endcap region ( $12.0^\circ < \theta_\gamma^{\text{LAB}} < 31.4^\circ$  or  $131.5^\circ < \theta_\gamma^{\text{LAB}} < 157.1^\circ$ ) in the CMS frame. The corresponding efficiency for signal events is 42% and 34% for electron and muon modes, respectively.
- Either of the specific GDL bits explained in Sec. 3.2.7 must be fired. The corresponding efficiency for signal events is 85% and 89% for electron and muon modes, respectively.

### 4.3 Final selection

Finally, we apply stringent criteria on the selected events. Below in the list, the circled numbers show the order of the reduction. Thereby, the number of selected events decreases as the index increments. Figures 4.3 to 4.9 show the distributions of the cut parameters at each step. The dots with error bars indicate an experimental distribution and the open and colored histograms represent MC distributions of signal and backgrounds, respectively. The MC distributions are scaled based on the number of entries just after the second selection. The MC distribution are overlaid on the experimental distribution. The detailed meanings of each background are explained in Sec. 4.4. The step-by-step reductions of the signal efficiencies and the number of selected events are summarized in Tables 4.3 and 4.4.

① The signal photon, which tends to be produced collinearly with lepton direction, must lie in a cone determined by the lepton-candidate direction that is defined by  $\cos\theta_{e\gamma} > 0.9848$  and  $\cos\theta_{\mu\gamma} > 0.9700$

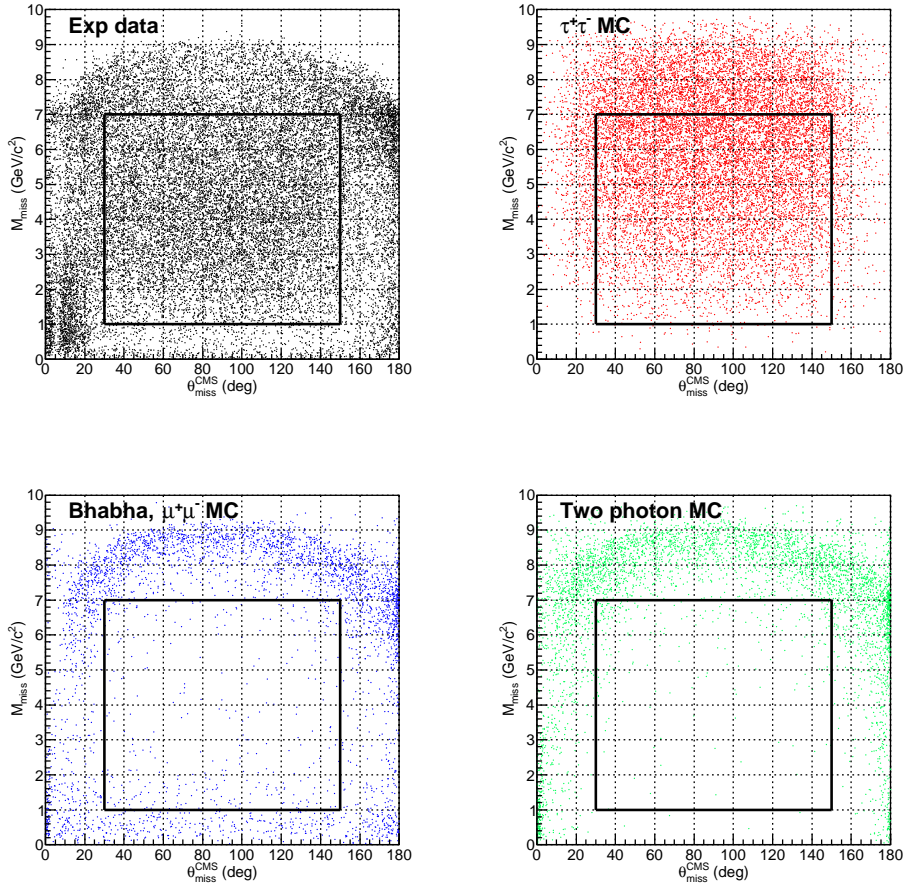


Figure 4.1: 2D-plots of  $\theta_{\text{miss}}^{\text{CMS}}$  vs  $M_{\text{miss}}$  for the experimental data,  $\tau^+\tau^-$ , Bhabha and two photon MC events. The black rectangle box indicates a requirement of the second selection.

Table 4.3: Reduction of efficiency in each step for  $\tau \rightarrow e\nu\bar{\nu}\gamma$  candidate.

Step after	$N_{\text{cand}}^{\text{MC}}$	$N_{\text{sig}}^{\text{MC}}$	$\varepsilon_{\text{sig}}(\%)$	Purity (%)	$N_{\text{cand}}^{\text{MC} \dagger}$	$N^{\text{EX}}$
2nd selection	7299848	1796214	6.45	24.6	1373878	1373878
①	6403839	1591564	5.72	24.9	1205243	1202834
①	6050803	1515469	5.44	25.0	1138800	1129166
②	5910310	1486277	5.34	25.1	1112358	1107275
③	5807107	1470467	5.28	25.3	1092935	1088418
④	5745691	1464212	5.26	25.5	1081376	1074840
⑤	5516655	1435304	5.16	26.1	1038270	1031535
⑥	4234513	1224733	4.40	28.9	796962	776834

$\dagger N_{\text{cand}}^{\text{MC}}$  means scaled number of MC events at the step just before ①

Table 4.4: Reduction of efficiency in each step for  $\tau \rightarrow \mu\nu\bar{\nu}\gamma$  candidate

Step after	$N_{\text{cand}}^{\text{MC}}$	$N_{\text{sig}}^{\text{MC}}$	$\varepsilon_{\text{sig}}(\%)$	Purity (%)	$N_{\text{cand}}^{\text{MC} \dagger}$	$N^{\text{EX}}$
2nd selection	1478977	376484	6.30	25.5	258089	258089
①	636228	275069	4.60	43.2	111025	114367
①	603237	262554	4.39	43.5	105268	107826
②	543512	253771	4.25	46.7	94846	96427
③	519598	250083	4.19	48.1	90672	92359
④	499350	249135	4.17	49.9	87139	89130
⑤	478862	244229	4.09	52.3	83564	85516
⑥	398970	228947	3.83	57.4	69622	71171

$\dagger N_{\text{cand}}^{\text{MC}}$  means scaled number of MC events at the step just before ①

in the CMS frame for the electron and muon modes, respectively. The different cut value is intended to allow broader distribution of  $\theta_{\mu\gamma}$  than electron mode (see Sec. 2.1).

① The pion candidate must have a likelihood ratio value of  $\mathcal{P}_\pi > 0.7$ .

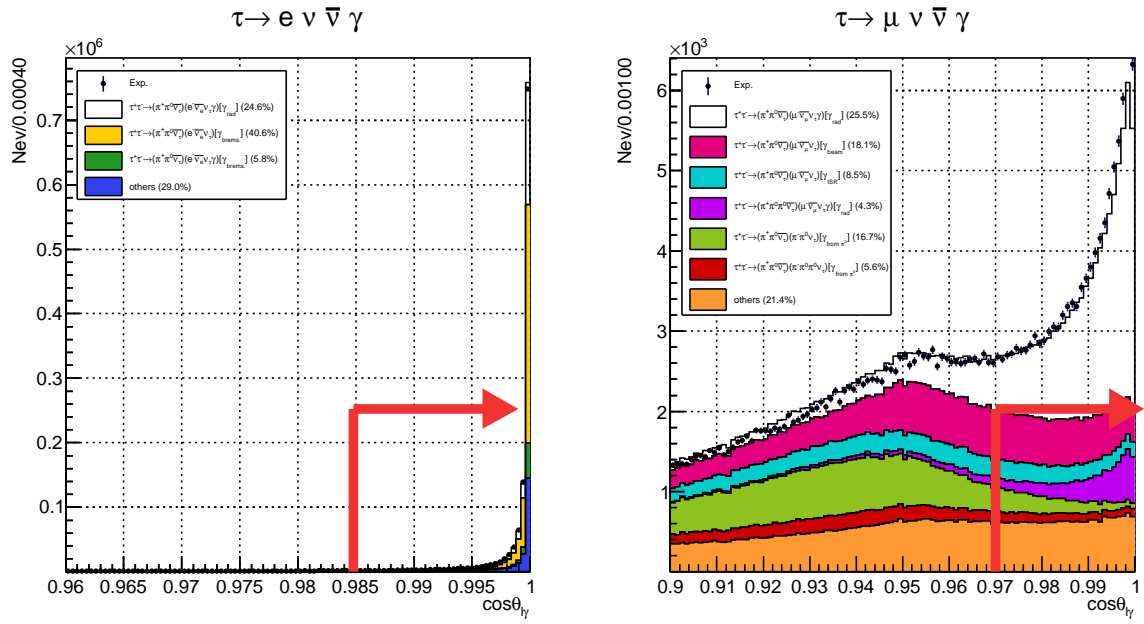
② The electron candidate must have a likelihood ratio value of  $\mathcal{P}_e > 0.9$  and the  $\chi^2$  of the track fitting is required to have  $\chi_{\text{track}}^2 < 200$ . The muon candidate must have a likelihood value of  $\mathcal{P}_\mu > 0.9$  and the  $\chi^2$  of the track is required to have  $\chi_{\text{track}}^2 < 150$ . The requirement of the  $\chi^2$  intends to reject bad quality track but does not have essential impact on efficiencies.

③ Reject other  $\pi^0$  possibilities: if the signal photon (inside aforementioned cone) candidate and either of the photons from the  $\pi^0$  (the daughter of the  $\rho$  candidate) form an invariant mass of the  $\pi^0$  ( $115 \text{ MeV}/c^2 < M_{\gamma\gamma} < 150 \text{ MeV}/c^2$ ), the event is rejected.

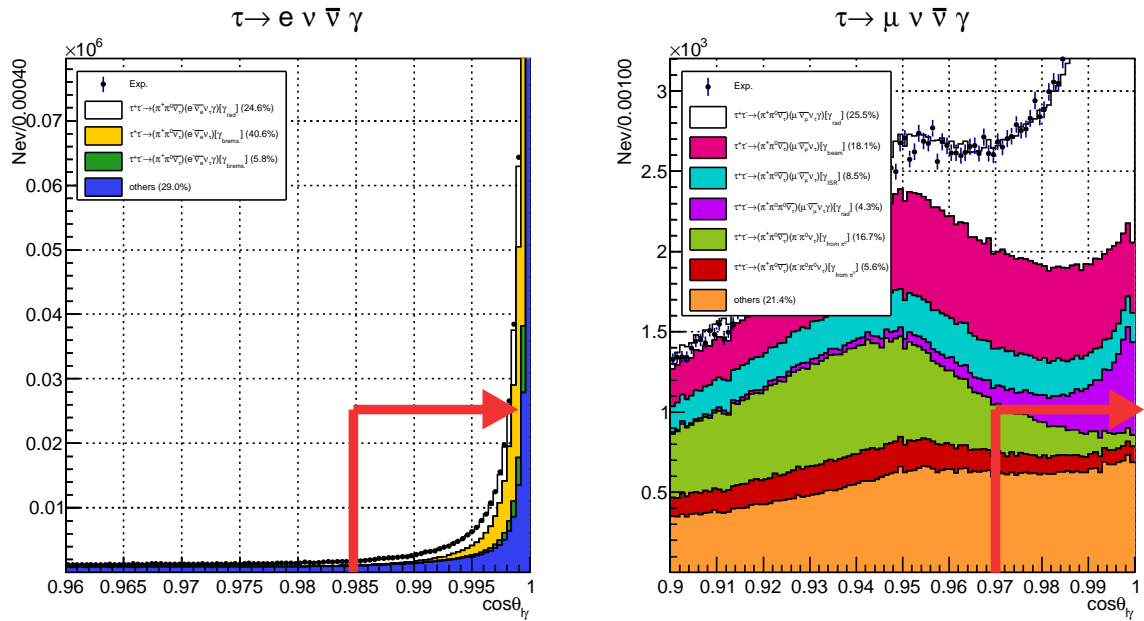
④ Angle between  $\ell\gamma$  and  $\pi^0$ : considering both  $\ell^-$  and  $\gamma$ , and  $\rho^+$  are boosted back-to-back each other in  $\tau^+\tau^-$  rest frame, we reject events if the direction of the combined momentum of the lepton and photon in the CMS frame orients in the hemisphere determined by the  $\rho^+$  candidate ( $\theta_{(\ell\gamma)\rho} > 90^\circ$ ).

⑤  $\rho^+$  mass: an invariant mass of charged and neutral pions must satisfy  $0.5 \text{ GeV}/c^2 < m_{\pi^\pm\pi^0} < 1.5 \text{ GeV}/c^2$ .

⑥ Sum of the laboratory energies of photons which are not associated with any charged track (denoted as  $E_{\text{extray}}^{\text{LAB}}$ ) must satisfy  $E_{\text{extray}}^{\text{LAB}} < 0.2 \text{ GeV}$  for  $\tau \rightarrow e\nu\bar{\nu}\gamma$  events and  $E_{\text{extray}}^{\text{LAB}} < 0.3 \text{ GeV}$  for  $\tau \rightarrow \mu\nu\bar{\nu}\gamma$  events. This requirement is essential in the suppression of various backgrounds. For example,  $\pi^0$ s produced from hadronic decays generate extra photon clusters. Moreover, fake clusters arising from the beam deposit energies in the ECL.

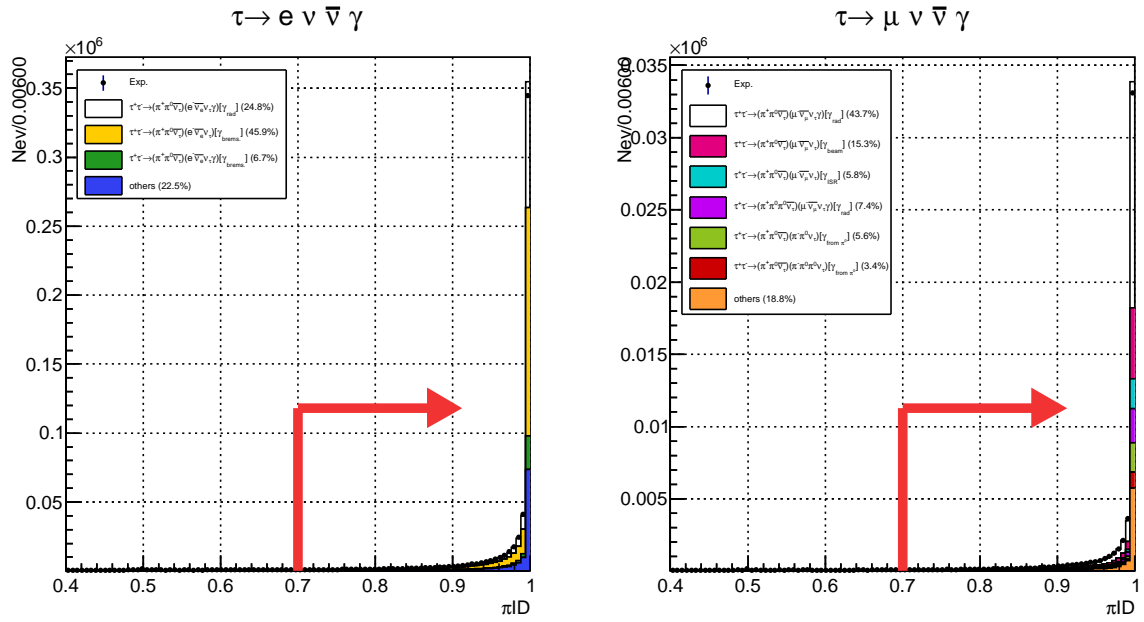


(a)

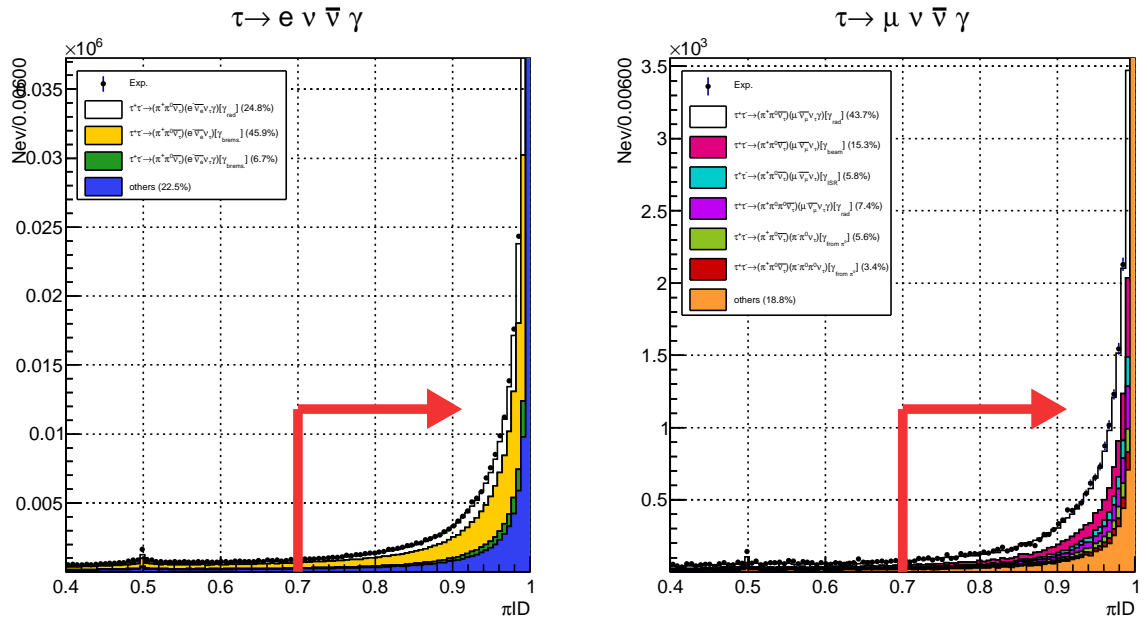


(b)

Figure 4.2: ①  $\rightarrow$  ②: Distribution of cosine of angle between the lepton and photon: (a) overall view and (b) enlarged view.

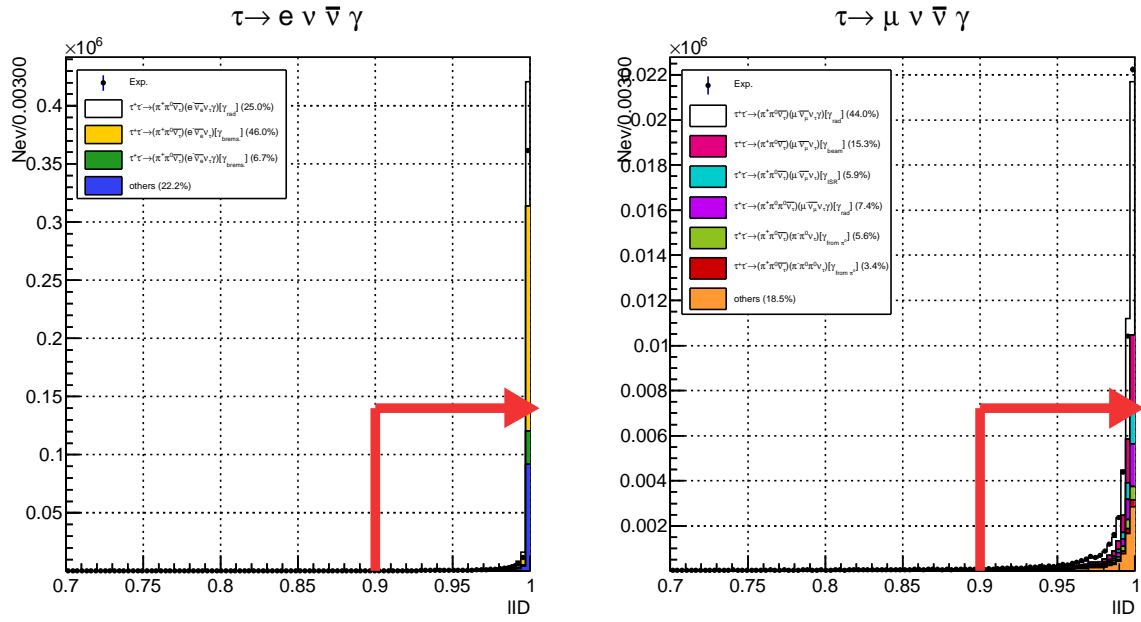


(a)

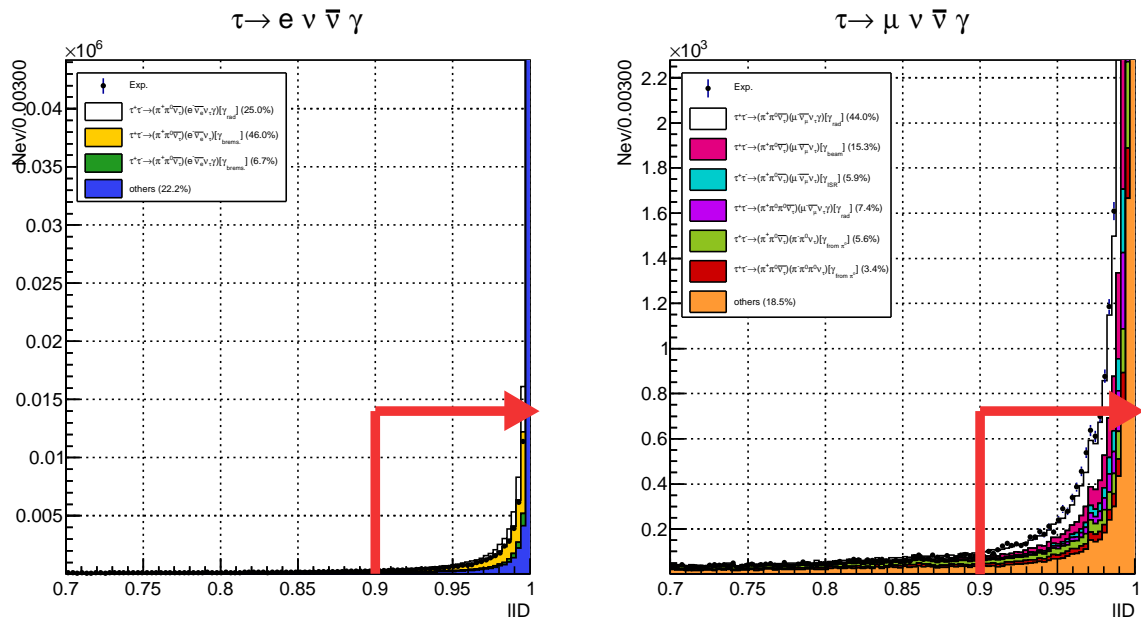


(b)

Figure 4.3: ① → ②: Distribution of likelihood( $\pi/K$ ): (a) overall view and (b) enlarged view.



(a)



(b)

Figure 4.4: ②  $\rightarrow$  ③: Distribution of likelihood( $\ell/\pi$ ): (a) overall view and (b) enlarged view.

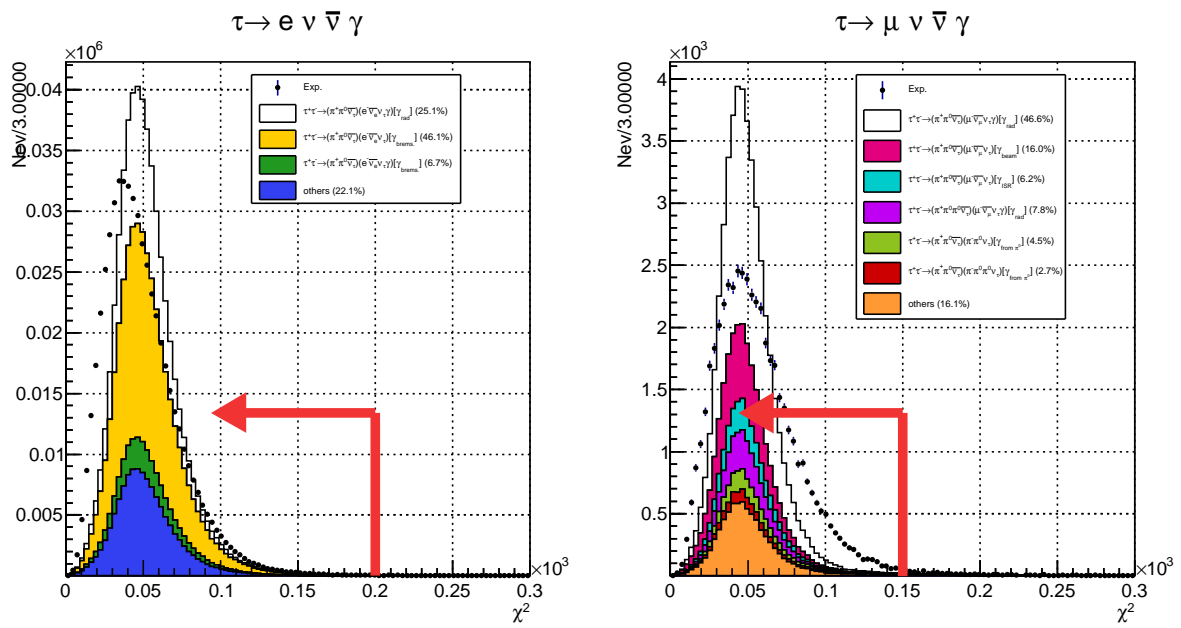
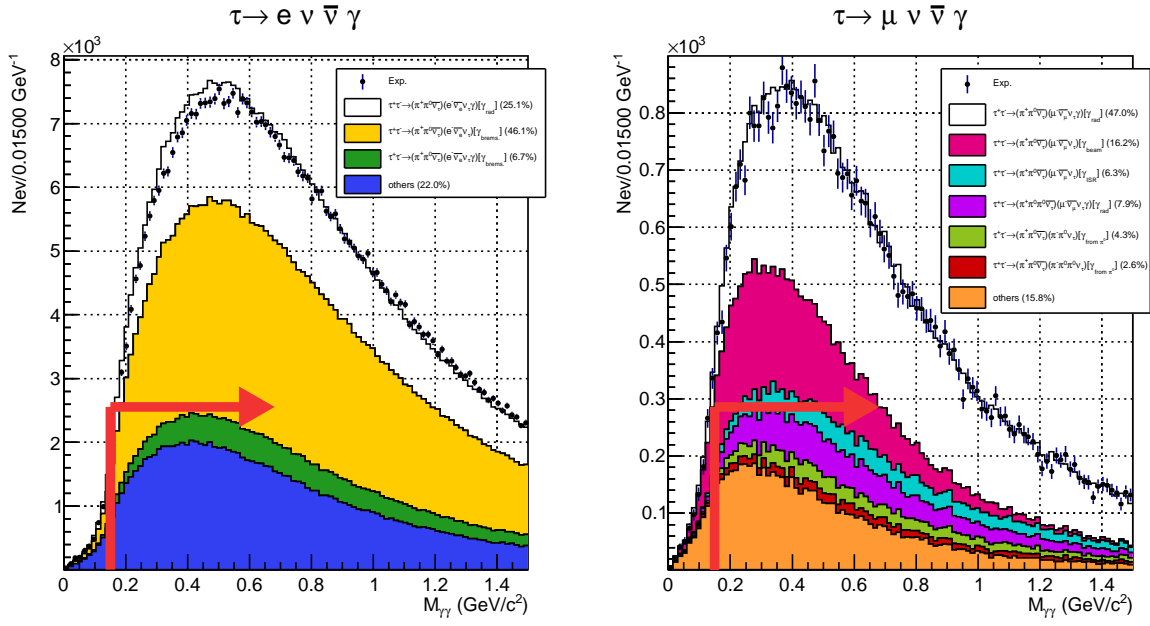
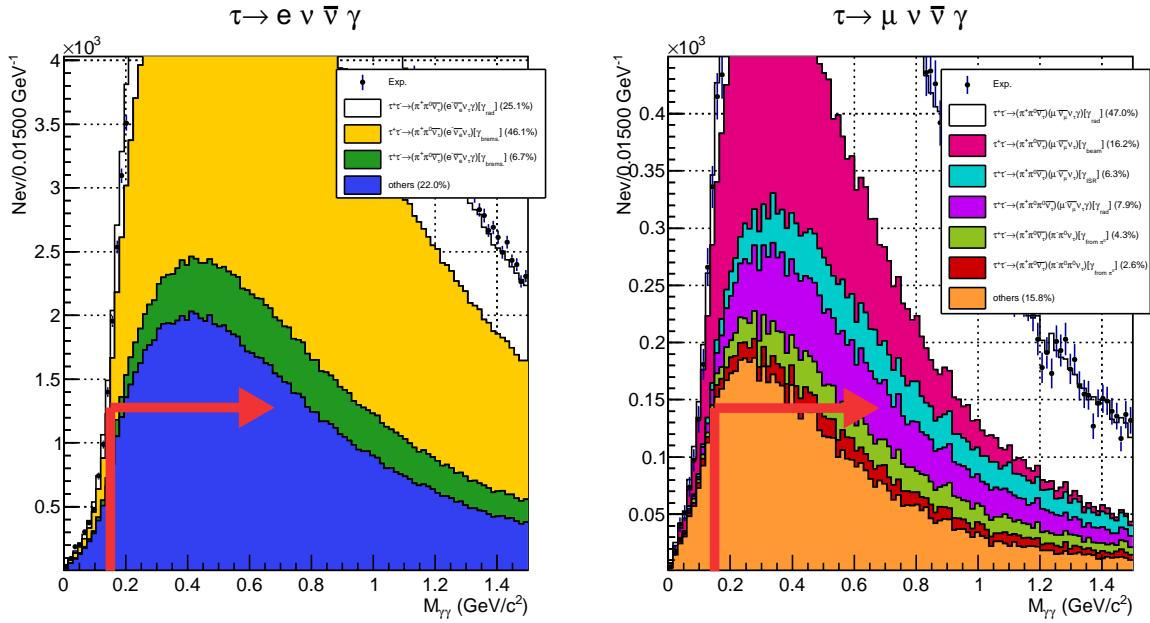


Figure 4.5: ②  $\rightarrow$  ③: Distribution of  $\chi_l^2$ .



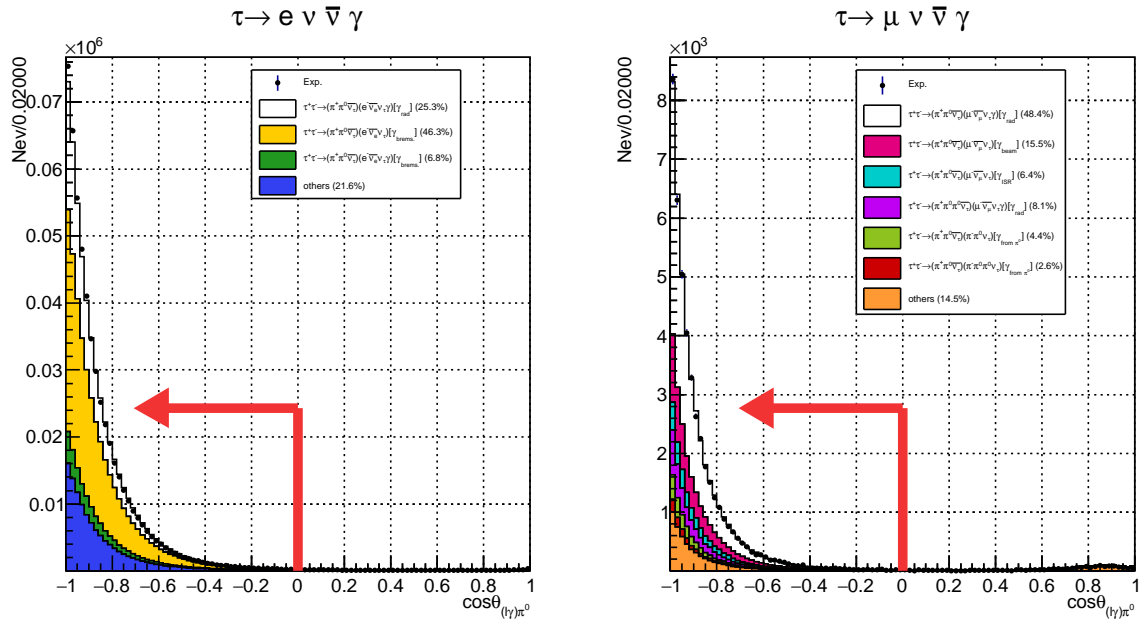


(a)

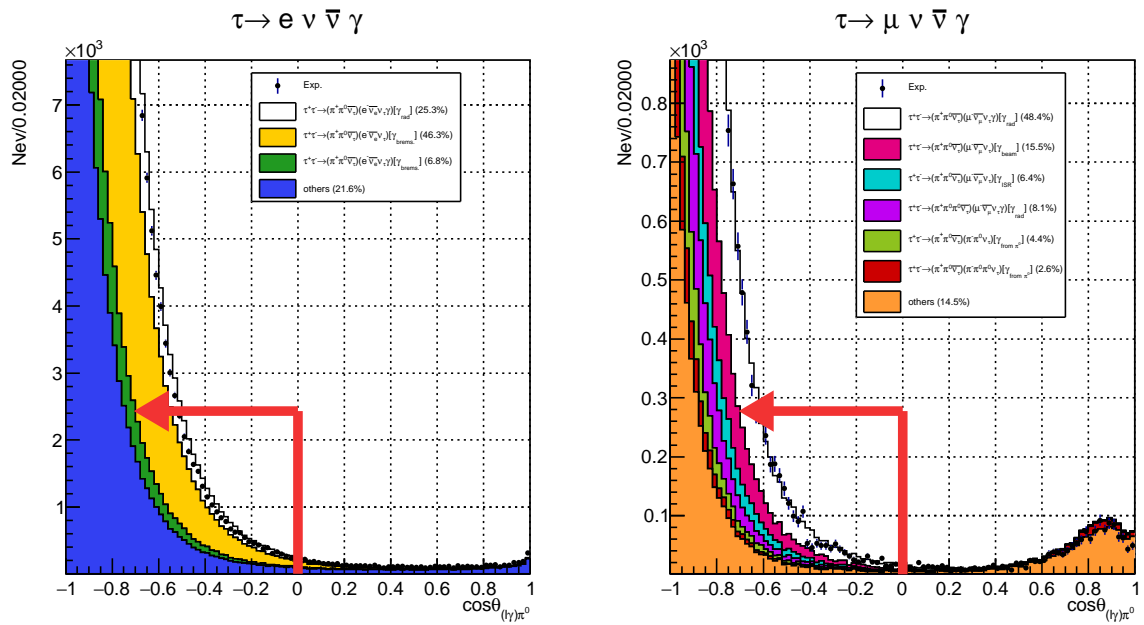


(b)

Figure 4.6: ③  $\rightarrow$  ④: Distribution of  $M_{\gamma\gamma}$ , where one  $\gamma$  is candidate of radiative photon and the other is  $\gamma$  reconstructed for  $\pi^0$ : (a) large scale and (b) enlarged.

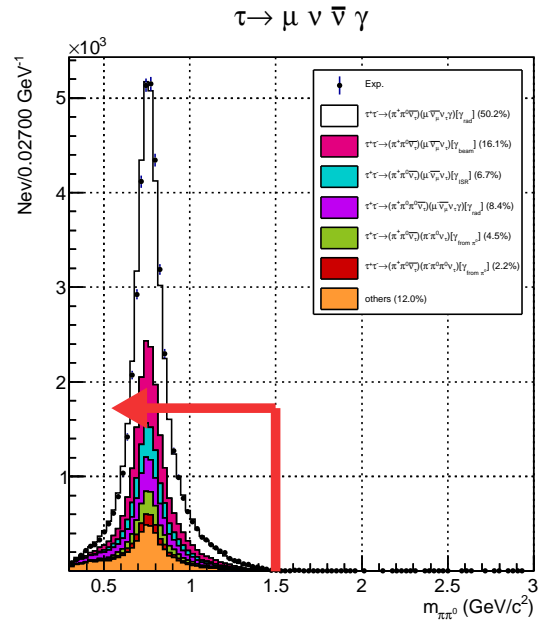
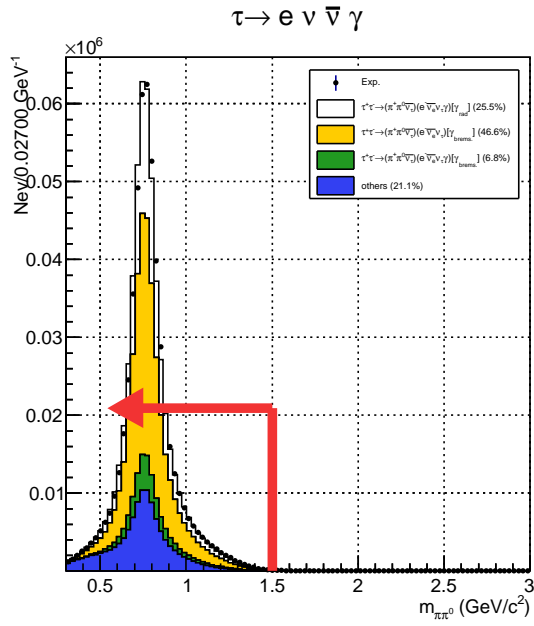


(a)

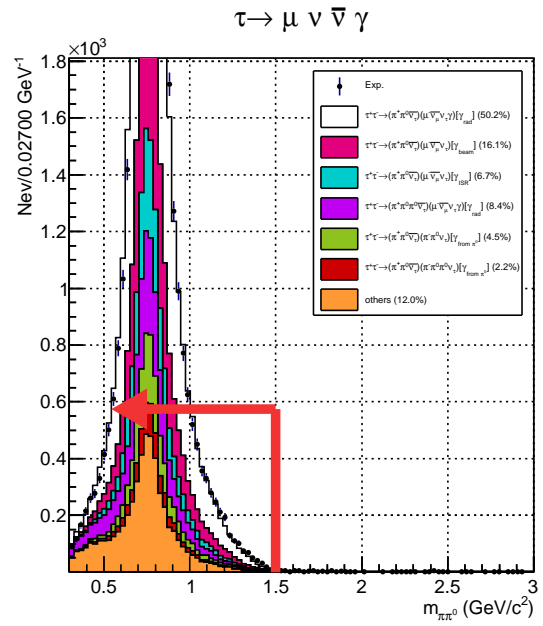
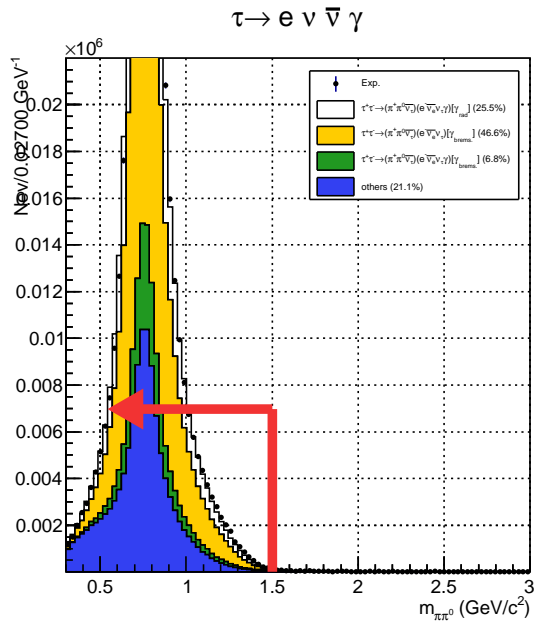


(b)

Figure 4.7: ④ → ⑤: Distribution of  $\cos\theta_{(\ell\gamma)\pi^0}$ : (a) overall view and (b) enlarged view.

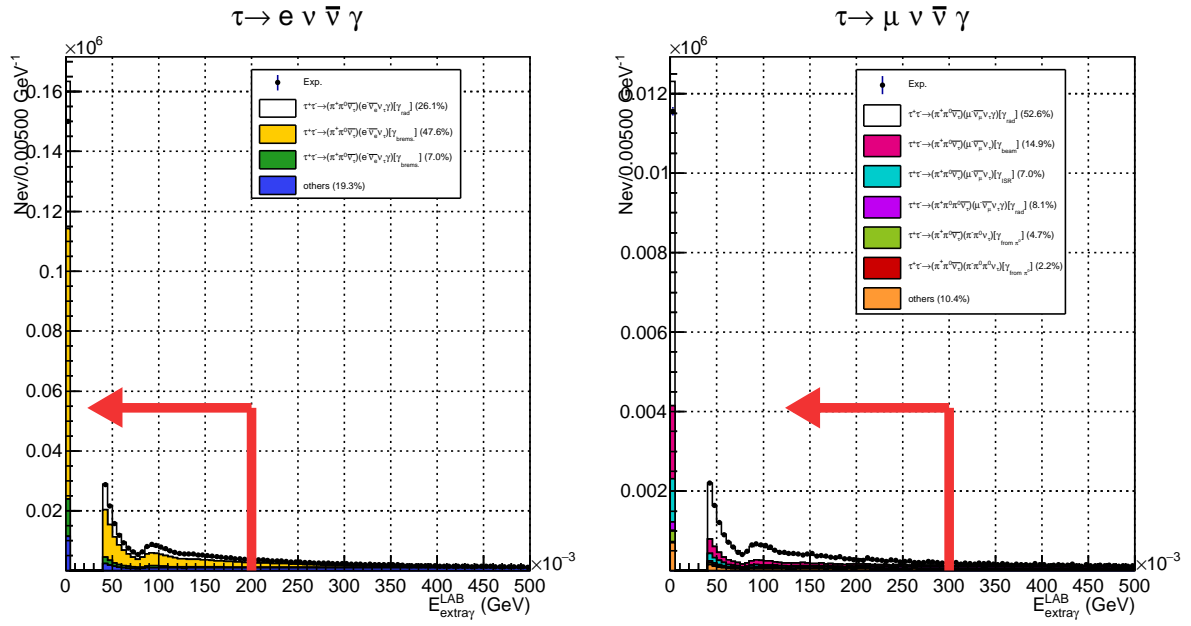


(a)

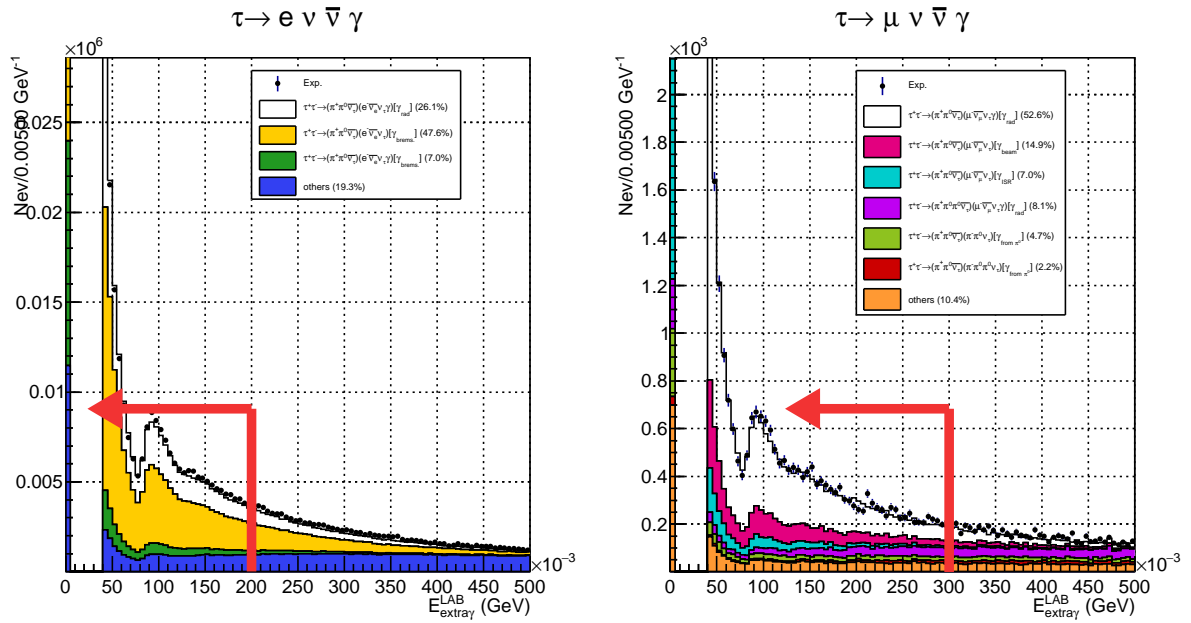


(b)

Figure 4.8: ⑤  $\rightarrow$  ⑥: Distribution of  $M_{\pi\pi}$ : (a) overall view and (b) enlarged view.



(a)



(b)

Figure 4.9:  $\textcircled{c}$   $\rightarrow$  final: Distribution of  $E_{\text{extray}}^{\text{LAB}}$ : (a) (a) overall view and (b) enlarged view.

Table 4.5: Background contributions for  $\tau^+\tau^- \rightarrow (\pi^+\pi^0\bar{\nu})(e^-\nu\bar{\nu}\gamma)$  candidates.

Process †	Fraction	Color
$\tau^+\tau^- \rightarrow (\pi^+\pi^0\bar{\nu})(e^-\nu\bar{\nu}\gamma)[\gamma_{\text{rad}}]$	28.9%	Open
(1) $\tau^+\tau^- \rightarrow (\pi^+\pi^0\bar{\nu})(e^-\nu\bar{\nu})[\gamma_{\text{brems.}}]$	52.8%	Yellow
(2) $\tau^+\tau^- \rightarrow (\pi^+\pi^0\bar{\nu})(e^-\nu\bar{\nu}\gamma)[\gamma_{\text{brems.}}]$	7.50%	Green
(3) Others	10.7%	Blue

† The bracket represents the source of photon.

## 4.4 Background components for the selected candidates

In this section, we present the signal and background contributions evaluated by MC simulation with selection criteria described in the last section. As explained below in detail, the fractions of background modes largely differ between electron and muon modes. This arises from the high rate of bremsstrahlung by a daughter electron. The small mass of electron makes the rate of bremsstrahlung high and this occupies the fraction of selected events.

### 4.4.1 $\tau^+\tau^- \rightarrow (\pi^+\pi^0\bar{\nu})(e^-\nu\bar{\nu}\gamma)$ decay candidates

Figures 4.10, 4.11, 4.12 and 4.13 show the distributions of photon energy  $E_\gamma$ , electron momentum  $P_e$ , cosine of angle between lepton and photon  $\cos\theta_{e\gamma}$  and angle itself for  $\tau^- \rightarrow e^-\nu\bar{\nu}\gamma$  candidates. Fraction of each background is summarized in Table 4.5.

- (1) Ordinary leptonic decay + bremsstrahlung,  $(e, \pi\pi^0) + \gamma_{\text{brems.}}$ : 52.8%

When an electron is accelerated by an electric field of atoms in detector, a photon is produced almost collinearly with the electron direction. In particular, the photons produced at detectors near the IP cannot be essentially distinguished from signal photon even if we try to veto the event based on the impact parameter of the electron track. Because of the quite similar feature to the signal events, *i.e.*, its energy and angular dependence, this occurrence is called *external bremsstrahlung*. This contribution is represented by a yellow histogram in Figs. 4.10 to 4.13.

- (2) Radiative leptonic decay occurred but the bremsstrahlung is reconstructed,  $(e\gamma, \pi\pi^0) + \gamma_{\text{brems.}}$ : 7.50%

Although the radiative leptonic decay  $\tau^- \rightarrow e^-\nu\bar{\nu}\gamma$  occurs, the extra bremsstrahlung is reconstructed as a signal photon. Since this event does not convey any information of the Michel parameters, we regard this event as a background. This contribution is represented by a green histogram.

- (3) Others: 10.7%

The rest backgrounds are treated as one category and we call them *others*. This contribution is represented by a blue histogram in Figs. 4.10 to 4.13. In Table 4.6, we show the list of sources on this category. The contributions come from a beam background and a failure of the reconstruction of  $\rho^+$  candidates due to contaminations from multi-pion decays such as  $\tau^+ \rightarrow \pi^+\pi^0\pi^0\bar{\nu}$ .

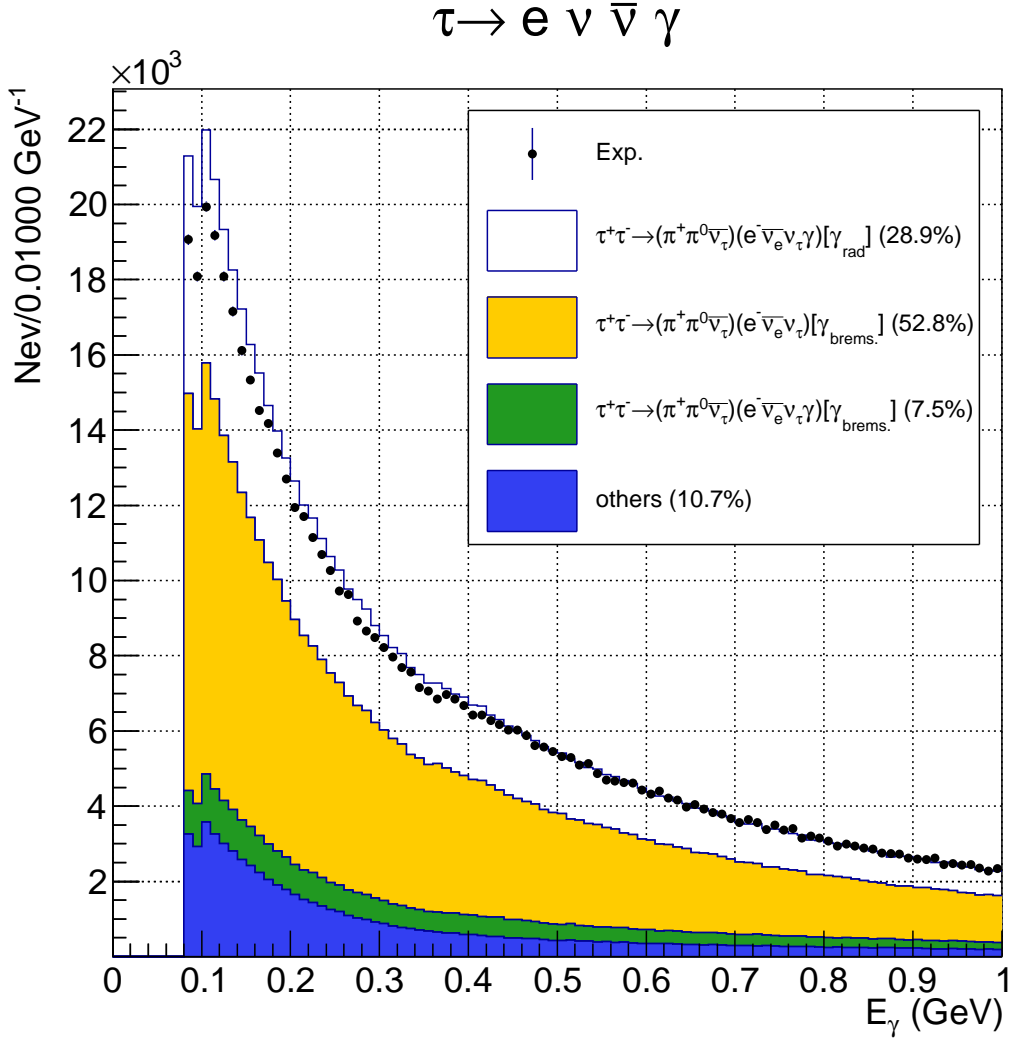


Figure 4.10: Distribution of the photon energy  $E_\gamma$  for  $\tau^+\tau^- \rightarrow (\pi^+\pi^0\bar{\nu})(e^-\nu\bar{\nu}\gamma)$  candidates. The bracket shows an origin of the reconstructed photon. Dots with error bars indicate experimental distribution while histograms are MC simulation. Open histogram represent signal MC while yellow, green and blue histograms represent an ordinary leptonic decay + bremsstrahlung, a radiative leptonic decay + bremsstrahlung and others.

Table 4.6: Background components in others for  $\tau^+\tau^- \rightarrow (\pi^+\pi^0\bar{\nu})(e^-\nu\bar{\nu}\gamma)$  candidates.

Process †	Fraction in others (%)
$(\pi^+\pi^0\bar{\nu})(e^-\nu\bar{\nu})[\gamma_{\text{beam}}]$	32
$(\pi^+\pi^0\pi^0\bar{\nu})(e^-\nu\bar{\nu}\gamma)[\gamma_{\text{rad}}]$	23
$(\pi^+\pi^0\bar{\nu})(e^-\nu\bar{\nu}\gamma)[\gamma_{\text{beam}}]$	9
$(\pi^+\pi^0\pi^0\bar{\nu})(e^-\nu\bar{\nu}\gamma)[\gamma_{\text{brems.}}]$	6
Others (each is smaller than 4%)	30

† The bracket represents the source of photon.

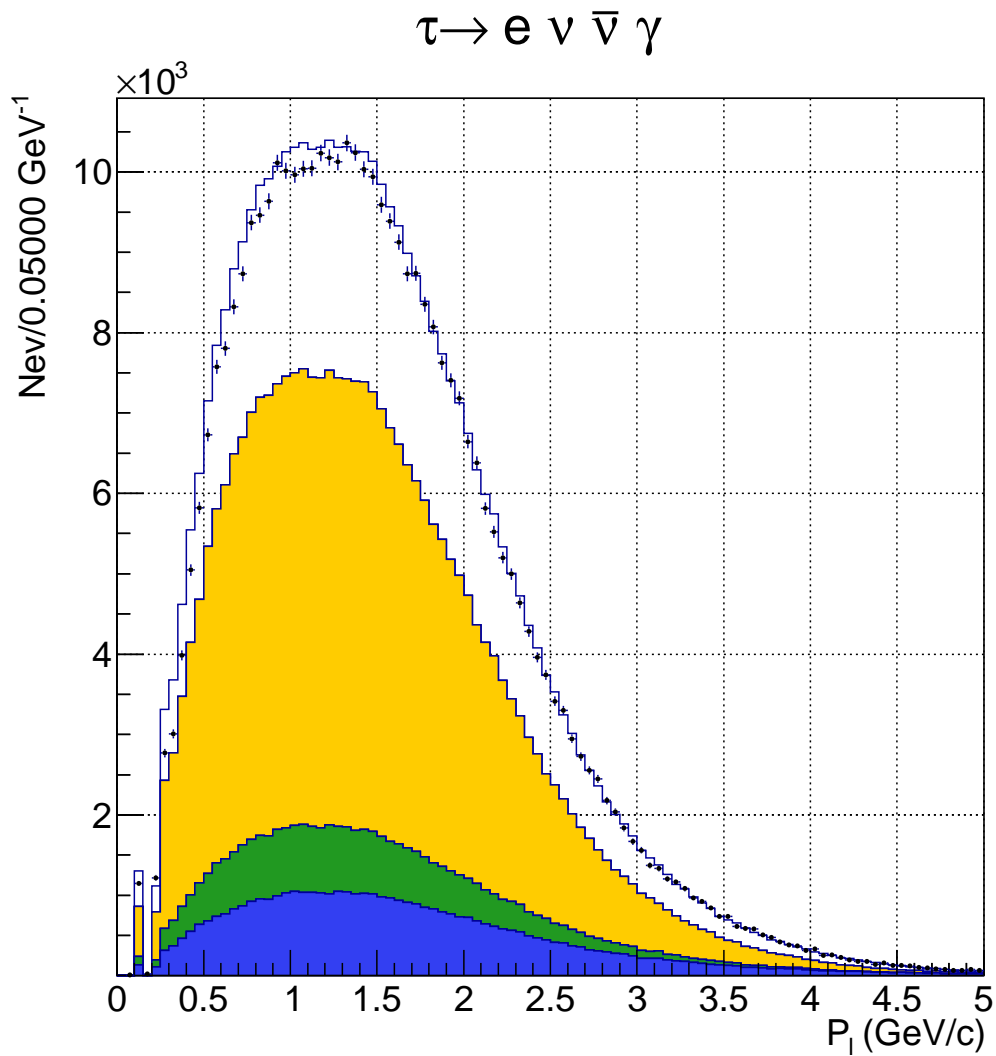


Figure 4.11: Distribution of the momentum of electron  $P_e$  for the  $\tau^+\tau^- \rightarrow (\pi^+\pi^0\bar{\nu})(e^-\nu\bar{\nu}\gamma)$  candidates. The correspondences of colors of histograms are same as Fig. 4.10.

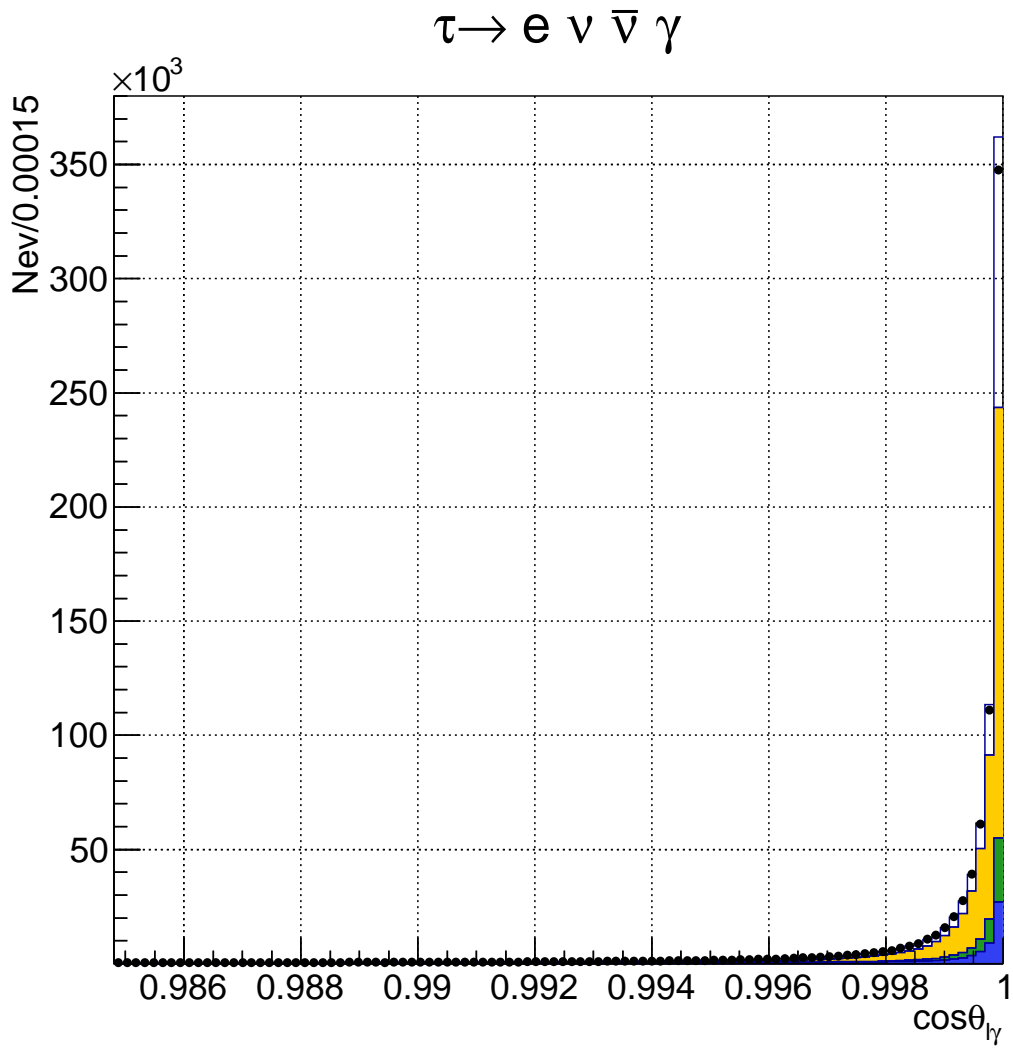


Figure 4.12: Distribution of the cosine of angle between the electron and photon  $\cos\theta_{l\gamma}$  for the  $\tau^+\tau^- \rightarrow (\pi^+\pi^0\bar{\nu})(e^-\nu\bar{\nu}\gamma)$  candidates. The correspondences of colors of histograms are same as Fig. 4.10.



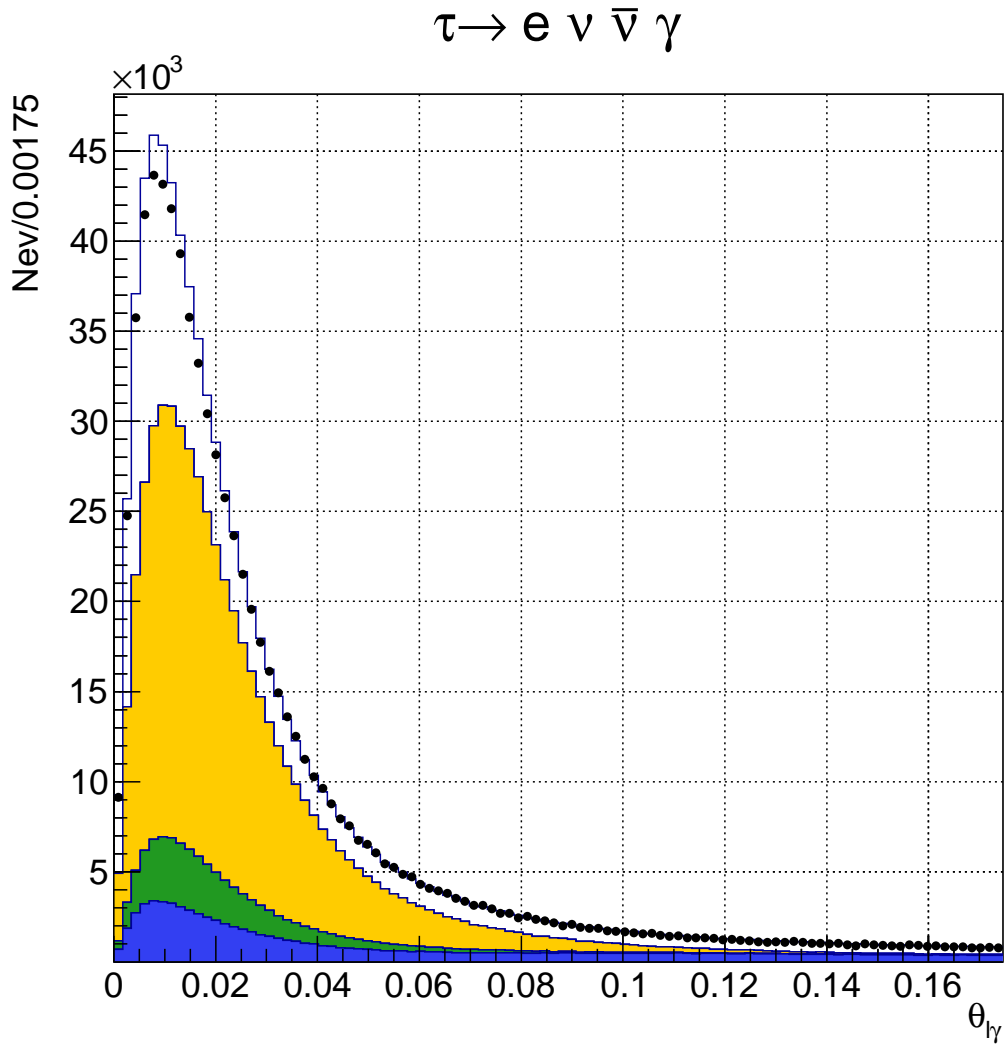


Figure 4.13: Distribution of the angle between the electron and photon  $\theta_{\ell\gamma}$  for the  $\tau^+\tau^- \rightarrow (\pi^+\pi^0\nu)(e^-\nu\bar{\nu}\gamma)$  candidates. The correspondences of colors of histograms are same as Fig. 4.10.

#### 4.4.2 $\tau^+\tau^- \rightarrow (\pi^+\pi^0\bar{\nu})(\mu^-\nu\bar{\nu}\gamma)$ decay candidates

For  $\tau^+\tau^- \rightarrow (\pi^+\pi^0\bar{\nu})(\mu^-\nu\bar{\nu}\gamma)$  candidates, we show the distributions of photon energy  $E_\gamma$ , muon momentum  $P_\mu$ , cosine of angle between muon and photon  $\cos\theta_{\mu\gamma}$  and angle itself in Figs. 4.16, 4.15, 4.14 and 4.17. Following information is summarized in Table 4.7.

- (1) Ordinary leptonic decay + beam background,  $(\mu, \pi\pi^0) + \gamma_{\text{beam}}$ : 16.2%

For the  $\tau^+\tau^- \rightarrow (\pi^+\pi^0\bar{\nu})(\mu^-\nu\bar{\nu}\gamma)$  decay candidates, the beam background has the largest fraction. The clusters in the ECL, originating from beam, behaves as photon and the event is wrongly reconstructed when it is combined with the ordinary leptonic decay  $\tau^- \rightarrow \mu^-\nu\bar{\nu}$ . Because the distribution of the beam background is determined by complex geometry and environment of the beam, it is impossible to reproduce the distribution only from the MC. For this reason, the energy deposit in the ECL from the beam background is recorded in the real experiment with random trigger and this information is overlaid to MC event. This contribution is represented by a magenta histogram in Figs. 4.14 to 4.17.

- (2) Ordinary leptonic decay + ISR/FSR,  $(\mu, \pi\pi^0) + \gamma_{\text{ISR/FSR}}$ : 7.7%

The initial and final state radiation (ISR/FSR) are processes in which photons are generated from vertices of  $e^+e^-$  and  $\tau^+\tau^-$ , respectively. Since  $\tau^\pm$  is a *long-lived* particle in that the interference between the ISR/FSR processes and decay amplitude of  $\tau$  is ignored, the radiative decay is definitely distinguished from ISR/FSR in the generator level. The ISR/FSR is reconstructed as signal photon and the event is selected when it combines with  $\tau^- \rightarrow \mu^-\nu\bar{\nu}$  decay. This contribution is represented by a water-blue histogram.

- (3) Three  $\pi$  events,  $(\mu\gamma, \pi\pi^0\pi^0)$ : 5.1%

When one  $\pi^0$  from  $\tau^+ \rightarrow \pi^+\pi^0\pi^0\bar{\nu}$  is lost, it is reconstructed as the  $\tau^+ \rightarrow \pi^+\pi^0\nu$  decay. Since the radiative decay  $\tau^- \rightarrow \mu^-\nu\bar{\nu}\gamma$  is properly reconstructed, this event still have a sensitivity on the Michel parameters. This contribution is is represented by a purple magenta histogram.

- (4)  $\rho$ - $\rho$  decay,  $(\pi\pi^0, \pi\pi^0)$ : 3.8%

When one photon from neutral pion is missed and the charged pion is mis-identified as muon, the event is wrongly selected. Though the probabilities are relatively small, the large branching ratio of  $\tau^- \rightarrow \rho^-\nu \rightarrow \pi^-\pi^0\nu$  decay ( $\sim 25\%$ ) gives a notable contribution to the  $\tau^- \rightarrow \mu^-\nu\bar{\nu}$  decay candidates. This contribution is represented by a light-green histogram.

- (5)  $3\pi$ - $\rho$  decay,  $(\pi\pi^0\pi^0, \pi\pi^0)$ : 1.2%

$\tau^- \rightarrow \pi^-\pi^0\pi^0\nu$  decay is mis-reconstructed as signal when  $\pi^-$  is mis-identified as  $\mu^-$  and three photons from two  $\pi^0$  are not vetoed even after the event selection. Though the fraction of  $3\pi$ - $\rho$  decay is small, the effect of this decay on the fitted Michel parameter is relatively high and we separately regard this decay as one of major background modes. This contribution is represented by a red histogram.

- (6) Others: 8.6%

Similarly to  $\tau^+\tau^- \rightarrow (\pi^+\pi^0\bar{\nu})(e^-\nu\bar{\nu}\gamma)$  decay candidates, the rest fractions are grouped as one category *others*. This contribution is represented by an orange histogram. In Table 4.8, we show the list of sources on this category. The contributions mainly come from a pion-misidentification as muon and contaminations from the beam backgrounds. In many cases, pions from various hadronic decays couple with the accidental beam background or a photon from  $\pi^0$ .

Table 4.7: Background contributions for  $\tau^+ \tau^- \rightarrow (\pi^+ \pi^0 \bar{\nu})(\mu^- \nu \bar{\nu} \gamma)$  candidates.

	Process †	Fraction	Color
	$\tau^+ \tau^- \rightarrow (\pi^+ \pi^0 \bar{\nu})(\mu^- \nu \bar{\nu} \gamma)[\gamma_{\text{rad}}]$	57.4%	Open
(1)	$\tau^+ \tau^- \rightarrow (\pi^+ \pi^0 \bar{\nu})(\mu^- \nu \bar{\nu})[\gamma_{\text{beam}}]$	16.2%	Magenta
(2)	$\tau^+ \tau^- \rightarrow (\pi^+ \pi^0 \bar{\nu})(\mu^- \nu \bar{\nu})[\gamma_{\text{ISR}}]$	7.7%	Water-blue
(3)	$\tau^+ \tau^- \rightarrow (\pi^+ \pi^0 \pi^0 \bar{\nu})(\mu^- \nu \bar{\nu} \gamma)[\gamma_{\text{rad}}]$	5.1%	Purple
(4)	$\tau^+ \tau^- \rightarrow (\pi^+ \pi^0 \bar{\nu})(\pi^- \pi^0 \nu)[\gamma_{\text{from } \pi^0}]$	3.8%	Light green
(5)	$\tau^+ \tau^- \rightarrow (\pi^+ \pi^0 \bar{\nu})(\pi^- \pi^0 \pi^0 \nu)[\gamma_{\text{from } \pi^0}]$	1.2%	Red
(6)	Others	8.6%	Others

† The bracket represents the source of photon.

Table 4.8: Background components in others for  $\tau^+ \tau^- \rightarrow (\pi^+ \pi^0 \bar{\nu})(\mu^- \nu \bar{\nu} \gamma)$  candidates.

Process †	Fraction in others (%)
$(\pi^+ \pi^0 \pi^0 \bar{\nu})(\mu^- \nu \bar{\nu})[\gamma_{\text{beam}}]$	8
$(\mu^+ \nu \bar{\nu})(\pi^- \pi^0 \pi^0 \nu)[\gamma_{\text{beam}}]$	8
$(\pi^+ \pi^0 \bar{\nu})(\mu^- \nu \bar{\nu} \gamma)[\gamma_{\text{beam}}]$	8
$(\mu^+ \nu \bar{\nu} \gamma)(\pi^- \pi^0 \nu)[\gamma_{\text{beam}}]$	7
$(\pi^+ \bar{\nu})(\pi^- \pi^0 \pi^0 \nu)[\gamma_{\text{from } \pi^0}]$	7
$(\pi^+ \pi^0 \bar{\nu})(\pi^- \pi^0 \pi^0 \nu)[\gamma_{\text{from } \pi^0}]$	6
$(\pi^+ \pi^0 \pi^0 \bar{\nu})(\pi^- \pi^0 \nu)[\gamma_{\text{from } \pi^0}]$	6
Others (each is smaller than 4%)	50

† The bracket represents the source of photon.

$$\tau \rightarrow \mu \nu \bar{\nu} \gamma$$

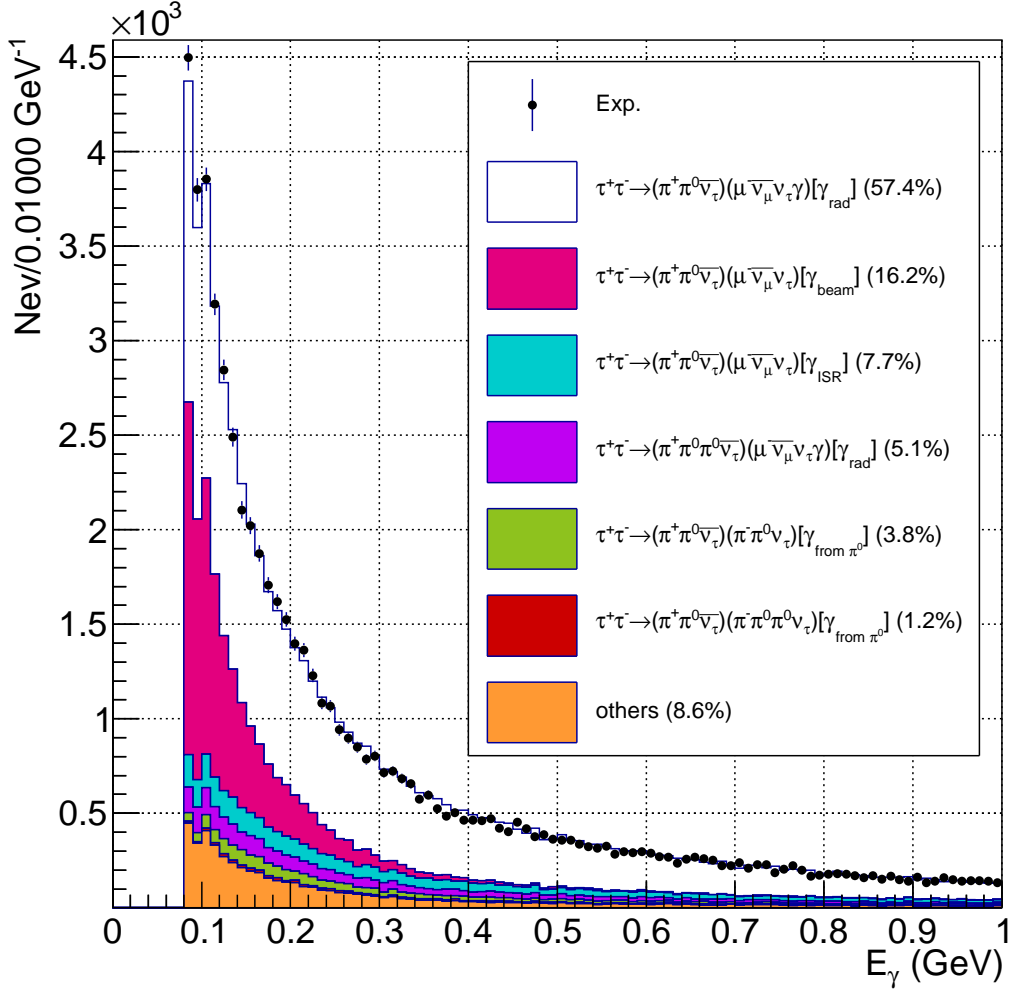


Figure 4.14: Distribution of the photon energy  $E_\gamma$  for the  $\tau^+\tau^- \rightarrow (\pi^+\pi^0\nu^-)(\mu^- \nu_\mu \bar{\nu}_\tau \gamma)$  decay candidates. The bracket shows an origin of the reconstructed photon. Dots with error bars indicate experimental distribution while histograms are MC simulation. The open histogram corresponds to signal MC distribution while colored histograms are background modes: (red) ordinary leptonic decay + beam background, (blue) ordinary leptonic decay + ISR/FSR gamma, (purple) three- $\pi$ , (green)  $\rho\rho$ , (brown)  $3\pi$ - $\rho$  and (orange) others.

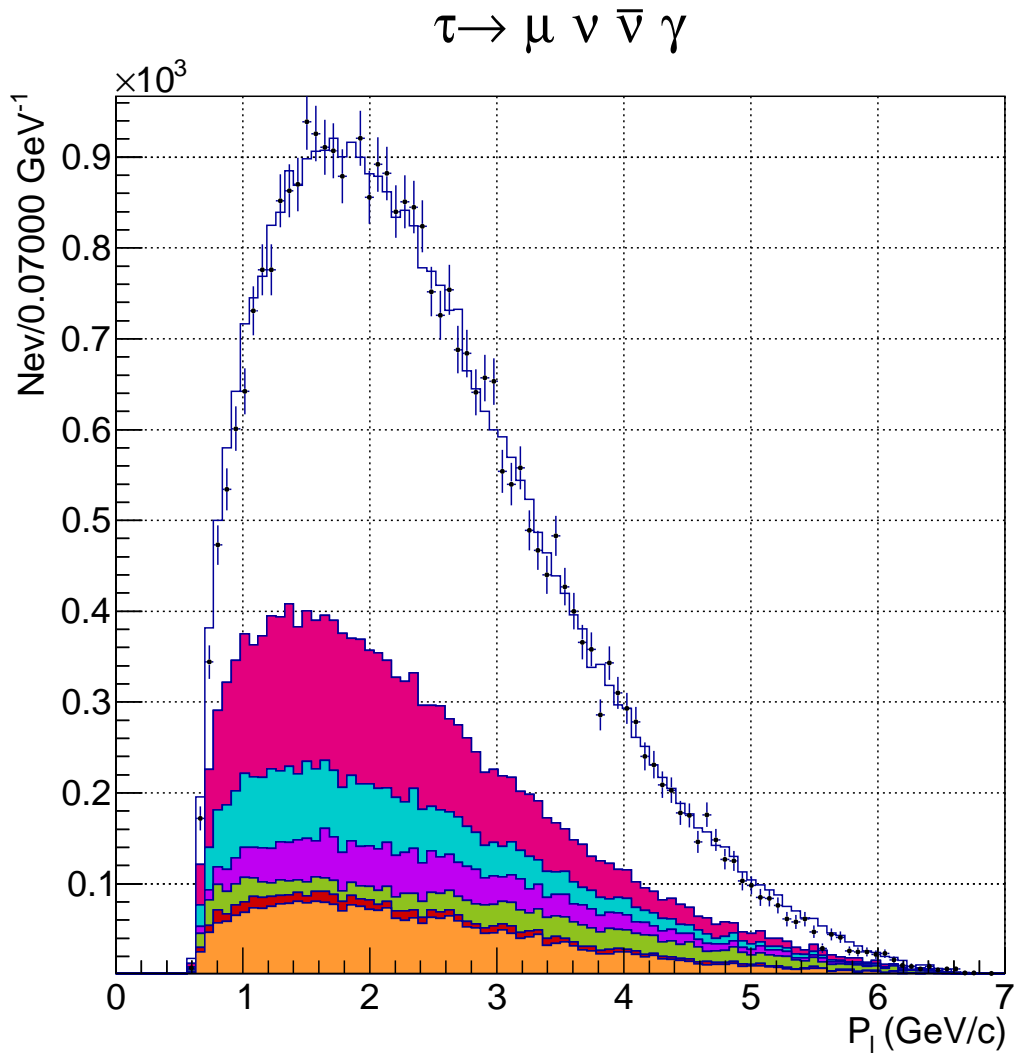


Figure 4.15: Distribution of the momentum of electron  $P_\mu$  for the  $\tau^+\tau^- \rightarrow (\pi^+\pi^0\nu)(\mu^-\nu\bar{\nu}\gamma)$  candidates. The correspondences of colors of histograms are same as Fig. 4.14.

$$\tau \rightarrow \mu \nu \bar{\nu} \gamma$$

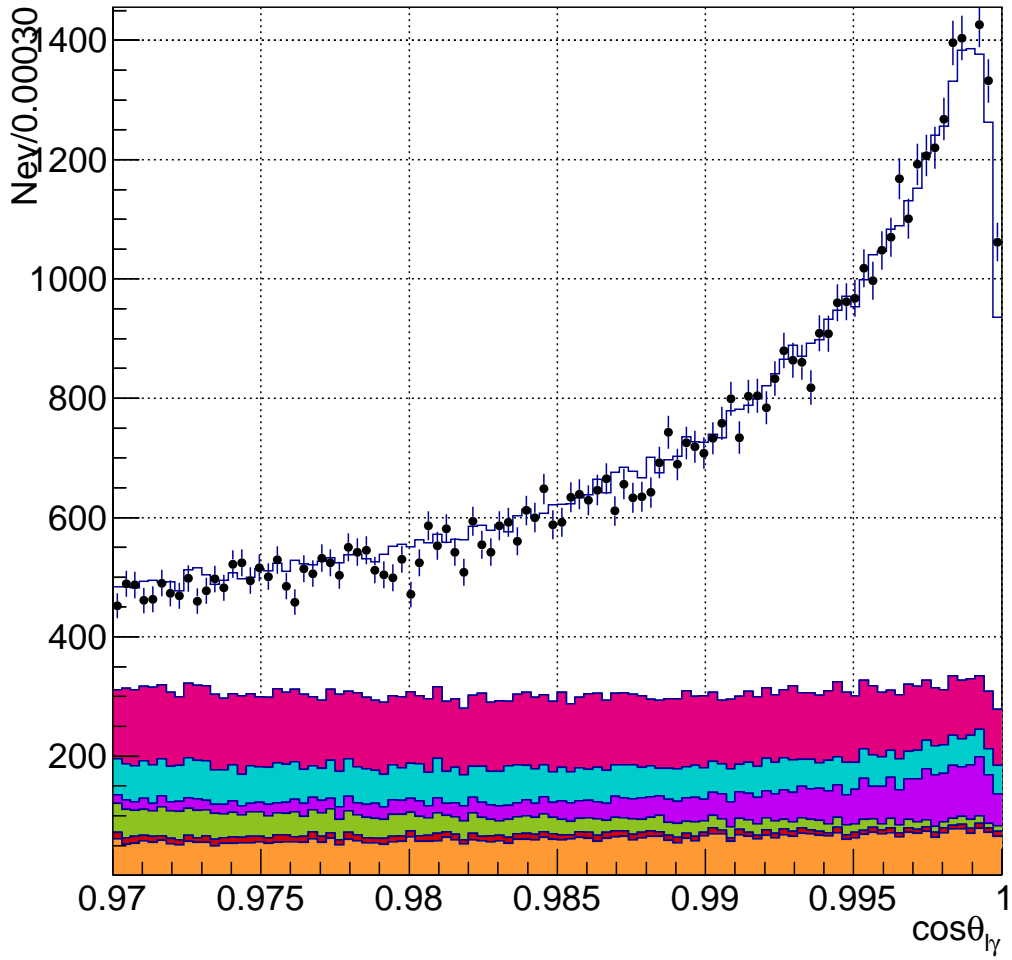


Figure 4.16: Distribution of the cosine of angle between muon and photon  $\cos\theta_{\ell\gamma}$  for the  $\tau^+\tau^- \rightarrow (\pi^+\pi^0\bar{\nu})(\mu^-\nu\bar{\nu}\gamma)$  decay candidates. The correspondences of colors of histograms are same as Fig. 4.14.

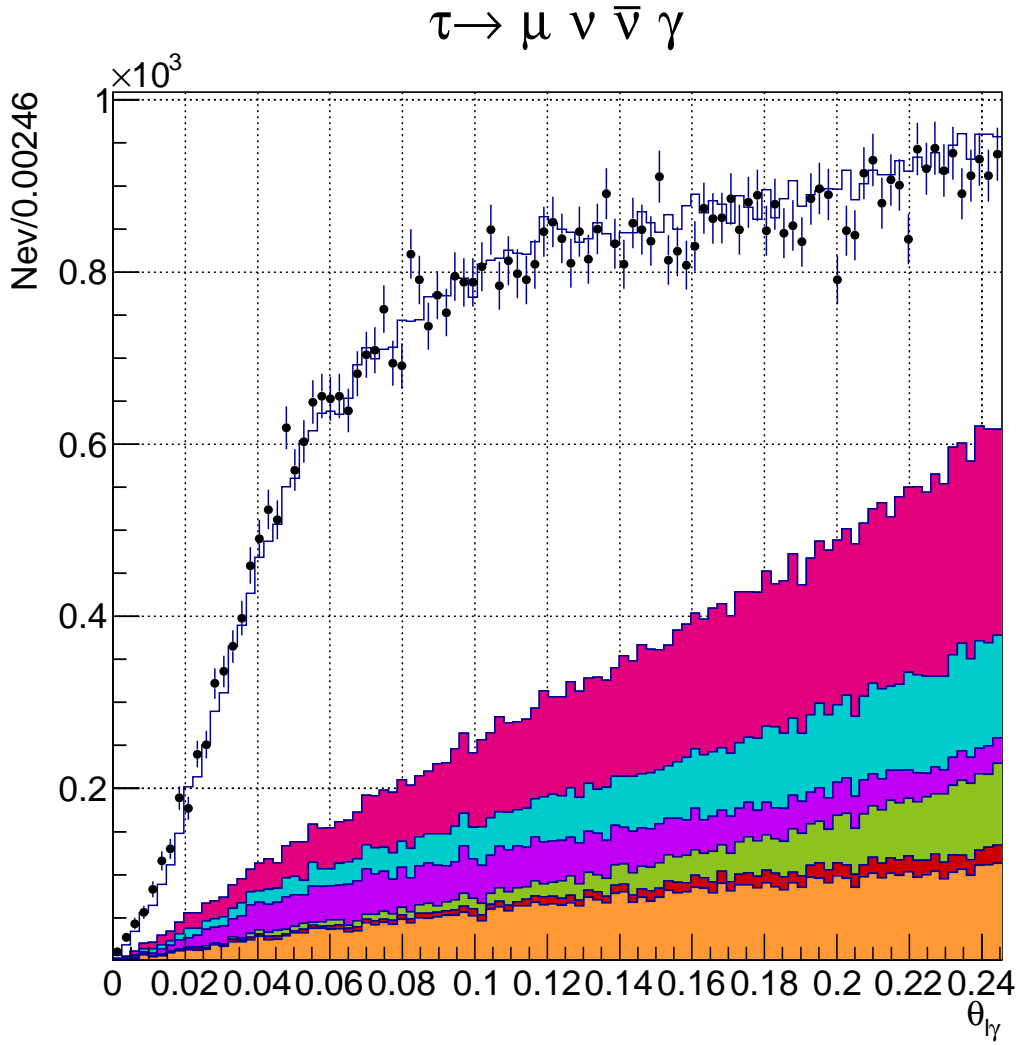


Figure 4.17: Distribution of the angle between muon and photon  $\theta_{l\gamma}$  for the  $\tau^+\tau^- \rightarrow (\pi^+\pi^0\nu)(\mu^-\nu\bar{\nu}\gamma)$  decay candidates. The correspondences of colors of histograms are same as Fig. 4.14.

## 4.5 Total efficiency

In this section, we present the efficiency of signal events evaluated by MC simulation. We prepared dedicated signal MC samples which contain  $7.504 \times 10^7$  events for each of four configurations:  $(e^- \gamma, \pi^+ \pi^0)$ ,  $(e^+ \gamma, \pi^- \pi^0)$ ,  $(\mu^- \gamma, \pi^+ \pi^0)$  and  $(\mu^+ \gamma, \pi^- \pi^0)$ . By default, the TAUOLA generator adopts the photon energy threshold:  $E_\gamma^* = m_\tau \times 0.001 \sim 1.8$  MeV to define the radiative decay. Based on the information of the generated events, the ratio of events in which  $E_\gamma^*$  exceeds 10 MeV is 66.6% for  $\ell = e$  and 68.5% for  $\ell = \mu$ , respectively. Thus the numbers of generated signal events defined by  $E_\gamma^* > 10$  MeV are  $2.50 \times 10^7$  for  $(e^- \gamma, \pi^+ \pi^0)$ ,  $(e^+ \gamma, \pi^- \pi^0)$  decays and  $2.57 \times 10^7$  for  $(\mu^- \gamma, \pi^+ \pi^0)$ ,  $(\mu^+ \gamma, \pi^- \pi^0)$  decays. With selection criteria described above, the number of selected events are

$$N_e^- \equiv N(e^- \gamma, \pi^+ \pi^0)^* = 1205449, \quad (4.1)$$

$$N_e^+ \equiv N(e^+ \gamma, \pi^- \pi^0) = 1195610, \quad (4.2)$$

$$N_\mu^- \equiv N(\mu^- \gamma, \pi^+ \pi^0) = 996808, \quad (4.3)$$

$$N_\mu^+ \equiv N(\mu^+ \gamma, \pi^- \pi^0) = 991504. \quad (4.4)$$

Divided by the number of generated signal events, the estimated efficiencies by MC are given as:

$$\bar{\epsilon}(e^- \gamma, \pi^+ \pi^0) = (4.83 \pm 0.09)\%, \quad (4.5)$$

$$\bar{\epsilon}(e^+ \gamma, \pi^- \pi^0) = (4.79 \pm 0.09)\%, \quad (4.6)$$

$$\bar{\epsilon}(\mu^- \gamma, \pi^+ \pi^0) = (3.9 \pm 0.1)\%, \quad (4.7)$$

$$\bar{\epsilon}(\mu^+ \gamma, \pi^- \pi^0) = (3.9 \pm 0.1)\%, \quad (4.8)$$

where the errors represent statistical uncertainties. The efficiency is determined based on the definition of radiative decay, *i.e.*, if  $E_\gamma^* > 10$  MeV the event is radiative. In this calculation, the radiative photon is not required to be properly reconstructed. For example, even if the extra bremsstrahlung from  $\tau^- \rightarrow e^- \nu \bar{\nu} \gamma$  is reconstructed as the signal photon, this event is still included in the calculation of efficiency.

As described in Chapter 6 and Appendix A, the MC does not well simulate the experimental efficiency particularly due to an imperfect trigger simulation so that an additional correction factor must be taken into account. With this modification, the efficiency turns out to decrease by 11% and 8% for  $(e\gamma, \pi\pi^0)$  and  $(\mu\gamma, \pi\pi^0)$  events, respectively.

---

\*As long as the Standard Model (SM) process is considered, the neutrino-less decay of the  $\tau$  is forbidden and we can uniquely determine the types of neutrinos based on lepton number conservation. Hereafter, without explicitly writing neutrinos, we often abbreviate the combination of both decays in a simplified form:  $(\mu, \pi\pi^0)$  means  $\tau \rightarrow \mu\nu\bar{\nu}$  and  $\tau \rightarrow \pi\pi^0\nu$ . Although the neutrino may change  $\nu$  or  $\bar{\nu}$  depending on the sign of the  $\tau$ , we do not persist on it because this does not affect any conclusions. Similarly, the charge assignment of particles depends on the contexts.



# Chapter 5

## Method of the measurement of the Michel parameters

In this chapter, we describe methods to extract the Michel parameters  $\bar{\eta}$  and  $\xi\kappa$ . Technical details like mathematical formulae and their derivations are found in the Appendix B.

### 5.1 Notations and conventions

In this chapter and Appendix B, we use following notations and conventions unless otherwise noted. The four vectors are denoted by small letters with italic characters like  $p$  and its energy and three vector components are denoted as  $E$  and  $\mathbf{P}$ . The capital letter  $P$  means magnitude of  $\mathbf{P}$ .  $\Omega$  is used to represent an angular component of three vectors and represents an abbreviation of a set  $\{\cos\theta, \phi\}$ . The general vectors are also denoted as bold letters  $\mathbf{x}$ . For example, a set of observed variables is often abbreviated as  $\mathbf{x}$ : particle-1 ( $P_1, \Omega_1$ ) and particle-2 ( $P_2, \Omega_2$ ) are put together to be represented as  $\mathbf{x} = \{P_1, \Omega_1, P_2, \Omega_2\}$ . Furthermore, we always use an asterisk as superscript like  $E^*$  to show it is evaluated in the  $\tau$  rest frame. While to show a value is evaluated in other frames, we also use a tilde, hat and double asterisk. The meanings of these superscripts change depending on each context and shall be explained on each occasion. In this analysis, we often use a variable which distributes according to a certain probability density function. We represent  $x \in f(x)$  for this situation that the  $x$  is distributed according to  $f(x)$ .

### 5.2 Unbinned maximum likelihood method

The Michel parameters  $\theta = \{\bar{\eta}, \xi\kappa\}$  are obtained by maximizing a likelihood function  $L$ , which is comprised of the product of a probability density function (PDF)  $P(\mathbf{x}|\theta)$  of each event:

$$L(\theta) = \prod_k P(\mathbf{x}^k), \quad (5.1)$$

where  $k$  is the index of event and  $\mathbf{x}$  represents a set of twelve-dimension observables, which is explicitly given by  $\mathbf{x} = \{P_\ell, \Omega_\ell, P_\gamma, \Omega_\gamma, P_\rho, \Omega_\rho, m_{\pi\pi}^2, \tilde{\Omega}_\pi\}$  and explained later in detail. In other words, the  $P(\mathbf{x})d\mathbf{x}$  is regarded as a probability such that the event having corresponding point  $\mathbf{x}$  lies inside a certain cube  $d\mathbf{x}$ . Technically, it is more useful to adopt a negative logarithmic likelihood function

$$\mathcal{L}(\theta) = -\log L = -\sum_k \log P(\mathbf{x}^k) \quad (5.2)$$

so that the exponential small value that appears in the right hand side of the Eq. (5.1) becomes easy to manage.

Thus the procedure is dissolved into the formulation of  $P(\mathbf{x})$ . Accounting for the event selection and the contamination from backgrounds, the total visible (properly normalized) PDF for the observable  $\mathbf{x}$  in each event is given by:

$$P(\mathbf{x}) = (1 - \sum_i \lambda_i) \cdot \frac{S(\mathbf{x})\varepsilon(\mathbf{x})}{\int d\mathbf{x}S(\mathbf{x})\varepsilon(\mathbf{x})} + \sum_i \lambda_i \frac{B_i(\mathbf{x})\varepsilon(\mathbf{x})}{\int d\mathbf{x}B_i(\mathbf{x})\varepsilon(\mathbf{x})}, \quad (5.3)$$

where  $S(\mathbf{x})$  is the signal PDF explained later in Sec. 5.4.1,  $B_i(\mathbf{x})$  is the distribution of the  $i$ -th category of background,  $\lambda_i$  is the fraction of each background and  $\varepsilon(\mathbf{x})$  is the selection efficiency of signal. The index  $i$  runs 1, 2, 3 and 1, 2, ..., 6 for electron and muon modes, respectively, and this indicates each category of background explained in Sec. 4.4 (also shown in Figs. 4.10 and 4.14 with each color). The PDF of the major background modes are described using their theoretical formulae while other minor contributions are treated as one category and described based on the MC simulation. The selection efficiency  $\varepsilon(\mathbf{x})$  is not generally common between the signal and backgrounds, the difference, however, is included in the definition of  $B_i(\mathbf{x})$ . The denominator of each term is a product of the average selection efficiency of each component and its normalization.

Due to the large dimension of the phase space, an evaluation of local efficiency  $\varepsilon(\mathbf{x})$  as a function of  $\mathbf{x}$  is almost impossible. However, this does not cause a substantial problem, since  $\varepsilon(\mathbf{x})$  is a common factor irrelevant from  $\theta$ , which results in an addition of a constant in the negative logarithmic likelihood maximization:  $\mathcal{L}(\theta) \supset -\sum_k \log \varepsilon(\mathbf{x}^k)$ . Therefore, the dependence of  $\varepsilon(\mathbf{x})$  on  $\mathbf{x}$  does not directly affect fitted value of the Michel parameters. The unnecessary of a tabulation of  $\varepsilon(\mathbf{x})$  is one of the most important keys of this analysis.

### 5.3 Average efficiency and normalization

We explain a manipulation of the terms in Eq. (5.3) before the description of PDF. All terms in the equation have forms given by

$$\frac{P_i}{\varepsilon(\mathbf{x})} = \lambda \cdot \frac{F(\mathbf{x})}{\int d\mathbf{x}F(\mathbf{x})\varepsilon(\mathbf{x})}, \quad (5.4)$$

where  $F$  is  $S$  or  $B_i$  in Eq. (5.3). Since the overall probability of each component should be unity,  $F(\mathbf{x})$  should satisfy the unitary condition:  $\int d\mathbf{x}F(\mathbf{x}) = 1$ . However, in some cases,  $F(\mathbf{x})$  which is not necessarily be normalized is easy to extract and we distinguish them by notating  $\tilde{F}(\mathbf{x})$  for the PDF which is not normalized. For  $\tilde{F}(\mathbf{x})$ , we are allowed to ignore constant factors such as many  $(2\pi)$  arising from the Lorentz-invariant phase space (LIPS). Right-hand side of Eq. (5.4) shows that this term does not depend on the normalization factor of  $F(\mathbf{x})$ . Therefore, it can be rewritten as

$$\frac{P_i}{\varepsilon(\mathbf{x})} = \lambda \cdot \frac{\tilde{F}(\mathbf{x})}{\int d\mathbf{x}\tilde{F}(\mathbf{x})\varepsilon(\mathbf{x})}. \quad (5.5)$$

The integration in the denominator is evaluated by selected MC events, which is distributed with respect to the SM predication:

$$\lambda \cdot \frac{\tilde{F}(\mathbf{x})}{\int d\mathbf{x}\tilde{F}(\mathbf{x})\varepsilon(\mathbf{x})} = \lambda \cdot \frac{\tilde{F}(\mathbf{x})}{\int d\mathbf{x}F^{\text{SM}}(\mathbf{x})\frac{\tilde{F}(\mathbf{x})\varepsilon(\mathbf{x})}{F^{\text{SM}}(\mathbf{x})}} \quad (5.6)$$

$$= \lambda \cdot \frac{\tilde{F}(\mathbf{x})}{\frac{\bar{\varepsilon}}{N_{\text{sel}}} \sum_{\mathbf{x}^k \in \varepsilon F^{\text{SM}}} \frac{\tilde{F}(\mathbf{x}^k)}{F^{\text{SM}}(\mathbf{x}^k)}} = \lambda \cdot \frac{\tilde{F}(\mathbf{x})}{\frac{\bar{\varepsilon}\sigma_{\text{SM}}}{N_{\text{sel}}} \sum_{\mathbf{x}^k \in \varepsilon F^{\text{SM}}} \frac{\tilde{F}(\mathbf{x}^k)}{\tilde{F}^{\text{SM}}(\mathbf{x}^k)}}, \quad (5.7)$$

$$\equiv \lambda \cdot \frac{\widetilde{F}(\mathbf{x})}{\bar{\varepsilon} \sigma_{\text{SM}} \left\langle \frac{\widetilde{F}}{\widetilde{F}^{\text{SM}}} \right\rangle} \quad (5.8)$$

where  $\bar{\varepsilon}$  is the average selection efficiency,  $N_{\text{sel}}$  is the number of selected events and  $\sigma^{\text{SM}}$  is magnitude of the normalization factor calculated as

$$\sigma^{\text{SM}} = \int d\mathbf{x} \widetilde{F}^{\text{SM}}(\mathbf{x}). \quad (5.9)$$

The bracket in Eq. (5.8) indicates the average for the selected SM distribution. Hereafter, we refer the factor which normalizes the Standard Model part  $\sigma_{\text{SM}} = \int d\mathbf{x} \widetilde{F}^{\text{SM}}(\mathbf{x})$  to an *absolute* normalization, while the relative factor  $\langle \widetilde{F}/\widetilde{F}^{\text{SM}} \rangle$  in Eq. (5.8) to a *relative* normalization.

## 5.4 Implementation of probability density functions

In this section, we present the description of the PDFs for the signal and backgrounds. For simplicity, we describe the technical details only for the signal description and skip explaining those of the backgrounds in the main text by just writing the concept of the formulation. The detailed information is given in Appendix B.

### 5.4.1 Description of the signal PDF

The differential decay width for the radiative leptonic decay of the  $\tau^-$  with a definite spin direction  $\mathbf{S}_{\tau^-}^*$  is given by

$$\frac{d\Gamma(\tau^- \rightarrow \ell^- \nu \bar{\nu} \gamma)}{dE_\ell^* d\Omega_\ell^* dE_\gamma^* d\Omega_\gamma^*} = (A_0^- + \bar{\eta} A_1^-) + (\mathbf{B}_0^- + \xi \kappa \mathbf{B}_1^-) \cdot \mathbf{S}_{\tau^-}^*, \quad (5.10)$$

where  $A_i^-$  and  $\mathbf{B}_i^-$  ( $i = 0, 1$ ) are known functions of the kinematic variables of the decay products,  $\Omega_a$  stands for a set of  $\{\cos\theta_a, \phi_a\}$  for a particle type  $a = (\ell \text{ or } \gamma)$  and the asterisk means that the variable is defined in the  $\tau$  rest frame. The explicit formula is given in the end of this Sec. 5.4.1. Equation 5.10 shows that  $\xi \kappa$  appears in the *spin-dependent* part of the decay width. This product can be measured by utilizing the well-known spin-spin correlation of the  $\tau$  pair in the  $e^- e^+ \rightarrow \tau^+ \tau^-$  reaction:

$$\frac{d\sigma(e^- e^+ \rightarrow \tau^-(\mathbf{S}_{\tau^-}^*) \tau^+(\mathbf{S}_{\tau^+}^*))}{d\Omega_\tau} = \frac{\alpha^2 \beta_\tau}{64 E_\tau^2} (D_0 + D_{ij} S_i^{-*} S_j^{+*}) \quad (i, j = 1, 2, 3), \quad (5.11)$$

where  $\alpha$  is the fine structure constant,  $\beta_\tau$  and  $E_\tau$  are the velocity and energy of the  $\tau$ , respectively,  $D_0$  is a form factor for the spin-independent part of the reaction and  $D_{ij}$  is a tensor describing the spin-spin correlation [63]:

$$D_0 = 1 + \cos^2 \theta + \frac{1}{\gamma_\tau^2} \sin^2 \theta, \quad (5.12)$$

$$D_{ij} = \begin{pmatrix} (1 + \frac{1}{\gamma_\tau^2}) \sin^2 \theta & 0 & \frac{1}{\gamma_\tau} \sin 2\theta \\ 0 & -\beta_\tau^2 \sin^2 \theta & 0 \\ \frac{1}{\gamma_\tau} \sin 2\theta & 0 & 1 + \cos^2 \theta - \frac{1}{\gamma_\tau^2} \sin^2 \theta \end{pmatrix}; \quad (5.13)$$

here,  $\theta$  is the polar angle of the  $\tau^-$  and  $\gamma_\tau = 1/\sqrt{1-\beta_\tau^2}$ . The plane formed by electron and tau movements are defined as  $xz$ -plane (or equivalently  $\phi = 0$  plane) and this is the reason why  $x$  and  $y$  components in Eq. (5.13) are not symmetrical.

The spin information on the partner  $\tau^+$  is extracted using the two-body decay  $\tau^+ \rightarrow \rho^+ \bar{\nu} \rightarrow \pi^+ \pi^0 \bar{\nu}$  whose differential decay width is given by

$$\frac{d\Gamma(\tau^+ \rightarrow \pi^+ \pi^0 \bar{\nu})}{d\Omega_\rho^* dm_{\pi\pi}^2 d\tilde{\Omega}_\pi} = A^+ + \mathbf{B}^+ \cdot \mathbf{S}_{\tau^+}^*; \quad (5.14)$$

$A^+$  and  $\mathbf{B}^+$  are the form factors for the spin-independent and spin-dependent parts, respectively, while the tilde indicates the variables are defined in the  $\rho$  rest frame and  $m_{\pi\pi}$  is an invariant mass of the two-body system of pions which is defined as  $m_{\pi\pi}^2 = (p_\pi + p_{\pi^0})^2$ . The formulae of the form factors are also given in the end of this section. Thus the total differential cross section of  $e^+ e^- \rightarrow \tau^+ \tau^- \rightarrow (\pi^+ \pi^0 \bar{\nu})(\ell^- \nu \bar{\nu} \gamma)$  process is given by:

$$\frac{d\sigma(\ell^- \gamma, \pi^+ \pi^0)}{dE_\ell^* d\Omega_\ell^* dE_\gamma^* d\Omega_\gamma^* d\Omega_\rho^* dm_{\pi\pi}^2 d\tilde{\Omega}_\pi d\Omega_\tau} \propto \frac{\beta_\tau}{E_\tau^2} \left[ D_0 (A_0^- + A_1^- \cdot \bar{\eta}) A^+ + D_{ij} (\mathbf{B}_0^- + \mathbf{B}_1^- \cdot \xi \kappa)_i \cdot \mathbf{B}_j^+ \right]. \quad (5.15)$$

To extract the visible differential cross section, we transform the differential variables into ones defined in the CMS using a Jacobian  $J (dE_\ell^* d\Omega_\ell^* dE_\gamma^* d\Omega_\gamma^* d\Omega_\rho^* d\Omega_\tau \rightarrow d\Phi dP_\ell d\Omega_\ell dP_\gamma d\Omega_\gamma dP_\rho d\Omega_\rho)$  \*:

$$J = J_1 J_2 J_3, \quad (5.16)$$

$$J_1 = \left| \frac{\partial(E_\ell^*, \Omega_\ell^*)}{\partial(P_\ell, \Omega_\ell)} \right| = \frac{P_\ell^2}{E_\ell P_\ell^*}, \quad (5.17)$$

$$J_2 = \left| \frac{\partial(E_\gamma^*, \Omega_\gamma^*)}{\partial(P_\gamma, \Omega_\gamma)} \right| = \frac{E_\gamma}{E_\gamma^*}, \quad (5.18)$$

$$J_3 = \left| \frac{\partial(\Omega_\rho^*, \Omega_\tau)}{\partial(P_\rho, \Omega_\rho, \Phi)} \right| = \frac{m_\tau P_\rho}{E_\rho P_\rho^* P_\tau}, \quad (5.19)$$

where the parameter  $\Phi$  is the angle along the arc explained in Sec. 2.5. The visible differential cross section is, therefore, obtained by an integration over  $\Phi$ :

$$\frac{d\sigma(\ell^- \gamma, \pi^+ \pi^0)}{dP_\ell d\Omega_\ell dP_\gamma d\Omega_\gamma dP_\rho d\Omega_\rho dm_{\pi\pi}^2 d\tilde{\Omega}_\pi} = \int_{\Phi_1}^{\Phi_2} d\Phi \frac{d\sigma(\ell^- \gamma, \pi^+ \pi^0)}{d\Phi dP_\ell d\Omega_\ell dP_\gamma d\Omega_\gamma dP_\rho d\Omega_\rho dm_{\pi\pi}^2 d\tilde{\Omega}_\pi} \quad (5.20)$$

$$= \int_{\Phi_1}^{\Phi_2} d\Phi \frac{d\sigma(\ell^- \gamma, \pi^+ \pi^0)}{dE_\ell^* d\Omega_\ell^* dE_\gamma^* d\Omega_\gamma^* d\Omega_\rho^* dm_{\pi\pi}^2 d\tilde{\Omega}_\pi d\Omega_\tau} \cdot J \quad (5.21)$$

$$\equiv \tilde{S}(\mathbf{x}), \quad (5.22)$$

where  $\tilde{S}(\mathbf{x})$  is the PDF of the signal and  $\mathbf{x}$  denotes the mentioned set of twelve measured variables:  $\mathbf{x} = \{P_\ell, \Omega_\ell, P_\gamma, \Omega_\gamma, P_\rho, \Omega_\rho, m_{\pi\pi}^2, \tilde{\Omega}_\pi\}$ .

Since the PDF is a linear combination of the Michel parameters  $\tilde{S}(\mathbf{x}) = \mathcal{E}_0(\mathbf{x}) + \mathcal{E}_1(\mathbf{x})\bar{\eta} + \mathcal{E}_2(\mathbf{x})\eta'' + \mathcal{E}_3(\mathbf{x})\xi\kappa$ , accounting for the discussion in Sec. 5.3 (Eqs. (5.6) to (5.8)), we evaluate the normalization as:

$$\lambda_{\text{sig}} \cdot \frac{\tilde{S}(\mathbf{x})}{\int d\mathbf{x} \tilde{S}(\mathbf{x}) \mathcal{E}(\mathbf{x})} = \lambda_{\text{sig}} \cdot \frac{\tilde{S}(\mathbf{x})}{\frac{\bar{\mathcal{E}}_{\text{SM}}}{N_{\text{sel}}} \sum_{\mathbf{x}^k \in \mathcal{E}_{\text{SM}}} \frac{\tilde{S}(\mathbf{x}^k)}{\tilde{S}^{\text{SM}}(\mathbf{x}^k)}} \quad (5.23)$$

$$= \lambda_{\text{sig}} \cdot \frac{\mathcal{E}_0(\mathbf{x}) + \mathcal{E}_1(\mathbf{x})\bar{\eta} + \mathcal{E}_2(\mathbf{x})\eta'' + \mathcal{E}_3(\mathbf{x})\xi\kappa}{\frac{\bar{\mathcal{E}}_{\text{SM}} \sigma_{\text{SM}}}{N_{\text{sel}}} \sum_{\mathbf{x}^k \in \mathcal{E}_{\text{SM}}} \frac{\mathcal{E}_0(\mathbf{x}^k) + \mathcal{E}_1(\mathbf{x}^k)\bar{\eta} + \mathcal{E}_2(\mathbf{x}^k)\eta'' + \mathcal{E}_3(\mathbf{x}^k)\xi\kappa}{\mathcal{E}_0(\mathbf{x}^k) + \mathcal{E}_1(\mathbf{x}^k)\bar{\eta}_{\text{SM}} + \mathcal{E}_2(\mathbf{x}^k)\eta''_{\text{SM}} + \mathcal{E}_3(\mathbf{x}^k)\xi\kappa_{\text{SM}}}} \quad (5.24)$$

\*For the derivation of Jacobians, see Appendix C.

$$= \lambda_{\text{sig}} \cdot \frac{\mathcal{E}_0(\mathbf{x}) + \mathcal{E}_1(\mathbf{x})\bar{\eta} + \mathcal{E}_2(\mathbf{x})\eta'' + \mathcal{E}_3(\mathbf{x})\xi\kappa}{\bar{\varepsilon}_{\text{SM}}\sigma_{\text{SM}} \sum_{\mathbf{x}^k \in \mathcal{E}_{\text{SM}}} \frac{\mathcal{E}_0(\mathbf{x}^k) + \mathcal{E}_1(\mathbf{x}^k)\bar{\eta} + \mathcal{E}_2(\mathbf{x}^k)\eta'' + \mathcal{E}_3(\mathbf{x}^k)\xi\kappa}{\mathcal{E}_0(\mathbf{x}^k)}} \quad (5.25)$$

$$\equiv \lambda_{\text{sig}} \cdot \frac{\mathcal{E}_0(\mathbf{x}) + \mathcal{E}_1(\mathbf{x})\bar{\eta} + \mathcal{E}_2(\mathbf{x})\eta'' + \mathcal{E}_3(\mathbf{x})\xi\kappa}{\bar{\varepsilon}_{\text{SM}}\sigma_{\text{SM}} \left[ 1 + \left\langle \frac{\mathcal{E}_1}{\mathcal{E}_0} \right\rangle \bar{\eta} + \left\langle \frac{\mathcal{E}_2}{\mathcal{E}_0} \right\rangle \eta'' + \left\langle \frac{\mathcal{E}_3}{\mathcal{E}_0} \right\rangle \xi\kappa \right]}, \quad (5.26)$$

where  $\sigma_{\text{SM}}$  and  $\langle \mathcal{E}_i/\mathcal{E}_0 \rangle$  ( $i = 1, 2, 3$ ) are the absolute and relative normalizations, respectively, and  $\bar{\varepsilon}_{\text{SM}}$  is an average selection efficiency for the SM distribution. In this calculation, we use the fact that  $\bar{\eta}_{\text{SM}} = \eta''_{\text{SM}} = \xi\kappa_{\text{SM}} = 0$ .

## Formulae

As mentioned, the differential decay width of the  $\tau^-$  is expressed as sum of spin independent  $A^-$  and dependent parts  $B^-$  as:

$$\frac{d\Gamma(\tau^- \rightarrow \ell^- \nu \bar{\nu} \gamma)}{dE_\ell^* d\Omega_\ell^* dE_\gamma^* d\Omega_\gamma^*} = A^- + \mathbf{B}^- \cdot \mathbf{S}_{\tau^-}^*, \quad (5.27)$$

both of which are functions of normalized kinetic parameters  $x$ ,  $y$  and  $d$  as [28]:

$$r = \frac{m_\ell}{m_\tau} \quad (5.28)$$

$$x = \frac{2E_\ell^*}{m_\tau} \quad (2r < x < 1 + r^2) \quad (5.29)$$

$$y = \frac{2E_\gamma^*}{m_\tau} \quad (0 < y < 1 - r) \quad (5.30)$$

$$d = 1 - \beta_\ell^* \cos \theta_{\ell\gamma} \quad (5.31)$$

$$y < \frac{2(1 + r^2 - x)}{2 - x + \cos \theta_{\ell\gamma} \sqrt{x^2 - 4r^2}} \quad (5.32)$$

$$A^-(x, y, d) = \frac{4\alpha G_F^2 m_\tau^3}{3(4\pi)^6} \sum_{i=0,1\dots 5} F_i r^i \quad (5.33)$$

$$\mathbf{B}^-(x, y, d) = -\frac{4\alpha G_F^2 m_\tau^3}{3(4\pi)^6} \sum_{i=0,1\dots 5} (\beta_i^* G_i \mathbf{n}_i^* + H_i \mathbf{n}_\gamma^*) r^i \quad (5.34)$$

$$\begin{aligned} F_0(x, y, d) = & \frac{1}{y} \left[ \frac{48}{d} (y^2 - y^3 + 2xy - 3xy^2 + 2x^2 - 4x^2y - 2x^3) \right. \\ & + 8(2xy^2 - 6xy + 7xy^3 - 6x^2 + 6x^2y + 14x^2y^2 + 6x^3 + 12x^3y) \\ & + 4d(6x^2y - 7x^2y^2 - 7x^2y^3 - 12x^3y - 9x^3y^2) + 6d^2x^3y^2(2 + y) \left. \right] \\ & + \frac{\rho}{y} \left[ \frac{32}{3d} (-3y^2 + 4y^3 - 6xy + 12xy^2 - 6x^2 + 16x^2y + 8x^3) \right. \\ & + \frac{32}{3} (-xy^2 + 3xy - 6xy^3 + 3x^2 - 5x^2y - 10x^2y^2 - 4x^3 - 8x^2y) \\ & + \frac{8d}{3} (-6x^2y + 9x^2y^2 + 12xy^3 + 16x^3y + 12x^3y^2) - \frac{16}{3} d^2x^3y^2(2 + y) \left. \right] \\ & + \frac{\bar{\eta}}{y} \left[ 16xy^2(2x + y - 1) - 8dx^2y^2(1 + y) \right] \quad (5.35) \end{aligned}$$

$$F_1(x, y, d) = \frac{\eta}{y} \left[ \frac{3}{2d} \{y^2 + 8x(1 - x - y)\} + \frac{3}{2}x \{-y^2 + 4(x + y + xy - 1)\} + 3dx^2y \left(\frac{y}{8} - 1\right) \right] \\ + \frac{\eta''}{y} \left[ -\frac{y^2}{2d} + \frac{xy^2}{2} - \frac{dx^2y^2}{8} \right] \quad (5.36)$$

$$F_2(x, y, d) = \frac{1}{y} \left[ \frac{192}{d^2} \left\{ \frac{y^2}{x} - \frac{y}{x} - 1 + 2y + x \right\} + \frac{16}{d} \{6y - 7y^2 - 6xy + 6x^2\} \right. \\ \left. + 16(xy^2 - 3xy - 3x^2 - 3x^2y) + 12.0dx^2y(2 + y) \right] \\ + \frac{\rho}{y} \left[ \frac{128}{3d^2} \left( \frac{3y}{x} - \frac{4y^2}{x} + 3 - 8y - 4x \right) + \frac{32}{3d} (-6y + 9y^2 - 8x + 10xy - 6x^2) \right. \\ \left. + \frac{32}{3} (-xy^2 + 4x + 3xy + 3x^2 + 3x^2y) - 8dx^2y(2 + y) \right] \\ + \frac{\bar{\eta}}{y} \left[ -\frac{32y^2}{d} - 16xy^2 \right] \quad (5.37)$$

$$F_3(x, y, d) = \frac{\eta}{y} \left[ \frac{384}{d^2} \left( -\frac{1}{x} + \frac{y}{x} + 1 \right) + \frac{192(x - y)}{d} - 96x \right] \quad (5.38)$$

$$F_4(x, y, d) = \frac{1}{y} \left[ -\frac{192}{d^2} \left( \frac{y}{x} + 1 \right) + \frac{96y}{d} \right] \\ + \frac{\rho}{y} \left[ \frac{128}{3d^2} \left( \frac{4}{x} + \frac{3y}{x} + 3 \right) - \frac{64y}{d} \right] \quad (5.39)$$

$$F_5(x, y, d) = 0 \quad (5.40)$$

$$G_0(x, y, d) = \frac{\xi}{y} \left[ \frac{16}{d} (-xy + \frac{2xy^2}{3} - 2x^2 + 3x^2y + 2x^3) \right. \\ \left. + 8(2x^2 - x^2y - \frac{5x^2y^2}{3} - 2x^3 - 3x^3y) + 4dx^3y(2 + y) \right] \\ + \frac{\xi\delta}{y} \left[ \frac{32}{d} (xy - \frac{10xy^2}{9} + 2x^2 - 4x^2y - \frac{8x^3}{3}) \right] \\ + \frac{\xi\kappa}{y} \left[ -\frac{16xy^2}{d} + 8x^2y^2 \right] \quad (5.41)$$

$$G_1(x, y, d) = 0 \quad (5.42)$$

$$G_2(x, y, d) = \frac{\xi}{y} \left[ \frac{64}{d^2} (1 - x - y) + \frac{16}{d} x(y - 2x) + 8x^2(2 + y) \right] \\ + \frac{\xi\delta}{y} \left[ \frac{128}{3d^2} (4x + 4y - 3) + \frac{32}{d} x \left( \frac{10x}{3} - y \right) - \frac{80}{3} x^2(2 + y) \right] \quad (5.43)$$

$$G_3(x, y, d) = 0 \quad (5.44)$$

$$G_4(x, y, d) = \frac{\xi}{y} \left[ \frac{64}{d^2} \right] + \frac{\xi\delta}{y} \left[ -\frac{640}{3d^2} \right]$$

$$G_5(x, y, d) = 0 \quad (5.45)$$

$$H_0(x, y, d) = \frac{\xi}{y} \left[ \frac{16}{d} (-y^2 + y^3 - xy + \frac{7xy^2}{3} + x^2y) + 8 \left( \frac{2xy^2}{3} - \frac{7xy^3}{3} + \right. \right. \\ \left. \left. + x^2y - 3x^2y^2 - x^3y \right) + 8dx^2y^2 \left( -\frac{1}{2} + \frac{7y}{6} + x \right) - d^2x^3y^3 \right] \\ + \frac{\xi\kappa}{y} \left[ \frac{16xy^2}{d} + 8xy^2(3x + 2y - 4) - 8dx^2y^3 \right] \quad (5.46)$$

$$H_1(x, y, d) = 0 \quad (5.47)$$

$$H_2(x, y, d) = \frac{\xi}{y} \left[ \frac{64y}{xd^2} (1 - x - y) + \frac{16y}{d} \left( x + \frac{7y}{3} - 2 \right) + 8xy \left( x - \frac{2y}{3} \right) - 4dx^2y^2 \right] \quad (5.48)$$

$$+ \frac{\xi\delta}{y} \left[ \frac{128y}{3xd^2} (4x + 4y - 3) + \frac{32y}{9d} (18 - 9x - 29y) + \frac{80xy}{9} (2y - 3x) + \frac{40dx^2y^2}{3} \right] \\ + \frac{\xi\kappa}{y} \left[ \frac{16xy^2}{d} + 8xy^2 (3x + 2y - 4) - 8dx^2y^3 \right] \quad (5.49)$$

$$H_3(x, y, d) = 0 \quad (5.50)$$

$$H_4(x, y, d) = \frac{\xi}{y} \left[ \frac{64y}{xd^2} - \frac{32y}{d} \right] + \frac{\xi\delta}{y} \left[ -\frac{640y}{3xd^2} + \frac{320y}{3d} \right] \quad (5.51)$$

$$H_5(x, y, d) = 0 \quad (5.52)$$

In the description of form factor, we use the CLEO model, where the differential decay width is expressed as [64, 65]:

$$\frac{d\Gamma(\tau^+ \rightarrow \pi^+ \pi^0 \bar{\nu})}{d\Omega_\rho^* dm_{\pi\pi}^2 d\widetilde{\Omega}_\pi} = A^+ + \mathbf{B}^+ \cdot \mathbf{S}_{\tau^+}^*. \quad (5.53)$$

The  $A^+$  and  $\mathbf{B}^+$  are given by following formulae:

$$A^+ = \frac{G_F^2 |V_{ud}|^2}{(4\pi)^5} \left[ 2(E_\pi^* - E_{\pi^0}^*) (p_\nu \cdot q) - E_\nu^* q^2 \right] \cdot \text{BPS} \quad (5.54)$$

$$\mathbf{B}^+ = -\frac{G_F^2 |V_{ud}|^2}{(4\pi)^5} \left[ \mathbf{P}_\pi^* \{ (q \cdot q) + 2(p_\nu \cdot q) \} + \mathbf{P}_{\pi^0}^* \{ (q \cdot q) - 2(p_\nu \cdot q) \} \right] \cdot \text{BPS} \quad (5.55)$$

where  $V_{ud}$  is the corresponding element of the Cabibbo-Kobayashi-Maskawa matrix and  $q$  is a four-vector defined by  $q = p_\pi - p_{\pi^0}$ . The factor BPS stands for a square of a relativistic Breit-Wigner function and a Lorentz-invariant phase space and they are calculated from the following formulae:

$$\text{BPS} = |\text{BW}(m_{\pi\pi})|^2 \left( \frac{2P_\nu^*}{m_\tau} \right) \left( \frac{2\widetilde{P}_\pi}{m_\rho} \right), \quad (5.56)$$

$$\text{BW}(m_{\pi\pi}) = \frac{\text{BW}_\rho + \beta \text{BW}'_{\rho'}}{1 + \beta}, \quad (5.57)$$

$$\text{BW}_\rho(m_{\pi\pi}) = \frac{m_\rho^2}{m_\rho^2 - m_{\pi\pi}^2 - im_\rho \Gamma_\rho(m_{\pi\pi}^2)}, \quad (5.58)$$

$$\text{BW}'_{\rho'}(m_{\pi\pi}) = \frac{m_{\rho'}^2}{m_{\rho'}^2 - m_{\pi\pi}^2 - im_{\rho'} \Gamma_{\rho'}(m_{\pi\pi}^2)}, \quad (5.59)$$

$$\Gamma_\rho(m_{\pi\pi}) = \Gamma_{\rho 0} \frac{m_\rho}{\sqrt{m_{\pi\pi}^2}} \left( \frac{\widetilde{P}_\pi(m_{\pi\pi}^2)}{\widetilde{P}_\pi(m_\rho^2)} \right)^3, \quad (5.60)$$

$$\Gamma_{\rho' 0}(m_{\pi\pi}) = \Gamma_{\rho' 0} \frac{m_{\rho'}}{\sqrt{m_{\pi\pi}^2}} \left( \frac{\widetilde{P}_\pi(m_{\pi\pi}^2)}{\widetilde{P}_\pi(m_{\rho'}^2)} \right)^3, \quad (5.61)$$

where  $P_\nu^*$  is the momentum of neutrino in the tau rest frame given by  $P_\nu^* = (m_\tau^2 - m_{\pi\pi}^2)/2m_\tau$  and  $\widetilde{P}_\pi(m^2)$  means momentum of pion in the  $\rho$  rest frame calculated by

$$\widetilde{P}_\pi(m^2) = \frac{\sqrt{[m^2 - (m_\pi + m_{\pi^0})^2][m^2 - (m_\pi - m_{\pi^0})^2]}}{2m}. \quad (5.62)$$

## 5.4.2 Description of the major background PDFs

As mentioned before, the difference of the efficiency between signal and background is included in the definition of the background PDF such that the normalized background PDF becomes

$$\frac{B_i(\mathbf{x})\varepsilon(\mathbf{x})}{\int d\mathbf{x}B_i(\mathbf{x})\varepsilon(\mathbf{x})}, \quad (5.63)$$

where  $\varepsilon(\mathbf{x})$  is the efficiency of the signal distribution. This manipulation can be categorized into three cases. Suppose that an intrinsic PDF of the background mode in question is  $B_{\text{int}}$ .

- **Case A: Particles are identical**

When all particles in the final states are common in both signal and backgrounds, we simply change the intrinsic signal PDF to that of background.

- **Case B: Particle lost**

When the background mode has an extra particle and it is not vetoed by the selection criteria, the background event is selected as signal candidate. In this case, the visible PDF is obtained by a convolution with a probability that the event is not rejected (*inefficiency*):

$$B_{\text{vis}}(\mathbf{x}) = \int d\mathbf{y}B_{\text{int}}(\mathbf{x}, \mathbf{y}) [1 - \varepsilon(\mathbf{y})], \quad (5.64)$$

where  $\mathbf{y}$  indicates variables of the extra particle and  $[1 - \varepsilon(\mathbf{y})]$  corresponds to the inefficiency.

- **Case C: Particle misidentification**

When a particle  $a$  is misidentified as either of signal particles  $b$  ( $a \neq b$ ), the difference of a factor is  $\varepsilon(b \rightarrow a)/\varepsilon(b \rightarrow b)$ . Therefore, the visible PDF simply becomes

$$B_{\text{vis}}(\mathbf{x}) = \frac{\varepsilon(b \rightarrow a)}{\varepsilon(b \rightarrow b)}(\mathbf{y})B_{\text{int}}(\mathbf{x}), \quad (5.65)$$

where  $\mathbf{y}$  indicates a set of variable for the misidentified particle.

### Bremsstrahlung (case A)

The two main backgrounds for  $\tau^+\tau^- \rightarrow (\pi^+\pi^0\bar{\nu})(e^-\nu\bar{\nu}\gamma)$  candidates come from the bremsstrahlung of electron. The probability of the emission of the photon for a given direction of the electron  $f(\theta_\ell)$  is expressed by:

$$f(\theta_\ell) = \frac{\tilde{L}/\sin\theta_\ell}{1 - \frac{E_{\gamma\text{min}}}{E_\ell} \log\left(\frac{E_{\gamma\text{min}}}{E_\ell}\right)}, \quad (5.66)$$

where  $\tilde{L}$  is a material budget in terms of radiation length and  $E_{\gamma\text{min}}$  is the energy threshold of the bremsstrahlung photon. The value  $E_{\gamma\text{min}} = 1$  MeV is chosen to satisfy the condition  $E_{\gamma\text{min}}/E_\ell \ll \sigma_{P_e}/P_e$ . The momentum and angular distribution of the produced electron and photon are given by  $d\Gamma/dP_\ell d\Omega_\ell d\Omega_\gamma$  as reported in Ref. [66]. Convolution of these quantities and the original PDF of the leptonic decays  $\tau^- \rightarrow e^-\nu\bar{\nu}(\gamma)$  produces the visible PDF of these processes.



## Beam background (case A)

Accidental fake ECL clusters from the beam are wrongly reconstructed as a signal photon and become a source of backgrounds. There are multiple sources of the beam backgrounds. The beam particles are scattered by the residual gas atoms and hit on the inner wall of the beam pipe. The secondary particles generated by the out-of-orbit beam make clusters in the ECL. Similarly, the beam is also scattered by an electric field formed by the beam itself: when the electric field is formed by the particles of the same bunch this is called Touschek effect, when it is formed by the other side of bunch it is called beam-beam scattering. Moreover, the synchrotron radiation also becomes the source of the background.

Since the precise simulation of these beam background is difficult, we record the data of energy deposit in ECL clusters in the real experiment with a random trigger. Then, the beam background is overlaid in the event of MC simulation.

In order to describe the PDF of the beam background, we basically follow the Case A procedure. However, there is a fundamental difficulty here, *i.e.*, the extraction of the intrinsic PDF of the beam background is not possible. For simplicity, we divide the overall phase space into two parts:  $\mathbf{x} = \{P_\ell, \Omega_\ell, P_\gamma, \Omega_\gamma, P_\rho, \Omega_\rho, m_{\pi\pi}^2, \tilde{\Omega}_\pi\} \rightarrow \{\mathbf{y}, \mathbf{z}\}$  with  $\mathbf{y} = \{P_\ell, \Omega_\ell, P_\rho, \Omega_\rho, m_{\pi\pi}^2, \tilde{\Omega}_\pi\}$  and  $\mathbf{z} = \{P_\gamma, \Omega_\gamma\}$ . Here,  $\mathbf{y}$  and  $\mathbf{z}$  are variables for the ordinary leptonic decay  $\tau^- \rightarrow \mu^- \nu \bar{\nu}$  and the beam background, respectively. With this notation, the selected distribution of  $\mathbf{z}$ , which is in fact accessible with MC simulation, can be expressed as:

$$P_{\text{sel}}(\mathbf{z}) = \frac{\int d\mathbf{y} \varepsilon(\mathbf{y})\varepsilon(\mathbf{z}|\mathbf{y})B_{\text{bm}}(\mathbf{z})B_{\text{ord}}(\mathbf{y})}{\int d\mathbf{y}d\mathbf{z} \varepsilon(\mathbf{y})\varepsilon(\mathbf{z}|\mathbf{y})B_{\text{bm}}(\mathbf{z})B_{\text{ord}}(\mathbf{y})} = \frac{B_{\text{bm}}(\mathbf{z}) \int d\mathbf{y} \varepsilon(\mathbf{y})\varepsilon(\mathbf{z}|\mathbf{y})B_{\text{ord}}(\mathbf{y})}{\int d\mathbf{y}d\mathbf{x} \varepsilon(\mathbf{x})B_{\text{bm}}(\mathbf{z})B_{\text{ord}}(\mathbf{y})}, \quad (5.67)$$

where  $B_{\text{bm}}(\mathbf{y})$  and  $B_{\text{ord}}(\mathbf{z})$  are intrinsic PDF of the ordinary leptonic decay and beam background, respectively. Removing  $B_{\text{bm}}(\mathbf{z})$  from the normalized PDF term, we get

$$\frac{B(\mathbf{x})\varepsilon(\mathbf{x})}{\int d\mathbf{x}B(\mathbf{x})\varepsilon(\mathbf{x})} = \frac{B_{\text{ord}}(\mathbf{y})B_{\text{bm}}(\mathbf{z})\varepsilon(\mathbf{x})}{\int d\mathbf{x}\varepsilon(\mathbf{x})B_{\text{ord}}(\mathbf{y})B_{\text{bm}}(\mathbf{z})} = \frac{P_{\text{sel}}(\mathbf{z})B_{\text{ord}}(\mathbf{y})}{\int d\mathbf{y} \varepsilon(\mathbf{y})\varepsilon(\mathbf{z}|\mathbf{y})B_{\text{ord}}(\mathbf{y})} \equiv \frac{P_{\text{sel}}(\mathbf{z})B_{\text{ord}}(\mathbf{y})}{\tilde{\varepsilon}(\mathbf{z})}. \quad (5.68)$$

Here,  $\tilde{\varepsilon}(\mathbf{z}) = \int d\mathbf{y} \varepsilon(\mathbf{y})\varepsilon(\mathbf{z}|\mathbf{y})B_{\text{ord}}(\mathbf{y})$  represents an effective efficiency of  $\mathbf{z}$  for a given  $\mathbf{y} \in B_{\text{ord}}(\mathbf{y})$  and can be extracted from the signal MC distribution.

## High polar angle ISR photons (case A)

The ISR process  $e^+e^- \rightarrow \tau^+\tau^-\gamma$  combines with the ordinary leptonic decay  $\tau^- \rightarrow \mu^- \nu \bar{\nu}$  to become a candidate of the signal. In our analysis, we distinguish the ISR process in two categories depending on the angle: collinear and high polar angle ISRs. In the former case, photon jets in the collinear region ( $\theta_{\gamma e} \ll m_e/E_{\text{beam}}$ ) is treated by means of the structure function [71]. These photons do not enter the acceptance of the detector, hence it results in the decrease of the energy of the  $\tau$  pairs and boost of the CMS. This is described in Sec.5.4.4. The latter photon is emitted inside the acceptance of detector and can be accidentally reconstructed as signal photon. The description of the PDF is straightforward because we only need to modify the cross section of the production  $e^+e^- \rightarrow \tau^+\tau^-$  into radiative one in Eq. (5.11) (of course, the differential decay width of the radiative decay should be changed to non-radiative one) as [67]:<sup>†</sup>

$$\frac{d\sigma(e^-e^+ \rightarrow \tau^-\tau^+)}{d\Omega_\tau} \rightarrow \frac{d\sigma(e^-e^+ \rightarrow \tau^-\tau^+\gamma)}{dP_\gamma d\Omega_\gamma d\Omega_\tau}. \quad (5.69)$$

<sup>†</sup>So far for the radiative cross section, the spin-spin correlation of the  $\tau^+\tau^-$  pair is taken into account only in this paper while spin-independent formulae are given in Refs. [68, 69]

### Three- $\pi$ background (case B)

If either of  $\pi^0$  from the three- $\pi$  decay  $\tau^+ \rightarrow \pi^+ \pi^0 \pi^0 \bar{\nu}$  is lost and the rest parts are reconstructed as  $\tau^+ \rightarrow \pi^+ \pi^0 \bar{\nu}$  decay, the process becomes the candidate of the signal. Since the intrinsic PDF of the three- $\pi$  events is given by

$$B_{3\pi}(\mathbf{x}, \mathbf{y}) = \frac{d\sigma(\ell\gamma, \pi\pi^0\pi^0)/\sigma}{dP_{\pi^0}d\Omega_{\pi^0}dP_{\ell}d\Omega_{\ell}dP_{\gamma}d\Omega_{\gamma}dm_{\pi\pi}^2d\widetilde{\Omega}_{\pi}} = \frac{d\sigma(\ell\gamma, \pi\pi^0\pi^0)/\sigma}{d\mathbf{x}d\mathbf{y}} \quad (5.70)$$

$$\text{with } \mathbf{x} = \{P_{\ell}, \Omega_{\ell}, P_{\gamma}, \Omega_{\gamma}, P_{\rho}, \Omega_{\rho}, m_{\pi\pi}^2, \widetilde{\Omega}_{\pi}\} \text{ and } \mathbf{y} = \{P_{\pi^0}, \Omega_{\pi^0}\}, \quad (5.71)$$

the visible PDF is calculated with the inefficiency of  $\pi^0$  as:

$$B_{\text{vis}}(\mathbf{x}) = \int d\mathbf{y} B_{3\pi}(\mathbf{x}, \mathbf{y}) 2 [1 - \varepsilon(\mathbf{y})]. \quad (5.72)$$

The factor of two comes from the number of counting for the  $\pi^0$ .

### $\rho$ - $\rho$ background (case B and case C)

The  $\tau^- \rightarrow \pi^- \pi^0 (\rightarrow \gamma\gamma) \nu$  decay is wrongly selected by the misidentification of  $\pi^- \rightarrow \mu^-$  and a failure of the rejection of a photon from  $\pi^0$  decay. The visible PDF of  $\tau_1^- \tau_2^+ \rightarrow (\pi_1^- \pi_1^0 (\rightarrow \gamma_1 \gamma_2) \nu) (\pi_2^+ \pi_2^0 \bar{\nu})$  process is given by

$$B_{\text{vis}}(\mathbf{x}) = \frac{\varepsilon_{\pi \rightarrow \mu}}{\varepsilon_{\mu \rightarrow \mu}} \int d\mathbf{y} B_{\rho-\rho}(\mathbf{x}, \mathbf{y}) 2 [1 - \varepsilon(\mathbf{y})], \quad (5.73)$$

$$B_{\rho-\rho}(\mathbf{x}, \mathbf{y}) = \frac{d\sigma/\sigma}{dP_{\pi_1}d\Omega_{\pi_1}dP_{\gamma_1}d\Omega_{\gamma_1}d\Omega_{\gamma_2}dP_{\rho_2}d\Omega_{\rho_2}dm_{\pi_2\pi_2}^2d\widetilde{\Omega}_{\pi_2}}, \quad (5.74)$$

$$\text{with } \mathbf{x} = \{P_{\pi_1}, \Omega_{\pi_1}, P_{\gamma_1}, \Omega_{\gamma_1}, P_{\rho_2}, \Omega_{\rho_2}, m_{\pi_2\pi_2}^2, \widetilde{\Omega}_{\pi_2}\} \text{ and } \mathbf{y} = \{\Omega_{\gamma_2}\}. \quad (5.75)$$

### 3 $\pi$ - $\rho$ background (case B and case C)

The  $\tau^- \rightarrow \pi^- \pi^0 \pi^0 (\rightarrow \gamma\gamma) \nu$  decay is similarly selected as the  $\rho$ - $\rho$  background: in this case two  $\pi^0$  are not rejected by the selection criteria. The visible PDF of  $\tau_1^- \tau_2^+ \rightarrow (\pi_1^- \pi_1^0 \pi_2^0 (\rightarrow \gamma_1 \gamma_2) \nu) (\pi_3^+ \pi_3^0 \bar{\nu})$  process is

$$B_{\text{vis}}(\mathbf{x}) = \frac{\varepsilon_{\pi \rightarrow \mu}}{\varepsilon_{\mu \rightarrow \mu}} \int d\mathbf{y} B_{3\pi-\rho}(\mathbf{x}, \mathbf{y}) 4 [1 - \varepsilon(\mathbf{y})], \quad (5.76)$$

$$B_{3\pi-\rho}(\mathbf{x}, \mathbf{y}) = \frac{d\sigma/\sigma}{dP_{\pi_1}d\Omega_{\pi_1}dP_{\gamma_1}d\Omega_{\gamma_1}d\Omega_{\gamma_2}dP_{\pi_2}d\Omega_{\pi_2}dP_{\rho_3}d\Omega_{\rho_3}dm_{\pi_3\pi_3}^2d\widetilde{\Omega}_{\pi_3}}, \quad (5.77)$$

$$\text{with } \mathbf{x} = \{P_{\pi_1}, \Omega_{\pi_1}, P_{\gamma_1}, \Omega_{\gamma_1}, P_{\rho_3}, \Omega_{\rho_3}, m_{\pi_3\pi_3}^2, \widetilde{\Omega}_{\pi_3}\} \text{ and } \mathbf{y} = \{P_{\pi_2^0}, \Omega_{\pi_2^0}\}. \quad (5.78)$$

## 5.4.3 Description of other background modes

The rest minor background modes are described effectively in the total PDF rather than the analytical description as presented above, because the number of channels in the category of *other background* are too large to describe them separately. Suppose that the selected events are only the combination of signal and the other backgrounds. The total PDF is given by

$$P(\mathbf{x}) = (1 - \lambda) \frac{\varepsilon(\mathbf{x})S(\mathbf{x})}{\int d\mathbf{x} \varepsilon(\mathbf{x})S(\mathbf{x})} + \lambda \frac{\varepsilon(\mathbf{x})B(\mathbf{x})}{\int d\mathbf{x} \varepsilon(\mathbf{x})B(\mathbf{x})}, \quad (5.79)$$

where  $\lambda$  is a total fraction of other background modes,  $S(\mathbf{x})$  and  $B(\mathbf{x})$  are PDFs of signal and backgrounds, and  $\varepsilon(\mathbf{x})$  is an efficiency of signal. Same as the major background modes, the difference of efficiency between signal and each background mode is included in the definition of  $B(\mathbf{x})$ . Here, we should regard the  $B(\mathbf{x})$  as a kind of intrinsic distribution for a fixed selection criteria. The background term is modified as

$$\frac{\varepsilon(\mathbf{x})B(\mathbf{x})}{\int d\mathbf{x} \varepsilon(\mathbf{x})B(\mathbf{x})} = \frac{\varepsilon(\mathbf{x})S_{\text{SM}}(\mathbf{x}) \int d\mathbf{x} \varepsilon(\mathbf{x})S_{\text{SM}}(\mathbf{x})}{\varepsilon(\mathbf{x})S_{\text{SM}}(\mathbf{x}) \int d\mathbf{x} \varepsilon(\mathbf{x})S_{\text{SM}}(\mathbf{x})} \frac{\varepsilon(\mathbf{x})B(\mathbf{x})}{\int d\mathbf{x} \varepsilon(\mathbf{x})B(\mathbf{x})} \quad (5.80)$$

$$= \frac{\varepsilon(\mathbf{x})S_{\text{SM}}(\mathbf{x})}{\bar{\varepsilon}_{\text{sig}}} \frac{B_{\text{sel}}(\mathbf{x})}{S_{\text{sel}}(\mathbf{x})}, \quad (5.81)$$

where  $\bar{\varepsilon}_{\text{sig}} = \int d\mathbf{x} \varepsilon(\mathbf{x})S_{\text{SM}}(\mathbf{x})$  is an average efficiency of signal and  $S_{\text{sel}}(\mathbf{x})$  and  $B_{\text{sel}}(\mathbf{x})$  are normalized PDFs of the selected signal and other background modes, which are given by

$$S_{\text{sel}}(\mathbf{x}) = \frac{\varepsilon(\mathbf{x})S_{\text{SM}}(\mathbf{x})}{\int d\mathbf{x} \varepsilon(\mathbf{x})S_{\text{SM}}(\mathbf{x})}, \quad (5.82)$$

$$B_{\text{sel}}(\mathbf{x}) = \frac{\varepsilon(\mathbf{x})B_{\text{SM}}(\mathbf{x})}{\int d\mathbf{x} \varepsilon(\mathbf{x})B_{\text{SM}}(\mathbf{x})}. \quad (5.83)$$

Thus finally we get

$$\frac{P(\mathbf{x})}{\varepsilon(\mathbf{x})} = (1 - \lambda) \frac{S(\mathbf{x})}{\bar{\varepsilon}_{\text{sig}}} + \lambda \frac{S_{\text{SM}}(\mathbf{x})}{\bar{\varepsilon}_{\text{sig}}} T(\mathbf{x}) \quad (5.84)$$

$$T(\mathbf{x}) \equiv \frac{B_{\text{sel}}(\mathbf{x})}{S_{\text{sel}}(\mathbf{x})}. \quad (5.85)$$

The extraction of  $T(\mathbf{x})$  is performed by Schmidt method [70]. As shown in Fig 5.1, the probability density at a certain point  $\mathbf{x}$  is obtained from a set of selected Monte Carlo sample by counting number of events around  $\mathbf{x}$ . In reality, however, it is not effective to count the number of event in the entire 12D phase space because the number of statistics is limited. Therefore, we divide the phase space into smaller subsets:  $T(\mathbf{x}) = T(\mathbf{x}_1) \cdot T(\mathbf{x}_2)$ , where  $\mathbf{x}_1$  and  $\mathbf{x}_2$  are variables of the subsets. Furthermore, it is also possible to freely change variable into another independent set  $\mathbf{y}$  according to  $\mathbf{x} = \mathbf{y} \cdot \frac{\partial(\mathbf{x})}{\partial(\mathbf{y})}$  because when we formulate  $T(\mathbf{x})$ , the Jacobians appearing in both numerator and denominator cancel each other. Therefore, it is required to factorize  $T(\mathbf{x})$  to the extent that the number of entry inside local region  $V$  is sufficient and exchange variables such that the nature of spectra is properly reflected on. In this analysis, we use the method below:

$$T(\tau \rightarrow e\nu\bar{\nu}\gamma)(\mathbf{x}) = T(P_\ell, \sqrt{1/P_\gamma}, \cos\theta_\ell) \cdot T(P_\rho, m_\rho^2) \cdot T(\phi_\rho + \phi_\ell, \phi_\gamma - \phi_\ell), \\ \cdot T(P_\ell, P_\gamma, \cos\tilde{\theta}_\pi) / T(P_\ell, P_\gamma) \cdot T\left(\frac{\epsilon_{\mu\nu\sigma\rho} P_\ell^\mu P_\gamma^\nu P_\pi^\sigma P_{\pi^0}^\rho}{E_\ell E_\gamma E_\pi E_{\pi^0}}\right) \quad (5.86)$$

$$T(\tau \rightarrow \mu\nu\bar{\nu}\gamma)(\mathbf{x}) = T(P_\ell, \sqrt{1/P_\gamma}) \cdot T(P_\rho, m_\rho^2) \cdot T(\phi_\rho + \phi_\ell, \phi_\gamma - \phi_\ell, \phi_\rho) \cdot T(\psi_{\ell\gamma}, \cos\theta_l). \quad (5.87)$$

The distribution of these variables are shown in Figs. 5.2 and 5.3 for  $\tau^- \tau^+ \rightarrow (e^- \nu \bar{\nu} \gamma)(\rho^+ \bar{\nu})$  and  $\tau^- \tau^+ \rightarrow (\mu^- \nu \bar{\nu} \gamma)(\rho^+ \bar{\nu})$  candidates, respectively.

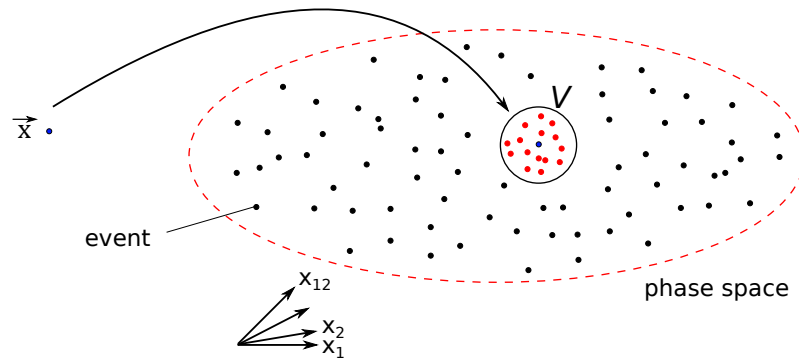


Figure 5.1: The probability density of selected sample at  $\mathbf{x}$  can be obtained by counting number of events around  $\mathbf{x}$ . The differential cross section  $\text{PDF}_{\text{sel}}(\mathbf{x}) = \frac{N_{\text{hit}}}{N_{\text{total}} V}$ .

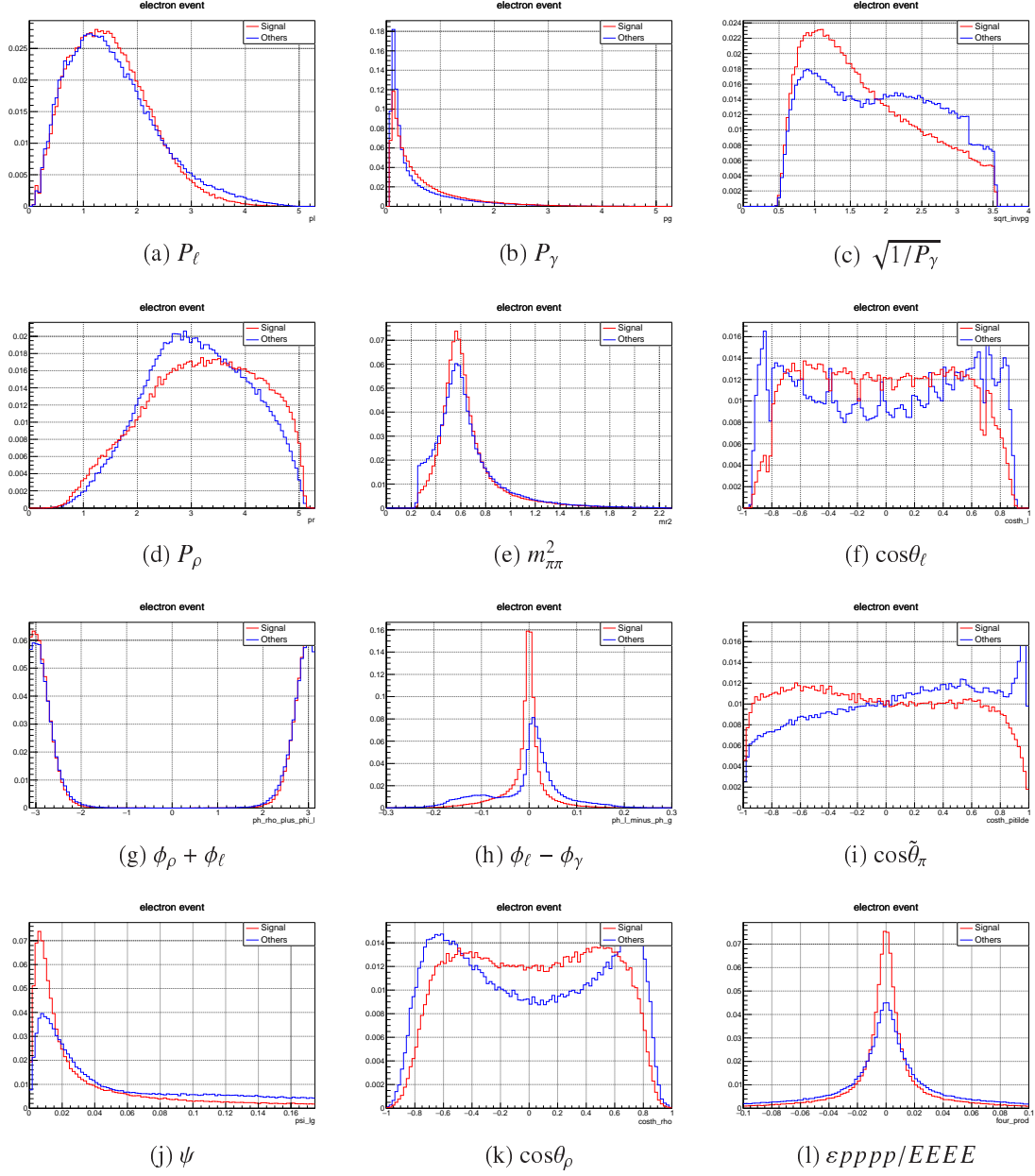


Figure 5.2: Distribution of various variables for  $\tau^-\tau^+ \rightarrow (e^-\nu\bar{\nu}\gamma)(\rho^+\bar{\nu})$  decay candidates. The red and blue lines are signal and *others* distributions, respectively. Both statistics are normalized so that both entries are same.

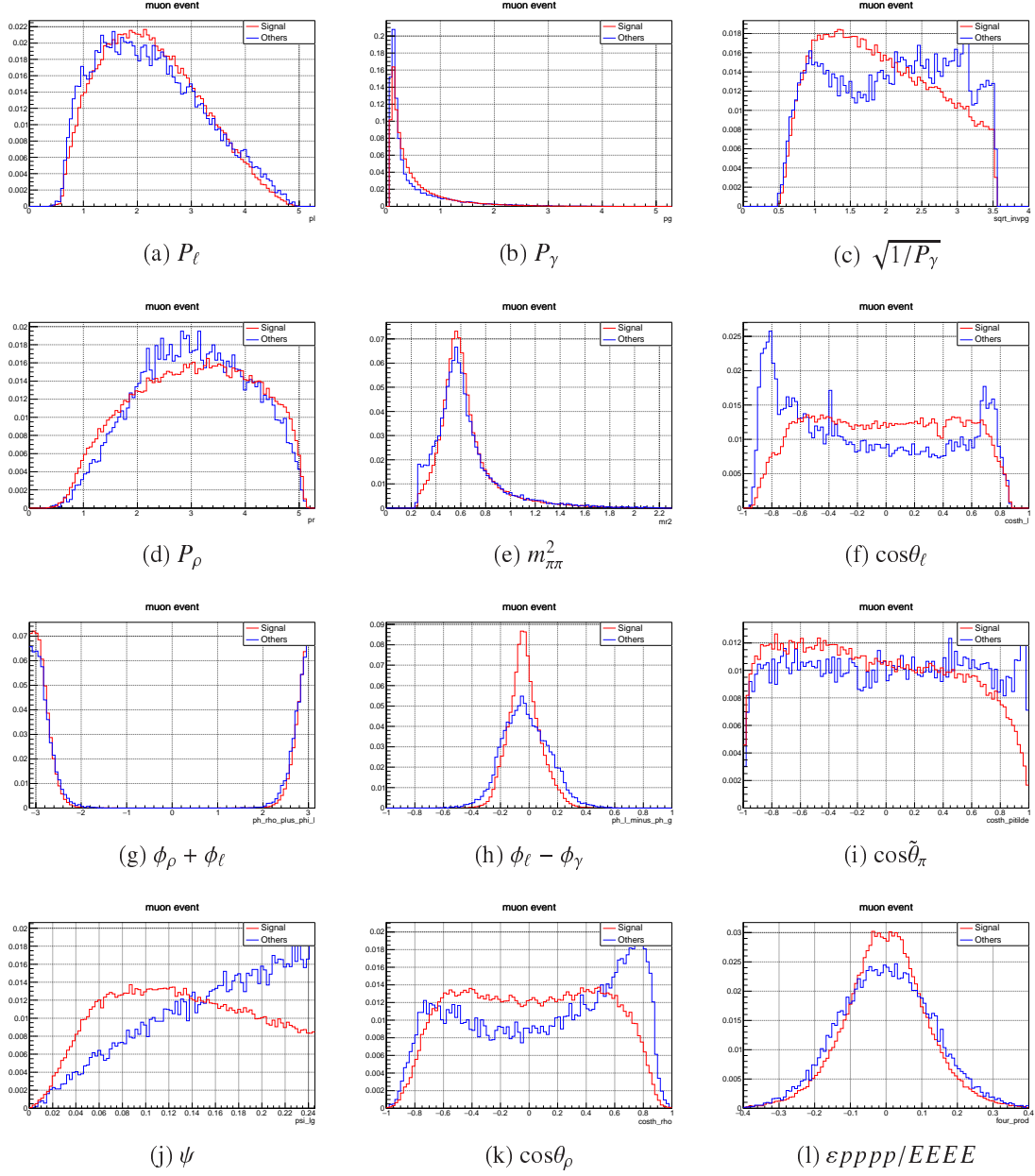


Figure 5.3: Distribution of various variables for  $\tau^-\tau^+ \rightarrow (\mu^-\nu\bar{\nu}\gamma)(\rho^+\bar{\nu})$  decay. The red and blue lines are signal and *others* distributions, respectively. Both statistics are normalized so that both entries are same.

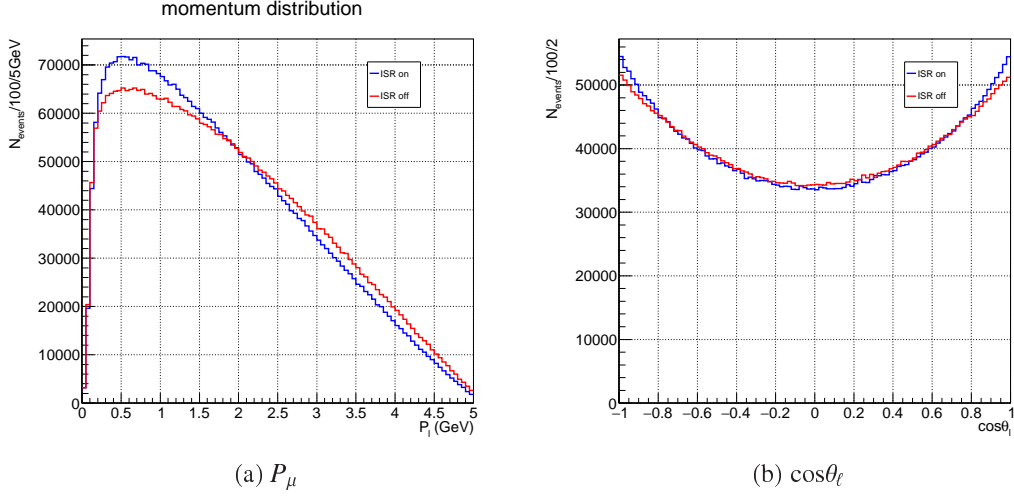


Figure 5.4: Distribution of the muon momentum for generated events in the CMS frame: (a) momentum  $P_\mu$  and (b) direction  $\cos\theta_\mu$ . Blue and red graphs represent distribution when the ISR effect is turned on and off, respectively.

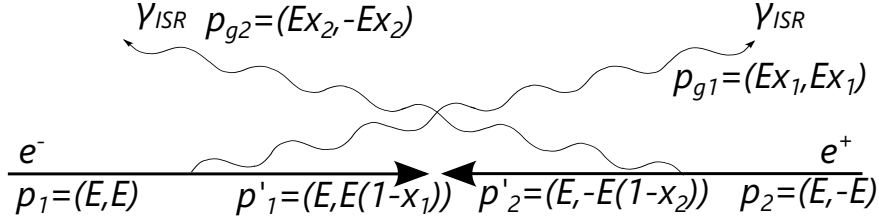


Figure 5.5: ISR emission can be regarded as Drell-Yan process.  $E$  represent energy of  $e^-$  and  $e^+$  in the  $ee$ -CMS frame.

#### 5.4.4 Implementation of the effect of collinear ISR

As mentioned before, the ISR is categorized into two groups depending on the direction of the emission of the photon vs that of beam. Since the dominant emission of the ISR is inside the region of  $\theta_{e\gamma} \sim m_e/E_{\text{beam}} = 10^{-4}$ , we treat this effect as a *collinear* ISR. Figure 5.4 shows the generated distribution of the momentum of the muon in the  $\tau \rightarrow \mu\nu\bar{\nu}$  decay. Because of the energy deposit of the beam by ISR emission, the momentum distribution shifts in smaller side. Furthermore, CMS of beam becomes not to coincide with  $\tau\tau$ -CMS frame. We take into account the energy loss by means of a structure function  $D(x)$  [71]. As Fig. 5.5 shows, ISR photons are assumed to be collinear with beam axis<sup>‡</sup> and the fraction of the energy deposit from  $e^-$  and  $e^+$  are  $x_1$  and  $x_2$ , respectively. Similarly to the well known Drell-Yan process, the probability of the ISR emission is described as a double convolution with function  $D(x)$ :

$$\begin{aligned}
 D(x) &= D^\gamma(x) + D^{ee}(x) \\
 D^\gamma(x) &= \frac{1}{2}\beta x^{\frac{\beta}{2}-1} \left[ 1 + \frac{3}{8}\beta - \frac{\beta^2}{48} \left( \frac{1}{3}L + \pi^2 - \frac{47}{8} \right) \right] - \frac{1}{4}\beta(2-x) \\
 &\quad + \frac{1}{32}\beta^2 \left[ 4(2-x) \log \frac{1}{x} - \frac{1+3(1-x)^2}{x} \log(1-x) - 6+x \right]
 \end{aligned}$$

<sup>‡</sup>It is known that the effect of large angle ISR is suppressed by an additional factor  $\alpha$  [68].

$$\begin{aligned}
D^{ee}(x) &= \left(\frac{\alpha}{\pi}\right)^2 \Theta\left(x - \frac{2m_e}{E}\right) \\
&\quad \left[ \frac{1}{12} \frac{(x - 2m_e/E)^{\beta/2}}{x} \left(\mathcal{L} - \frac{5}{3}\right)^2 \left(1 + (1-x)^2 + \frac{1}{6}\beta\left(\mathcal{L} - \frac{5}{3}\right)\right) \right. \\
&\quad \left. + \frac{L^2}{4} \left(\frac{2}{3} \frac{1 - (1-x)^3}{1-x}\right) + \frac{x}{2} + (2-x)\log(1-x) \right]
\end{aligned}$$

where  $\Theta$  is the step function,  $\beta = \frac{2\alpha}{\pi}(L-1)$ ,  $L = \log\left(\frac{s}{m_e^2}\right)$  and  $\mathcal{L} = \log\left(\frac{sx^2}{m_e^2}\right)$ . Thus the original PDF  $P_{\text{org}}(s)$  for an invariant mass squared  $s$  is modified to

$$P_{\text{vis.}}(s) = \int_0^1 dx_1 \int_0^1 dx_2 D(x_1)D(x_2)P_{\text{org}}(s(1-x_1)(1-x_2)) \cdot J, \quad (5.88)$$

where  $J$  is a Jacobian which converts the differential variables from  $\tau\tau$ -CMS frame to the CMS of beam and given as products of three Jacobians:  $J_a = P_a^2 E'_a / P_a'^2 E_a$  for  $a = l, \gamma, \rho$ . The superscript prime indicates that it is defined in the  $\tau\tau$ -CMS frame.

### 5.4.5 Implementation of the effect of detector resolution

The observed momenta and energies of particles are distorted by measurement with detectors. This effect is taken into account based on the information of the error of the detector. The response of detector is described by a resolution function  $\mathcal{R}(\mathbf{x}, \mathbf{x}')$ , where  $\mathbf{x}$  and  $\mathbf{x}'$  are, respectively variables for observed and true values. In the presence of the distortion, the visible PDF is written as:

$$P^{\text{vis.}}(\mathbf{x}) = \int d\mathbf{x}' P(\mathbf{x}') \mathcal{R}(\mathbf{x}, \mathbf{x}'). \quad (5.89)$$

In this analysis, we assume that the resolution function is a product of each particle:  $\mathcal{R}(\mathbf{x}, \mathbf{x}') = \mathcal{R}(P_\ell, \Omega_\ell) \cdot \mathcal{R}(P_\gamma, \Omega_\gamma) \cdot \mathcal{R}(P_\pi, \Omega_\pi) \cdot \mathcal{R}(P_{\gamma'}, \Omega_{\gamma'}) \cdot \mathcal{R}(P_{\rho'}, \Omega_{\rho'})$ , where  $\gamma'$  means it is generated from the signal  $\pi^0$ . The resolution function of the charged track— $\ell$  and  $\pi$ —is given by

$$\mathcal{R}(\mathbf{P}, \mathbf{P}') = \frac{1}{(2\pi)^{3/2} \sqrt{\det E}} \exp\left\{-\frac{\Delta\mathbf{P}^T E^{-1} \Delta\mathbf{P}}{2}\right\}, \quad \Delta\mathbf{P} = \mathbf{P} - \mathbf{P}', \quad (5.90)$$

where  $E$  is an inverse of the variance-covariance matrix defined in the Cartesian coordinate system and  $\mathbf{P}$  is a momentum of the reconstructed particle. The  $E$  has a form  $\text{diag}(1/\sigma_1^2, \dots, 1/\sigma_n^2)$  if all variables are not correlated. Since the trajectory of charged track is fitted by the Helix parameters, the error matrix is also given in this format, hence we convert it with Jacobian as  $\Delta\mathbf{H}^T E^{-1} \Delta\mathbf{H} \rightarrow \Delta\mathbf{P}^T J^{-1} E^{-1} J \Delta\mathbf{P} \equiv \Delta\mathbf{P}^T E_{\text{Cartesian}}^{-1} \Delta\mathbf{P}$ , where  $\Delta\mathbf{H}$  is a vector formed by the helix parameters and  $J$  is the Jacobian defined as  $J = \partial\mathbf{H}/\partial\mathbf{P}$ . The MC distribution of the error matrix is calibrated using cosmic ray and scaled so that the distribution becomes the Gaussian distribution.

For the reconstruction of photon, it is known that the difference of energy  $\Delta E = E - E'$  is not symmetric Gaussian as the case of the charged track. The asymmetric response is described by the logarithmic Gaussian, which is obtained by exchange of variable  $x = \log(\epsilon - \Delta E)$  where  $x$  follows Gaussian distribution.  $\epsilon$  determines the maximum available energy and  $\Delta E$  characterizes the degree of asymmetry. The angular response of the detector is given as errors of  $\theta_\gamma$  and  $\phi_\gamma$  with simple diagonal form:  $(\theta, \phi)^T E^{-1} (\theta, \phi) = (\theta, \phi)^T \text{diag}(1/\sigma_\theta^2, 1/\sigma_\phi^2) (\theta, \phi)$ . Similarly to the case of charged particle, it is converted to Cartesian distribution. These parameters are calibrated using  $e^+e^- \rightarrow \gamma\gamma$  process and confirmed by  $\pi^0 \rightarrow \gamma\gamma$  and  $\eta^0 \rightarrow \gamma\gamma$  decays measuring their invariant masses [72].



## 5.5 Fitting

As described above, the visible PDF for an observed event  $\mathbf{x}$  is formulated:

$$P(\mathbf{x}) = (1 - \sum_i \lambda_i) \cdot \frac{S(\mathbf{x})\varepsilon(\mathbf{x})}{\int d\mathbf{x}S(\mathbf{x})\varepsilon(\mathbf{x})} + \sum_i \lambda_i \frac{B_i(\mathbf{x})\varepsilon(\mathbf{x})}{\int d\mathbf{x}B_i(\mathbf{x})\varepsilon(\mathbf{x})},$$

By means of this PDF, for a given set of selected events, we construct the (negative) logarithmic likelihood function as

$$\mathcal{L}(\bar{\eta}, \xi\kappa) = -\log\left(\prod_k P(\mathbf{x}^k)\right) = -\sum_k \log(P(\mathbf{x}^k)). \quad (5.91)$$

As Eq. (5.91) shows, the free parameters are only Michel parameters  $\bar{\eta}, \xi\kappa$  and  $\lambda_i$  are fixed to values evaluated by MC simulation. The associated uncertainties of  $\lambda_i$  are taken into account as systematic uncertainties.

## 5.6 Validation of fitter

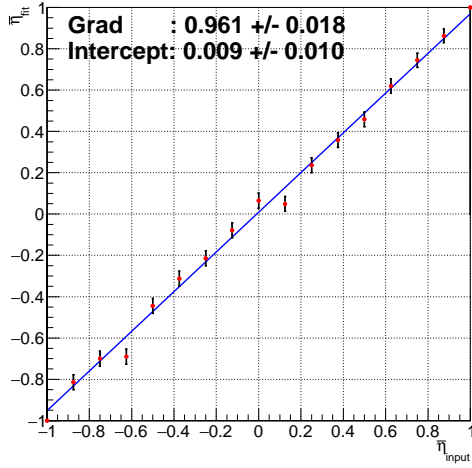
### 5.6.1 Linearity of fitter

In order to validate our fitter, we check the linearity response to the Michel parameters which are not the SM values. Figure 5.6 shows the linearity of the fitter for each Michel parameter value. Each point is statistically independent and obtained by using 9.2 M generated events for  $\tau^- \rightarrow e^- \nu \bar{\nu} \gamma$  and 2.3M events for  $\tau^- \rightarrow \mu^- \nu \bar{\nu} \gamma$ . According to the figures, we can observe a good linearity of the fitter.

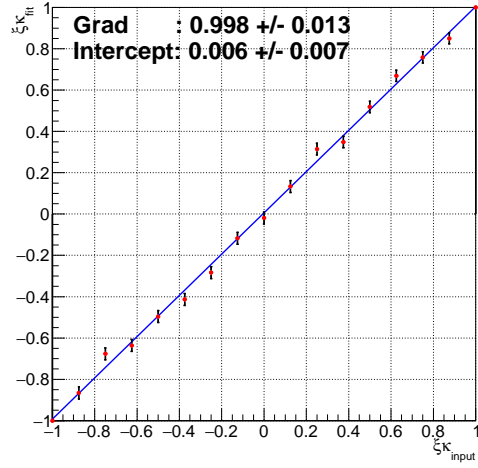
Furthermore, we also check same confirmation for the selected sample, where selection criteria are applied. Figures 5.7c and 5.7d show the linearities for selected statistics, where 4.7 M  $\tau^- \rightarrow \mu^- \nu \bar{\nu} \gamma$  decay events are fitted. Still the linear response can be properly seen. We also attempt to fit 4.4 M  $\tau^- \rightarrow e^- \nu \bar{\nu} \gamma$  selected events and only result of  $\xi\kappa$  shows robust linearity as seen in Fig 5.7b. The linearity of  $\bar{\eta}$  is degraded due to its low sensitivity. Intuitively, this result seems strange based on the sensitivities obtained fitting Michel parameters to the generated events, because statistical uncertainty should be proportional to the inverse of square root of event number. However, as explained in the next section, it is found that the low sensitivity of  $\bar{\eta}$  comes from selection with  $\cos\theta_{\ell\gamma}$ , which is necessary to choose events.

### 5.6.2 Dependence of sensitivity on selection criteria

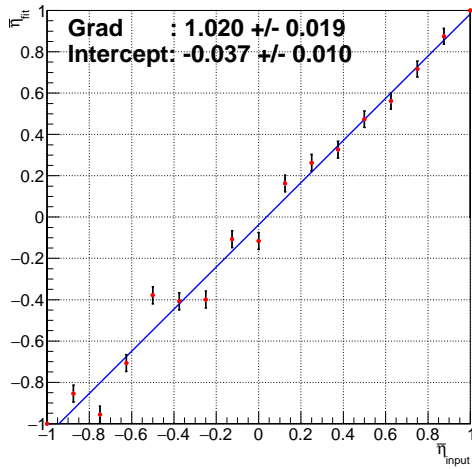
In the last section, we see that the sensitivities of Michel parameters obtained by the selected sample are degraded compared to those of the original generated events. This situation can be explained by the effect of selection criteria. Figures 5.8 and 5.9 show sensitivity dependences on  $E_\gamma$  and  $\cos\theta_{\ell\gamma}$ . Since statistical uncertainty should be proportional to the inverse of square root of the event number, we use  $\sigma \sqrt{N}$  to evaluate the effect of selection, where  $\sigma$  is a statistical uncertainty of Michel parameters and  $N$  is a number of fitted events. According to these figures, we can clearly observe that the sensitivities change even if the effect of decrease of event number is compensated by the factor of  $\sqrt{N}$ . This is equivalent to remark that the importance of events in phase space is not uniform: events which have higher energy photons and smaller  $\cos\theta_{\ell\gamma}$  values give the large impact on the fitted values of Michel parameters. In particular, the condition of angle between lepton and photon is crucial because lower cut of the  $\cos\theta_{\ell\gamma}$  enhances the fraction of backgrounds. It is ideal to relax these conditions as loose as possible, however, we cannot help using the selection criteria to retain realistic purities.



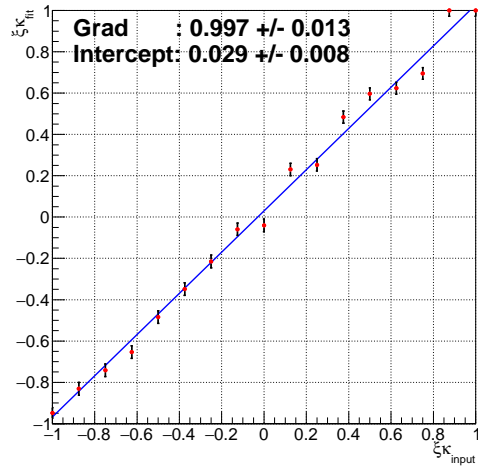
(a)  $\bar{\eta}_e$



(b)  $(\xi\kappa)_e$

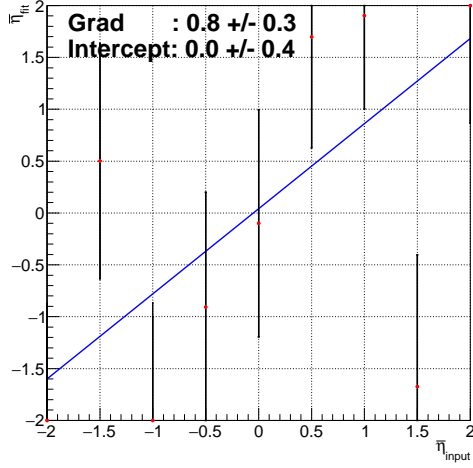


(c)  $\bar{\eta}_\mu$

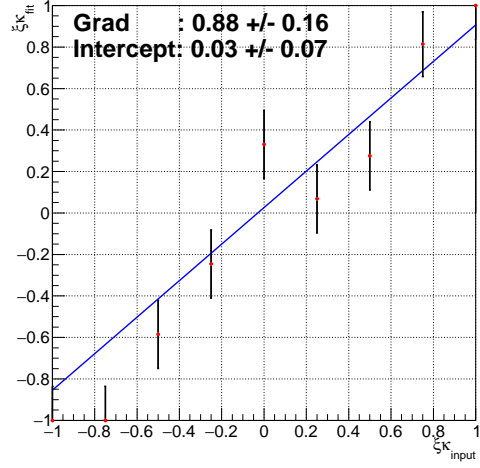


(d)  $(\xi\kappa)_\mu$

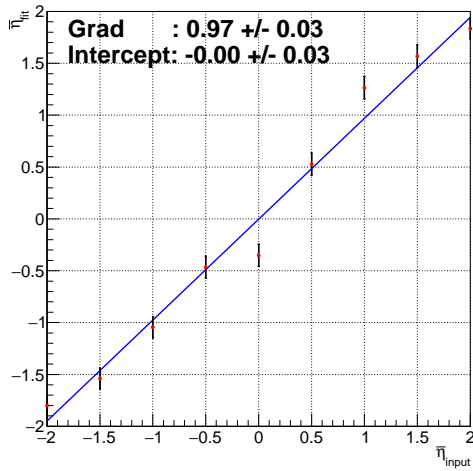
Figure 5.6: Linearity of fitter obtained using 9.2 M generated events for  $\tau \rightarrow e\nu\bar{\nu}\gamma$  and 2.3 M events for  $\tau \rightarrow \mu\nu\bar{\nu}\gamma$ : (a)(b)  $\bar{\eta}$  and  $\xi\kappa$  for  $\tau \rightarrow e\nu\bar{\nu}\gamma$ , (c)(d)  $\bar{\eta}$  and  $\xi\kappa$  for  $\tau \rightarrow \mu\nu\bar{\nu}\gamma$ . The horizontal axis represents value of input Michel parameter and vertical axis represents the fitted Michel parameter. The blue line is a fitted linear function and its gradient and intercept are shown.



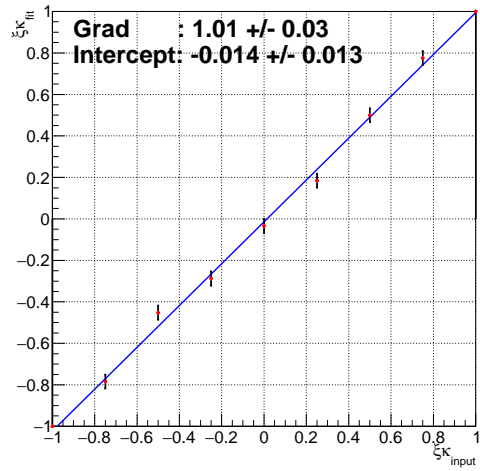
(a)  $\bar{\eta}_e$



(b)  $(\xi\kappa)_e$

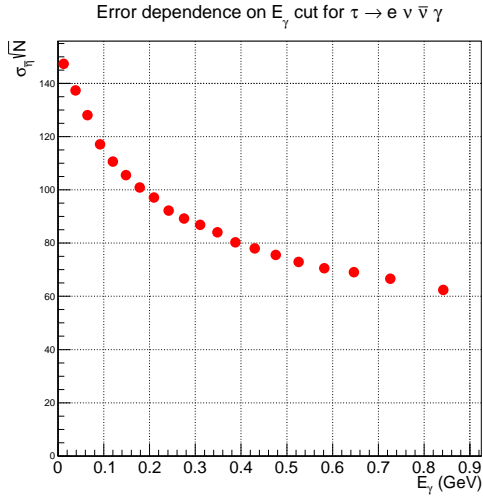


(c)  $\bar{\eta}_\mu$

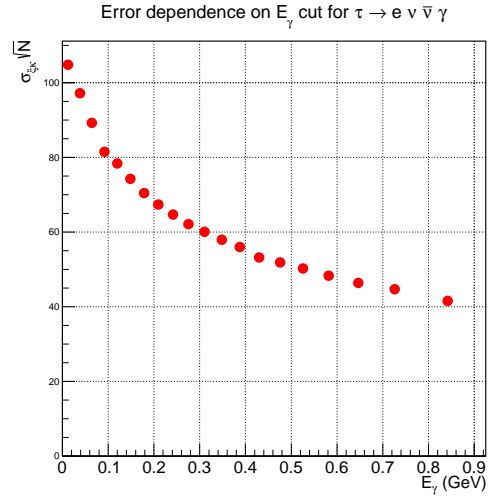


(d)  $(\xi\kappa)_\mu$

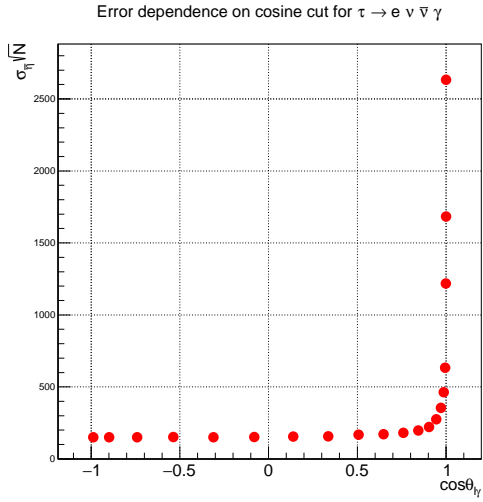
Figure 5.7: Linearity of fitter obtained using 4.4 M selected events for  $\tau \rightarrow e\nu\bar{\nu}\gamma$  and 4.7 M events for  $\tau \rightarrow \mu\nu\bar{\nu}\gamma$ . The horizontal axis represents value of input Michel parameter and vertical axis represents the fitted Michel parameter (a)(b)  $\bar{\eta}$  and  $\xi\kappa$  for  $\tau^- \rightarrow e^- \nu\bar{\nu}\gamma$ , (c)(d)  $\bar{\eta}$  and  $\xi\kappa$  for  $\tau^- \rightarrow \mu^- \nu\bar{\nu}\gamma$ . The blue line is a fitted linear function and its gradient and intercept are shown.



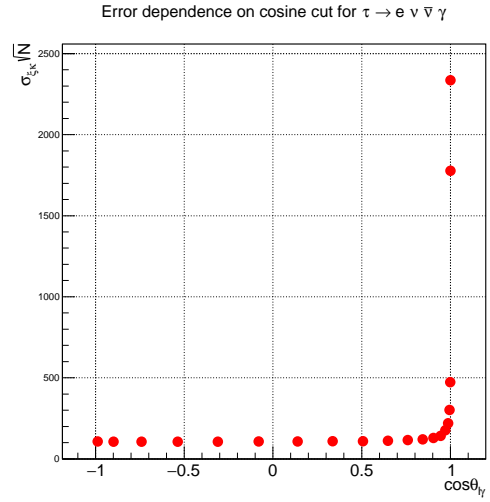
(a)  $\sigma_{\bar{\eta}}-E_\gamma$  cut



(b)  $\sigma_{\xi\kappa}-E_\gamma$  cut

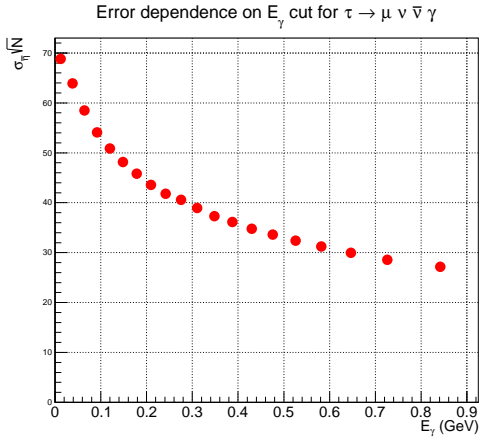


(c)  $\sigma_{\bar{\eta}}-\cos\theta_{e\gamma}$  cut

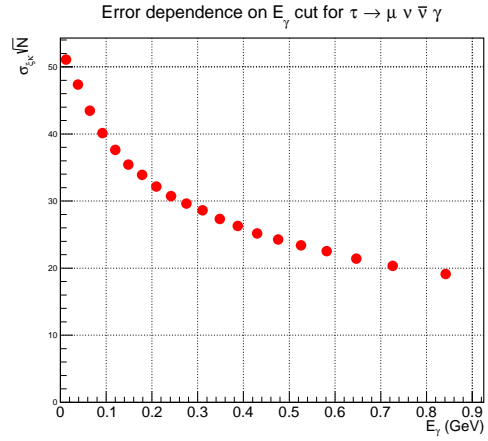


(d)  $\sigma_{\xi\kappa}-\cos\theta_{e\gamma}$  cut

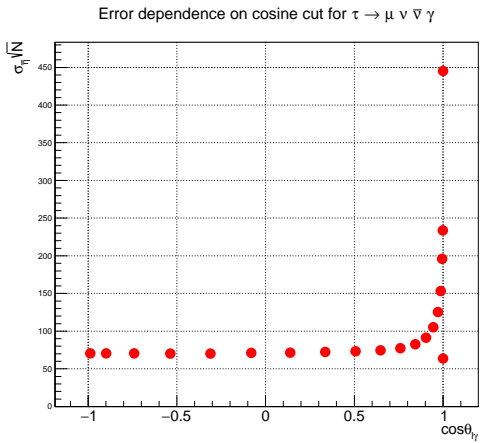
Figure 5.8: Dependence of sensitivities of Michel Parameters for  $\tau \rightarrow e \nu \bar{\nu} \gamma$  decay: (a)(b)  $E_\gamma$  dependences on  $\bar{\eta}$  and  $\xi\kappa$ : (c)(d)  $\cos\theta_{e\gamma}$  dependences on  $\bar{\eta}$  and  $\xi\kappa$ . The vertical axis represents a normalized sensitivity defined as  $\sigma \sqrt{N}$ .



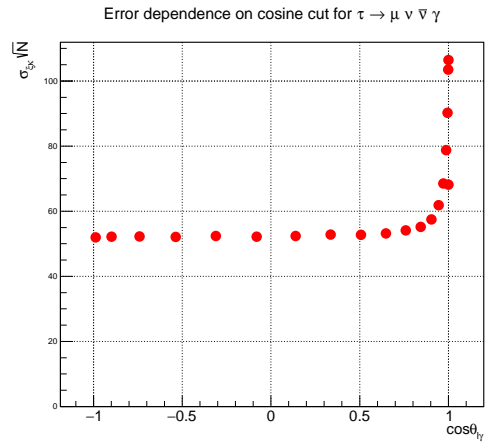
(a)  $\sigma_{\bar{\eta}}-E_\gamma$  cut



(b)  $\sigma_{\xi\kappa}-E_\gamma$  cut



(c)  $\sigma_{\bar{\eta}}-\cos\theta_{\mu\gamma}$  cut



(d)  $\sigma_{\xi\kappa}-\cos\theta_{\mu\gamma}$  cut

Figure 5.9: Dependence of sensitivities of Michel Parameters for  $\tau \rightarrow \mu\nu\bar{\nu}\gamma$  decay: (a)(b)  $E_\gamma$  dependences on  $\bar{\eta}$  and  $\xi\kappa$ : (c)(d)  $\cos\theta_{e\gamma}$  dependences on  $\bar{\eta}$  and  $\xi\kappa$ . The vertical axis represents a normalized sensitivity defined as  $\sigma\sqrt{N}$ .

### 5.6.3 Fitting Michel parameters with background PDFs

For the experimental situation, we cannot distinguish the events according to their sources. With MC events, however, we can separately turn on and off each contribution. The PDFs of each background mode is confirmed by mixing the background mode in question and fitting Michel parameters with the PDF of signal.<sup>§</sup> Figures 5.10 and 5.11 show the contours of the likelihood for the mixed sample for  $(e\gamma, \pi\pi^0)$  and  $(\mu\gamma, \pi\pi^0)$ , respectively. In both cases, the analytical implementations are more or less proper.

On the contrary, we can observe bias due to the inclusion of *others*. In particular, these *others* always tend to shift  $\xi\kappa$  in the negative side. As a matter of fact, the  $3\pi-\rho$  decay, which is explained in Sec. 5.4.2, was previously included in the fraction of the others for  $\tau^-\tau^+ \rightarrow (\mu^-\nu\bar{\nu}\gamma)(\pi^+\pi^0\bar{\nu})$  candidates. However, we found that the effective description of  $3\pi-\rho$  in the *others* shifted the fitted Michel parameter (especially  $\xi\kappa$ ), and decided to describe it analytically. This is one of a proof that the simplification of the  $T = B_{\text{sel}}/S_{\text{sel}}$  defined in Eq. (5.85) into smaller subsets (like as we did in Eq. (5.86) or (5.87)) fails to reflect the high dimension correlations in the total PDF. We tried more than fifty ways to simplify the  $T$ , but the tendencies were always more or less similar:  $\xi\kappa$  tends to move into negative side. Up to now, we compromised on the current method and this is included as a source of systematic bias.

Figure 5.12 shows contours of the likelihood functions for the combined statistics, where all backgrounds are included in the total PDFs. The central values of fitted Michel parameters are

$$\bar{\eta}^e = -2.5, \quad (5.92)$$

$$(\xi\kappa)^e = -0.25, \quad (5.93)$$

$$\bar{\eta}^\mu = 0.67, \quad (5.94)$$

$$(\xi\kappa)^\mu = -0.22. \quad (5.95)$$

We regard these residuals from the SM values of  $\bar{\eta} = \xi\kappa = 0$  as systematic uncertainties due to the limited precision of background descriptions. The magnitudes of these biases are less than  $1\sigma$  statistical uncertainties of experimental events. Conversely, the precision of PDF descriptions can be justified within this level.

---

<sup>§</sup>Although we do not present in this thesis, we have also checked each PDF by fitting other Michel parameters. For example,  $(\ell, \pi\pi^0)$  decay has a sensitivity on  $\eta, \rho, \xi$  and  $\xi\kappa$ . Therefore, it is possible to confirm the PDF by fitting them. Furthermore, since the PDF of  $(\pi\pi^0, \pi\pi^0)$  decay has a  $\xi_\rho$  parameter (the differential decay width of  $\tau^+ \rightarrow \pi^+\pi^0\bar{\nu}$  is proportional to  $A + \xi_\rho \mathbf{B} \cdot \mathbf{S}_\tau^*$  and we use the SM value  $\xi_\rho = 1$  in Eq. (5.55)), we also confirmed this PDF by fitting  $\xi_\rho$ .

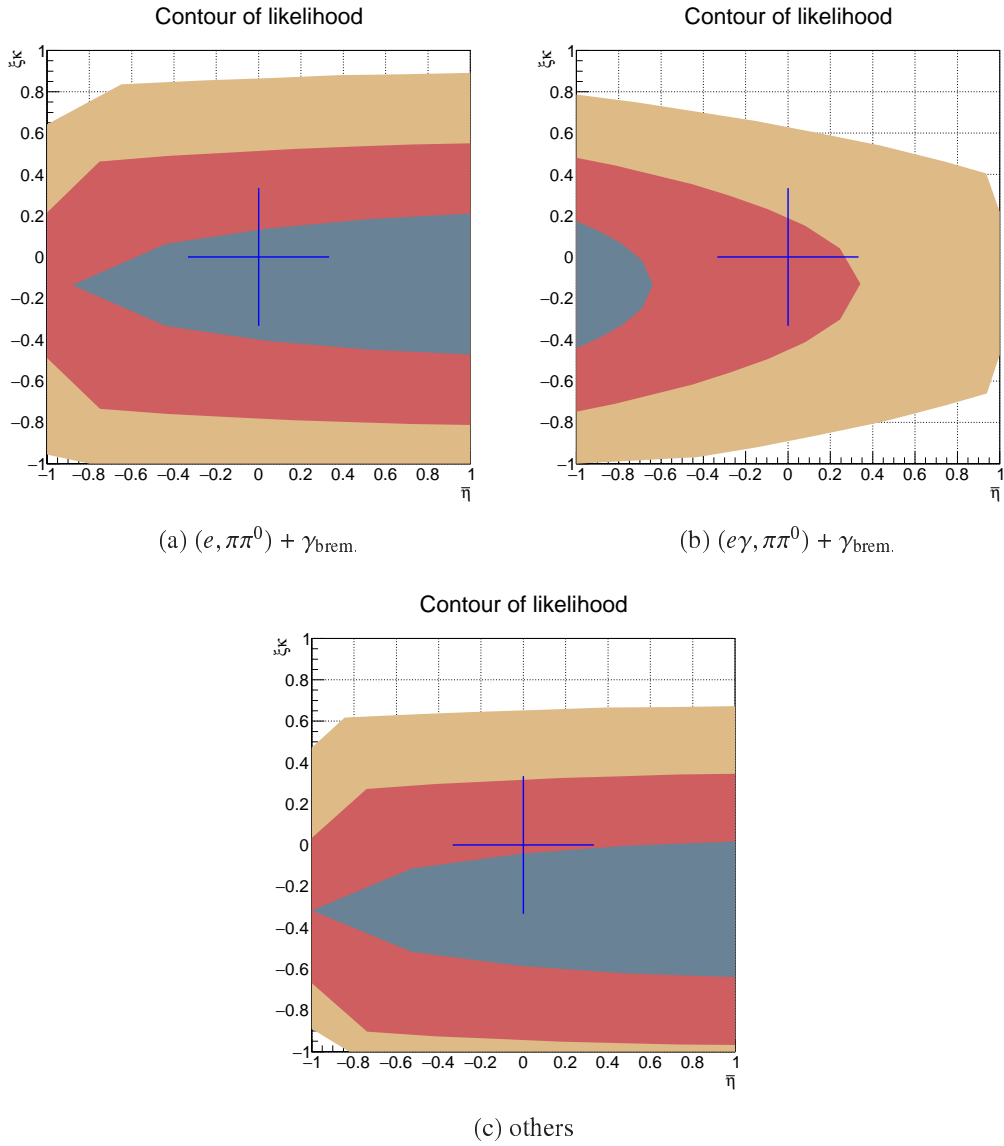


Figure 5.10: Contour of the likelihood obtained with contaminated sample. (a)  $(e, \pi\pi^0) + \gamma_{\text{brem.}}$ , (b)  $(e\gamma, \pi\pi^0) + \gamma_{\text{brem.}}$  and (c) others, are mixed to  $(e\gamma, \pi\pi^0)$  statistics. Horizontal and vertical axes represent  $\bar{\eta}$  and  $\xi\kappa$ . Contours correspond to  $\Delta L = 0.5$ ,  $\Delta L = 4 \times 0.5$  and  $\Delta L = 9 \times 0.5$  in order from inside to outside. Cross hairs represent the SM prediction.

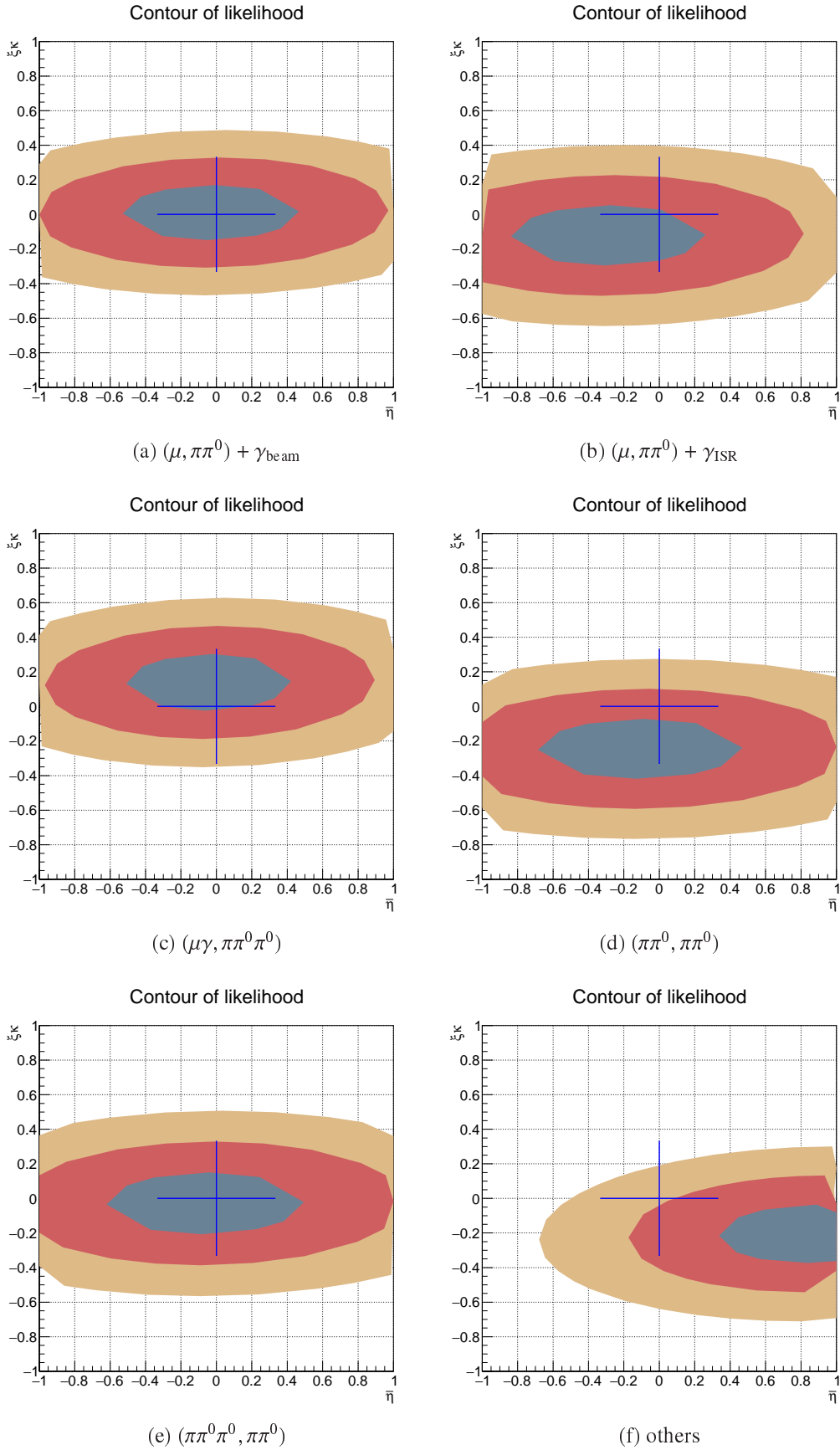
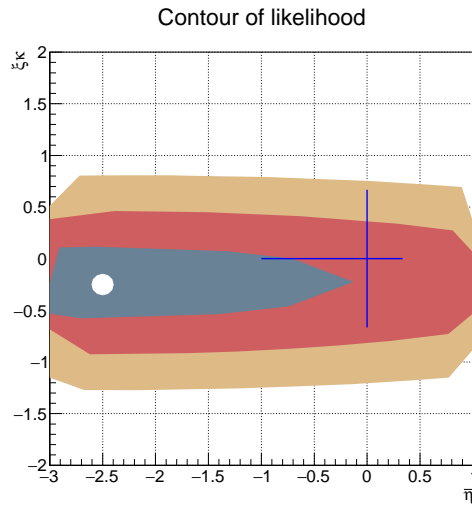
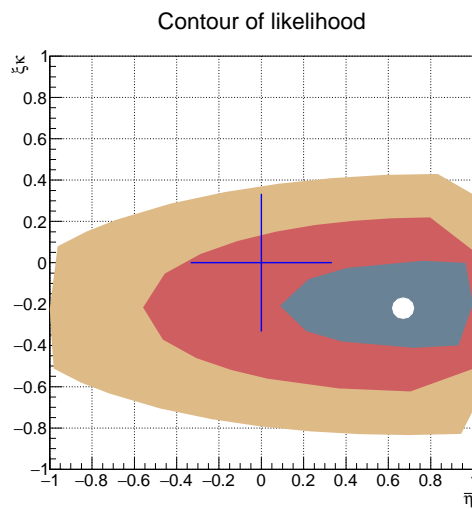


Figure 5.11: Contour of the likelihood obtained with contaminated sample. (a)  $(\mu, \pi\pi^0) + \gamma_{\text{beam}}$ , (b)  $(\mu, \pi\pi^0) + \gamma_{\text{ISR}}$ , (c)  $(\mu\gamma, \pi\pi^0\pi^0)$ , (d)  $(\pi\pi^0, \pi\pi^0)$ , (e)  $(\pi\pi^0\pi^0, \pi\pi^0)$  and (f) others, are mixed to  $(\mu\gamma, \pi\pi^0)$  statistics. Horizontal and vertical axes represent  $\bar{\eta}$  and  $\xi\kappa$ . Contours correspond to  $\Delta L = 0.5$ ,  $\Delta L = 4 \times 0.5$  and  $\Delta L = 9 \times 0.5$  in order from inside to outside. Cross hairs represent the SM prediction.

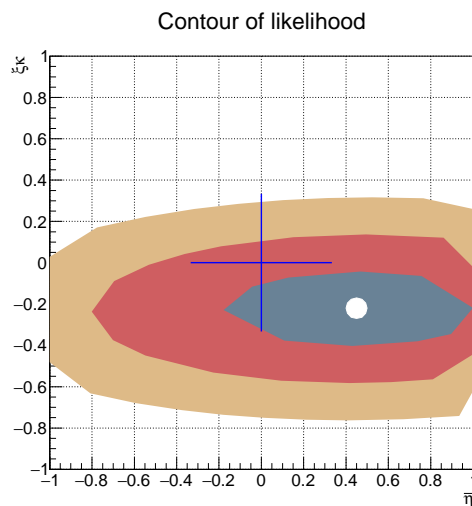




(a) All  $\tau \rightarrow e\nu\bar{\nu}\gamma$  candidates are fitted.



(b) All  $\tau \rightarrow \mu\nu\bar{\nu}\gamma$  candidates are fitted.



(c) All  $\tau \rightarrow \ell\nu\bar{\nu}\gamma$  ( $\ell = e$  and  $\mu$ ) candidates are fitted.

Figure 5.12: Contours of the likelihood function for combined statistics: (a) all  $\tau \rightarrow e\nu\bar{\nu}\gamma$  candidates, (b) all  $\tau \rightarrow \mu\nu\bar{\nu}\gamma$  candidates and (c) combined. Contours correspond to  $\Delta L = 0.5$ ,  $\Delta L = 4 \times 0.5$  and  $\Delta L = 9 \times 0.5$  in order from inside to outside. Cross hairs represent the SM prediction and white circle corresponds to the best fit value of Michel parameters.

### Stability of Michel parameters on $E_{\text{extray}}^{\text{LAB}}$

We also checked the stability of fitted Michel parameters on the variation of  $E_{\text{extray}}^{\text{LAB}}$  value. Generally, the fractions of backgrounds change as the requirement varies and we can confirm the validity of the PDFs. Figure 8.2 shows the obtained Michel parameters. The variations of the fitted values are within their statistical uncertainties.

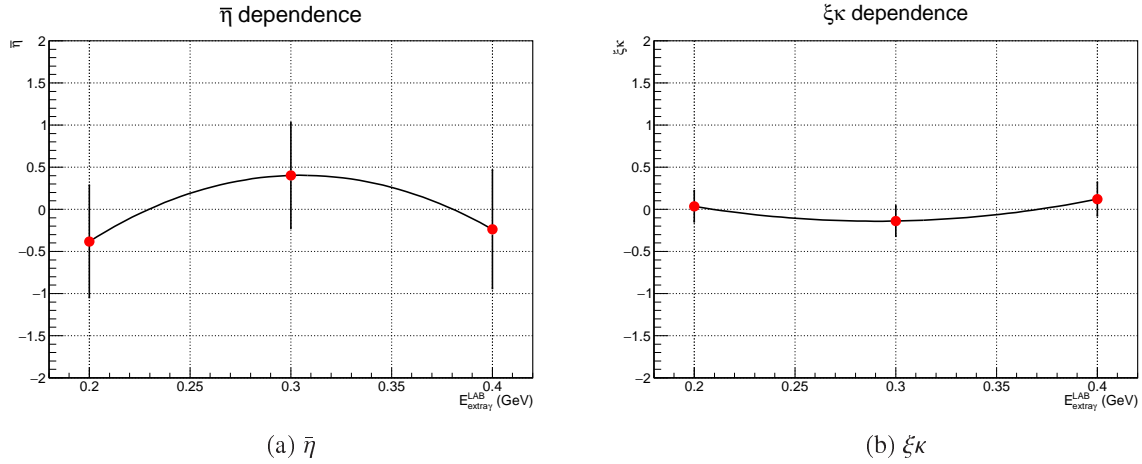


Figure 5.13: Dependence of  $E_{\text{extray}}^{\text{LAB}}$  cut on  $\bar{\eta}$  (a) and  $\xi\kappa$  (b). Horizontal and vertical axes are extragamma energy cut and fitted Michel parameters respectively. The red markers with error bars correspond center values and their statistical errors.

# Chapter 6

## Analysis of the experimental data

As described in 5.4, the Michel parameters are measured by fitting the total PDF defined as

$$P^{\text{total}}(\mathbf{x}) = (1 - \sum_i \lambda_i) \frac{\varepsilon(\mathbf{x})S(\mathbf{x})}{\int d\mathbf{x} \varepsilon(\mathbf{x})S(\mathbf{x})} + \sum_i \lambda_i \frac{\varepsilon(\mathbf{x})B_i(\mathbf{x})}{\int d\mathbf{x} \varepsilon(\mathbf{x})B_i(\mathbf{x})}, \quad (6.1)$$

and the dependence of  $\varepsilon(\mathbf{x})$  cancels when we formulate the logarithmic likelihood function. Suppose that  $\varepsilon(\mathbf{x})$  changes  $\varepsilon(\mathbf{x}) \rightarrow \varepsilon(\mathbf{x})R(\mathbf{x})$ , where  $R(\mathbf{x})$  is a correction factor which represents the change of selection efficiency. Following totally the same procedure as explained in Sec. 5.4, the normalization of signal term becomes

$$\frac{\sigma_{\text{sig}}^{\text{SM}} \bar{\varepsilon}_{\text{sig}}}{N_{\text{sel}}} \sum_{\mathbf{x}^i \in \mathcal{E}\tilde{S}^{\text{SM}}} \frac{\tilde{S}(\mathbf{x}^i)R(\mathbf{x}^i)}{\tilde{S}^{\text{SM}}(\mathbf{x}^i)} \quad (6.2)$$

$$= \frac{\sigma_{\text{sig}}^{\text{SM}} \bar{\varepsilon}_{\text{sig}}}{N_{\text{sel}}} \sum_{\mathbf{x}^i \in \mathcal{E}\tilde{S}^{\text{SM}}} \frac{[\mathcal{E}_0(\mathbf{x}^i) + \mathcal{E}_1(\mathbf{x}^i) \cdot \bar{\eta} + \mathcal{E}_2(\mathbf{x}^i) \cdot \eta'' + \mathcal{E}_3(\mathbf{x}^i) \cdot \xi\kappa] R(\mathbf{x}^i)}{\mathcal{E}_0(\mathbf{x}^i)}, \quad (6.3)$$

Consequently, the relative normalization is modified:

$$\left\langle \frac{\mathcal{E}_i}{\mathcal{E}_0} \right\rangle_{\mathbf{x} \in \mathcal{E}\tilde{S}^{\text{SM}}} \rightarrow \left\langle \frac{\mathcal{E}_i}{\mathcal{E}_0} R \right\rangle_{\mathbf{x} \in \mathcal{E}\tilde{S}^{\text{SM}}}, \quad (6.4)$$

which means that every event is weighted with additional factor  $R(\mathbf{x})$ . In the presence of  $R(\mathbf{x})$ , the normalizations of background terms also change and result in an additional factor  $R_i = \langle R \rangle_{\mathbf{x} \in B_i}$ .

The difference of the efficiency between the real experiment and MC simulation is taken into account by extracting the  $R(\mathbf{x})$ . We tabulate  $R(\mathbf{x})$  as products of corrections from a trigger efficiency and reconstruction efficiencies of all particles.

### 6.1 Trigger efficiency corrections \*

The information of the trigger is stored as bits from the global decision logic (GDL), whose each bit corresponds to each source of the trigger. The GDL data are packed with eight bytes format, hence at maximum 64 sources of information are extracted. As explained in Sec. 3.2.7, all events are required to be fired by following specific bits: *ffs\_zt2*, *klm\_opn*, *klm\_b2b*, *clst4* and *hie*. Figure 6.1 shows the distribution of GDL trigger bits for both MC simulation and the experiment separately for SVD1 and SVD2 cases, respectively. As the figure shows, it is apparent that the MC does not simulate the trigger signals so precisely.

---

\* Hereafter, several correction factors are evaluated. The binning of those factors are summarized in Sec. 6.4

Figures 6.2 and 6.3 show dependence of the trigger efficiency on the momentum and angle of lepton for both decay modes— $(e\gamma, \pi\pi^0)$  and  $(\mu\gamma, \pi\pi^0)$ —for SVD1 and SVD2, respectively. In particular,  $(e\gamma, \pi\pi^0)$  case, we can see quite strong dependence on both variables. It is known that this effect arises from an improper calibration of the energy threshold of Bhabha veto. For this reason, we are required to obtain the correction factor  $R_{\text{trg}} = \varepsilon^{\text{EX}}/\varepsilon^{\text{MC}}$  to take into account the systematic effect from trigger simulation.

To evaluate  $R_{\text{trg}}$ , we first separate the events into two categories depending on the source of trigger: one is a charged trigger  $Z$  and the other is a neutral trigger  $N$ , which are defined as:

$$Z = \begin{cases} \text{ffs\_zt2 or klm\_opn or klm\_b2b} & \text{for SVD1} \\ \text{klm\_opn or klm\_b2b} & \text{for SVD2} \end{cases}, \quad (6.5)$$

$$N = \text{clst4 or hie}. \quad (6.6)$$

Noting that the charged and neutral triggers are physically independent signals, we can recognize that the charged trigger efficiency is  $\varepsilon_Z = N_{N\&Z}/N_N$  and  $\varepsilon_N = N_{N\&Z}/N_Z$  because the factor from other efficiencies should cancel. Since an event is triggered unless both triggers are inactive, the efficiency is obtained as

$$\varepsilon_{\text{trg}} = 1 - (1 - \varepsilon_N)(1 - \varepsilon_Z) = \varepsilon_N + \varepsilon_Z - \varepsilon_N\varepsilon_Z. \quad (6.7)$$

As a matter of fact, Figs 6.2 and 6.3 are obtained by this Eq. (6.7). The efficiency correction  $R_{\text{trg}}$  is obtained by comparing the difference of Eq. (6.7) between the experiment and MC simulation as:

$$R_{\text{trg}} = \frac{\left(\frac{N_{N\&Z}}{N_N}\right)_{\text{EX}} + \left(\frac{N_{N\&Z}}{N_Z}\right)_{\text{EX}} - \left(\frac{N_{N\&Z}}{N_N} \cdot \frac{N_{N\&Z}}{N_Z}\right)_{\text{EX}}}{\left(\frac{N_{N\&Z}}{N_N}\right)_{\text{MC}} + \left(\frac{N_{N\&Z}}{N_Z}\right)_{\text{MC}} - \left(\frac{N_{N\&Z}}{N_N} \cdot \frac{N_{N\&Z}}{N_Z}\right)_{\text{MC}}}. \quad (6.8)$$

In this analysis, we obtain  $R_{\text{trg}}$  as a function of  $P_\ell^{\text{LAB}}$ ,  $\cos\theta_\ell^{\text{LAB}}$  and  $\omega_h$  as products of two 2D PDFs as

$$R_{\text{trg}} = R_{\text{trg}}(P_\ell^{\text{LAB}}, \cos\theta_\ell^{\text{LAB}}) \frac{R_{\text{trg}}(P_\ell^{\text{LAB}}, \omega_h)}{R_{\text{trg}}(P_\ell^{\text{LAB}})}, \quad (6.9)$$

where  $\omega_h$  is called *helicity sensitive* parameter and calculated by following formula:

$$\omega_h = \int_{\Phi \in [\Phi_1, \Phi_2]} d\Phi \frac{\mathbf{B}' \cdot \mathbf{n}_z^*}{A'} \quad (6.10)$$

where  $A'$  and  $\mathbf{B}'$  are spin-independent and spin-dependent terms defined in the signal PDF (Eqs. (5.54) and (5.55)). This  $\omega_h$  represents an average magnitude of the polarization of  $\tau^+ \rightarrow \pi\pi^0\bar{\nu}$  in the direction of the movement of  $\tau^+$  [73]. The idea of this tabulation (Eq. (6.9)) is to take into account the correlations among three variables as many as possible without loss of statistics per each bin. The correction factor  $R_{\text{trg}}$  is shown in Figs 6.4 and 6.5 for  $\tau^- \rightarrow e^- \bar{\nu}\gamma$  and  $\tau^- \rightarrow \mu^- \bar{\nu}\gamma$  candidates, respectively. Although we evaluate this factor in two dimensional space as Eq. (6.9), they are projected onto one axis to observe them easily.

## 6.2 Particle selection efficiency corrections

The systematic effect from particle selection efficiencies are also included in  $R$ . The total effects is assumed to be factorized into products of all particles:  $R_{\text{tot}} = R_\ell R_\gamma R_\pi R_{\pi^0}$ . All of these factors are extracted as functions of momenta and cosine of polar angles for corresponding particles. For charged tracks (the lepton and pion), we regard the correction factor as a product of the charged-track reconstruction efficiency and the PID selection efficiency as  $R_{l,\pi} = R_{\text{rec}} R_{\text{PID}}$ .

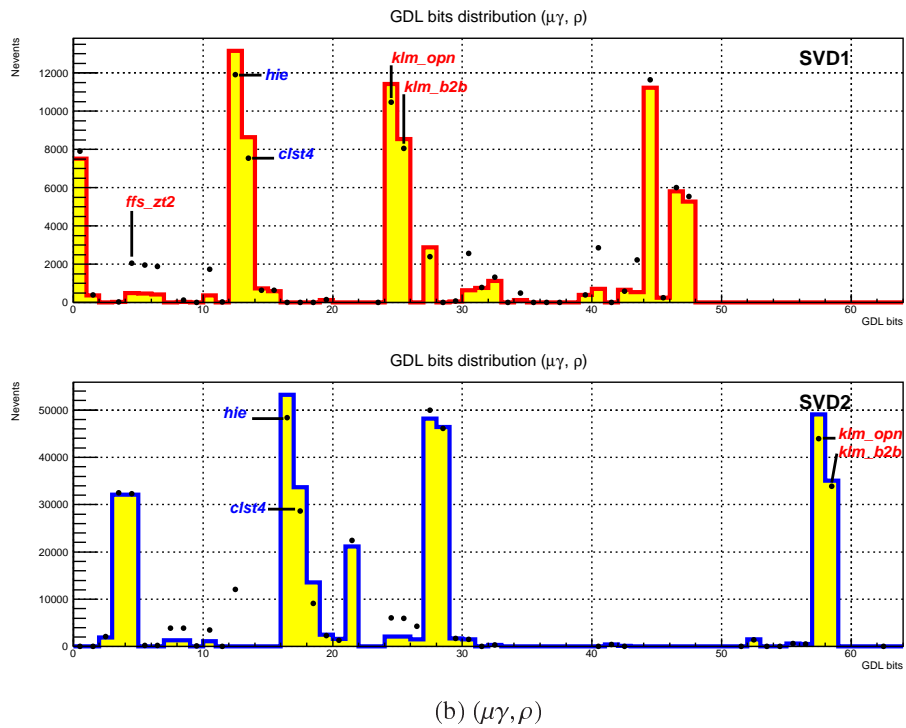
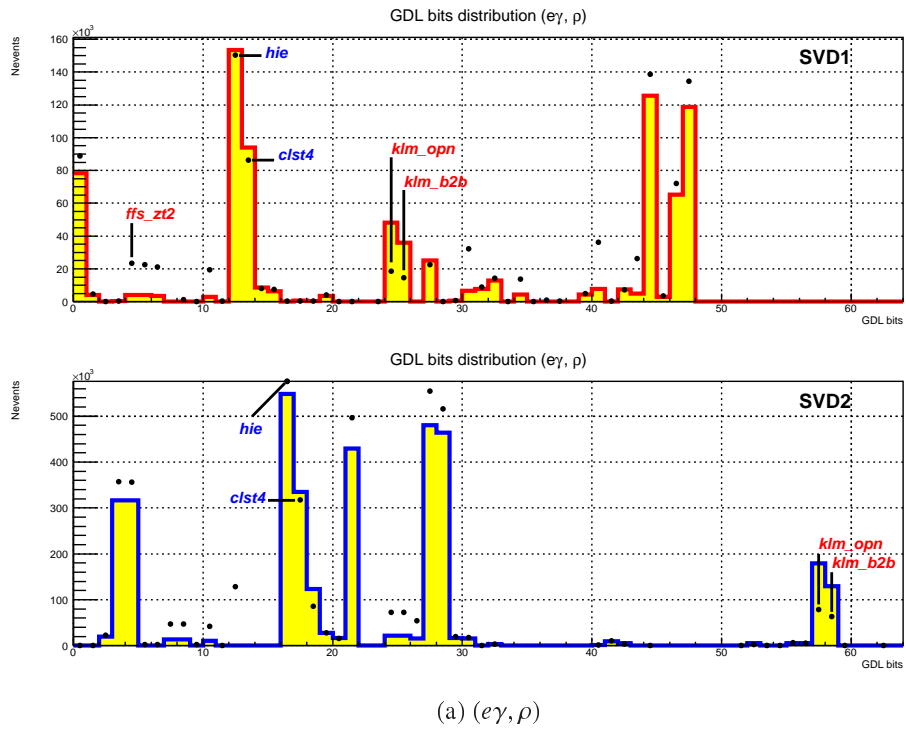


Figure 6.1: GDL trigger bits distribution: (a)  $(e^-\gamma, \rho^+)$  decay candidate and (b)  $(\mu^-\gamma, \rho^+)$  decay candidate. For both cases, upper figures represent the distribution obtained with SVD1 term and lower figures represent the distribution for SVD2 term. Horizontal axis is number of GDL bits. Filled histograms and black point indicate MC simulation and real experiment. The number of MC events is scaled to that of experimental data based on the number of entries.

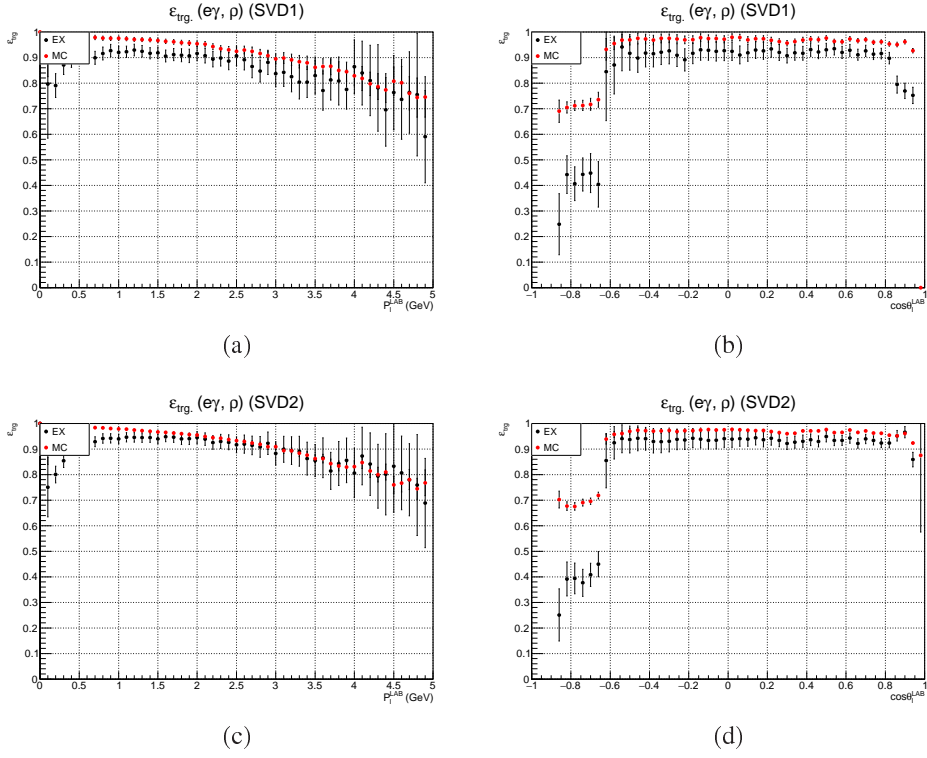


Figure 6.2: Trigger efficiency for  $(e^- \gamma, \rho^+)$  decay. (a)(b)  $P_\ell^{\text{LAB}}$  and  $\cos\theta_\ell^{\text{LAB}}$  dependence for SVD1 configuration, (c)(d)  $P_\ell^{\text{LAB}}$  and  $\cos\theta_\ell^{\text{LAB}}$  dependence for SVD2 configuration. Red marker corresponds to MC and black marker is experiment.

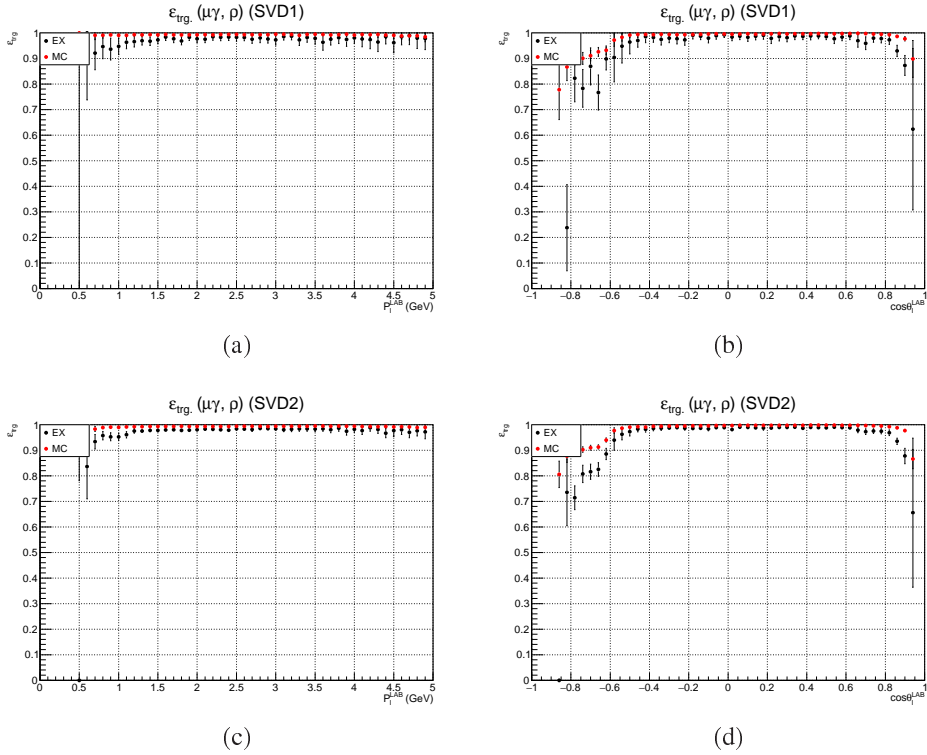


Figure 6.3: Trigger efficiency for  $(\mu^- \gamma, \rho^+)$  decay. (a)(b)  $P_\ell^{\text{LAB}}$  and  $\cos\theta_\ell^{\text{LAB}}$  dependence for SVD1 configuration, (c)(d)  $P_\ell^{\text{LAB}}$  and  $\cos\theta_\ell^{\text{LAB}}$  dependence for SVD2 configuration. Red marker corresponds to MC and black marker is experiment.

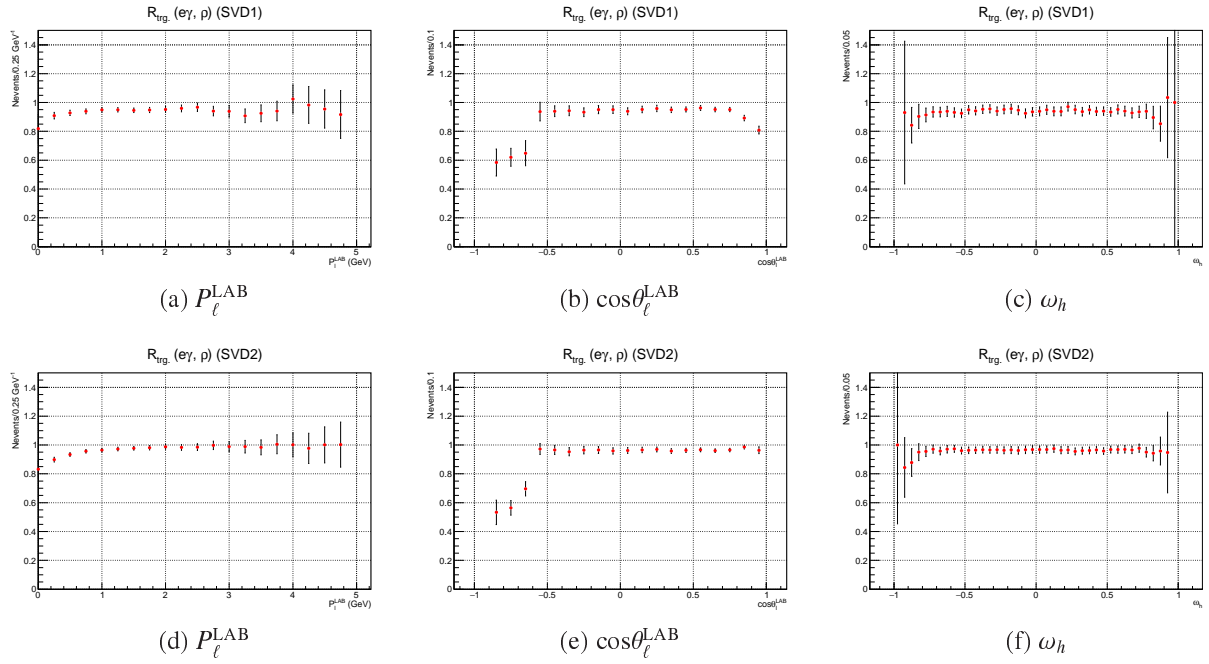


Figure 6.4: Correction factor of the trigger efficiency  $R_{\text{trg}}$  for  $(e^- \gamma, \rho^+)$  decay. (a)(b)(c)  $P_{\ell}^{\text{LAB}}$ ,  $\cos\theta_{\ell}^{\text{LAB}}$  and  $\omega_h$  dependence for SVD1, (d)(e)(f) for SVD2.

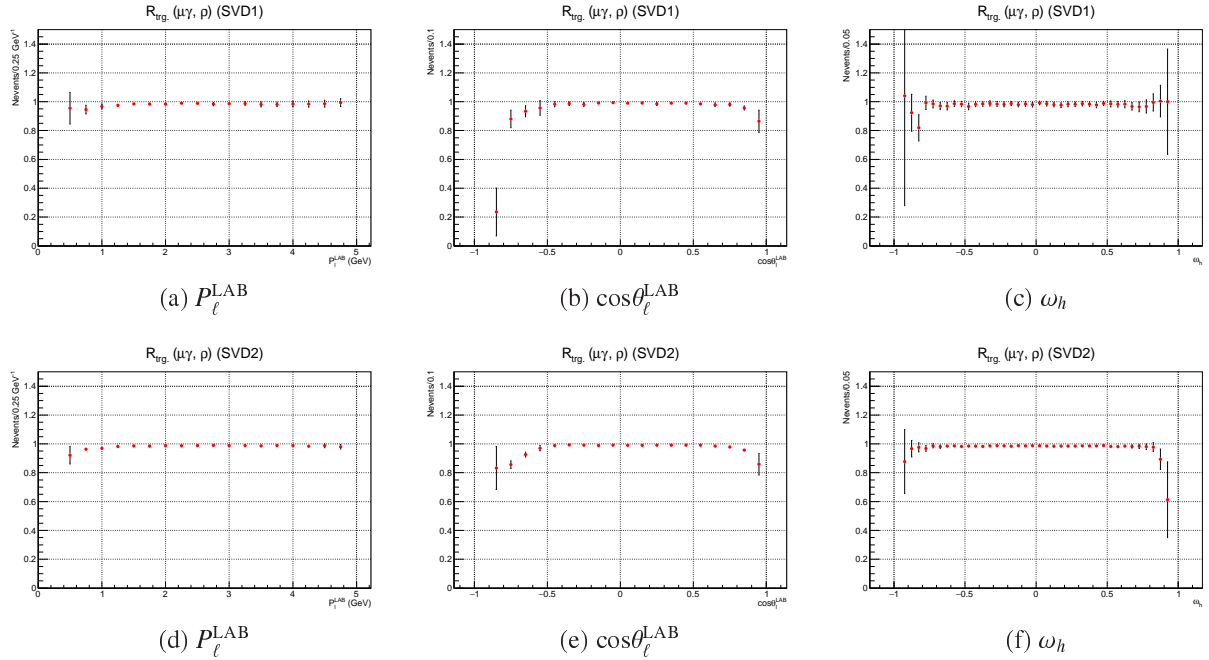


Figure 6.5: Relative factor of the trigger efficiency  $R_{\text{trg}}$  for  $(\mu^- \gamma, \rho^+)$  decay. (a)(b)(c)  $P_{\ell}^{\text{LAB}}$ ,  $\cos\theta_{\ell}^{\text{LAB}}$  and  $\omega_h$  dependence for SVD1, (d)(e)(f) for SVD2.

The pion PID correction factor is obtained by the measurement of  $D^{*+}$  decay  $D^{*+} \rightarrow D^0 \pi^+ \rightarrow (K^- \pi^+) \pi_s^+$ . Because the difference of mass between  $D^{*+}$  and  $D^0$  is small ( $\sim 140$  MeV), the momentum of  $\pi_s^+$  from  $D^{*+}$  decay is small (the  $s$  in the subscript stands for *soft*) and this characteristic track enables us to specify the process without PID of  $D^0$  daughters. Since  $D^0 \rightarrow K^+ \pi^-$  decay is CKM-suppressed ( $\mathcal{B}(D^0 \rightarrow K^+ \pi^-)/\mathcal{B}(D^0 \rightarrow K^- \pi^+) \sim 0.4\%$ ), we can assume that the charges of two pions are same. Therefore, we can determine the  $\pi^+$  candidate uniquely from the two rest charged tracks. Then, the efficiency of pion identification for a certain  $\pi$ -likelihood value is extracted observing the  $\pi^+$  track of  $D^0$  daughter by

$$\varepsilon_{\pi\text{ID}} = \frac{\text{number of } \pi \text{ tracks identified as } \pi}{\text{number of } \pi \text{ tracks}}, \quad (6.11)$$

and the correction factor is extracted by the comparison of the efficiencies between the experiment and MC simulation as  $R = \varepsilon_{\pi\text{ID}}^{\text{EXP}}/\varepsilon_{\pi\text{ID}}^{\text{MC}}$ .

The lepton PID correction is taken from two photon process  $e^+e^- \rightarrow e^+e^-\ell^+\ell^-$  ( $\ell = e, \text{ or } \mu$ ). After a rejection of cosmic rays with an opening angle of  $\ell^+\ell^-$  pair, events are selected if either of lepton satisfies  $\mathcal{P}_\ell > 0.99$  ( $\ell = e \text{ or } \mu$ ). The lepton identification efficiency is obtained using the accompanying track as

$$\varepsilon_{\ell\text{ID}} = \frac{\text{number of } \ell \text{ tracks identified as } \ell}{\text{number of } \ell \text{ tracks}}. \quad (6.12)$$

Similarly to  $\pi\text{ID}$  case, the correction factor is extracted as  $R = \varepsilon_{\ell\text{ID}}^{\text{EXP}}/\varepsilon_{\ell\text{ID}}^{\text{MC}}$ . These PID correction factors are conventional ones used in many Belle analyses.

The common factor of  $R_{\text{rec}}$  is obtained using the decay of four-charged track events and explained in Sec. 6.3.

## 6.2.1 $\pi^0\text{ID}$ and $\gamma\text{ID}$ efficiency corrections

$\pi^0$  and  $\gamma$  ID efficiency corrections are obtained by analyzing two decays,  $\tau^+\tau^- \rightarrow (\pi^+\pi^0\bar{\nu})(\pi^-\pi^0\nu)$  and  $\tau^+\tau^- \rightarrow (\pi^+\pi^0\bar{\nu})(\pi^-\nu)$ . The  $\pi^0$  efficiency is formulated by comparing the number of selected and generated events as:

$$\varepsilon_{\pi^0} = \frac{N_{\text{sel}}(\pi\pi^0, \pi\pi^0)/N_{\text{prod}}(\pi\pi^0, \pi\pi^0)}{N_{\text{sel}}(\pi, \pi\pi^0)/N_{\text{prod}}(\pi, \pi\pi^0)} = \frac{N_{\text{sel}}(\pi\pi^0, \pi\pi^0)}{N_{\text{sel}}(\pi, \pi\pi^0)} \cdot \frac{N_{\text{prod}}(\pi, \pi\pi^0)}{N_{\text{prod}}(\pi\pi^0, \pi\pi^0)} \quad (6.13)$$

$$= \frac{N_{\text{sel}}(\pi\pi^0, \pi\pi^0)}{N_{\text{sel}}(\pi, \pi\pi^0)} \frac{\mathcal{B}(\pi, \pi\pi^0)}{\mathcal{B}(\pi\pi^0, \pi\pi^0)}, \quad (6.14)$$

where  $N_{\text{prod}}$  and  $N_{\text{sel}}$  mean number of produced and selected events. The last factor is a ratio of branching ratio and can be ignored because they are precisely measured within a few sub percents and cancels in the calculation of the correction factor when the MC events are generated according to the measured branching ratios.

The selection criteria for common particles ( $\pi$  and  $\pi\pi^0$ ) are basically arbitrary because the efficiencies cancel. On the other hand, for the rest  $\pi^0$ , it is required to apply completely same selection criteria as that of signal, which are not shared in both numerator and denominator. The event selection is composed of two stages: preselection of  $\tau^+\tau^-$  and final selection. The preselection of  $\tau^+\tau^-$  is common to the event selection explained in Sec. 4.1. In the selection of these candidates, it is not necessarily important to increase its purity because we extract the local value by binning momentum and direction. For example, the reconstruction of  $\tau^+ \rightarrow \pi^+\pi^0\bar{\nu}$  is contaminated from several multi-pion decays like  $\tau^+ \rightarrow \pi^+\pi^0\pi^0\bar{\nu}$ ,  $\tau^+ \rightarrow \pi^+\pi^0\pi^0\pi^0\bar{\nu}$  and so on, however, this does not cause serious problems because the type of particle is same and we do not reject event by a veto of such extra



Table 6.1: Selection criteria for  $(\pi\pi^0, \pi\pi^0)$  and  $(\pi, \pi\pi^0)$  candidates <sup>†</sup>

①: Common charged $\pi$ is selected by $\mathcal{P}_\pi > 0.98$ and $\mathcal{P}_\mu < 0.01$ .
②: Common $\pi^0$ is selected by $115 \text{ MeV}/c^2 < M_{\gamma\gamma} < 150 \text{ MeV}/c^2$ , where $\gamma$ is selected with energy threshold $E_\gamma > 40 \text{ MeV}$ .
③: Common pair of $\pi\pi^0$ should form $\rho$ candidate with $0.5 \text{ GeV}/c^2 < M_{\pi\pi^0} < 1.5 \text{ GeV}/c^2$ .
④: A $\pi^0$ which is not common is selected with same selection criteria as that of signal $\pi^0$ .
⑤: A $\gamma$ which is not common is selected with same selection criteria as that of signal $\gamma$ .
⑥: When $\gamma$ efficiency correction is extracted, a $\pi^0 \rightarrow \gamma\gamma$ candidate which is not common is selected with a loose cut $80 \text{ MeV}/c^2 < M_{\gamma\gamma} < 190 \text{ MeV}/c^2$ . The $\gamma$ candidate is randomly chosen from the two photons.

<sup>†</sup> Common means particles are shared in both denominator and numerator in Eq. (6.14).

Table 6.2: Fractions of selected candidates <sup>†</sup>

$(\pi\pi^0, \pi\pi^0)$ candidate	$(\pi\gamma, \pi\pi^0)$ candidate	$(\pi, \pi\pi^0)$ candidate
$(\pi\pi^0, \pi\pi^0)$ 40%	$(\pi\pi^0, \pi\pi^0)$ 37%	$(\pi\pi^0, \pi\pi^0)$ 28%
$(\pi\pi^0\pi^0, \pi\pi^0)$ 26%	$(\pi\pi^0\pi^0, \pi\pi^0)$ 24%	$(\pi, \pi\pi^0)$ 20%
$(\pi\pi^0\pi^0, \pi)$ 8%	$(\pi\pi^0\pi^0, \pi)$ 9%	$(\pi\pi^0\pi^0, \pi\pi^0)$ 15%
$(\pi\pi^0\pi^0, \mu)$ 4%	$(\pi\pi^0, \pi)$ 7%	$(\pi\pi^0\pi^0, \pi)$ 9%
others 20%	$(\pi\pi^0\pi^0, \mu)$ 4%	$(\pi\pi^0, \mu)$ 7%
	others 20%	others 20%

particles. The only problem is the contamination from muon instead of the charged pion reconstruction, which may have a different behavior in the detector. In our extraction, the inclusion of muon is less than 10%, hence, we ignore this. Using Eq. (6.14) and noting the cancellation of the factor of branching ratio, we obtain the  $R_{\pi^0}$  as:

$$R_{\pi^0} = \frac{\varepsilon_{\pi^0}^{\text{EX}}}{\varepsilon_{\pi^0}^{\text{MC}}} = \frac{N_{\text{sel}}^{\text{EX}}(\pi\pi^0, \pi\pi^0)}{N_{\text{sel}}^{\text{MC}}(\pi\pi^0, \pi\pi^0)} \cdot \frac{N_{\text{sel}}^{\text{MC}}(\pi, \pi\pi^0)}{N_{\text{sel}}^{\text{EX}}(\pi, \pi\pi^0)}. \quad (6.15)$$

The  $\gamma$ ID efficiency correction can be also tabulated using same decays, where one of two photons from  $\pi^0$  is randomly selected. Similarly to  $\pi^0$  case, same selection criteria as signal must be applied for  $\gamma$  candidates. Thus the formula is explicitly written as

$$R_\gamma = \frac{\varepsilon_\gamma^{\text{EX}}}{\varepsilon_\gamma^{\text{MC}}} = \frac{N_{\text{sel}}^{\text{EX}}(\pi\gamma, \pi\pi^0)}{N_{\text{sel}}^{\text{MC}}(\pi\gamma, \pi\pi^0)} \cdot \frac{N_{\text{sel}}^{\text{MC}}(\pi, \pi\pi^0)}{N_{\text{sel}}^{\text{EX}}(\pi, \pi\pi^0)}. \quad (6.16)$$

In Tables 6.1 and 6.2, we summarize the selection criteria and the contribution of various modes for  $(\pi\pi^0, \pi\pi^0)$ ,  $(\pi\gamma, \pi\pi^0)$  and  $(\pi, \pi\pi^0)$  candidates. The measured  $R_{\pi^0}$  and  $R_\gamma$  are shown in Figs. 6.6 and 6.7 as functions of momenta and directions for each particle.

<sup>†</sup>The others mainly come from multi-pion decays  $n\pi$  ( $n \geq 4$ ).

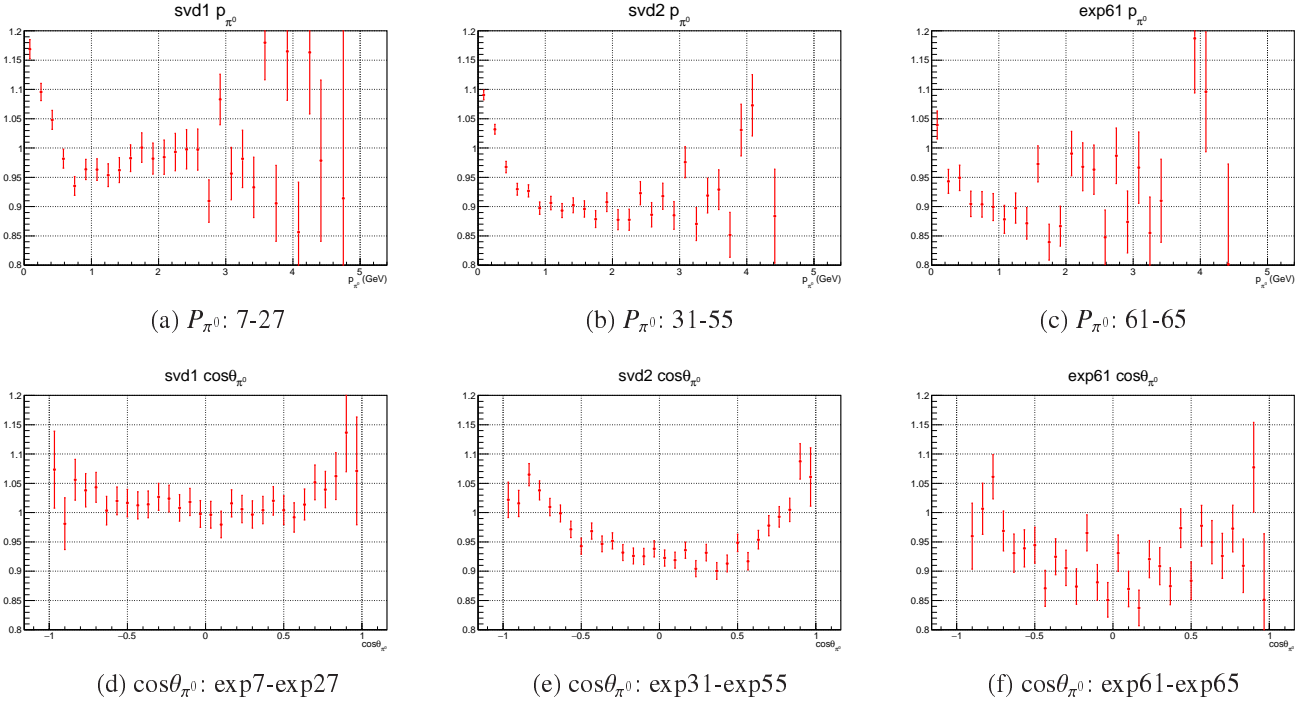


Figure 6.6:  $\pi^0$ ID efficiency correction  $R$  as a function of momenta of  $\pi^0$ : (a)(b)(c)  $P_{\pi^0}$  dependence for the run identification number 7-27, 31-55 and 61-65, (d)(e)(f)  $\cos\theta_{\pi^0}$  dependence for the same identification numbers.

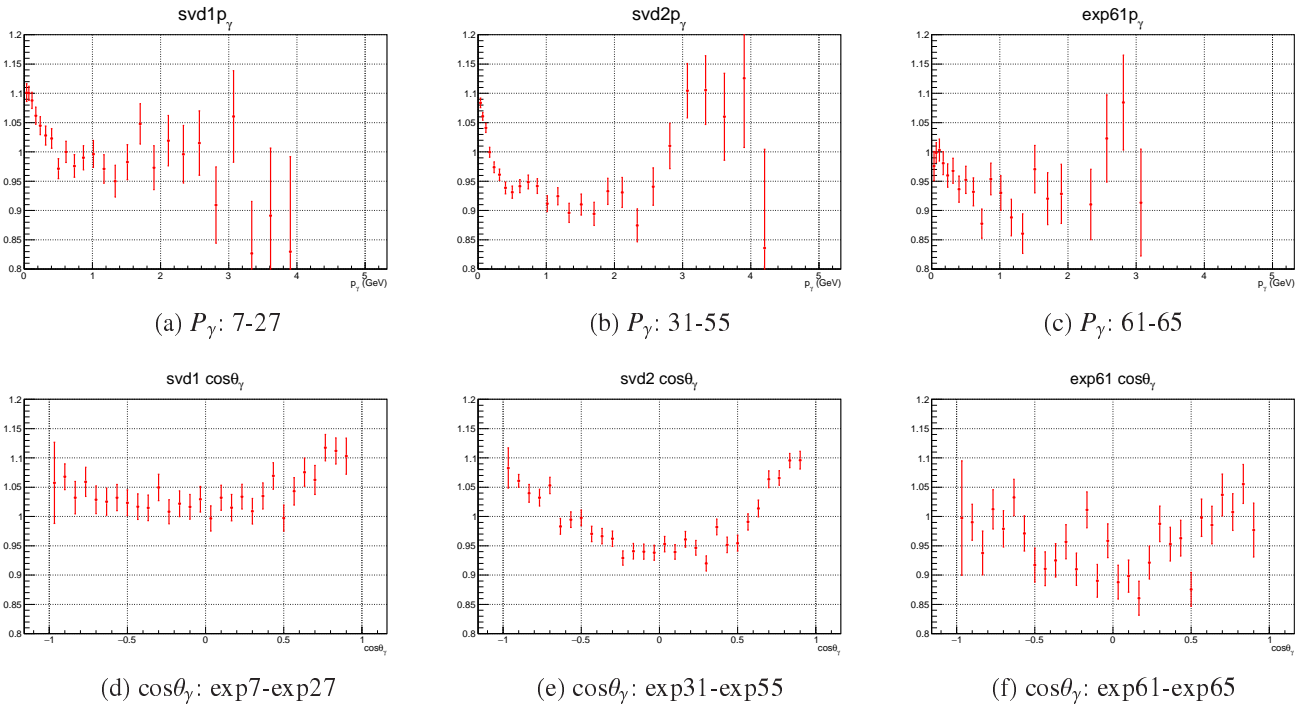


Figure 6.7:  $\gamma$ ID efficiency correction  $R$  as a function of momenta of  $\gamma$ : (a)(b)(c)  $P_{\gamma}$  dependence for run identification number 7-27, 31-55 and 61-65, (d)(e)(f)  $\cos\theta_{\gamma}$  dependence for the same identification numbers.

### 6.3 Reconstruction efficiency corrections

In many analysis of  $B$  meson at Belle, the information of  $D^{*+} \rightarrow D^0(\rightarrow K_S \pi^+ \pi^-) \pi_s^+$  decay is conventionally used to extract the charged track reconstruction efficiency. Similarly to measurement of  $\pi$ ID efficiency correction explained above, the characteristic low momentum track of  $\pi_s^+$  (from  $D^{*+} \rightarrow D^0 \pi_s^+$ ) is utilized to select events and the mathematical constraints of masses of  $D^0$  and  $K_S$  allow us to determine the momentum of a lost charged pion (from  $K_S \rightarrow \pi^+ \pi^-$  decay) only from partially observed information. However, the typical momentum of the pion from this process tends to be low (up to  $\sim 1$  GeV/ $c$ ) and not so useful for this analysis. Moreover, the requirement of the track reconstruction used in this analysis is not same as previous study, thereby we need to separately obtain the efficiency correction for this analysis.

The track reconstruction efficiency correction  $R_{\text{rec}}$  is obtained using four-charged track events from  $\tau^+ \tau^-$  decay where one side of tau decays leptonically and the other side decays into three charged pions. Suppose that  $(\ell^-, \pi^+ \pi^- \pi^+)$  decay occurs. The charged tracks are selected by the same selection criteria as our main analysis (as explained in Chapter 4, the charged track is required to satisfy  $d_r < 2$  cm,  $|d_z| < 5$  cm and  $P_t^{\text{LAB}} > 0.1$  GeV/ $c$ ). Moreover, we require just one negative sign lepton candidate which has a lepton likelihood ratio of  $\mathcal{P}_e > 0.98$  or  $\mathcal{P}_\mu > 0.98$ . In this case, the number of events which have four reconstructed tracks becomes

$$N_4 = N_0 \varepsilon_+^2 \varepsilon_- \eta_- \varepsilon_{\text{other}}^{(4)}, \quad (6.17)$$

where  $N_0$  is a number of produced events,  $\eta_-$  is a product of the efficiencies of both lepton identification and negative charged track reconstruction,  $\varepsilon_\pm$  is the efficiency of the charged track reconstruction and  $\varepsilon_{\text{other}}^{(4)}$  is other efficiencies for four-charged track events that is explained later. Similarly, we can calculate corresponding number for three charged track events as

$$N_3^+ = N_0 \eta_- \varepsilon_+^2 (1 - \varepsilon_-) \varepsilon_{\text{other}}^{(3)}, \quad (6.18)$$

$$N_3^- = 2N_0 \eta_- \varepsilon_- \varepsilon_+ (1 - \varepsilon_+) \varepsilon_{\text{other}}^{(3)}, \quad (6.19)$$

where the sign of  $N_3^\pm$  represents the net charge of observed tracks. Here, the factor of two in Eq. (6.19) appears from way of counting for positively-charged tracks. Note that the subscript 3 does not mean number of produced tracks but reconstructed ones. Therefore, we obtain following relations as:

$$\frac{N_4}{N_4 + \xi N_3^+} = \varepsilon_-, \quad (6.20)$$

$$\frac{N_4}{N_4 + \xi N_3^- / 2} = \varepsilon_+, \quad (6.21)$$

where we defined  $\xi = \varepsilon_{\text{other}}^{(4)} / \varepsilon_{\text{other}}^{(3)}$ . As described later, we do not apply different selection criteria separately for the three and four track events, therefore, we can decompose the factor of the other efficiencies into contribution of the trigger and common selection criteria as  $\varepsilon_{\text{other}}^{(i)} = \varepsilon_{\text{trg}}^{(i)} \varepsilon_{\text{com}}^{(i)}$  ( $i = 3, 4$ ). The correction factor of the trigger can be obtained in the same way as explained in Sec. 6.1. In this extraction, we use an average value of  $\varepsilon_{\text{other}}^{(3)}$  and  $\varepsilon_{\text{trg}}^{(4)}$  according to the observed events.

In order to extract kinematic dependence on the reconstruction efficiency correction, we modify Eq. (6.20) as:

$$\frac{\Delta N_4(P^{\text{LAB}}, \cos\theta^{\text{LAB}})}{N_4 + \xi N_3^+} = \frac{N_{\text{prod}}(P^{\text{LAB}}, \cos\theta^{\text{LAB}}) \varepsilon_-(P^{\text{LAB}}, \cos\theta^{\text{LAB}})}{N_{\text{prod}}^{\text{tot}}}, \quad (6.22)$$

where  $\Delta N_4(P^{\text{LAB}}, \cos\theta^{\text{LAB}})$  represents number of entry inside a certain bin tabulated based on the momentum and angle of the negative pion candidate. The factor of  $N_{\text{prod}}(P^{\text{LAB}}, \cos\theta^{\text{LAB}}) / N_{\text{prod}}^{\text{tot}}$  in

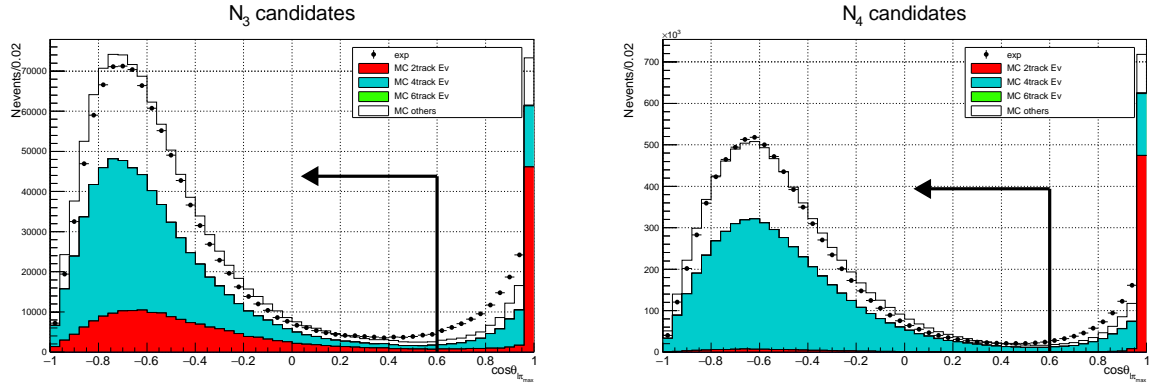


Figure 6.8: Distribution of a cosine of angle between lepton and pion candidates. Red, water blue and green histograms, respectively represent two, four and six track events, where these numbers mean those of produced ones. White histogram represents other contributions like  $\tau \rightarrow nh \geq K_S$ ,  $\tau \rightarrow \pi\pi\pi\pi^0$  ( $n \geq 1$ ) and two photon process. The cosine is defined as maximum value among the combinations of  $(\ell^-, \pi_1^+)$  and  $(\ell^-, \pi_2^+)$  (vice versa for an opposite charge configuration).

the right hand side of Eq. (6.22) represents the fraction of the produced events which have specific momentum and cosine of the polar angle.

Since the factor of  $\varepsilon_{\text{com}}$  does not appear in Eq. (6.22) as long as same selection criteria are applied for three and four track events, the obtained reconstruction efficiency is stable for the common selection and we can utilize this nature to enhance purity. In particular, to suppress gamma conversion process  $\gamma \rightarrow ee$ , we apply a loose selection criteria in the angle between the lepton candidate and other positively-charged track events. Furthermore, we discard events if either of the two positive pion candidates has a large lepton identification probability, *i.e.*, we reject if  $\mathcal{P}_e > 0.15$  or  $\mathcal{P}_\mu > 0.15$ . The situation of the selection is shown in Figs. 6.8 and 6.9. The obtained purity is summarized in Table 6.3.

Whole story also holds for reversal charge configuration  $(\ell^+, \pi^- \pi^+ \pi^-)$  once the sign of  $N_3$  is swapped. Moreover, in principle, these formulae hold for other four-track decay processes like  $(\ell^-, \pi^+ \pi^- \pi^+ \pi^0)$  and  $(\ell^-, \pi^+ \pi^- \pi^+ \pi^0 \pi^0)$  only if we do not apply any selection criteria for other photons. However, we decided to regard them as backgrounds. To reduce these decays, we apply the extra gamma energy cut  $E_{\text{extray}}^{\text{ECL}} < 0.5$  GeV as shown in Fig. 6.10.

The reconstruction efficiency correction  $R_{\text{rec}}$  is obtained by calculating the ratio of Eq. (6.22) between the experiment and MC simulation as:

$$R_{\text{rec}} = \frac{\left[ \frac{\Delta N_4}{N_4 + \xi N_3} \right]^{\text{EX}}}{\left[ \frac{\Delta N_4}{N_4 + \xi N_3} \right]^{\text{MC}}}, \quad (6.23)$$

where the first factor of the right hand side of Eq. (6.22) is assumed to be canceled. For MC events, we use only four-track events ( $(\ell^-, \pi\pi\pi\pi^0)$   $n \geq 1$  decays are excluded) to obtain table of  $\Delta N_4(P^{\text{LAB}}, \cos\theta^{\text{LAB}})$  while that of experiment is calculated based on the observed number of entries and the expected amount of the contamination evaluated by MC: the expected number of background events for the experiment is evaluated bin-by-bin using a sideband region defined by  $E_{\text{extray}}^{\text{ECL}} > 0.5$  GeV. The signal contamination for the sideband region is estimated to be  $\sim 34\%$  for both  $N_3$  and  $N_4$  events.

Figure 6.11 shows obtained reconstruction efficiency correction  $R_{\text{rec}}$  as a function of momentum of charged track  $P_{\text{ch}}$  and cosine of zenith angle  $\cos\theta_{\text{ch}}$ . The average values of the reconstruction and trigger efficiencies are summarized in Table 6.5.

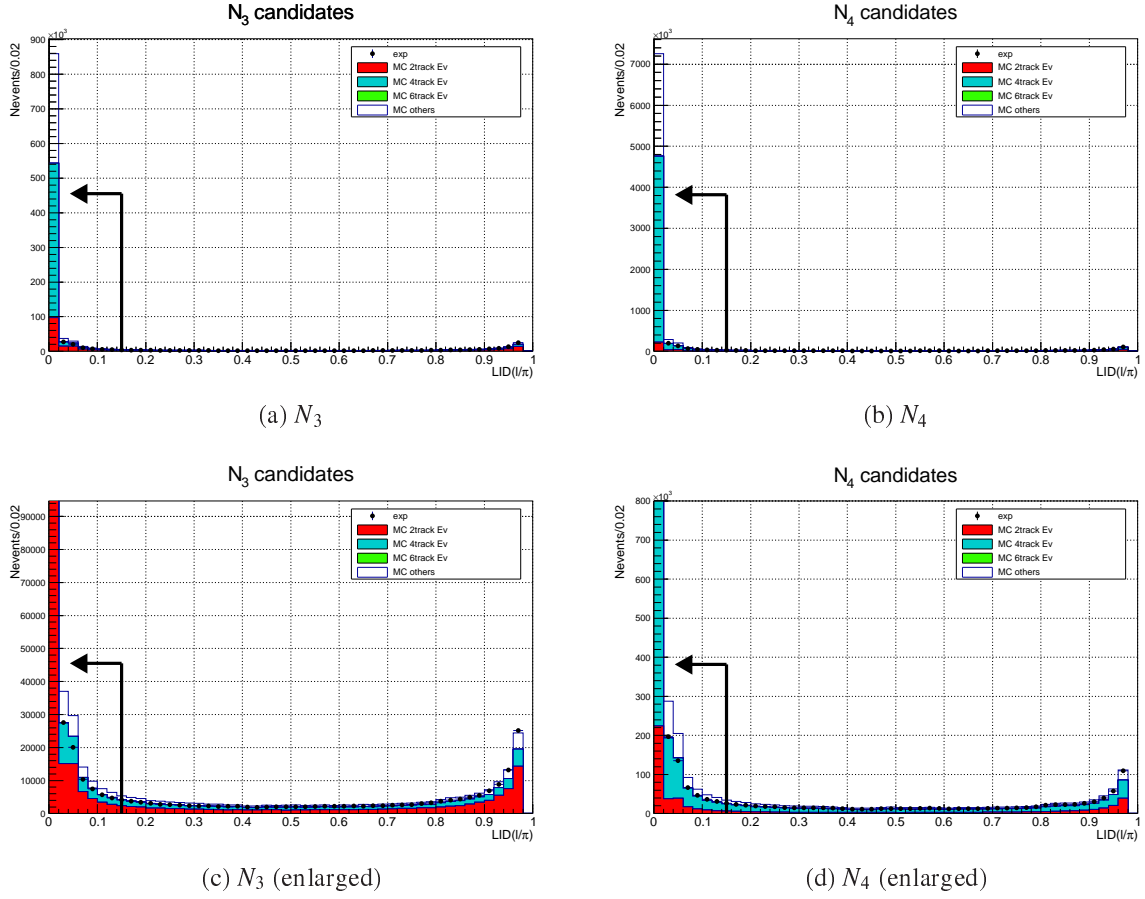


Figure 6.9: Distribution of likelihood ratio value  $\mathcal{P}_\ell$ . Meanings of colors are same as Fig 6.8. The  $\mathcal{P}_\ell$  is defined as the maximum value of  $\mathcal{P}_e$  or  $\mathcal{P}_\mu$  for the two positively-charged pion candidates.

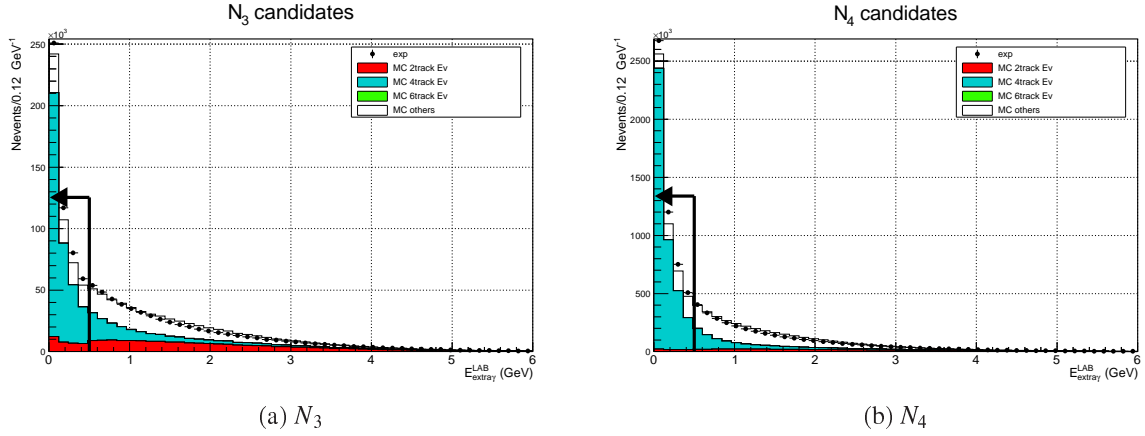


Figure 6.10: Distribution of extra gamma energy  $E_{\text{extray}}^{\text{ECL}}$ . Meanings of colors are same as Fig 6.8.

Table 6.3: Information of selected events

$N_{\text{rec}}$	$N_{\text{prod}}^{2\text{track}}$ (%)	$N_{\text{prod}}^{4\text{track}}(\text{ex. } K_S)$ (%)	$N_{\text{other}}$ (%)
3	6	74	19
4	< 1	86	13

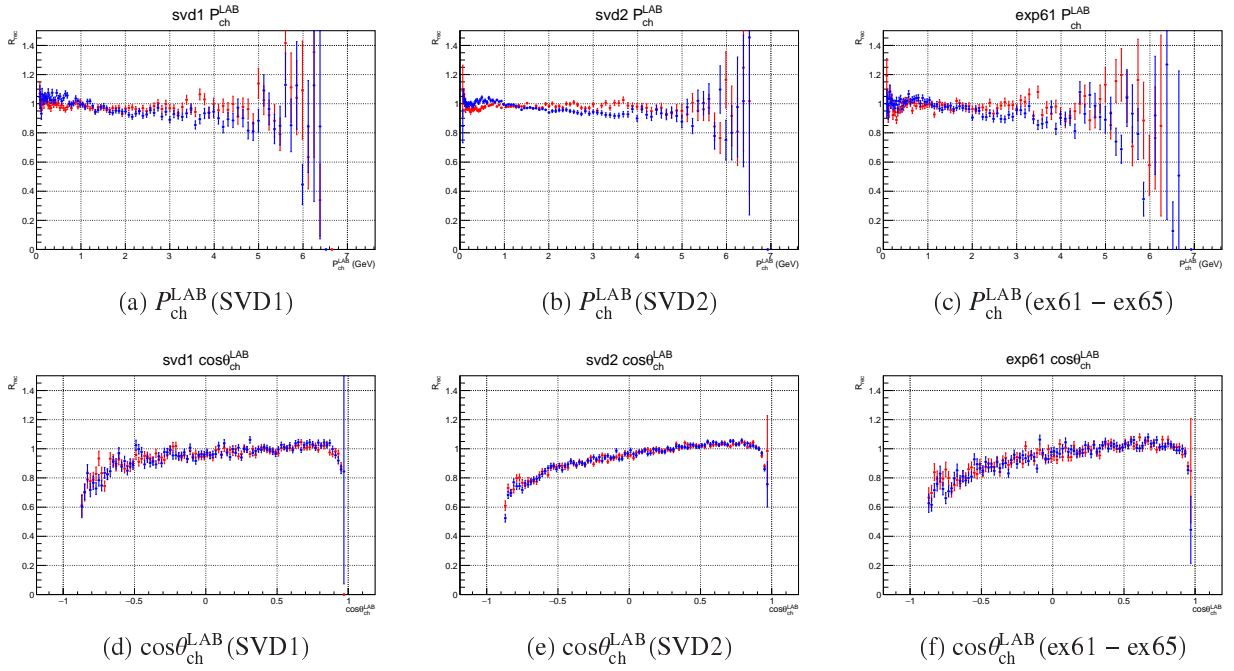


Figure 6.11: Track reconstruction efficiency correction  $R_{\text{rec}}$  as a function of momentum and direction of positively (red) and negatively (blue) charged particles: (a)(b)(c) momentum dependence on  $R_{\text{rec}}$  for the run identification number 7 to 27, 31 to 55 and 61 to 65; (d)(e)(f) angle dependence for same experimental configurations.

Table 6.4: Average reconstruction and trigger efficiencies

Run ID	$\varepsilon_+$ (%)	$\varepsilon_-$ (%)	$\varepsilon_{\text{trg.}}^{(3)}$ (%)	$\varepsilon_{\text{trg.}}^{(4)}$ (%)	$\xi$
<b>Experiment</b>					
7 to 27	91.0	91.0	90.7	97.6	1.076
31 to 55	90.4	90.8	71.1	83.3	1.172
61 to 65	91.1	91.0	69.4	82.3	1.185
<b>MC</b>					
7 to 27	92.4	92.5	94.2	98.7	1.049
31 to 55	92.7	92.7	85.9	94.2	1.097
61 to 65	92.8	93.0	91.1	97.3	1.067

Table 6.5: Information of tabulations

Tables	Argument	# bin	Determination of the indices
Trigger	$R(P_i^{LAB}, \cos \theta_\ell^{LAB}) \cdot \frac{R(P_\ell^{LAB}, \omega_h)}{R(P_\ell^{LAB})}$	$([i, 10], [j, 10]) \cdot \frac{([i, 10], [k, 10])}{[i, 10]}$	$i : P_i$ is uniformly divided into ten bins between $[0, 5]$ GeV/ $c$ $j : \cos \theta_\ell^{LAB}$ is uniformly divided into ten bins between $[-1, 1]$ $k : \omega_h$ is uniformly divided into ten bins between $[-1, 1]$
$\pi$ ID	$R(P_\pi^{LAB}, \cos \theta_\pi^{LAB})$	$([i, 32], [j, 12])$	Divisions (unit is in GeV/ $c$ ) $i : [0, 0.5], [0.5, 0.6], \dots, [2.9, 3.0], [3.0, 3.2], \dots, [3.4, 3.6], [3.6, 4.0], [4.0, 4.5], [4.5, \infty]$ . Divisions $j : [-1, -0.612, -0.511, -0.300, -0.152, 0.017, 0.209, 0.355, 0.435, 0.542, 0.692, 0.842, 1]$
$e$ ID	$R(P_e^{LAB}, \theta_e^{LAB})$	$([i, 10], [j, 7])$	$i : P_e$ is uniformly divided into ten bins between $[0, 5]$ GeV/ $c$ Divisions (unit is in degree) $j : [18, 25, 35, 40, 60, 125, 132, 151]$
$\mu$ ID	$R(P_\mu^{LAB}, \theta_\mu^{LAB})$	$([i, 10], [j, 7])$	$i : P_\mu$ is uniformly divided into ten bins between $[0, 5]$ GeV/ $c$ Divisions (unit is in degree) $j : [17, 25, 37, 51, 117, 130, 145, 150]$
$\pi^0$ reconstruction	$R(P_{\pi^0}, \cos \theta_{\pi^0})$	$([i, 10], [j, 10])$	$i : P_{\pi^0}$ is uniformly divided into ten bins between $[0, 5]$ GeV/ $c$ $j : \cos \theta_{\pi^0}$ is uniformly divided into ten bins between $[-1, 1]$
$\gamma$ reconstruction	$R(P_\gamma, \cos \theta_\gamma)$	$([i, 10], [j, 10])$	$i : P_\gamma$ is uniformly divided into ten bins between $[0, 25]$ (GeV/ $c$ ) <sup>2</sup> $j : \cos \theta_\gamma$ is uniformly divided into ten bins between $[-1, 1]$
Charged track reconstruction	$R(P^{LAB}, \cos \theta^{LAB})$	$([i, 10], [j, 10])$	$i : P^{LAB}$ is uniformly divided into ten bins between $[0, 7]$ GeV/ $c$ $j : \cos \theta^{LAB}$ is uniformly divided into ten bins between $[-1, 1]$

## 6.4 Binning of correction factors

In this section, we summarize the method of binning. In table 6.5, information of the bins used for the correction factors are listed. The notation  $[i, 10]$  in the column “# bin” represents that the index  $i$  is divided into 10 bins.

The bins of angular variables in the pion and lepton identifications are determined by taking into account the detector geometries. The  $\cos \theta_\pi$  division is based on the ACC crystal location while  $\theta_e$  and  $\theta_\mu$  are divided according to the separation of the ECL and KLM regions, respectively.

The tables of  $\pi^0$  and  $\gamma$  reconstruction efficiency corrections on angular variables are divided uniformly not in the laboratory frame but in the CMS frame because this makes the distribution broad. For  $\gamma$  case, considering the dense convergence in the low-momentum region, we specify the index of bin by  $i = [N_{\text{bin}} \sqrt{P_\gamma/P_{\text{max}}}]$  so that the division of lower-momentum bins becomes small, where the bracket  $[ ]$  is the Gauss’s ceiling function and  $[x]$  indicates a maximum integer which does not exceed  $x$ .

The number of bins is determined in such a way as to make the entries of bins have reasonable amounts (approximately a few percent in its statistical uncertainty).

Note that the plots presented before are obtained using different divisions from those of real analysis and of being summarized here. We divided the phase space with larger number of cells for drawing one-dimension plots because the dependence of efficiency correction becomes clearer.

## 6.5 Confirmation of the correction $R$

In the presence of  $R$ , the selected PDF of events is modified as

$$P^{\text{total}}(\mathbf{x}) = (1 - \sum_i \lambda_i) \frac{\varepsilon(\mathbf{x})S(\mathbf{x})}{\int d\mathbf{x} \varepsilon(\mathbf{x})S(\mathbf{x})} + \sum_i \lambda_i \frac{\varepsilon(\mathbf{x})B_i(\mathbf{x})}{\int d\mathbf{x} \varepsilon(\mathbf{x})B_i(\mathbf{x})}, \quad (6.24)$$

$\Downarrow$

$$P^{\text{total}}(\mathbf{x}) = (1 - \sum_i \lambda_i) \frac{\varepsilon(\mathbf{x})R(\mathbf{x})S(\mathbf{x})}{\int d\mathbf{x} \varepsilon(\mathbf{x})R(\mathbf{x})S(\mathbf{x})} + \sum_i \lambda_i \frac{\varepsilon(\mathbf{x})R(\mathbf{x})B_i(\mathbf{x})}{\int d\mathbf{x} \varepsilon(\mathbf{x})R(\mathbf{x})B_i(\mathbf{x})}. \quad (6.25)$$

As a result, we are able to check the effect of  $R$  by directly applying it as a weight for the selected PDF. Since the denominator of Eq. (6.25) is simply a certain number, we can neglect the dependence of  $R$  by normalizing the MC distribution based on the area of the histograms. Furthermore, it is worth to note that the fit result does not depend on the absolute magnitude of  $R$  because additional factor  $c$  for  $R \rightarrow cR$  disappears when we formulate log-likelihood function. Thus it is justified to verify  $R$  by simply seeing its *shape* without taking care of the absolute height of histograms. From Figs. 6.12 to 6.15, we show the original and corrected histograms of the momenta and directions for lepton, photon, neutral pion and charged pion in the laboratory frame, which totally form twelve-dimension observables. With this correction, we can see improvements in the shape. In particular, reasonable agreement in the angle distribution of lepton in the backward region  $\cos \theta_\ell < -0.6$  is observed. The notable disagreement in the forward direction of  $\cos \theta_\mu > 0.8 - 0.9$  comes from an inaccurate extraction of correction factor of  $\mu$ ID efficiency. This effects are separately evaluated by excluding this region (see Sec. 7.2.4).



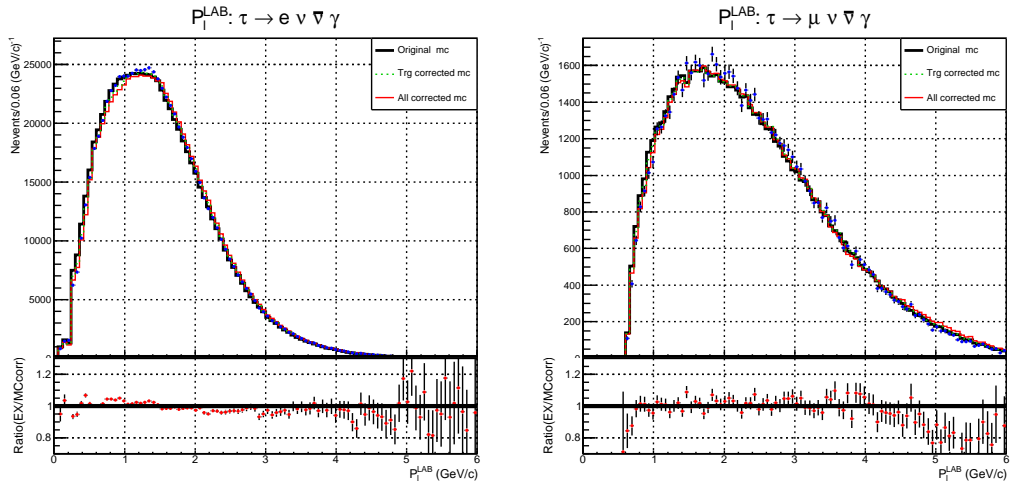
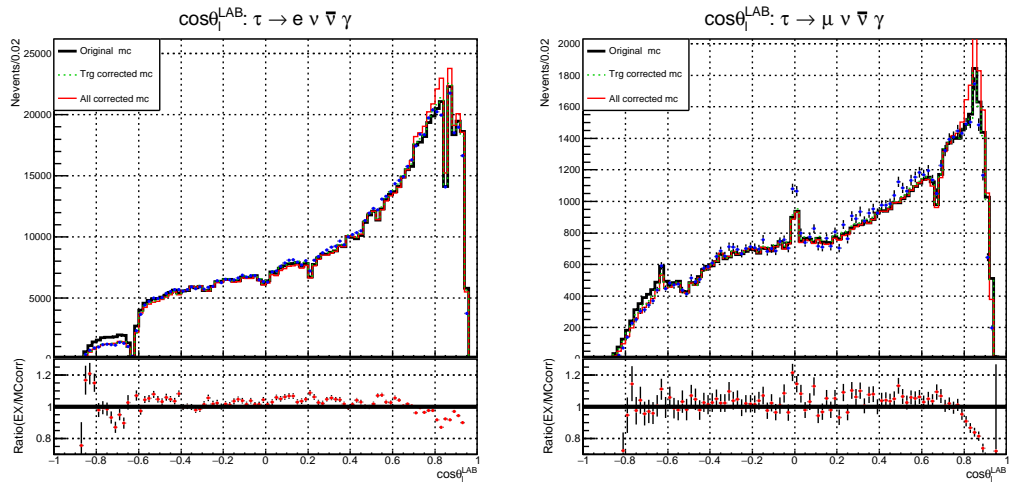
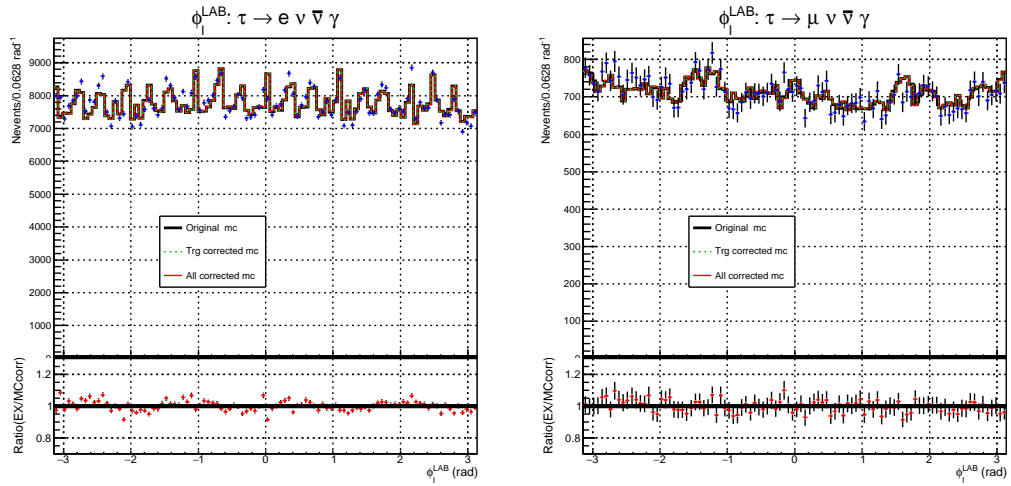
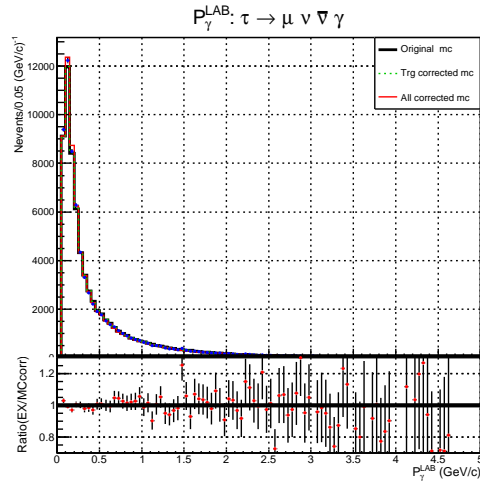
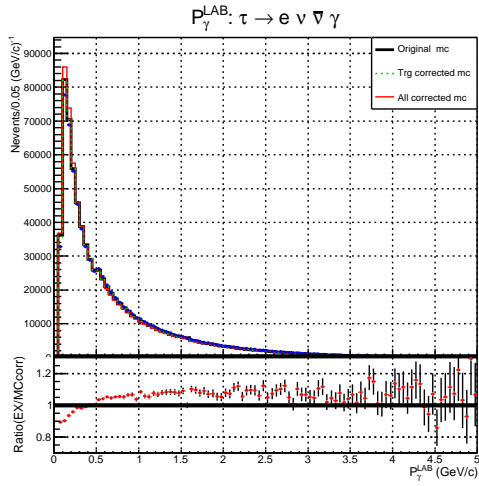
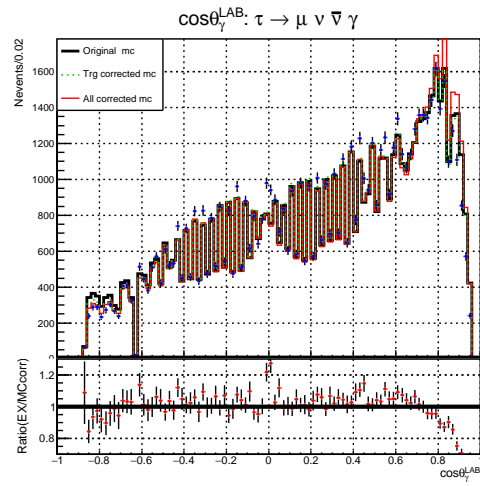
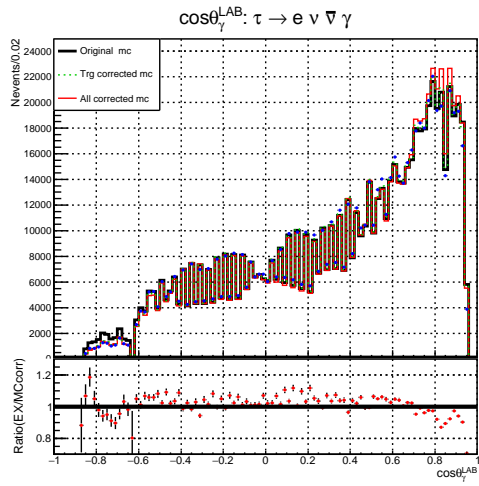
(a)  $P_\ell$ (b)  $\cos\theta_\ell$ (c)  $\phi_\ell$ 

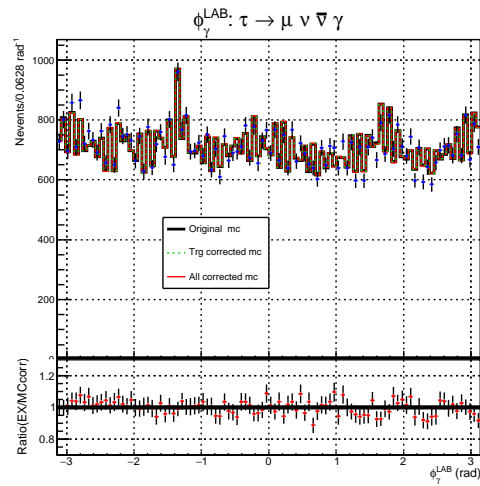
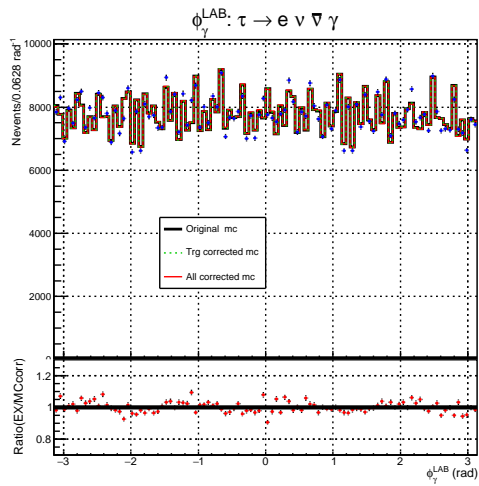
Figure 6.12: Distribution of lepton variables for  $\tau^- \rightarrow e^- \bar{\nu} \gamma$  (left) and  $\tau^- \rightarrow \mu^- \bar{\nu} \gamma$  (right): (a)  $P_\ell$ , (b)  $\cos\theta_\ell$  and (c)  $\phi_\ell$ . Solid black and red lines represent original and corrected MC histograms. Dashed green line represents corrected MC histogram based only on the trigger correction  $R_{\text{trg}}$ . Points with errors means experiment. In the bottom, the ratio of experimental number out of corrected histogram is shown.



(a)  $P_\gamma$

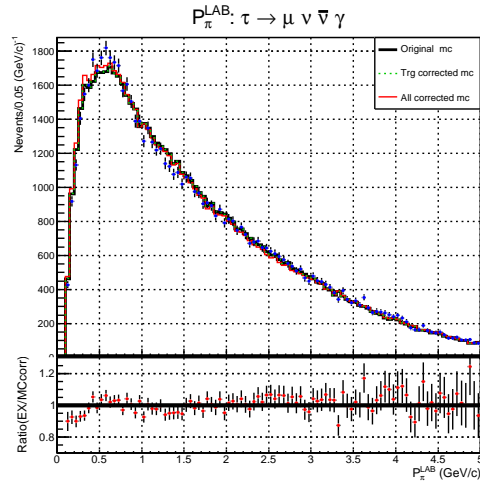
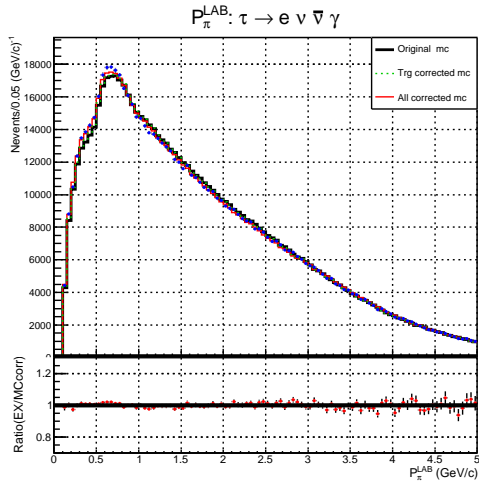


(b)  $\cos\theta_\gamma$

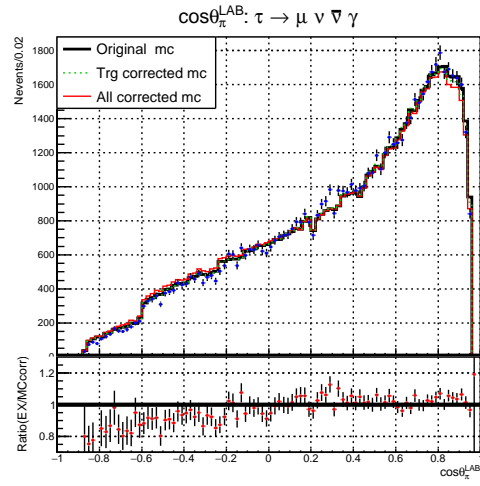
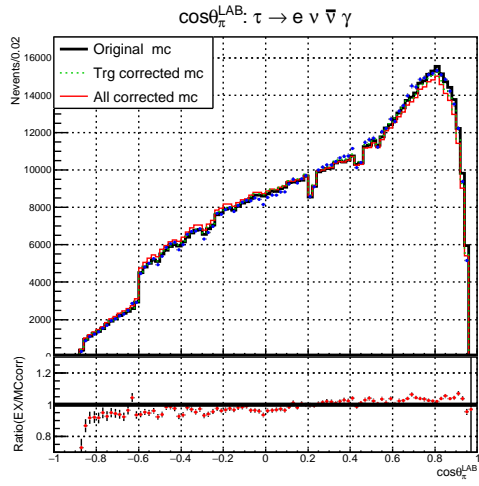


(c)  $\phi_\gamma$

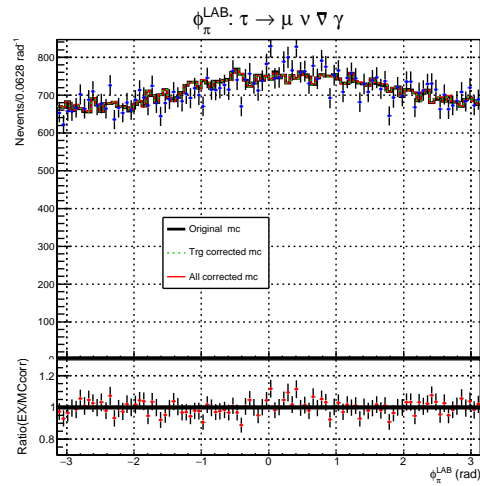
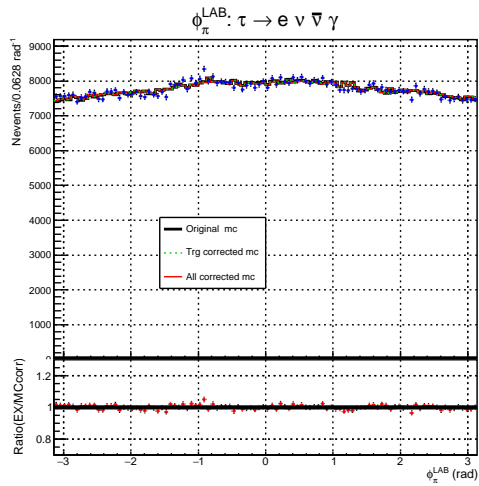
Figure 6.13: Distribution of photon variables for  $\tau^- \rightarrow e^- \bar{\nu} \gamma$  (left) and  $\tau^- \rightarrow \mu^- \bar{\nu} \gamma$  (right): (a)  $P_\gamma$ , (b)  $\cos\theta_\gamma$  and (c)  $\phi_\gamma$ . The meanings of each color of line are same as Fig. 6.12.



(a)  $P_\pi$

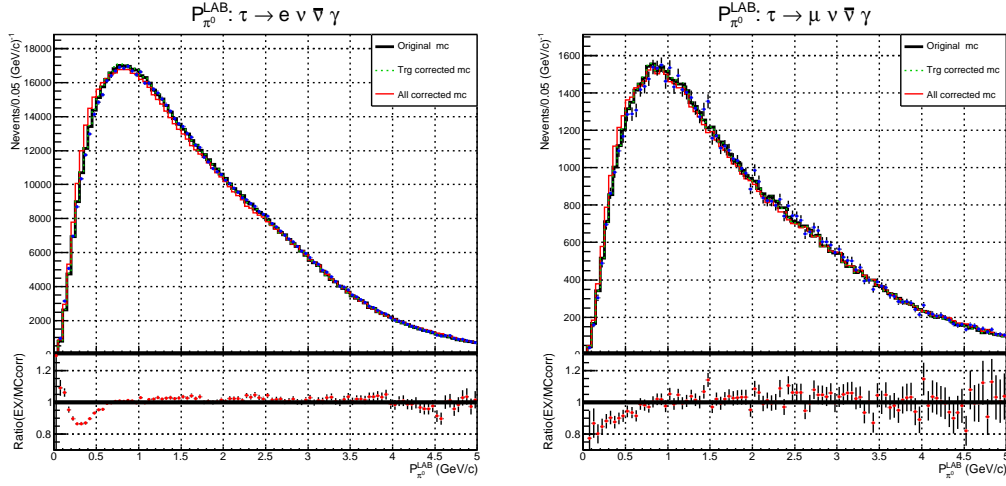


(b)  $\cos\theta_\pi$

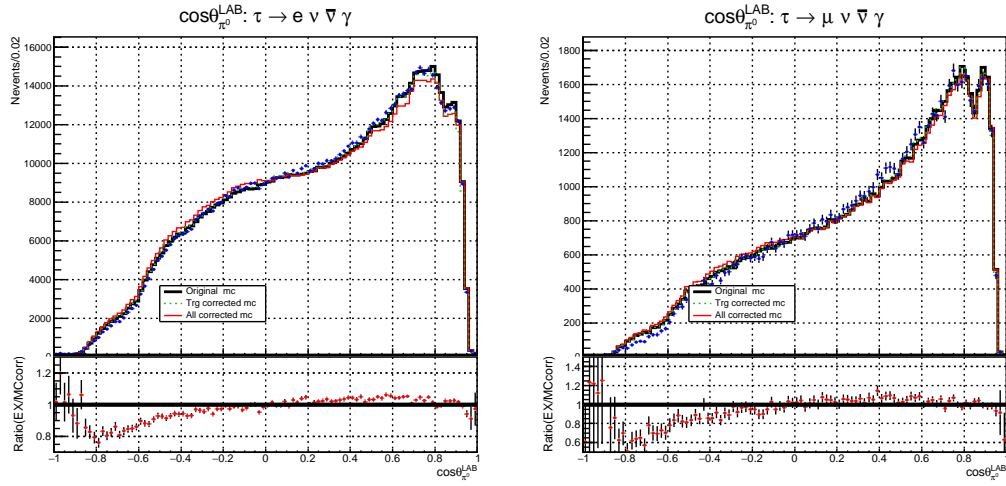


(c)  $\phi_\pi$

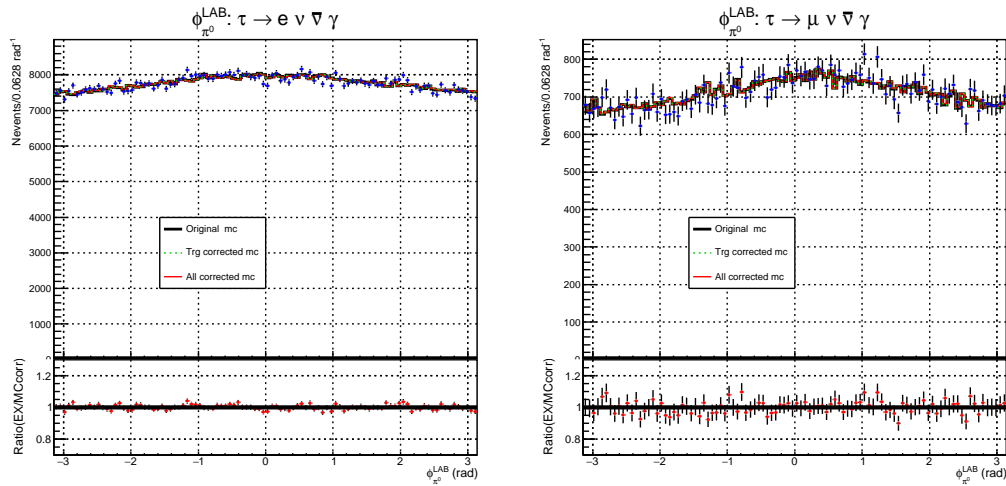
Figure 6.14: Distribution of the charged pion observables for  $\tau^- \rightarrow e^- \nu \bar{\nu} \gamma$  (left) and  $\tau^- \rightarrow \mu^- \nu \bar{\nu} \gamma$  (right): (a)  $P_\pi$ , (b)  $\cos\theta_\pi$  and (c)  $\phi_\pi$ . The meanings of each color of line are same as Fig. 6.12.



(a)  $P_{\pi^0}$



(b)  $\cos\theta_{\pi^0}$



(c)  $\phi_{\pi^0}$

Figure 6.15: Distribution of the neutral pion variables for  $\tau^- \rightarrow e^- \nu \bar{\nu} \gamma$  (left) and  $\tau^- \rightarrow \mu^- \nu \bar{\nu} \gamma$  (right): (a)  $P_{\pi^0}$ , (b)  $\cos\theta_{\pi^0}$  and (c)  $\phi_{\pi^0}$ . The meanings of each color of line are same as Fig. 6.12.

# Chapter 7

## Evaluation of uncertainties

### 7.1 Statistical uncertainties

The statistical errors of fitted Michel parameters are obtained from information of the change of likelihood function. The PDF of fitted parameters is assumed to be Gaussian  $P \propto \exp\{-\frac{(\theta-\theta_0)^2}{2\sigma_\theta^2}\}$  for  $\theta = \bar{\eta}$  or  $\xi\kappa$ , hence the errors  $\sigma_\theta$  are evaluated as magnitude of residual such that negative logarithmic likelihood function  $\mathcal{L} = -\log P = \frac{(\theta-\theta_0)^2}{2\sigma_\theta^2}$  moves by 1/2. The errors are evaluated to be  $\bar{\eta}^e = 5.0$ ,  $\bar{\eta}^\mu = 1.5$ ,  $(\xi\kappa)^e = 0.8$  and  $(\xi\kappa)^\mu = 0.5$ .

### 7.2 Systematic errors

In Table 7.1, we summarize contributions of systematic sources. The detail of each item is explained in following subsections.

#### 7.2.1 Systematic uncertainty from branching ratios

In this analysis, the fractions of multiple background modes are evaluated using generic MC sample, where input of the branching ratios are taken from previous measurements. The systematic uncertainties due to the finite accuracy of these measurements are estimated based on the world average values summarized by the particle data group (PDG) (Ref. [7]). The obtained fractions of  $\lambda_i$  ( $i$  is an index of background modes) are separately varied  $\lambda_i \rightarrow \lambda_i(1 + \Delta\mathcal{B}_i/\mathcal{B}_i)$  and variations fitted Michel parameters are assigned as corresponding errors, where  $\mathcal{B}_i$  means the branching ratio. In Table 7.2, we summarize the systematic contributions from the input of branching ratio.

#### 7.2.2 Uncertainty from the relative normalization

As explained in Sec. 5.4.1, the relative normalization of PDF is evaluated by using generated MC events. Since the normalized PDF of signal is

$$P^{\text{sig}}(\mathbf{x}) = \frac{\mathcal{E}_0 + \mathcal{E}_1 \cdot \bar{\eta}_{\text{SM}} + \mathcal{E}_2 \cdot \eta''_{\text{SM}} + \mathcal{E}_3 \cdot \xi\kappa_{\text{SM}}}{\int d\mathbf{x} \mathcal{E}_0 + \mathcal{E}_1 \cdot \bar{\eta}_{\text{SM}} + \mathcal{E}_2 \cdot \eta''_{\text{SM}} + \mathcal{E}_3 \cdot \xi\kappa_{\text{SM}}} = \frac{\mathcal{E}_0}{\int d\mathbf{x} \mathcal{E}_0} = \frac{\mathcal{E}_0}{\sigma_{\text{sig}}}, \quad (7.1)$$

Table 7.1: List of systematic contributions

Item	$\sigma_{\bar{\eta}}^e$	$\sigma_{\xi\kappa}^e$	$\sigma_{\bar{\eta}}^\mu$	$\sigma_{\xi\kappa}^\mu$	explained in
Input of branching ratio	3.8	0.05	0.25	0.01	7.2.1
Relative normalizations	3.8	0.69	0.13	0.04	7.2.2
Absolute normalizations	1.0	0.01	0.03	0.001	7.2.3
Exp/MC corrections	1.9	0.14	0.09	0.10	7.2.4
Formulation of PDFs	2.5	0.24	0.67	0.22	7.2.5
Effect of cluster overlap in ECL	2.2	0.46	0.02	0.06	7.2.6
Detector resolution	0.74	0.20	0.22	0.02	7.2.7
$E_\gamma$ cut	0.91	0.22	-	-	7.2.9
Beam energy spread	negligible	negligible	negligible	negligible	7.2.8
total	6.8	0.93	0.77	0.25	

Table 7.2: Systematic contributions from input of branching ratio

item	$\sigma_{\bar{\eta}}^e$	$\sigma_{\xi\kappa}^e$	$\sigma_{\bar{\eta}}^\mu$	$\sigma_{\xi\kappa}^\mu$
$(e\gamma, \pi\pi^0)$	3.7	0.04	-	-
$(e, \pi\pi^0) + \gamma_{\text{brems.}}$	0.6	0.01	-	-
$(e\gamma, \pi\pi^0) + \gamma_{\text{brems.}}$	0.6	0.02	-	-
$(\mu\gamma, \pi\pi^0)$	-	-	0.23	0.005
$(\mu, \pi\pi^0) + \gamma_{\text{beamBG}}$	-	-	0.04	0.001
$(\mu, \pi\pi^0) + \gamma_{\text{ISR}}$	-	-	0.03	negligible
$(\mu\gamma, \pi\pi^0\pi^0)$	-	-	0.04	0.005
$(\pi\pi^0, \pi\pi^0)$	-	-	0.07	negligible
$(\pi\pi^0\pi^0, \pi\pi^0)$	-	-	0.07	negligible
total	3.8	0.05	0.25	0.007

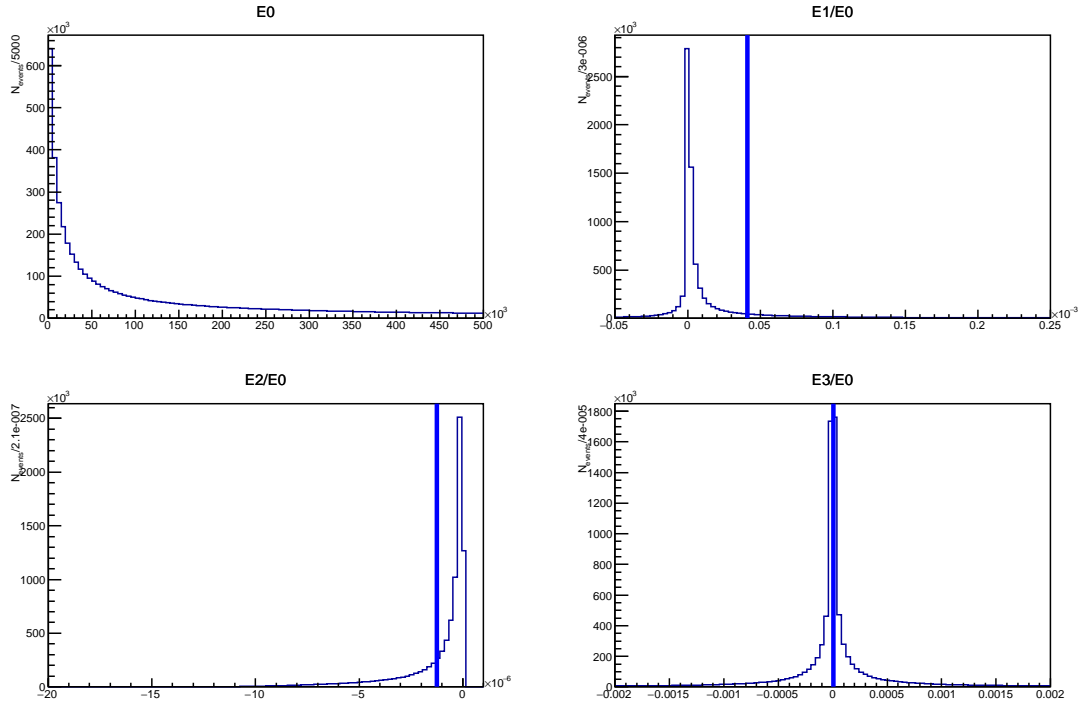


Figure 7.1: Histograms of coefficients of  $\mathcal{E}_0$ ,  $\mathcal{E}_1/\mathcal{E}_0$ ,  $\mathcal{E}_2/\mathcal{E}_0$ ,  $\mathcal{E}_3/\mathcal{E}_0$  for  $\tau \rightarrow e\nu\bar{\nu}\gamma$  events. Blue line represents an average. The calculated relative normalization coefficients are as follows:  $\mathcal{E}_1/\mathcal{E}_0 = (3.84 \pm 0.01) \times 10^{-5}$ ,  $\mathcal{E}_2/\mathcal{E}_0 = (-1.2588 \pm 0.0005) \times 10^{-6}$ ,  $\mathcal{E}_3/\mathcal{E}_0 = (6.8 \pm 0.7) \times 10^{-6}$ .

then, the normalization of signal PDF becomes

$$\int d\mathbf{x} \varepsilon(\mathbf{x}) \mathcal{E}_i(\mathbf{x}) = \int d\mathbf{x} P^{\text{sig}}(\mathbf{x}) \varepsilon(\mathbf{x}) \frac{\mathcal{E}_i(\mathbf{x})}{P^{\text{sig}}(\mathbf{x})} = \sigma_{\text{sig}} \int d\mathbf{x} \varepsilon(\mathbf{x}) P^{\text{sig}}(\mathbf{x}) \frac{\mathcal{E}_i}{\mathcal{E}_0} \quad (7.2)$$

$$= \frac{\sigma_{\text{sig}} \bar{\mathcal{E}}_{\text{sig}}}{N_{\text{sel}}} \sum_{\mathbf{x}^i \in \mathcal{E} P^{\text{sig}}} \frac{\mathcal{E}_i(\mathbf{x}^i)}{\mathcal{E}_0(\mathbf{x}^i)} \equiv \frac{\sigma_{\text{sig}} \bar{\mathcal{E}}_{\text{sig}}}{N_{\text{sel}}} \left\langle \frac{\mathcal{E}_i(\mathbf{x})}{\mathcal{E}_0(\mathbf{x})} \right\rangle. \quad (7.3)$$

The average of ratio  $\mathcal{E}_i(\mathbf{x})/\mathcal{E}_0(\mathbf{x})$  for selected events according to the PDF of signal is considered as a relative normalization. Figure 7.1 and Fig. 7.2 show the distributions of  $\mathcal{E}_0(\mathbf{x})$  and  $\mathcal{E}_i(\mathbf{x})/\mathcal{E}_0(\mathbf{x})$  for  $\tau^+\tau^- \rightarrow (\pi^+\pi^0\bar{\nu})(e^-\nu\bar{\nu}\gamma)$  and  $\tau^+\tau^- \rightarrow (\pi^+\pi^0\bar{\nu})(\mu^-\nu\bar{\nu}\gamma)$  events, respectively. To obtain these histograms, 17 M and 12 M selected events are used for electron and muon modes, respectively. Using central limit theorem, we evaluate the statistical uncertainties of  $\langle \mathcal{E}_i(\mathbf{x})/\mathcal{E}_0(\mathbf{x}) \rangle$  by the root mean square of  $\mathcal{E}_i(\mathbf{x})/\mathcal{E}_0(\mathbf{x})$  divided by  $\sqrt{N_{\text{MC}}}$ , where  $N_{\text{MC}}$  is the number of used events mentioned above.

The impact of the uncertainties of the normalization on the fitted Michel parameters is estimated by artificially shifting the center values and evaluating the movement of fitted Michel parameters. The effect of the uncertainties are listed in Table 7.3. This relative normalization is one of the major sources of uncertainties for the electron mode. This comes from the fact that the PDF of  $\tau^- \rightarrow \ell^- \nu \bar{\nu} \gamma$  decay has a strong peculiarity in  $m_\ell \rightarrow 0$  and makes the convergence of  $1/N_{\text{MC}} \sum_i \mathcal{E}_i(\mathbf{x})/\mathcal{E}_0(\mathbf{x})$  slow. However, a simulation of large amount of signal event is very time-consuming and we decided to use the mentioned numbers.\*

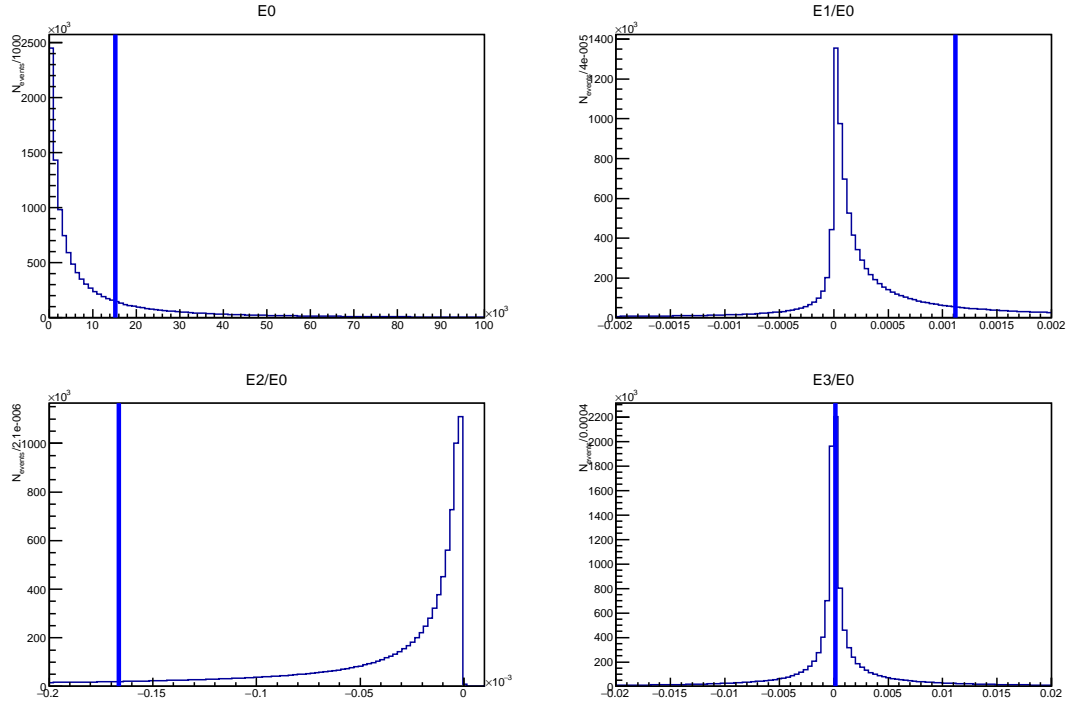


Figure 7.2: Histograms of coefficients of  $\mathcal{E}_0$ ,  $\mathcal{E}_1/\mathcal{E}_0$ ,  $\mathcal{E}_2/\mathcal{E}_0$ ,  $\mathcal{E}_3/\mathcal{E}_0$  for  $\tau \rightarrow \mu\nu\bar{\nu}\gamma$  events. Blue line represents an average. The calculated relative normalization coefficients are as follows:  $\mathcal{E}_1/\mathcal{E}_0 = (1.112 \pm 0.0013) \times 10^{-3}$ ,  $\mathcal{E}_2/\mathcal{E}_0 = (-1.665 \pm 0.001) \times 10^{-4}$ ,  $\mathcal{E}_3/\mathcal{E}_0 = (1.40 \pm 0.04) \times 10^{-4}$ .

Table 7.3: Systematic errors from relative normalization

source of error	$\sigma_{\tilde{\eta}}^e$	$\sigma_{\xi_K}^e$	$\sigma_{\tilde{\eta}}^\mu$	$\sigma_{\xi_K}^\mu$
$\mathcal{E}_1/\mathcal{E}_0$	3.8	0.05	0.12	0.014
$\mathcal{E}_2/\mathcal{E}_0^\dagger$	-	-	-	-
$\mathcal{E}_3/\mathcal{E}_0$	0.12	0.69	0.01	0.04
total	3.8	0.69	0.13	0.04

$\dagger$  In this analysis,  $\eta''$  is always set to be the SM value  $\eta'' = 0$ , hence the dependence on the corresponding normalization  $\mathcal{E}_2/\mathcal{E}_0$  is zero.



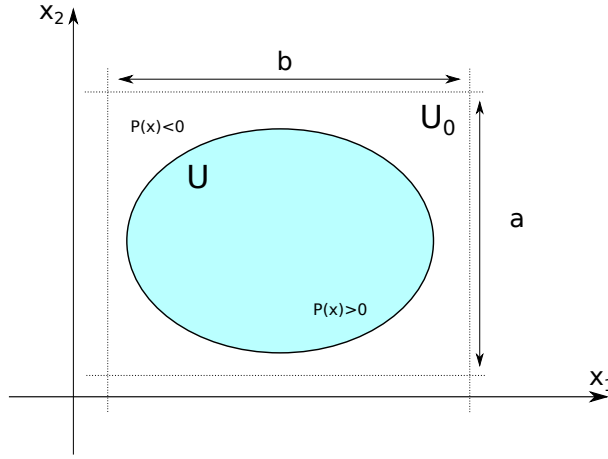


Figure 7.3: Conceptual view of the integration of PDF in 2D plane. The filled part represents the region such that PDF becomes positive. The events are uniformly generated in entire phase space which encloses the valid region. The volume of generated phase space is calculated as  $V_0 = ab$ .

### 7.2.3 Uncertainty from the absolute normalization

As described in Sec. 5.3, the absolute normalization is defined as an integration of PDF:  $\sigma = \int dx P(x)$ . This value is calculated by MC method where events are uniformly distributed in the entire phase space as:

$$\sigma = \frac{V_0}{N_{\text{gen}}} \sum_{\mathbf{x}^i \in 1/V_0} \bar{P}(\mathbf{x}^i), \quad (7.4)$$

$$\bar{P}(\mathbf{x}) = \begin{cases} P(\mathbf{x}) & \mathbf{x} \in U \\ 0 & \mathbf{x} \in U_0 - U \end{cases} \quad (7.5)$$

where  $U_0$  is the phase space and  $V_0$  is its volume,  $U$  is its subspace such that the PDF becomes positive and  $N_{\text{gen}}$  is the number of generated events. This illustrative idea in two dimension case is shown in Fig 7.3.

The uncertainties from the absolute normalizations are evaluated by the central limit theorem similarly to the case of relative normalization. Since  $\sigma$  always appears with fraction  $\lambda_i$ , this effect shifts of Michel parameters in the same way as the error from the input of the branching ratio. The contributions are listed in Table 7.4.

### 7.2.4 Uncertainties from correction factors and inefficiencies

In this analysis, we obtain correction factor of signal efficiency  $R = \varepsilon(\mathbf{x})^{\text{EX}}/\varepsilon(\mathbf{x})^{\text{MC}}$ , where this factor is written as products of corrections from the particle reconstruction efficiencies and trigger efficiency. The estimated factors have errors due to finite statistics of events and this systematic impact is estimated by varying the center values and evaluating the variation of fitted Michel parameters explained below. The errors of correction factors themselves are evaluated assuming the Poisson distribution, where the statistical uncertainty of a number of bin is calculated by its square root.

This uncertainty of correction factor affects the fitted Michel parameter through two ways. Suppose the correction factor shifts  $R \rightarrow R + \delta R$ . In the presence of systematic uncertainties  $\delta R$ , the total

---

\*In this analysis, it took approximately five weeks to fully calculate the events.

Table 7.4: Systematic errors from absolute normalization

item	$\sigma_{\bar{\eta}}^e$	$\sigma_{\xi\kappa}^e$	$\sigma_{\bar{\eta}}^\mu$	$\sigma_{\xi\kappa}^\mu$
$(e\gamma, \pi\pi^0)$	1.0	0.01	-	-
$(e, \pi\pi^0) + \gamma_{\text{brems.}}$	0.2	negligible	-	-
$(e\gamma, \pi\pi^0) + \gamma_{\text{brems.}}$	negligible	negligible	-	-
$(\mu\gamma, \pi\pi^0)$	-	-	0.007	0.0001
$(\mu, \pi\pi^0) + \gamma_{\text{beamBG}}$	-	-	0.008	0.0002
$(\mu, \pi\pi^0) + \gamma_{\text{ISR}}$	-	-	0.021	0.0001
$(\mu\gamma, \pi\pi^0\pi^0)$	-	-	0.011	0.0014
$(\pi\pi^0, \pi\pi^0)$	-	-	0.014	0.0003
$(\pi\pi^0\pi^0, \pi\pi^0)$	-	-	0.003	0.0001
total	1.0	0.01	0.03	0.0014

PDF becomes

$$P^{\text{total}}(\mathbf{x}) = (1 - \sum_i \lambda_i) \frac{\varepsilon(\mathbf{x})R(\mathbf{x})S(\mathbf{x})}{\int d\mathbf{x} \varepsilon(\mathbf{x})R(\mathbf{x})S(\mathbf{x})} + \sum_i \lambda_i \frac{\varepsilon(\mathbf{x})R(\mathbf{x})B_i(\mathbf{x})}{\int d\mathbf{x} \varepsilon(\mathbf{x})R(\mathbf{x})B_i(\mathbf{x})}, \quad (7.6)$$

$$\Downarrow$$

$$(1 - \sum_i \lambda_i) \frac{\varepsilon(\mathbf{x})[R + \delta R](\mathbf{x})S(\mathbf{x})}{\int d\mathbf{x} \varepsilon(\mathbf{x})[R + \delta R](\mathbf{x})S(\mathbf{x})} + \sum_i \lambda_i \frac{\varepsilon(\mathbf{x})[R + \delta R](\mathbf{x})B_i(\mathbf{x})}{\int d\mathbf{x} \varepsilon(\mathbf{x})[R + \delta R](\mathbf{x})B_i(\mathbf{x})}, \quad (7.7)$$

where  $S(\mathbf{x})$  and  $B_i(\mathbf{x})$  are PDFs of the signal and  $i$ -th background, whose fractions are  $(1 - \sum_i \lambda_i)$  and  $\lambda_i$ , respectively, and  $\varepsilon(\mathbf{x})$  is the efficiency of MC. As explained many times, the variation of  $\delta R$  in the numerator of Eq. (7.7) does not affect the fitted Michel parameters since overall factor disappears when we formulate likelihood function. The expression of the denominator (normalization) of signal PDF becomes

$$\int d\mathbf{x} \varepsilon(\mathbf{x})[R + \delta R](\mathbf{x})S(\mathbf{x}) = \frac{\bar{\varepsilon}_{\text{sig}}^{\text{MC}} \sigma_{\text{sig}}}{N_{\text{sel}}} \sum_{\mathbf{x} \in \varepsilon S} [R + \delta R](\mathbf{x}) \frac{\mathcal{E}_0 + \mathcal{E}_1 \bar{\eta} + \mathcal{E}_3 \xi\kappa}{\mathcal{E}_0} \quad (7.8)$$

$$= \bar{\varepsilon}_{\text{sig}}^{\text{MC}} \sigma_{\text{sig}} \left\langle [R + \delta R] \left( 1 + \frac{\mathcal{E}_1}{\mathcal{E}_0} \bar{\eta} + \frac{\mathcal{E}_3}{\mathcal{E}_0} \xi\kappa \right) \right\rangle \quad (7.9)$$

$$= \bar{\varepsilon}_{\text{sig}}^{\text{MC}} \sigma_{\text{sig}} \left[ \langle R + \delta R \rangle + \left\langle (R + \delta R) \frac{\mathcal{E}_1}{\mathcal{E}_0} \right\rangle \bar{\eta} + \left\langle (R + \delta R) \frac{\mathcal{E}_3}{\mathcal{E}_0} \right\rangle \xi\kappa \right] \quad (7.10)$$

$$= \bar{\varepsilon}_{\text{sig}}^{\text{MC}} \sigma_{\text{sig}} \langle R + \delta R \rangle \left[ 1 + \frac{\left\langle (R + \delta R) \frac{\mathcal{E}_1}{\mathcal{E}_0} \right\rangle}{\langle R + \delta R \rangle} \bar{\eta} + \frac{\left\langle (R + \delta R) \frac{\mathcal{E}_3}{\mathcal{E}_0} \right\rangle}{\langle R + \delta R \rangle} \xi\kappa \right]. \quad (7.11)$$

This is the residual of normalization explained in Chapter 6. Thus the effect of  $\delta R$  can be divided into the absolute and relative parts:

$$\delta(\text{abs}) = \langle R + \delta R \rangle - \langle R \rangle \quad (7.12)$$

$$\delta(\text{rel}) = \frac{\left\langle (R + \delta R) \frac{\mathcal{E}_i}{\mathcal{E}_0} \right\rangle}{\langle R + \delta R \rangle} - \frac{\left\langle R \frac{\mathcal{E}_i}{\mathcal{E}_0} \right\rangle}{\langle R \rangle} \quad (7.13)$$

Because the error of the absolute normalization  $\delta(\text{abs})$  is just a number which appears with fraction  $\lambda_i$ , this affects the fitted Michel parameters in the same way as the uncertainties from the input of branching ratio explained in Sec. 7.2.1.

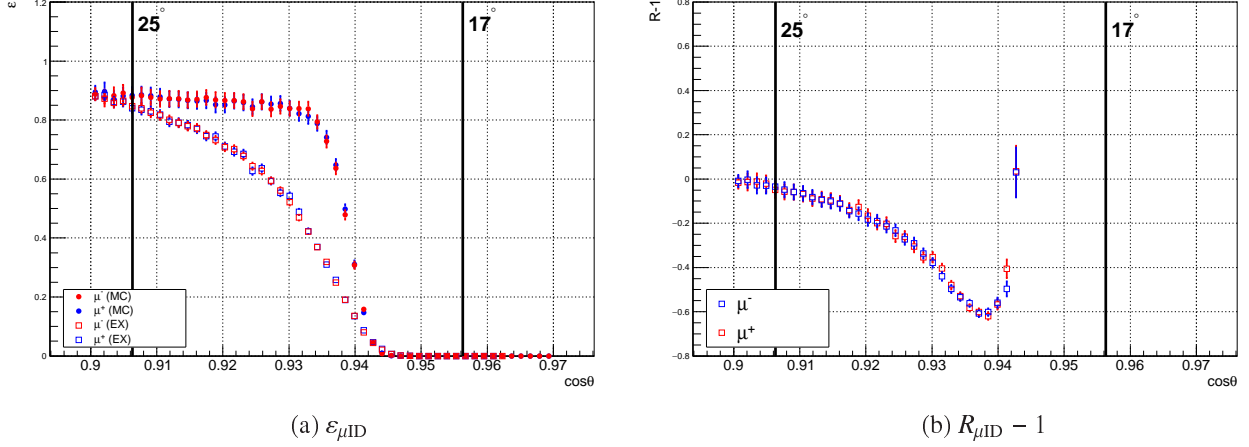


Figure 7.4: Muon identification efficiency and correction factor as a function of  $\cos\theta_{\mu}^{\text{LAB}}$  measured using  $e^+e^- \rightarrow \mu^+\mu^-$  process. Red and blue points represent positively and negatively charged muons, respectively. The black lines mean boundaries of the most forward bin  $17^\circ < \theta_{\mu}^{\text{LAB}} < 25^\circ$ .

In the case of background, the corresponding term also receives uncertainties from the absolute part, where the average  $\langle \rangle$  is calculated with respect to the background events in question.

Based on the above two categorizations—absolute and relative normalizations—we found that former contribution was negligible. The variation of the factor  $\delta(\text{abs})$  for every source of decay turns out to be less than 0.2%, hence it is sufficiently smaller than the errors from branching ratios. This comes from the fact that  $\delta(\text{abs})$  is linear in  $R$  and reduces to  $\delta(\text{abs}) = \langle \delta R \rangle$ . On the contrary, the effect of  $\delta(\text{rel})$  is notable.

While the  $R$  is defined as a correction factor of the signal efficiency (common between signal and background), the errors of the inefficiencies differently affect the fitted Michel parameters. This uncertainty of inefficiencies contributes to the fitted Michel parameters not only through the denominator of corresponding term but also from the numerator. Therefore, we simply compared the fitted results obtained with  $\varepsilon_{\text{inef.}}$  and  $\varepsilon_{\text{inef.}} + \delta\varepsilon_{\text{inef.}}$ , where  $\varepsilon_{\text{inef.}}$  is the measured inefficiency.

The measured  $\mu$ -ID efficiency value  $R_{\mu\text{ID}}$  exhibits strong decrease as the polar angle reaches very forward direction  $\theta_{\mu}^{\text{LAB}} < 25^\circ$ . Such forward muon cannot penetrate into sufficient number of the RPC/iron plates in the KLM and resulting efficiency shows a crucial dependence on the polar angle at edges. Although most of  $R_{\mu\text{ID}}$  values are consistent with  $R_{\mu\text{ID}} \sim 1$  within a few sigmas, estimated values of the forward region are typically  $R_{\mu\text{ID}} \sim 0.5$ . According to the study of  $\mu$ ID efficiency correction using  $e^+e^- \rightarrow \mu^+\mu^-$  pair production,  $R_{\mu\text{ID}}$  value rapidly decreases at  $0.910 < \cos\theta_{\mu} < 0.940$  (or equivalently  $20^\circ < \theta_{\mu} < 24^\circ$ ) as shown in Fig. 7.4. The forward part of  $\mu$ ID efficiency is tabulated using a division  $0.906 < \cos\theta_{\mu}^{\text{LAB}} < 0.956$  ( $17^\circ < \theta_{\mu}^{\text{LAB}} < 25^\circ$ ) and adoption of its average therein gives the distortion on the spectra. Alternatively, we use  $R_{\mu\text{ID}} = 1$  for the direction of  $\mu$  in  $17^\circ < \theta_{\mu}^{\text{LAB}} < 25^\circ$ , and the resulting systematic effect is estimated by excluding the events, which amounts to approximately 1.5% of total candidates. We regard the variation of the fitted Michel parameters as the corresponding uncertainty.

The evaluated contributions from correction factors and inefficiencies are summarized in Table 7.5

## 7.2.5 Uncertainty due to imperfect formulation of PDFs

As is demonstrated in Sec. 5.6.3, we validate our formulation of background PDFs by fitting the Michel parameters to the combined statistics of signal and the background mode in question. Since

Table 7.5: Systematic errors from obtained tables

Item	$\sigma_{\bar{\eta}}^e$	$\sigma_{\xi\kappa}^e$	$\sigma_{\bar{\eta}}^\mu$	$\sigma_{\xi\kappa}^\mu$
Contribution of $\delta R$ through relative normalization				
Trigger efficiency	0.5	0.10	0.04	0.03
$\ell$ ID efficiency	negligible	0.01	0.08	0.09
$\pi$ ID efficiency	negligible	negligible	negligible	negligible
$\pi^0$ ID efficiency	0.4	0.09	negligible	0.01
$\gamma$ efficiency	0.14	0.03	0.015	0.02
Contribution from inefficiency tables				
$(e\gamma, \pi\pi^0) + \gamma_{\text{brems}}$ inefficiency	1.8	0.04	-	-
$(\mu\gamma, \pi\pi^0\pi^0)$ inefficiency	-	-	0.001	negligible
$(\pi\pi^0, \pi\pi^0)$ inefficiency	-	-	0.002	0.02
$(\pi\pi^0, \pi\pi^0)$ $\mu$ mis-ID	-	-	0.001	negligible
$(3\pi, \pi\pi^0)$ inefficiency	-	-	negligible	negligible
total	1.9	0.14	0.09	0.10

signal events are generated based on the SM distributions, the deviation of fitted Michel parameters from SM prediction  $\bar{\eta} = \xi\kappa = 0$  is a systematic bias due to imperfect formulations of PDFs. We estimated the systematic bias by simply taking the residuals of the results. This effects mainly come from the simplification of high-dimension correlation performed in the description of the *others* as mentioned in Sec. 5.6.3.

## 7.2.6 Uncertainty from the simulation of overlap in the ECL clusters

The confirmation whether the MC method simulates the experimental events with sufficient accuracy or not is generally difficult especially in analyses of high-dimension phase space. Moreover, neither definition of the quantification nor its visualization is straightforward. The projected histogram onto one-dimension axis (like we describe in Sec. 6.5) reveals the validity to some extent, however, this is not necessarily sufficient because the measurement of Michel parameters is, in other words, a verification of the correlation in the high-dimension phase space.

In this analysis, we can mainly rely on the evaluation of the high-dimension correlation by MC calculation for separate tracks because two charged tracks (one for  $\ell^-$  and the other for  $\pi^+$ ) are almost back-to-back and the reconstructions of three photons (two for  $\pi^0 \rightarrow \gamma\gamma$  and the rest one for signal) is irrelevant each other. The only exception is the case when the ECL cluster of electron track is very close to that of signal photon so that both clusters have an overlap as illustrated in Fig. 7.5. To confirm this effect, we check the distribution of angle between positions of two clusters  $\theta_{\text{ECL}(\ell\gamma)}^{\text{LAB}}$  as drawn in Fig. 7.6. Here, we define  $\theta_{\text{ECL}(\ell\gamma)}^{\text{LAB}}$  as an opening angle of these clusters measured from the interaction point. The effect of the New Physics on  $\theta_{\text{ECL}(\ell\gamma)}^{\text{LAB}}$  can be considered to be less sensitive because  $\theta_{\text{ECL}(\ell\gamma)}^{\text{LAB}}$  is mainly determined by the geometrical design of the detector. The difference of distribution in  $\theta_{\text{ECL}(\ell\gamma)}^{\text{LAB}} \rightarrow 0$  between the experiment and MC simulation is regarded as the systematic uncertainty due to the simulation of the overlap.

Comparing the distribution of  $\theta_{\text{ECL}(\ell\gamma)}^{\text{LAB}}$ , we can see an agreement to some extent between the experiment and MC simulation. To quantify the corresponding error, we extracted a ratio of PDFs between the experiment and MC simulation for  $\theta_{\text{ECL}(\ell\gamma)}^{\text{LAB}}$  as:

$$R = R(\theta_{\text{ECL}(\ell\gamma)}^{\text{LAB}}). \quad (7.14)$$

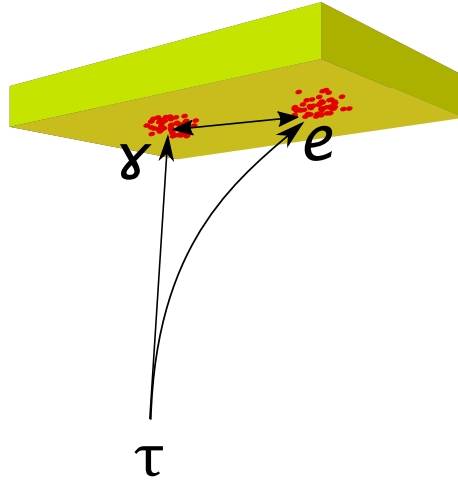


Figure 7.5: Conceptual view of two clusters in ECL. The curvature of lepton becomes small as the momentum is large which result in the merge of two ECL clusters.

The effect of  $R$  can be evaluated in a similar way as the evaluation of efficiency correction explained in Sec. 7.3. The errors are estimated to be  $\sigma_{\bar{\eta}}^e = 2.2$ ,  $\sigma_{\xi\kappa}^e = 0.5$ ,  $\sigma_{\bar{\eta}}^\mu = 0.02$  and  $\sigma_{\xi\kappa}^\mu = 0.06$ .

### 7.2.7 Uncertainty from the detector resolution

The impact of the detector resolution is estimated by the comparison of the fitted values of Michel parameters with and without the convolution of resolution function of  $\mathcal{R}$  explained in Sec. 5.4.5. The corresponding errors are  $\sigma_{\bar{\eta}}^e = 0.74$ ,  $\sigma_{\xi\kappa}^e = 0.20$ ,  $\sigma_{\bar{\eta}}^\mu = 0.22$  and  $\sigma_{\xi\kappa}^\mu = 0.02$ .

### 7.2.8 Uncertainty from the beam Energy spread

The error of beam energy is calibrated based on the mass constraint of  $B$  meson, which result in the accuracy of order of 0.1 MeV for the run dependent values. This magnitude corresponds to only 0.002%, therefore, we can basically expect that this error is negligible. Nevertheless, we confirmed this could be really ignored. We calculated PDFs of signal and backgrounds where the beam energy were shifted on purpose and evaluated the variation of the fitted Michel parameters. The magnitude of the change of the fitted Michel parameters are of order of at most ten to minus forth<sup>†</sup> and we conclude that the effect of variation of beam energy is negligible.

### 7.2.9 Uncertainty from $E_\gamma$ distribution

As shown in Fig. 4.10, in low energy region ( $E_\gamma \sim 100$  MeV), we can observe the discrepancy in the photon energy distribution between the real experiment and MC simulation. This may come from the limited precision of bremsstrahlung simulation. As demonstrated in Sec. 2.4, the effects of nonzero values of  $\bar{\eta}$  and  $\xi\kappa$  on the photon energy shape are small, hence it can be guessed that this discrepancy does not strongly affect the fitted Michel parameters. Nevertheless, we evaluated this effect by varying the selection criteria of photon energy threshold to be  $E_\gamma = 150$  MeV. The shifts of fitted Michel parameters are  $\sigma_{\bar{\eta}}^e = 0.91$  and  $\sigma_{\xi\kappa}^e = 0.22$ . This variation reduces the amount of statistics by approximately 18% and thus there is a chance that the statistical fluctuation is simply reflected on the variation of fitted parameters. This evaluation is, therefore, conservative estimation.

<sup>†</sup>This error includes the precision of the reproducibility of PDF calculation itself.

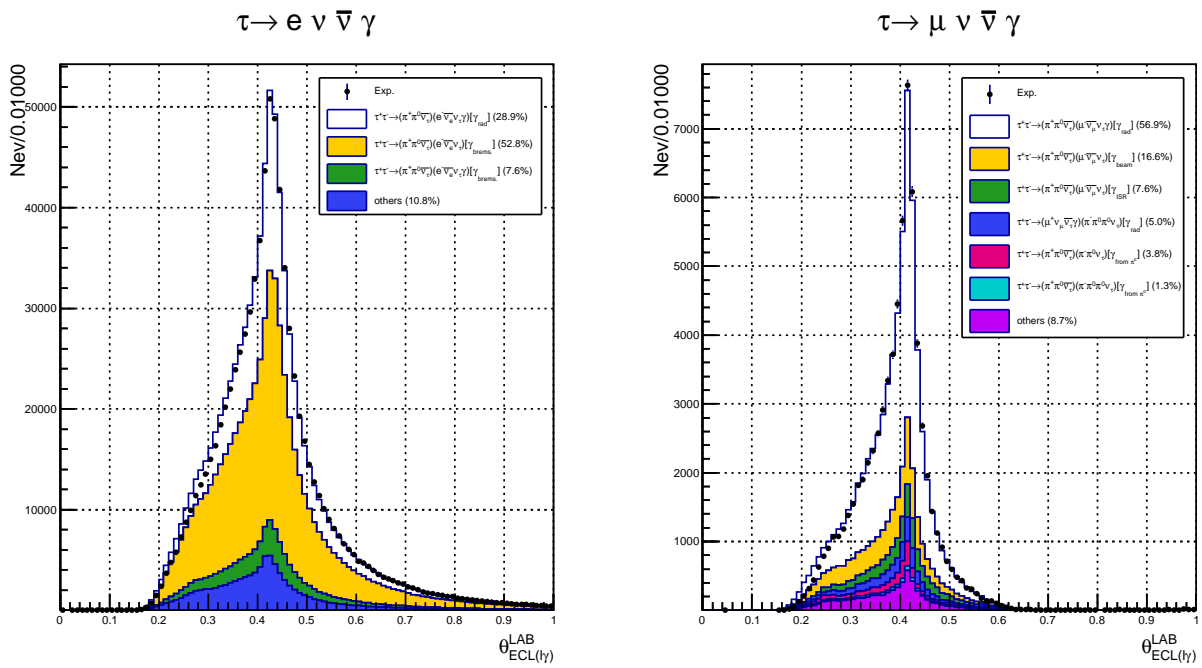


Figure 7.6: Distribution of angle  $\theta_{\text{ECL}(\ell\gamma)}^{\text{LAB}}$  for  $\tau^- \rightarrow \ell^- \nu \bar{\nu} \gamma$ : (left)  $\ell = e$  and (right)  $\ell = \mu$ . The meanings of filled colors are explained in captions of Figs. 4.10 and 4.14 for  $\ell = e$  and  $\ell = \mu$ , respectively.

# Chapter 8

## Results and discussion

### 8.1 Fit result

As presented in the last section, the evaluated uncertainties for  $\bar{\eta}$  using  $\tau \rightarrow e\nu\bar{\nu}\gamma$  events is much larger than the expected sensitivity for  $\tau \rightarrow \mu\nu\bar{\nu}\gamma$  decay and it is reasonable to extract  $\bar{\eta}$  value from only  $\tau \rightarrow \mu\nu\bar{\nu}\gamma$  events. Using selected 776834 and 71171 events for  $\tau \rightarrow e\nu\bar{\nu}\gamma$  and  $\tau \rightarrow \mu\nu\bar{\nu}\gamma$  candidates, respectively, we performed the fit procedure and obtained results as:

$$\xi\kappa^e = -0.4 \pm 0.8 \pm 0.9, \quad (8.1)$$

$$\bar{\eta}^\mu = -1.3 \pm 1.5 \pm 0.8, \quad (8.2)$$

$$\xi\kappa^\mu = 0.8 \pm 0.5 \pm 0.25. \quad (8.3)$$

where first errors are statistical and second systematic. These obtained values are consistent with the SM prediction. Figure 8.1 shows the contour of the likelihood function for  $\tau \rightarrow \mu\nu\bar{\nu}\gamma$  events. The  $\xi\kappa$  are also obtained by combined fit as

$$\xi\kappa = 0.5 \pm 0.4 \pm 0.2, \quad (8.4)$$

where first error is statistical and second is systematic. The systematic uncertainty is naively estimated by

$$\frac{1}{\sigma_{\text{comb}}^2} = \frac{1}{\sigma_e^2} + \frac{1}{\sigma_\mu^2}. \quad (8.5)$$

We also obtained dependence of  $E_{\text{extray}}^{\text{LAB}}$  cut on the fitted Michel parameters as shown in 8.2. In the extraction of  $\bar{\eta}$ , we used  $\tau \rightarrow \mu\nu\bar{\nu}\gamma$  while for  $\xi\kappa$ , combined result using  $\tau \rightarrow e\nu\bar{\nu}\gamma$  and  $\tau \rightarrow \mu\nu\bar{\nu}\gamma$  decays are shown. We can see stability of fitted Michel parameters within errors. Figure 8.3 shows a plot of a residual of likelihood function  $\Delta L = L - L_{\text{max}}$  projected onto one axis. We can observe a smooth and quadratic shape of the likelihood function around its maximum value.

### 8.2 Goodness of fit

In many application of the high energy physics, people often use  $\chi^2$  fit to extract desired parameter. The benefit of the  $\chi^2$  fit is a fact that the PDF of  $\chi^2$  value is already known, hence people can easily evaluate the goodness of fit. In other words, the properties of  $\chi^2$  distribution like average and  $p$ -value can be extracted analytically based on a given degree of freedom. On the other hand, as is often discussed, an evaluation of goodness of fit for the unbinned-maximum likelihood method is not straightforward due to non-existence of a general PDF of the maximized likelihood value. Moreover,

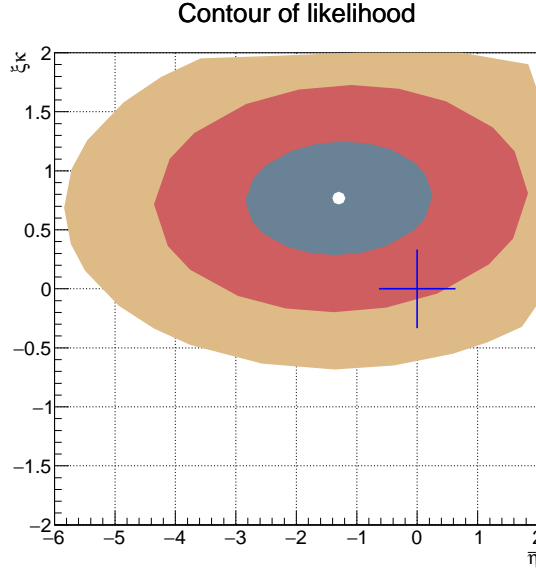


Figure 8.1: Contours of the likelihood function obtained using 69622 events for  $\tau \rightarrow \mu\nu\bar{\nu}\gamma$  candidates. Three circles correspond to  $\Delta L = 1/2, 4/2$  and  $9/2$  contours from inside to outside and mean statistical uncertainties. The cross is the SM prediction.

it is also well known that the absolute maximum value of likelihood function itself does not tell any information about its goodness.\*

As summarized in Ref. [75], there are several alternative solutions for the evaluation of the goodness of a fitting result obtained by the unbinned-maximum likelihood method. Among all presented in the reference, we, in this work, attempt to use *point-to-point dissimilarity* method. The idea of this method is to use evaluation parameter  $T$  defined as

$$T = \frac{1}{2} \int d\mathbf{x} (P_{\text{EX}}(\mathbf{x}) - P_{\text{fit}}(\mathbf{x}))^2, \quad (8.6)$$

where  $P_{\text{EX}}(\mathbf{x})$  is a (unknown) PDF of the real experimental data and  $P_{\text{fit}}(\mathbf{x})$  is the fitted PDF obtained by the unbinned maximum likelihood method. This  $T$  becomes its minimum  $T = 0$  only if  $P_{\text{EX}} = P_{\text{fit}}$ . Therefore, the  $T$  value can be used to score the similarity of spectra between real and fitted distributions, *i.e.*, its smaller value indicates that fit is decent. Here, a more general form of  $T$  is defined as

$$T = \frac{1}{2} \int d\mathbf{x} d\mathbf{x}' (P_{\text{EX}}(\mathbf{x}) - P_{\text{fit}}(\mathbf{x})) (P_{\text{EX}}(\mathbf{x}') - P_{\text{fit}}(\mathbf{x}')) \psi(|\mathbf{x} - \mathbf{x}'|), \quad (8.7)$$

where  $\psi(|\mathbf{x} - \mathbf{x}'|)$  is a certain weighting function. Although  $P_{\text{EX}}(\mathbf{x})$  is not known (if we know, we do not need to fit a function), Eq. (8.6) is evaluated for the selected experiment and MC events as:

$$T = \frac{1}{N_{\text{MC}}(N_{\text{MC}} - 1)} \sum_{\substack{i>j \\ \mathbf{x}^i, \mathbf{x}^j \in P_{\text{MC}}}}^{N_{\text{MC}}} \psi(|\mathbf{x}^i - \mathbf{x}^j|) + \frac{1}{N_{\text{EX}}(N_{\text{EX}} - 1)} \sum_{\substack{i>j \\ \mathbf{y}^i, \mathbf{y}^j \in P_{\text{EX}}}}^{N_{\text{EX}}} \psi(|\mathbf{y}^i - \mathbf{y}^j|) - \frac{1}{N_{\text{MC}}N_{\text{EX}}} \sum_{\substack{i,j \\ \mathbf{x}^i \in P_{\text{MC}} \\ \mathbf{y}^j \in P_{\text{EX}}}}^{N_{\text{MC}}, N_{\text{EX}}} \psi(|\mathbf{x}^i - \mathbf{y}^j|), \quad (8.8)$$

\*For example, as presented in Ref. [74], a likelihood function constructed from a PDF of particle decay time ( $f(t) = e^{-t/\tau}/\tau$  for a given lifetime  $\tau$ ) has a definite maximum value for any given number of events  $N$  and their average  $\bar{t}$  regardless of the shape of real distribution. Since it is obvious that numerous distributions can give the same average value  $\bar{t}$ , the test using absolute value of the likelihood function does not score the *goodness of fit*.



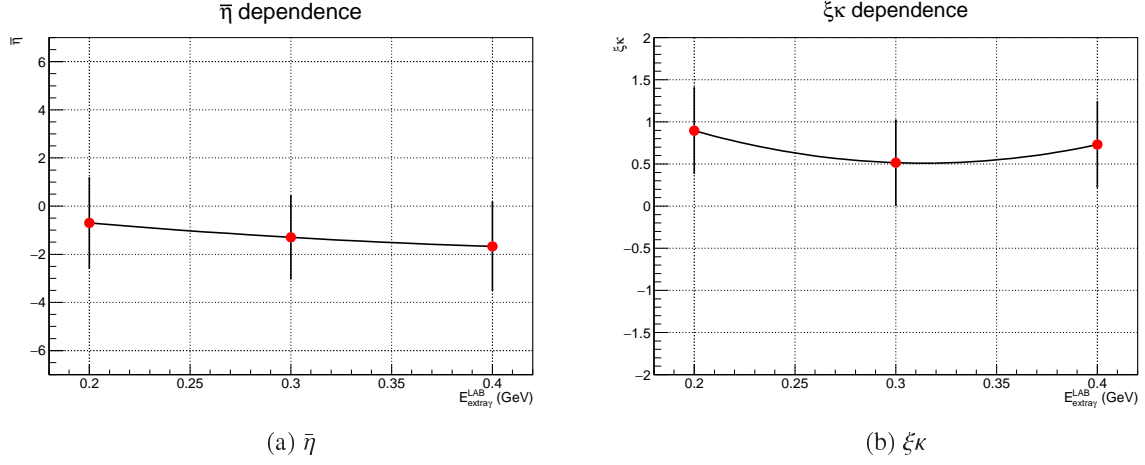


Figure 8.2: Dependence of  $E_{\text{extray}}^{\text{LAB}}$  cut on (a)  $\bar{\eta}$  (b) and  $\xi\kappa$ . Horizontal and vertical axes are extra gamma energy cut and fitted Michel parameters, respectively. The red markers with error bars correspond center values and their errors, where both statistical and systematic errors are considered.

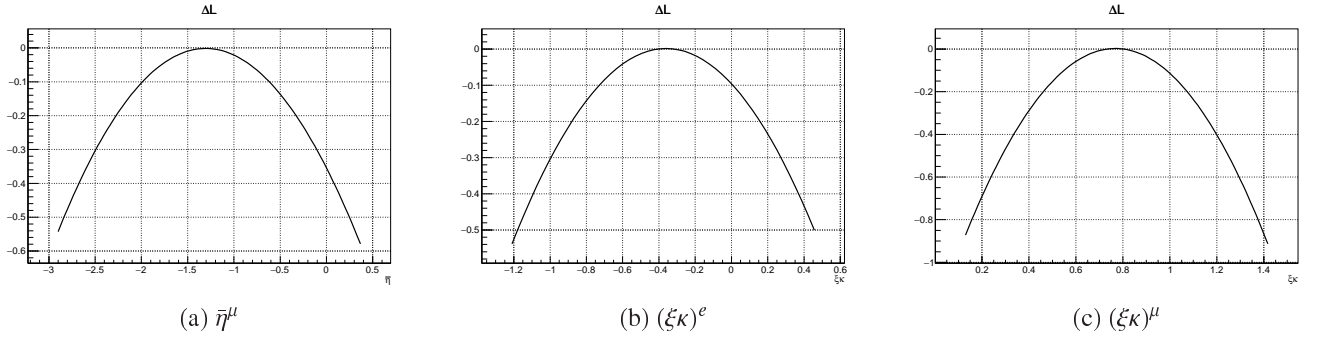


Figure 8.3: Plot of  $\Delta L$  as a function of Michel parameters: (a)  $L(\bar{\eta}^\mu)$  when  $\xi\kappa$  is set to the fitted value: (b)  $L(\xi\kappa^e)$  when  $\bar{\eta} = \bar{\eta}_{\text{SM}} = 0$ : (c)  $L(\xi\kappa^\mu)$  when  $\bar{\eta}$  is set to the fitted value.

where  $\mathbf{x}$  and  $\mathbf{y}$  indicate the selected MC and the real experimental events, respectively. In our application, we modify Eq. (8.8) with  $P_{\text{fit}}(\mathbf{x}) \rightarrow P_{\text{fit}}(\mathbf{x})w(\mathbf{x})$  to give

$$\begin{aligned}
T = & \frac{1}{N_{\text{MC}}(N_{\text{MC}} - 1)} \sum_{\substack{i>j \\ \mathbf{x}^i, \mathbf{x}^j \in P_{\text{MC}}}}^{N_{\text{MC}}} \psi(|\mathbf{x}^i - \mathbf{x}^j|) w(\mathbf{x}^i) w(\mathbf{x}^j) \\
& + \frac{1}{N_{\text{EX}}(N_{\text{EX}} - 1)} \sum_{\substack{i>j \\ \mathbf{y}^i, \mathbf{y}^j \in P_{\text{EX}}}}^{N_{\text{EX}}} \psi(|\mathbf{y}^i - \mathbf{y}^j|) - \frac{1}{N_{\text{MC}} N_{\text{EX}}} \sum_{\substack{i,j \\ \mathbf{x}^i \in P_{\text{MC}} \\ \mathbf{y}^j \in P_{\text{EX}}}}^{N_{\text{MC}}, N_{\text{EX}}} \psi(|\mathbf{x}^i - \mathbf{y}^j|) w(\mathbf{x}^i), \quad (8.9)
\end{aligned}$$

where  $w(\mathbf{x})$  is given by

$$w(\mathbf{x}) = \frac{P^{\text{BSM}}(\mathbf{x})}{P^{\text{SM}}(\mathbf{x})} R(\mathbf{x}). \quad (8.10)$$

Here,  $P(\mathbf{x})$  is the total PDF given by Eq. (5.3) and BSM and SM mean the Michel parameters are set to the fitted and SM values, respectively. In Eq. (8.9), the variation of distribution by the Michel parameters are taken into account through the weight  $w(\mathbf{x})$ .

As demonstrated in Ref. [75], it is justified to drop the first term in Eq. (8.9) because its statistical fluctuations should be negligible for  $N_{\text{MC}} \gg N_{\text{EX}}$ . In our approach, however, rather than discarding this term, we adopt a little bit correct method:

$$\begin{aligned} & \frac{1}{N_{\text{MC}}(N_{\text{MC}} - 1)} \sum_{\substack{i>j \\ \mathbf{x}^i, \mathbf{x}^j \in P_{\text{MC}}}}^{N_{\text{MC}}} \psi(|\mathbf{x}^i - \mathbf{x}^j|) w(\mathbf{x}^i) w(\mathbf{x}^j) \\ \rightarrow & \frac{1}{N_{\text{MC}}(N_{\text{EX}} - 1)} \sum_{\substack{i>j \\ \mathbf{x}^i, \mathbf{x}^j \in P_{\text{MC}}}}^{N_{\text{MC}}, N_{\text{EX}}} \psi(|\mathbf{x}^i - \mathbf{x}^j|) w(\mathbf{x}^i) w(\mathbf{x}^j) \end{aligned}$$

where number of calculation is reduced from  $N_{\text{MC}}(N_{\text{MC}} - 1)$  to  $N_{\text{MC}}(N_{\text{EX}} - 1)$  so that the calculation becomes manageable to be same order as second term. This simplification is, in fact, necessary to reduce the cost of calculation. Thus we use

$$\tilde{T} = \frac{1}{N_{\text{MC}}(N_{\text{EX}} - 1)} \sum_{\substack{i>j \\ \mathbf{x}^i, \mathbf{x}^j \in P_{\text{MC}}}}^{N_{\text{MC}}, N_{\text{EX}}} \psi(|\mathbf{x}^i - \mathbf{x}^j|) w(\mathbf{x}^i) w(\mathbf{x}^j) \quad (8.11)$$

$$+ \frac{1}{N_{\text{EX}}(N_{\text{EX}} - 1)} \sum_{\substack{i>j \\ \mathbf{y}^i, \mathbf{y}^j \in P_{\text{EX}}}}^{N_{\text{EX}}} \psi(|\mathbf{y}^i - \mathbf{y}^j|) - \frac{1}{N_{\text{MC}} N_{\text{EX}}} \sum_{\substack{i,j \\ \mathbf{x}^i \in P_{\text{MC}} \\ \mathbf{y}^j \in P_{\text{EX}}}}^{N_{\text{MC}}, N_{\text{EX}}} \psi(|\mathbf{x}^i - \mathbf{y}^j|) w(\mathbf{x}^i), \quad (8.12)$$

as a signature of the goodness of fit. The decision of the function  $\psi$  is not trivial but we follow the method of Ref. [76], where it is given by  $\psi(d) = e^{-d^2/2\sigma^2}$ . Here,  $d$  is a distance in the twelve-dimension phase space  $\{P_\ell, \Omega_\ell, P_\gamma, \Omega_\gamma, P_\rho, \Omega_\rho, m_{\pi\pi}^2, \tilde{\Omega}_\pi\}$  defined simply with  $d_{i,j}^2 = |P_{\ell_i} - P_{\ell_j}|^2 + \dots + |\tilde{\phi}_{\pi_i} - \tilde{\phi}_{\pi_j}|^2$ , and  $\sigma$  is a measure to define the spread of distribution. The variables in the twelve-dimension phase space are linearly projected into open interval  $(0, 1)$  so that the volume of the overall phase space becomes unity. The  $\sigma$  is determined by an equation

$$1 = V_{12} N_{\text{EX}} (10\sigma)^{12}, \quad (8.13)$$

where  $V_{12}$  is a volume of the twelve-dimension unity sphere and given by  $V_{12} = \pi^6 / \Gamma(12/2 + 1) = \pi^6 / 720$ . In other words,  $10 \times \sigma$  is chosen as an average distance between a closest event when  $N_{\text{EX}}$  events are uniformly distributed in the phase space. The factor of ten is chosen to account for a dense concentration of events in the phase space.

With described definition of  $\tilde{T}$ , we can score the goodness of fit: however, distribution of  $\tilde{T}$  itself when  $P_{\text{EX}} = P_{\text{fit}}$  is not known. This means that we are not able to calculate the  $p$ -value. To estimate the distribution of  $\tilde{T}$ , we adopt *permutation test*, where randomly pooled  $N_{\text{EX}}$  and  $N_{\text{MC}}$  events are used to generate sequence of  $\tilde{T}$  values, *i.e.*, for every shuffled set of pseudo ‘‘experimental’’ and ‘‘MC’’ events, we calculate  $\tilde{T}$  in the same way as real one. We repeat this procedure  $N_{\text{try}} = 100$  times and count events that satisfy  $\tilde{T}_{\text{real}} < \tilde{T}_{\text{pseudo}}$ . We take the fraction as an estimator of  $p$ -value. In the real evaluation of  $\tilde{T}$ , however, it is not possible to use whole available events in terms of reasonable CPU calculation due to its rapid increase of iteration:  $\sim N_{\text{MC}} \times N_{\text{EX}} \times N_{\text{try}}$ . Therefore, we divide both MC and experimental sample into small subsets so that they typically contain  $5 \times 10^4$  and  $10^4$  events, respectively. Figures 8.4 and 8.5 show distributions of  $\tilde{T}$  for electron and muon modes, respectively. Since  $p$ -value should distribute uniformly in the interval  $(0, 1)$  if the real and fitted functions are totally same, the appearance of widely spread values may suggest a good performance of our fit. At the same time, however, we should put emphasis on the fact that the method explained above simply cannot reject the *badness of fit*.

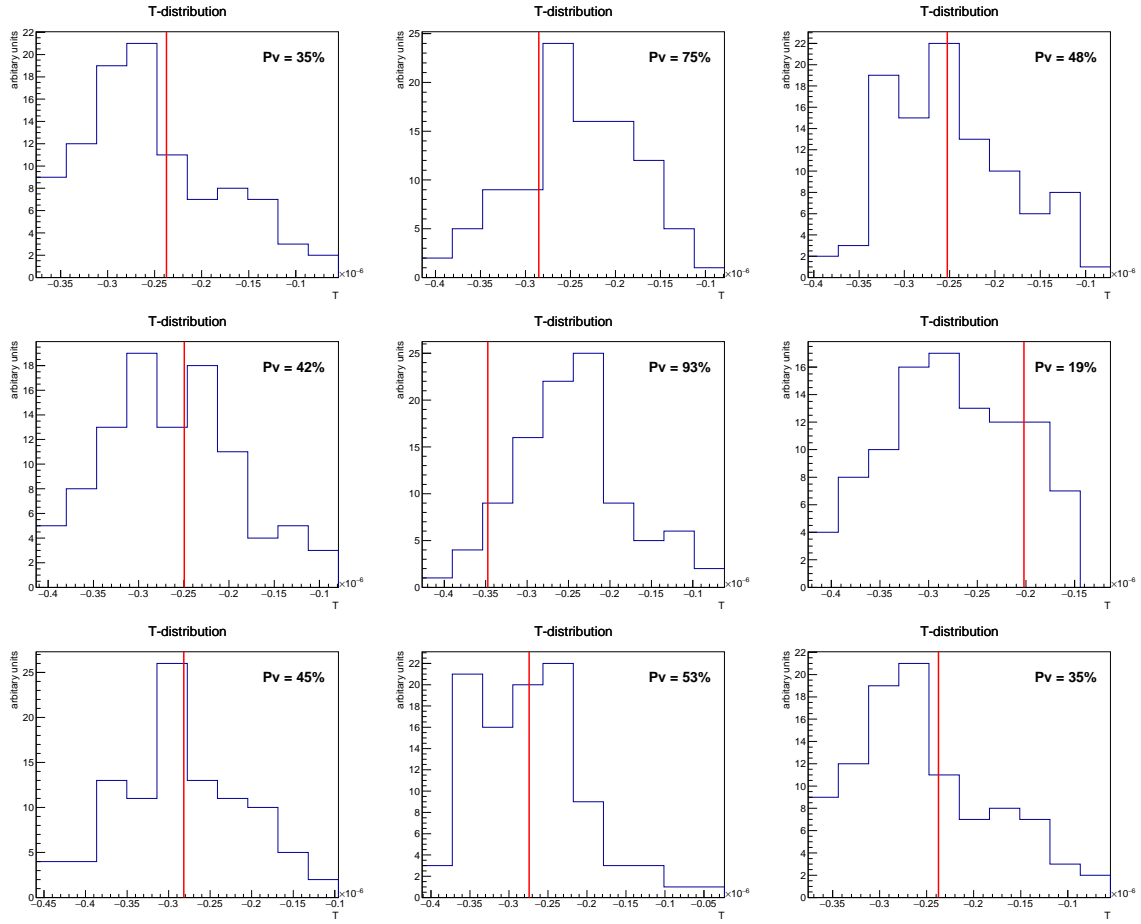


Figure 8.4: Distribution of  $\tilde{T}$  values for nine different sets (which are chosen randomly) for electron mode. The line shows real  $\tilde{T}$  value from fitted sample and histograms are distributions obtained with the permuted sets.

### 8.3 Upper limits on couplings $g_{ij}^N$

As introduced in Sec. 1.4,  $\bar{\eta}$  is represented as a sum of non-negative terms, hence the upper limit of the  $\bar{\eta}$  parameter gives also upper limits of each term. Here, again we show the explicit formula of  $\bar{\eta}$  and  $\xi\kappa$  below

$$\bar{\eta} = |g_{RL}^V|^2 + |g_{LR}^V|^2 + \frac{1}{8} \left( |g_{RL}^S + 2g_{RL}^T|^2 + |g_{LR}^S + 2g_{LR}^T|^2 \right) + 2 \left( |g_{RL}^T|^2 + |g_{LR}^T|^2 \right), \quad (8.14)$$

$$\xi\kappa = |g_{RL}^V|^2 - |g_{LR}^V|^2 + \frac{1}{8} \left( |g_{RL}^S + 2g_{RL}^T|^2 - |g_{LR}^S + 2g_{LR}^T|^2 \right) + 2 \left( |g_{RL}^T|^2 - |g_{LR}^T|^2 \right). \quad (8.15)$$

The distribution on the  $\bar{\eta}$  in the vicinity of the optimal value is well described by Gaussian PDF. Though it may draw controversy, if we allow  $\bar{\eta} < 0$  region as possible area (in practice, measured value can become negative as well) the upper limit of  $\bar{\eta}$  at 95% confidence level is given by

$$\bar{\eta} < 1.5 \quad (95\% \text{ C.L.}).$$

Of all terms in Eq. (8.14), there are essential impacts only on the first and last two terms in terms of sensitivity because the rest terms are suppressed by a factor of 1/8. Moreover, if we take into account existing values shown in Table 8.1 [7], the upper limit of  $\bar{\eta}$  gives notable impact only on  $|g_{RL}^T|$ . Putting zero into other terms in Eq. (8.14), we obtain  $|g_{RL}^T| < 0.9$  (95% C.L.).

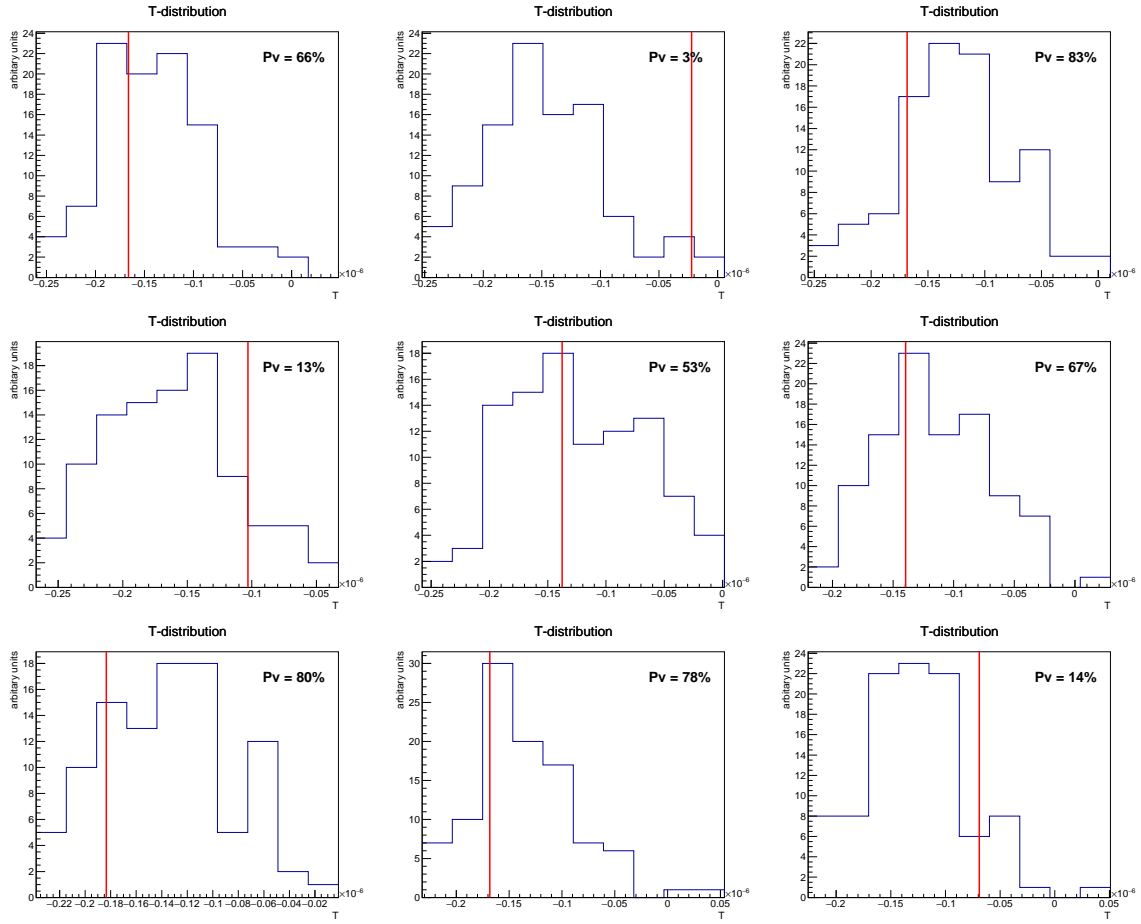


Figure 8.5: Distribution of  $\tilde{T}$  values for nine different sets (which are chosen randomly) for muon mode. The line shows real  $\tilde{T}$  value from fitted sample and histograms are distributions obtained with the permuted sets.

Moreover, from Eqs. (8.14) and (8.15), sum of  $\bar{\eta}$  and  $\xi\kappa$  is also written as combination of non-negative terms as

$$\bar{\eta} + \xi\kappa = 2 |g_{RL}^V|^2 + \frac{1}{4} |g_{RL}^S + 2g_{RL}^T|^2 + 4 |g_{RL}^T|^2. \quad (8.16)$$

From combined measured value  $\bar{\eta} + \xi\kappa = -0.8 \pm 1.8$ , we can similarly obtain its upper limit

$$\bar{\eta} + \xi\kappa < 2.1 \quad (95\% \text{ C.L.}),$$

which leads  $|g_{RL}^V| < 1.0$  and  $|g_{RL}^T| < 0.7$  (95% C.L.). If we assume that these coupling constants are real—which means that T or CP is conserved—we can simplify Eq. (8.16) and draw allowed range of  $g_{RL}^S$  and  $g_{RL}^T$  values for different value of  $|g_{RL}^V|^2$  (95% C.L.) as shown in Fig. 8.7.

We can also give a different consideration using another linear combination of the Michel parameters as

$$\bar{\eta} - \xi\kappa = 2 |g_{LR}^V|^2 + \frac{1}{4} |g_{LR}^S + 2g_{LR}^T|^2 + 4 |g_{LR}^T|^2 < 1.1 \quad (95\% \text{ C.L.})$$

but this turns out to be less effective for already existing constraints on  $g_{LR}^S$ ,  $g_{LR}^V$  and  $g_{LR}^T$  couplings. Relying only on the measurement of  $\bar{\eta}$  and  $\xi\kappa$ , we cannot improve already obtained constrained limit. However, it is possible to improve constraints by simultaneously combining experimental values of

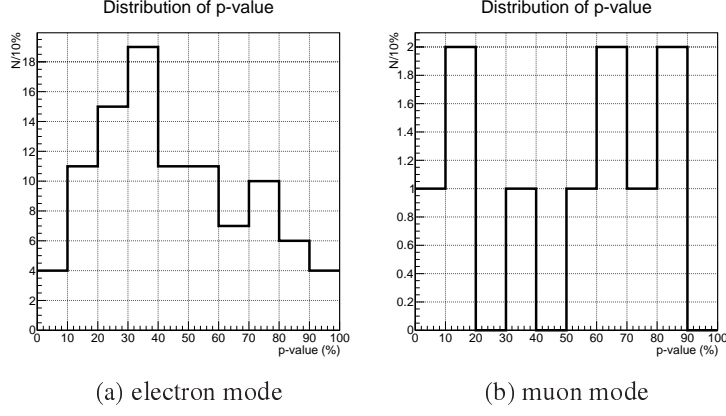


Figure 8.6: Distribution of  $p$  value: (a) electron mode using one hundred different sets (b) muon mode using ten different sets.

other Michel parameters. In particular,  $\rho$  parameter shares same six  $g_{ij}^N$ s with  $\bar{\eta}$  and  $\xi\kappa$

$$\rho = \frac{3}{4} - \frac{3}{4} \left( |g_{LR}^V|^2 + |g_{RL}^V|^2 + 2|g_{LR}^T|^2 + 2|g_{RL}^T|^2 + \Re \left( g_{LR}^S g_{LR}^{T*} + g_{RL}^S g_{RL}^{T*} \right) \right). \quad (8.17)$$

Combining  $\rho$  and  $\xi\kappa$

$$-\frac{4}{3} \left( \rho - \frac{3}{4} \right) + \xi\kappa = 2|g_{RL}^V|^2 + \frac{9}{2}|g_{RL}^T|^2 + \frac{1}{8}|g_{RL}^S|^2 - \frac{1}{2}|g_{LR}^T|^2 - \frac{1}{8}|g_{LR}^S|^2 + \Re \left( \frac{3}{2}g_{LR}^S g_{LR}^{T*} + \frac{1}{2}g_{RL}^S g_{RL}^{T*} \right). \quad (8.18)$$

The magnitude of negative terms can be evaluated based on Table 8.1 as

$$\frac{1}{2}|g_{LR}^T|^2 + \frac{1}{8}|g_{LR}^S|^2 < 0.12 \quad (95\% \text{ C.L.}) \quad (8.19)$$

Moreover, the terms in the last parenthesis in Eq. (8.18) arise from the contribution of the interference between scalar and tensor type interactions and disappear when we consider one type of particle BSM. In this scenario, the rest positive terms are thus evaluated to be

$$2|g_{RL}^V|^2 + \frac{9}{2}|g_{RL}^T|^2 + \frac{1}{8}|g_{RL}^S|^2 < 1.35, \quad (95\% \text{ C.L.}) \quad (8.20)$$

which gives

$$|g_{RL}^V| < 0.82 \quad (95\% \text{ C.L.}), \quad (8.21)$$

$$|g_{RL}^T| < 0.55 \quad (95\% \text{ C.L.}) \quad (8.22)$$

In particular, Eq. (8.22) is competitive with PDG value that was obtained by combing results of multiple experiments.

## 8.4 Couplings with right-handed lepton

As described in Sec. 1.4, the  $\xi\kappa$  parameter is related to a normalized probability that  $\tau$  couples with a right-handed daughter lepton  $Q_{\ell_R}^\tau$ . This value has not been measured yet for the tau lepton. Taking

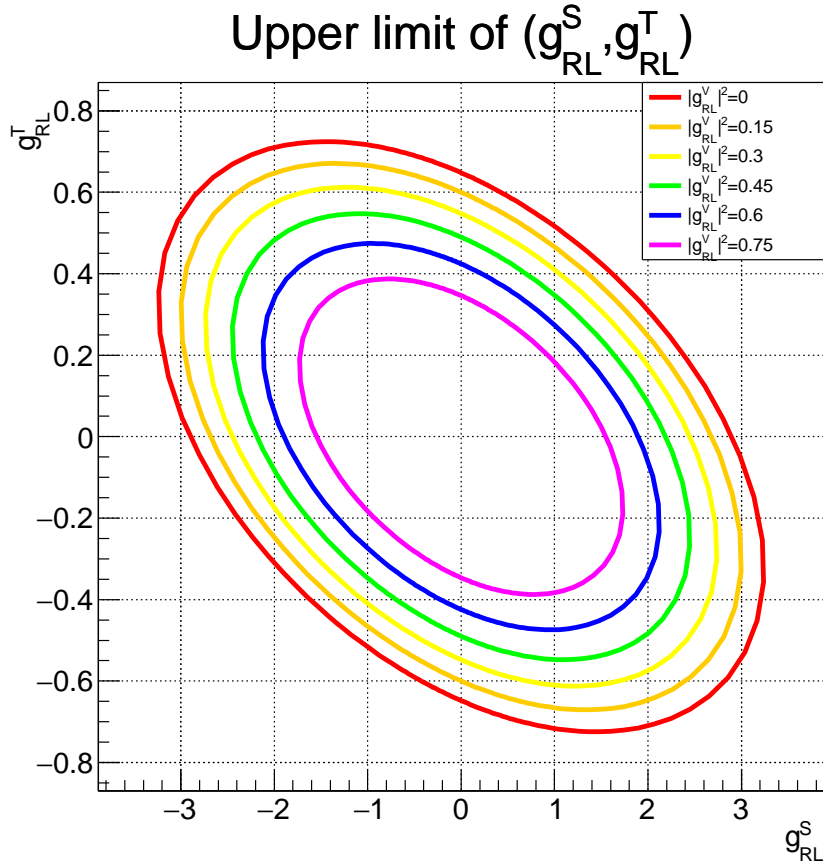


Figure 8.7: Upper limit of  $g_{RL}^S$  and  $g_{RL}^T$  at 95% confidence level depending on various  $|g_{RL}^V|^2$  values. Inner regions enclosed by ellipses are allowed. Here we assume  $g_{RL}^S$  and  $g_{RL}^T$  are real.

Table 8.1: Upper limit of various couplings  $g_{ij}^N$  (95% C.L.) [7]

$\tau \rightarrow e\nu\bar{\nu}$		
$ g_{RR}^S  < 0.70$	$ g_{RR}^V  < 0.17$	
$ g_{LR}^S  < 0.99$	$ g_{LR}^V  < 0.13$	$ g_{LR}^T  < 0.082$
$ g_{RL}^S  < 2.01$	$ g_{RL}^V  < 0.52$	$ g_{RL}^T  < 0.51$
$ g_{LL}^S  < 2.01$	$ g_{LL}^V  < 1.005$	
$\tau \rightarrow \mu\nu\bar{\nu}$		
$ g_{RR}^S  < 0.72$	$ g_{RR}^V  < 0.18$	
$ g_{LR}^S  < 0.95$	$ g_{LR}^V  < 0.12$	$ g_{LR}^T  < 0.079$
$ g_{RL}^S  < 2.01$	$ g_{RL}^V  < 0.52$	$ g_{RL}^T  < 0.51$
$ g_{LL}^S  < 2.01$	$ g_{LL}^V  < 1.005$	

into account that  $\xi\delta$  and  $\xi$  parameters had been precisely measured by  $\tau \rightarrow \ell\nu\bar{\nu}$  decays, substitutions of the SM values  $\xi\delta = 0.75$  and  $\xi = 1.0$  lead  $Q_{\ell_R}^\tau = 2\xi\kappa$ . In the same way as  $\bar{\eta}$ , we evaluate the upper limit of  $\xi\kappa < 1.2$  at 95% confidence level. Thus we obtain the upper limit as

$$Q_{\ell_R}^\tau < 2.4 \quad (95\% \text{ C.L.}) \quad (8.23)$$

Obviously, we cannot make any conclusive decision at current precision. It is desired to do further precision tests by future experiments.

## 8.5 Relationship with the right-left symmetric model

As mentioned in the introduction, the measurement of Michel parameters strongly contributes to the constraint of physics models BSM which have different chirality structure from the SM. The right-left symmetric model [80, 81] predicts right-handed charged-weak current and exhibits Michel parameters BSM. The precise measurement of  $\xi\kappa$  parameter, indeed, constrains a mixing parameter of this model, however, it turns out to be impossible to give essential constraint with current precision. It is required to improve the sensitivity by two order of magnitude to make it have an influence on the BSM parameters. The discussion is given in Appendix F.

# Chapter 9

## Measurement of the branching ratio

$$\mathcal{B}(\tau^- \rightarrow \ell^- \nu \bar{\nu} \gamma)$$

In this chapter, we present the measurement of branching ratio of  $\mathcal{B}(\tau^- \rightarrow \ell^- \nu \bar{\nu} \gamma)$  for  $\ell = e$  or  $\mu$  based on further optimization of selection criteria for already selected events described in Chapter 4. We give a small discussion on the obtained results of branching ratios.

### 9.1 Event selection

Since our goal of this measurement is to achieve an accuracy of a few percents, tens of thousands events turn out to be sufficient in terms of statistical uncertainty. Unlike the measurement of Michel parameters, we can optimize selection criteria more stringently so that the purity of signal becomes sufficiently high  $\sim 70\%$ . Moreover, rather than tuning selection criteria based on an optimization of statistical uncertainty\*, we put highly emphasis on the reduction of systematic uncertainties.

To avoid duplicative generation of MC events, we start from already selected events except the  $E_{\text{extra}}^{\text{LAB}}$  cut, which is dedicated to the Michel parameter measurement. The additional selection criteria are summarized in Table 9.1. Here, to determine selection criteria, we take into account following things:

- ① and ④: these selection criteria are intended for reduction of the systematic uncertainty from  $\ell$ ID efficiency correction. Because of notable backgrounds in forward and backward parts, the correction factors  $R_{\ell\text{ID}}$  in this region are not precisely estimated and we exclude them.
- ②: this requirement is also intended to reduce  $R_{\ell\text{ID}}$  correction uncertainties.
- ③⑥: both selection criteria play crucial roles in the suppression of backgrounds.

Figures 9.1 to 9.5 show the situations of the additional selections. The black points with error bars indicate experimental distributions and open and colored histograms represent MC simulations for signal and background modes, respectively. Each color of histogram is same as explanations in Sec. 4.4. To draw MC histograms, the scale factor is determined according to the number of entries just after the second selection described in Chapter 4.

The step-by-step reduction of the signal efficiency and the number of selected events are summarized in Tables 9.2 and 9.3.

---

\*In many optimization of selection criteria, people often maximize a figure of merit defined by  $\text{FOM} = S / \sqrt{S + B}$ , where  $S$  and  $B$  are numbers of signal and backgrounds, respectively. The idea of this optimization is to enhance the ratio of signal number in terms of statistical fluctuation of both signal and backgrounds.



Table 9.1: Additional selection criteria

Electron mode	
①:	The electron direction must lie region defined by $\theta_e^{\text{LAB}} < 126^\circ$ .
②:	The electron momentum must exceed $E_e^{\text{LAB}} > 1.5 \text{ GeV}$ .
③:	The invariant mass of combined momenta of $e$ and $\gamma$ must exceed $M_{e\gamma} > 0.1 \text{ GeV}/c^2$ .
④:	The extra gamma energy $E_{\text{extray}}^{\text{LAB}}$ must be smaller than $0.2 \text{ GeV}$ .
Muon mode	
⑤:	The muon direction must lie region defined by $51^\circ < \theta_\mu^{\text{LAB}} < 117^\circ$ .
⑥:	CMS angle between $\mu$ and $\gamma$ must satisfy $\cos\theta_{\mu\gamma} > 0.99$ .
⑦:	The extra gamma energy $E_{\text{extray}}^{\text{LAB}}$ must be smaller than $0.3 \text{ GeV}$ .

Table 9.2: Reduction of efficiency in each step for  $\tau^+\tau^- \rightarrow (\pi^+\pi^0\bar{\nu})(e^-\nu\bar{\nu}\gamma)$  candidates.

Step after	$N_{\text{cand}}^{\text{MC}}$	$N_{\text{sig}}^{\text{MC}}$	$\varepsilon_{\text{sig}}(\%)$	purity (%)	$N_{\text{cand}}^{\text{MC} \dagger}$	$N^{\text{EX}}$
2nd selection ‡	7299848	2218523	7.96	30.4	1373878	1373878
Common cut	5466585	1810009	6.49	33.1	1028846	1023518
①	5326747	1775999	6.37	33.3	1002528	1005165
②	2419038	838600	3.01	34.7	455278	460944
③	88214	55331	0.198	62.7	16602	16395
④	67677	47515	0.170	70.2	12737	12302

†  $N_{\text{cand}}^{\text{MC}}$  means scaled number of MC events at the step just after preselection.

‡ The difference in number of signal events and efficiency from Table 4.3 comes from definition of signal. Herein, all radiative events are inclusively counted.

Table 9.3: Reduction of efficiency in each step for  $\tau^+\tau^- \rightarrow (\pi^+\pi^0\bar{\nu})(\mu^-\nu\bar{\nu}\gamma)$  candidates.

Step	$N_{\text{cand}}^{\text{MC}}$	$N_{\text{sig}}^{\text{MC}}$	$\varepsilon_{\text{sig}}(\%)$	purity (%)	$N_{\text{cand}}^{\text{MC} \dagger}$	$N^{\text{EX}}$
2nd selection	1478977	376484	6.30	25.5	258089	258089
Common cut	463368	242321	4.06	52.3	80860	83062
⑤	280847	155064	2.60	55.2	49009	52316
⑥	131722	87477	1.46	66.4	22986	24909
⑦	115564	82633	1.38	71.5	20167	21624

†  $N_{\text{cand}}^{\text{MC}}$  means scaled number of MC events at the step just after preselection.

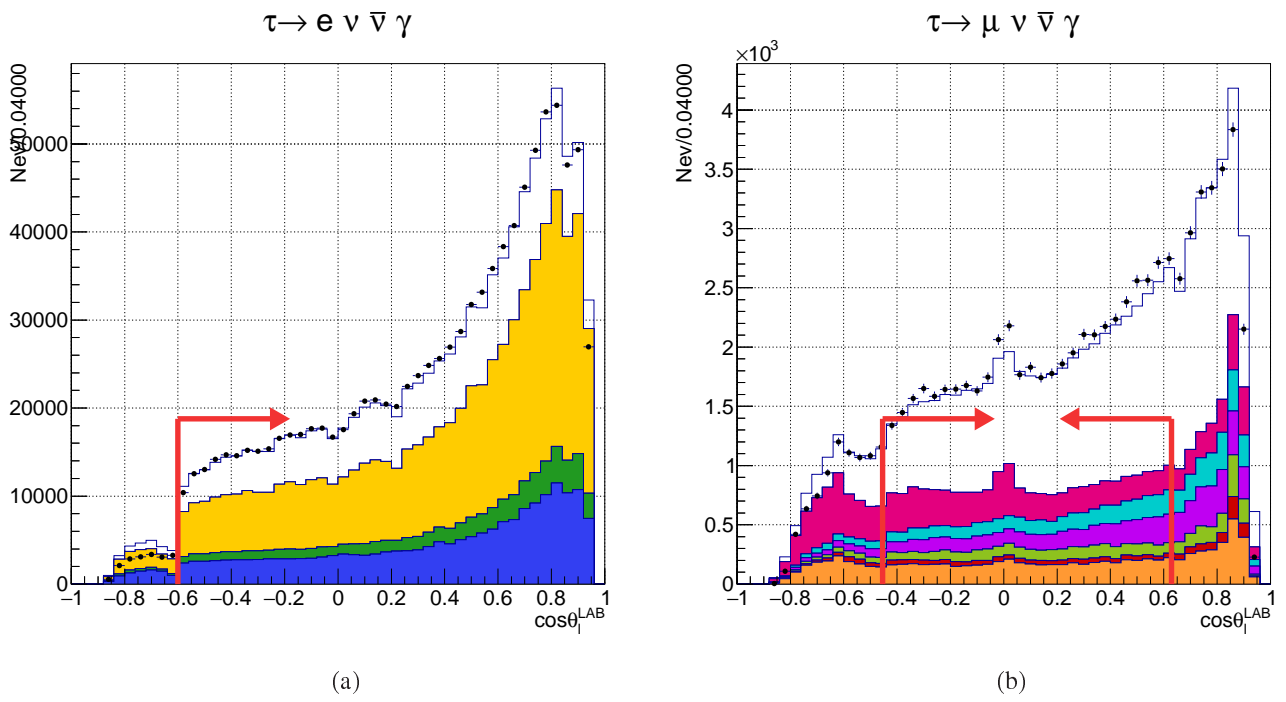


Figure 9.1: ① ⑤: Distribution of the cosine of polar angle of lepton: (a) electron mode (b) muon mode.

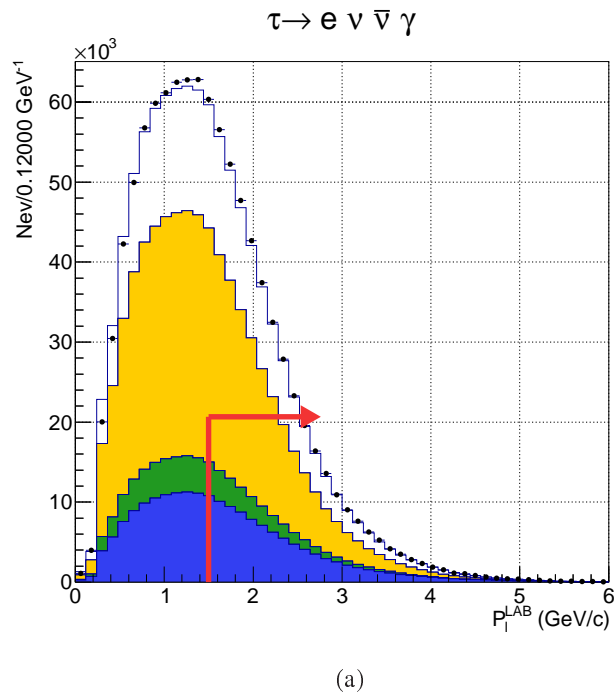


Figure 9.2: ②: Distribution of momentum of electron.



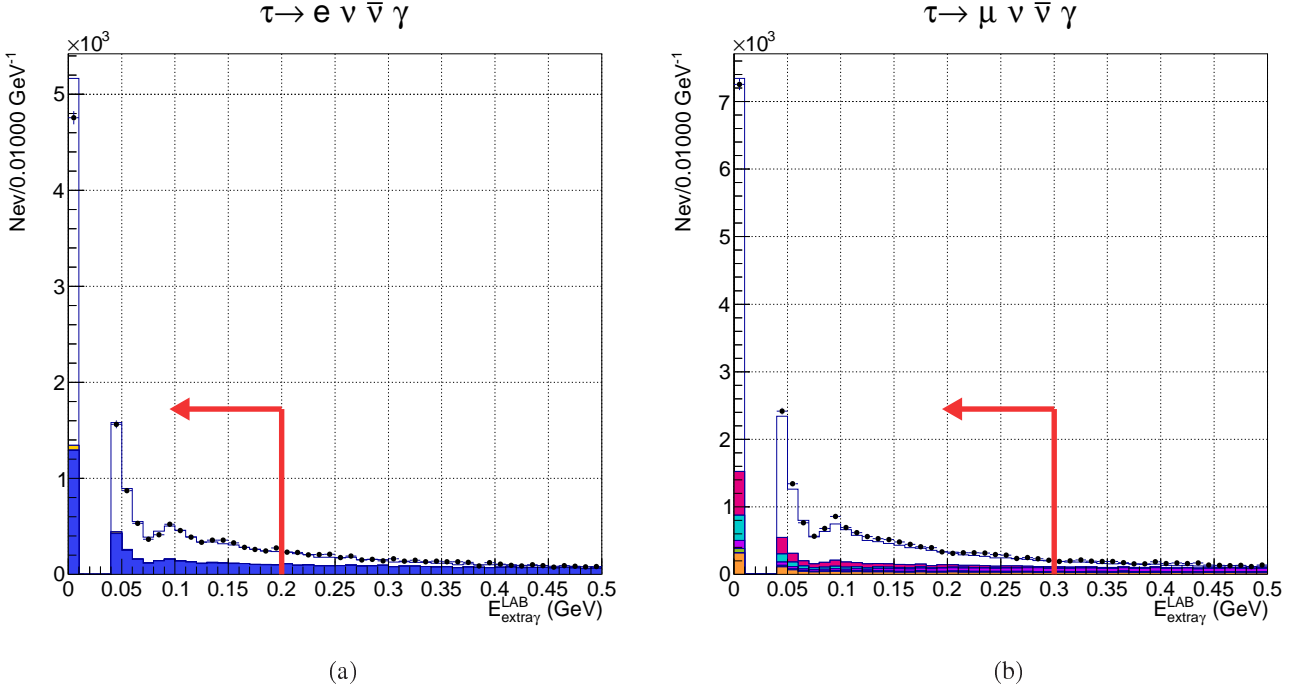


Figure 9.5: ④ ⑦: Distribution of  $E_{\text{extray}}^{\text{LAB}}$ : (a) electron mode (b) muon mode.

## 9.2 Method

The branching ratio can be determined using equation

$$\mathcal{B}(\tau^+ \rightarrow \pi^+ \pi^0 \bar{\nu}) \mathcal{B}(\tau^- \rightarrow \ell^- \nu \gamma) = \frac{N_{\text{obs}}(1 - f_{\text{bg}})}{2\sigma_{\tau\tau} L \bar{\varepsilon}}, \quad (9.1)$$

where  $\mathcal{B}(\tau^+ \rightarrow \pi^+ \pi^0 \bar{\nu}) = (25.52 \pm 0.09)\%$  [7] is a branching ratio of  $\tau^+ \rightarrow \pi^+ \pi^0 \bar{\nu}$  decay,  $N_{\text{obs}}$  is the number of observed events,  $f_{\text{bg}}$  is fraction of background events,  $\sigma_{\tau\tau} = (0.919 \pm 0.003) \text{ nb}^{-1}$  is the cross section of  $e^+ e^- \rightarrow \tau^+ \tau^-$  production at  $\Upsilon(4S)$  resonance energy,  $L = (703 \pm 10) \text{ fb}^{-1}$  is the integrated luminosity for  $\Upsilon(4S)$  resonance energy, and  $\bar{\varepsilon}$  is an average selection efficiency of signal events.

The  $\bar{\varepsilon}$  is evaluated by MC simulation. Here, as explained in Sec. 2.1, the definition of *radiative* decay is events whose energy of gamma in tau rest frame exceeds 10 MeV. The correction between the experimental distribution and MC simulation is performed by using  $R(\mathbf{x}) = \varepsilon^{\text{EX}}(\mathbf{x})/\varepsilon^{\text{MC}}(\mathbf{x})$ , which is originally extracted to measure the Michel parameters (the detailed method of the extraction is explained in Chapter 6). The average selection efficiency of MC simulation is expressed as:

$$\bar{\varepsilon}^{\text{MC}} = \int d\mathbf{x} S(\mathbf{x}) \varepsilon^{\text{MC}}(\mathbf{x}), \quad (9.2)$$

where  $S(\mathbf{x})$  is the PDF of signal and  $\varepsilon^{\text{MC}}(\mathbf{x})$  is the selection efficiency. Since what we need is an efficiency in the experimental situation, we change Eq. (9.2) by

$$\bar{\varepsilon}^{\text{EX}} = \int d\mathbf{x} S(\mathbf{x}) \varepsilon^{\text{EX}}(\mathbf{x}) = \int d\mathbf{x} S(\mathbf{x}) \varepsilon^{\text{MC}}(\mathbf{x}) \frac{\varepsilon^{\text{EX}}(\mathbf{x})}{\varepsilon^{\text{MC}}(\mathbf{x})} \quad (9.3)$$

$$\equiv \int d\mathbf{x} S(\mathbf{x}) \varepsilon^{\text{MC}}(\mathbf{x}) R(\mathbf{x}) = \frac{\bar{\varepsilon}^{\text{MC}}}{N_{\text{sel}}} \sum_{\mathbf{x} \in S} R(\mathbf{x}) = \bar{\varepsilon}^{\text{MC}} \bar{R}. \quad (9.4)$$

Thus we evaluate the average of  $\bar{R}$  according to the selected signal distribution and multiply it with the selection efficiency of the MC simulation.

### 9.3 Evaluation of systematic uncertainties

In Table 9.4, we summarize contributions of systematic uncertainties. To estimate systematic uncertainty of  $\bar{R}$  values, we use following method.

The systematic uncertainties of  $R_{\ell\text{ID}}$  and  $R_{\pi\text{ID}}$  values are estimated by a comparison of the efficiencies of the experiment and MC simulation and observation of time variation (dependence on the run ID numbers). For  $R_{\ell\text{ID}}$  case, we confirm it using  $J/\psi \rightarrow \ell^+ \ell^-$  process. This check is intended to take into account the difference of environment because two-photon process  $e^+ e^- \rightarrow e^+ e^- \ell^+ \ell^-$  is much cleaner than typical  $B$  and  $\tau$  decays.

The systematic uncertainties of  $R_{\pi^0\text{ID}}$  and  $R_{\gamma\text{ID}}$  values are estimated by a comparison between  $\langle R \rangle$  and unity, where the bracket is evaluated with respect to signal events.

The bin-by-bin values of such systematic uncertainties should be considered as 100% correlated values. Therefore, this contribution is evaluated as an average  $\delta\bar{R}_{\text{syst.}} = \langle \delta R_{\text{syst.}} \rangle$ , where the bracket  $\langle \rangle$  means it is evaluated with respect to selected events. On the other hand, the statistical fluctuation of bins should be regarded as independent values, hence we vary the central value of each bin  $R_i$  and see the change of  $\delta\bar{R}_{\text{stat.}} = \langle R + \delta R \rangle - \langle R \rangle$ . We repeat the variation ten times and the average of the residuals  $\langle \delta\bar{R}_{\text{stat.}} \rangle$  is taken as its uncertainties. It turns out that such statistical fluctuations are negligible compared to the systematic errors of overall bins.

The uncertainty of  $\mathcal{B}(\tau^+ \rightarrow \pi^+ \pi^0 \bar{\nu})$  is taken from PDG average value [7] and that of  $\sigma(e^+ e^- \rightarrow \tau^+ \tau^-)$  is taken according to Ref. [77].

The statistical uncertainty of MC events are basically ignored because its fluctuation is small for  $N_{\text{MC}} \gg N_{\text{EX}}$ . The uncertainty of  $N_{\text{obs}}$  are purely statistical ones.

The evaluation of systematic effect of purity  $f_{\text{bg}}$  is estimated based on a sideband information. The sideband events are selected by following criteria:  $M_{e\gamma} < 0.1 \text{ GeV}/c^2$  and  $0.90 < \cos\theta_{e\gamma} < 0.94$  for the electron mode and  $0.90 < \cos\theta_{\mu\gamma} < 0.99$  for the muon mode, where other selection criteria are common with that of signal extraction. Suppose that  $N_S$  and  $N_B$  are number of selected events in signal and background regions and  $b$  is number of background events in signal region. Using MC simulation, we estimate a ratio  $A = b/N_B$ . Both signal and background regions are close in phase space, then the background composition of these regions are assumed to be close as well. Thus it is justified  $A^{\text{EX}} \sim A^{\text{MC}}$  and the number of background events in signal region is estimated as

$$b^{\text{EX}} = N_B^{\text{EX}} A^{\text{EX}} \sim N_B^{\text{EX}} A^{\text{MC}}. \quad (9.5)$$

Because  $b^{\text{MC}}$  is obtained directly from MC simulation, a comparison between  $b^{\text{MC}}$  and Eq. (9.5) enables us to evaluate the systematic effect due to the background inclusion. The systematic uncertainties from the estimation of  $b$  are 4.4% for electron and 5.0% for muon modes, respectively. Taking each fraction into account, we estimate resulting accuracies of purity are 1.3% and 1.5%.

The effect of detector response are estimated by varying selection cut parameters. Table 9.5 lists up the evaluated systematic contributions from variation of selection criteria. We checked the effect of selection criteria of photon energy threshold in the laboratory frame and parameters listed in Table 9.1, because, of all selection criteria, they have essential impacts on the reduction of efficiency. The magnitude of variation of photon energy threshold is determined based on the information of linearity of energy response. According to Ref. [43], a systematic shift between incident photon energy vs measured energy was observed, particularly below 100 MeV and the magnitude was approximately 2%. We varied the threshold by 5 MeV (which corresponds to  $\sim 5\%$ ) including the margin factor. The variation of other selection criteria are determined based on the propagation of

the error matrix of momenta and energies. In a similar way as the inclusion of detector response in the calculation of PDF (explained in Sec. 5.4.5), precision of the measurement of cut parameters are estimated by a residual  $\delta = x_{\text{org}} - x_{\text{shift}}$ , where  $x_{\text{org}}$  and  $x_{\text{shift}}$  are the original measured and shifted values, respectively, and  $x_{\text{shift}}$  are determined according to the error matrix. The root mean square (RMS) of  $\delta$  defines the order of variation: for the momentum and energy, we vary  $3 \times \text{RMS}$ , whereas constructed parameters, namely,  $M_{e\gamma}$  and  $\cos \theta_{\mu\gamma}$ , are varied by  $1 \times \text{RMS}$ . Of all variations, notable systematic uncertainty is observed in the cut by  $M_{e\gamma}$ . As Fig. 9.3 suggests, this is reasonable because the selection by  $M_{e\gamma} > 0.2 \text{ GeV}/c^2$  is one of the most stringent selection criteria to reduce the external bremsstrahlung.

In this measurement, we defined the radiative decay  $\tau^- \rightarrow \ell^- \nu \bar{\nu} \gamma$  by the condition of photon energy threshold of  $E_\gamma^* = 10 \text{ MeV}$  in the tau rest frame. More concretely, to evaluate the selection efficiency by MC simulation, we do not use events whose energy of photons are less than the threshold. In the real experiment, however, we cannot precisely determine the photon energy in the tau rest frame (because we are not able to specify not only the tau direction but also the energy of tau), accordingly there is a chance that a soft event, which has a smaller-energy photon than threshold, is reconstructed also as a signal. The cut value of photon energy in the laboratory frame are 80 MeV and 100 MeV in the barrel and endcap regions, respectively, and this requires an enhancement of boost at least by a factor of ten, *i.e.*,  $\gamma(1 + \beta) \sim 10$  when direction of boost and photon movement are same. Indeed, this is barely possible in a limited phase space and it turns out that the soft events are included in the selected events with fractions of 1.1% and 0.3% for electron and muon events, respectively. We take these fractions as sources of systematic uncertainties due to the experimental ambiguity of  $E_\gamma^*$  threshold.

We also checked the impact of a variation of shape of photon energy spectrum mainly due to the uncertainty of theoretical model. As explained many times, we measure the branching ratio defined with the threshold of  $E_\gamma^* = 10 \text{ MeV}$  on the basis of the photon energy requirement  $E_\gamma = 80 \text{ MeV}$  (or 100 MeV) in the CMS. That is to say, we estimate the total number of radiative events ( $E_\gamma^* > 10 \text{ MeV}$ ), denoted as  $N_{10}$ , using the number of partially selected events with  $E_\gamma > 80$  (100) MeV, denoted as  $N_{80}$ . It follows from this that this measurement relies on the ratio  $N_{10}/N_{80}$  (equivalently the shape of photon energy spectrum) which is mainly determined by theoretical assumption. However, the inputs of parameter which affects the shape—masses of electron, muon and tau, and beam energies—are precisely measured and do not seriously vary the ratio  $N_{10}/N_{80}$ . Indeed, we varied these values by 5%, which is obviously conservative evaluation, and found that  $N_{10}/N_{80}$  shifted only 0.06%.

## 9.4 Result

In Table 9.6, we show the result of measurements separately for the four configurations:  $(e^- \gamma, \pi^+ \pi^0)$ ,  $(e^+ \gamma, \pi^- \pi^0)$ ,  $(\mu^- \gamma, \pi^+ \pi^0)$  and  $(\mu^+ \gamma, \pi^- \pi^0)$ . They are combined to give

$$\mathcal{B}(\tau^\pm \rightarrow e^\pm \nu \bar{\nu} \gamma)_{E_\gamma^* > 10 \text{ MeV}} = (1.82 \pm 0.02 \pm 0.10) \times 10^{-2}, \quad (9.6)$$

$$\mathcal{B}(\tau^\pm \rightarrow \mu^\pm \nu \bar{\nu} \gamma)_{E_\gamma^* > 10 \text{ MeV}} = (3.68 \pm 0.02 \pm 0.15) \times 10^{-3}, \quad (9.7)$$

where first error is statistic and second is systematic. We also obtained these branching ratio as a function of  $E_{\text{extra}}^{\text{LAB}}$  cut value as shown in Fig. 9.6.

### 9.4.1 Ratio of branching ratio $Q = \mathcal{B}(\tau^- \rightarrow e^- \nu \bar{\nu} \gamma) / \mathcal{B}(\tau^- \rightarrow \mu^- \nu \bar{\nu} \gamma)$

As summarized in Table 9.4, the dominant systematic contribution comes from the reconstruction efficiency correction for  $\pi^0$ . This uncertainty can be removed when we measure the ratio of branching

Table 9.4: List of various systematic contributions (%)

Item	$(e^- \gamma, \pi^+ \pi^0)$	$(e^+ \gamma, \pi^- \pi^0)$	$(\mu^- \gamma, \pi^+ \pi^0)$	$(\mu^+ \gamma, \pi^- \pi^0)$
$R_{\text{trg}}$	1.2	1.2	0.7	0.7
$R_{\gamma\text{ID}}$	1.0	1.0	0.4	0.4
$R_{\ell\text{ID}}$	1.9	1.9	1.1	1.1
$R_{\pi\text{ID}}$	0.7	0.7	0.7	0.7
$R_{\pi^0\text{ID}}$	3.6	3.6	3.3	3.3
$R_{\text{rec}}$	0.7	0.7	0.7	0.7
Luminosity	1.4	1.4	1.4	1.4
$\mathcal{B}(\tau \rightarrow \pi\pi^0\nu)$	0.4	0.4	0.4	0.4
$\sigma(ee \rightarrow \tau\tau)$	0.3	0.3	0.3	0.3
$f_{\text{bg}}$	1.3	1.3	1.5	1.5
Detector response	1.5	1.5	0.6	0.6
Ambiguity of $E_\gamma^*$ threshold	1.1	1.1	0.3	0.3
Model uncertainty	negligible	negligible	negligible	negligible
Total	5.3	5.3	4.3	4.3

Table 9.5: Systematic contributions due to detector response

Cut ID	Variation of selection criteria	$\Delta\mathcal{B}/\mathcal{B}$ (%)
<b>Electron mode</b>		
$E_\gamma^{\text{LAB}}$ threshold : $E_\gamma^{\text{LAB}} < 80$ MeV (or 100 MeV)	5 MeV	0.05
①: $\theta_e^{\text{LAB}} < 126^\circ$	$3.4^\circ$	0.01
②: $E_e^{\text{LAB}} > 1.5$ GeV	9 MeV/c	0.01
③: $M_{e\gamma} > 0.1$ GeV/c <sup>2</sup>	14 MeV/c <sup>2</sup>	1.3
④: $E_{\text{extray}}^{\text{LAB}} < 0.2$ GeV	50 MeV	0.7
Total		1.5
<b>Muon mode</b>		
$E_\gamma^{\text{LAB}}$ threshold : $E_\gamma^{\text{LAB}} < 80$ MeV (or 100 MeV)	5 MeV	0.05
⑤: $51^\circ < \theta_\mu^{\text{LAB}} < 117^\circ$	$1.7^\circ$	0.3
⑥: $\cos\theta_{\mu\gamma} > 0.99$	0.002	0.5
⑦: $E_{\text{extray}}^{\text{LAB}} < 0.3$ GeV	50 MeV	0.05
Total		0.6

Table 9.6: Summary of result

item	$(e^- \gamma, \pi^+ \pi^0)$	$(e^+ \gamma, \pi^- \pi^0)$	$(\mu^- \gamma, \pi^+ \pi^0)$	$(\mu^+ \gamma, \pi^- \pi^0)$
$N_{\text{obs}}$	$6188 \pm 79$	$6114 \pm 78$	$10458 \pm 102$	$11170 \pm 106$
$1 - f_{\text{bg}}^\dagger$ (%)	$70.2 \pm 0.9$	$70.2 \pm 0.9$	$71.5 \pm 1.0$	$71.5 \pm 1.0$
$\bar{\epsilon}^{\text{MC}}$ (%)	0.172	0.169	1.26	1.27
$\bar{R}$	$0.85 \pm 0.04$	$0.85 \pm 0.04$	$0.93 \pm 0.03$	$0.93 \pm 0.03$
$\bar{\epsilon}^{\text{EX}}$ (%)	$0.146 \pm 0.007$	$0.144 \pm 0.007$	$1.28 \pm 0.05$	$1.29 \pm 0.05$
$\mathcal{B}_{E_\gamma^* > 10 \text{ MeV}}$ (%)	$1.81 \pm 0.02 \pm 0.10$	$1.82 \pm 0.02 \pm 0.10$	$0.356 \pm 0.003 \pm 0.015$	$0.377 \pm 0.003 \pm 0.016$

<sup>†</sup> The definition of signal is different from the main analysis. In the measurement of the branching ratio, events generated as radiative leptonic decay and whose photon energy exceeds  $E_\gamma^* = 10 \text{ MeV}$  are inclusively treated as signal. Therefore, for instance, even if the bremsstrahlung of electron in  $\tau^- \rightarrow e^- \nu \bar{\nu} \gamma$  is reconstructed as signal photon, it is still categorized as signal.

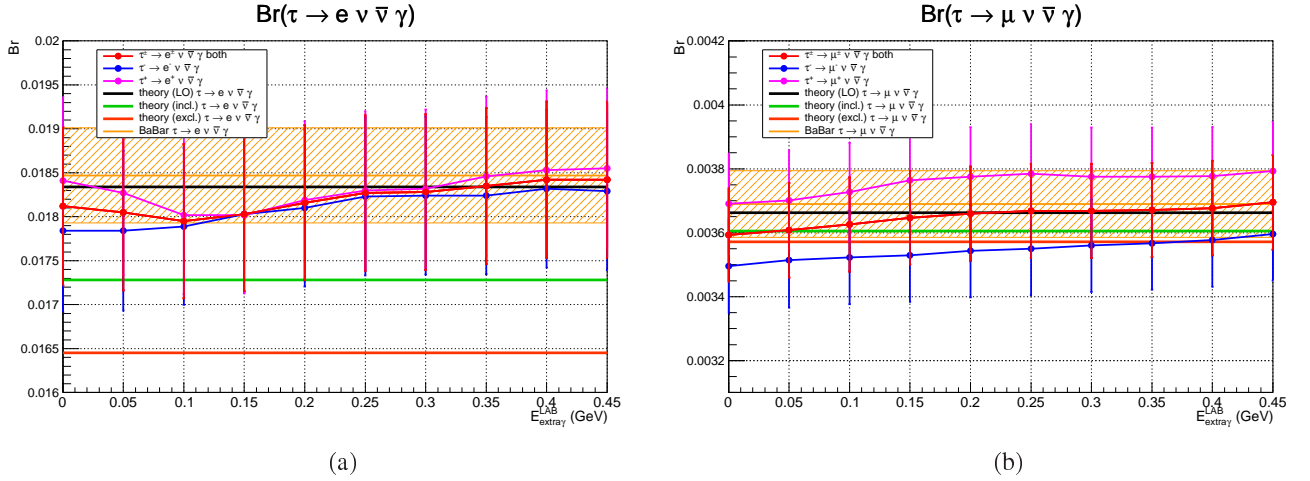


Figure 9.6: Branching ratio of  $\tau^- \rightarrow \ell^- \nu \bar{\nu} \gamma$  decay as a function of  $E_{\text{extray}}^{\text{LAB}}$  cut: (a)  $\ell = e$  and (b)  $\ell = \mu$ . Red, blue and magenta lines respectively represent branching ratio of  $\tau^\pm \rightarrow \ell^\pm \nu \bar{\nu} \gamma$ ,  $\tau^- \rightarrow \ell^- \nu \bar{\nu} \gamma$  and  $\tau^+ \rightarrow \ell^+ \nu \bar{\nu} \gamma$ . Orange region shows result of the measurement by BaBar [37]. Black, green and red lines are theoretical predictions for LO, inclusive and exclusive modes, respectively [40]. The error includes both statistical and systematic uncertainties.



Table 9.7: Comparison of the ratio  $Q$  ( $E_\gamma^* > 10$  MeV)

<b>Theory</b>	
Leading order	5.007
Next leading order incl.	4.793
Next leading order excl.	4.605
<b>Experiment</b>	
CLEO	$4.9 \pm 0.3 \pm 0.6$ [36]
BaBar	$5.01 \pm 0.06 \pm 0.19$ † [37]
This measurement	$4.95 \pm 0.06 \pm 0.20$

† Systematic uncertainty is naively calculated from reference values, where cancellation is not taken into account.

ratio  $Q = \mathcal{B}(\tau^- \rightarrow e^- \nu \bar{\nu} \gamma) / \mathcal{B}(\tau^- \rightarrow \mu^- \nu \bar{\nu} \gamma)$ . Moreover, other common systematic sources,  $R_{\text{rec}}$ ,  $R_{\pi\text{ID}}$ , the integrated luminosity, the branching ratio of  $\tau^+ \rightarrow \pi^+ \pi^0 \bar{\nu}$  decay and the cross section  $\sigma(e^+ e^- \rightarrow \tau^+ \tau^-)$  also disappear. The obtained ratio is

$$Q = \frac{\mathcal{B}(\tau^- \rightarrow e^- \nu \bar{\nu} \gamma)_{E_\gamma^* > 10 \text{ MeV}}}{\mathcal{B}(\tau^- \rightarrow \mu^- \nu \bar{\nu} \gamma)_{E_\gamma^* > 10 \text{ MeV}}} = 4.95 \pm 0.06 \pm 0.20, \quad (9.8)$$

where the first error is statistic and second is systematic. As the information of  $Q$  value is summarized in Table 9.7, our result well supports the LO calculation as well as the measurement of BaBar experiment.

## 9.5 Discussion

### 9.5.1 Treatment of double photons

As mentioned in the introduction, the branching ratio measurement by BaBar experiment is consistent with the theoretical LO calculation but not with NLO prediction for  $\tau^- \rightarrow e^- \nu \bar{\nu} \gamma$  decay mode. However, there is a room for discussion because of the treatment of two photons in NLO calculation. In Ref. [40], the authors define three types of decays: an *inclusive mode* is defined as an event which has at least one hard photon, an *exclusive mode* is defined as an event which has one and only one hard photon and *doubly decay* which has two hard photons. Here, the hard photon means the energy exceeds 10 MeV in  $\tau$  rest frame. Figure 9.7a shows a schematic view of the energy configuration of two photons.

In this measurement, we reject additional photons in two ways. First, if two photons whose energies exceed 80 MeV enter the cone around lepton direction, the events are rejected. However, even if two photons are generated inside the cone, their clusters in ECL can merge and behave as a single emission once both photons are produced towards almost same direction (typically a few degrees in laboratory frame). The other is a rejection using the extra gamma energy which is defined as a sum of all photon clusters which do not have associated charged tracks. Since the photon cluster candidates are determined if the energy exceed 40 MeV, a soft photon which does not reach this energy thresholds can survive from our selection criteria. Consequently, there is a possibility that we fail to reject additional photons if their energies are small. Here, it is worthy to note that these experimental thresholds are not so far from a threshold used in theoretical calculation (10 MeV) because the boost

of  $\tau$  by  $\gamma \sim 3$  causes an enhancement of photon energy in laboratory frame. This situation is drawn in Fig. 9.7b. Because of the factor of boost, the magnitude relationship between the experimental and theoretical energy thresholds is obscure but at least there is an additional region in  $(E_{\gamma_1}, E_{\gamma_2})$  plane in which we experimentally fail to veto the additional photon even if we attempt to measure the exclusive branching ratio. Thus above discussion may imply that experimental measurement should show a value between the exclusive and inclusive branching ratios. With current accuracy, we cannot conclude whether our result agrees with the prediction of inclusive branching ratio but it is reasonable to reject that of exclusive one.

To evaluate the effect of NLO effects more precisely, it is inevitable to update the generator of  $\tau^- \rightarrow \ell^- \nu \bar{\nu} \gamma$ . Current version of the TAUOLA generator does not take into account the NLO effects, hence the double emission of photons are not properly excluded, *i.e.*, the efficiency of a single emission of photon is neither well defined nor estimated. This improvements would be also important for muonic decay to reduce a possible systematic bias on the search for its lepton flavor violating decays like  $\mu^+ \rightarrow e^+ \gamma$  and  $\mu^+ \rightarrow e^+ e^- e^+$ . In Appendix D, we introduce the theoretical information of the doubly radiative decay with generated distributions of final state kinematic variables.

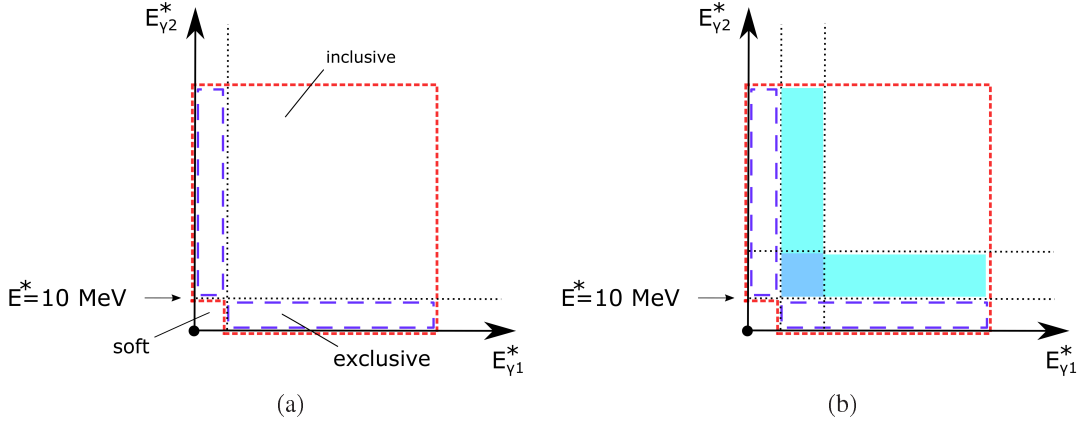


Figure 9.7: Schematic view of energy of two photons: (a) an inclusive mode is represented by a region enclosed by a red dashed-line while an exclusive mode is drawn by blue rectangles: (b) experimentally it is difficult to definitely reject weak photons even if they exceed the theoretical energy threshold, which result in a possibility to include filled region.

## 9.5.2 Anomalous four-point interaction

As pointed in Ref. [78], the kinematic properties of emitted photon reflects the inner structure of decay and thus the radiative leptonic decay can reveal a certain physics BSM in a different way from the ordinary leptonic decay. However, unfortunately, there are not so many available theoretical studies dedicated to the radiative mode.

We then consider the addition of anomalous four-point scalar and tensor interactions in the SM Lagrangian as:<sup>†</sup>

$$\mathcal{L} \supset \frac{g}{\sqrt{2}} W^\mu \left[ \bar{\psi}(v_\tau) \gamma_\mu \frac{1 - \gamma^5}{2} \psi(\tau) - \frac{ek_\tau^S}{m_\tau} A_\mu \bar{\psi}(v_\tau) \psi(\tau) + \frac{iek_\tau^T}{m_\tau} A^\nu \bar{\psi}(v_\tau) \sigma_{\mu\nu} \psi(\tau) \right] + \text{h.c.}, \quad (9.9)$$

where  $\kappa_\tau^S$  and  $\kappa_\tau^T$  characterize the magnitudes of these interactions. From theoretical point of view, the naive inclusion of Eq. (9.9) does not make sense due to the violation of Gauge invariance. However, there is a possibility that these terms can appear as parts of  $U(1) \otimes SU(2)$  symmetric interactions of  $\bar{\psi}(v_\tau) |D|^2 \psi(\tau)$  and  $\bar{\psi}(v_\tau) \sigma_{\mu\nu} i [iD^\mu, iD^\nu] \psi(\tau)$ , where  $D_\mu$  is the covariant differential operator.

<sup>†</sup> Similar interactions have been studied in the spectrum of  $\tau^- \rightarrow \ell^- \nu \bar{\nu}$  by DELPHI collaboration [79].

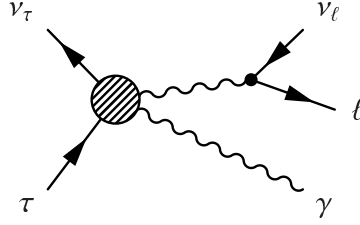


Figure 9.8: Feynman diagram of anomalous four point scalar and tensor interactions.

As the Feynman diagram is shown in Fig. 9.8, the anomalous interaction gives an additional amplitude of  $\mathcal{M}_a$  for  $\tau^- \rightarrow \ell^- \nu \bar{\nu} \gamma$  decay and interferes with that of the SM as:

$$|\mathcal{M}_{\text{tot}}|^2 = |\mathcal{M}_{\text{SM}} + \mathcal{M}_a|^2 \sim |\mathcal{M}_{\text{SM}}|^2 + 2\Re\{\mathcal{M}_{\text{SM}}\mathcal{M}_a^*\}, \quad (9.10)$$

where we ignored small factor of  $|\mathcal{M}_a|^2$ . The shift of spectrum by  $2\Re\{\mathcal{M}_{\text{SM}}\mathcal{M}_a^*\}$  is given by

$$\Delta \left( \frac{d\Gamma(\tau \rightarrow \ell \nu \bar{\nu} \gamma)}{dx dy d\Omega_\ell^* d\Omega_\gamma^*} \right)_S = -\frac{4m_\tau^5 G_F^2 \alpha \kappa_\tau^S x \beta_\ell^*}{3(4\pi)^6 z} \left[ -z \left\{ (1 + \lambda^2 - x - y + z)(z - 3x) + (y - z)(x - z - 2\lambda^2) \right\} + 3y(z - 2\lambda^2)(1 + \lambda^2 - x - y + z) \right], \quad (9.11)$$

for the scalar type interaction and

$$\Delta \left( \frac{d\Gamma(\tau \rightarrow \ell \nu \bar{\nu} \gamma)}{dx dy d\Omega_\ell^* d\Omega_\gamma^*} \right)_T = -\frac{4m_\tau^5 G_F^2 \alpha \kappa_\tau^T x \beta_\ell^*}{3(4\pi)^6 z} \left[ z(-3x + x^2 + 13xy - 9y + 9y^2) + z^2(-7x - 17y + 7) + 6z^3 + \lambda^2 \left\{ -18y + 18xy + 18y^2 + z(8 - 3x - 37y) + 9z^2 \right\} - 18\lambda^4 y \right], \quad (9.12)$$

for the tensor type interactions, where  $x$ ,  $y$ ,  $z$  and  $\lambda$  are normalized kinematic variables defined as  $x = 2E_\ell^*/m_\tau$ ,  $y = 2E_\gamma^*/m_\tau$ ,  $z = 2p_\gamma \cdot p_\ell/m_\tau^2 = xy(1 - \beta_\ell^* \cos \theta_{\ell\gamma}^*)/2$  and  $\lambda = m_\ell/m_\tau$ , respectively. Integrating the differential variables numerically in the phase space, we obtain

$$\Gamma(\tau^- \rightarrow \ell^- \nu \bar{\nu} \gamma)_{E_\gamma^* > 10 \text{ MeV}} = \Gamma_{E_\gamma^* > 10 \text{ MeV}}^{\text{SM}} \left( 1 + c_\ell \kappa_\tau^N \right), \quad (N = S, T) \quad (9.13)$$

$$c_e^S = 2.01 \times 10^{-3}, \quad (9.14)$$

$$c_\mu^S = 8.73 \times 10^{-3}, \quad (9.15)$$

$$c_e^T = 6.17 \times 10^{-3}, \quad (9.16)$$

$$c_\mu^T = 3.19 \times 10^{-2}. \quad (9.17)$$

Taking into account the good agreement of the observed branching ratio with that of the SM theoretical prediction,  $|\Delta\mathcal{B}(\tau^- \rightarrow \mu \nu \bar{\nu} \gamma)/\mathcal{B}(\tau^- \rightarrow \mu \nu \bar{\nu} \gamma)| < 4.3\%$  gives

$$|\kappa_\tau^S| < 4.9 \quad (68\% \text{ C.L.}), \quad (9.18)$$

$$|\kappa_\tau^T| < 1.3 \quad (68\% \text{ C.L.}) \quad (9.19)$$

This is the first attempt to constrain these coefficients.

# Chapter 10

## Future prospects and conclusion

### 10.1 Future experiment and expected improvements

The Belle II is an upgrade project of the Belle experiment using Super KEKB accelerator and Belle I detector, which is planning to start physics data taking from 2017. The key of the next-generation project is to achieve 40 times higher instantaneous luminosity than KEKB ( $L = 8.0 \times 10^{35} \text{cm}^{-2}\text{s}^{-1}$ ) and collect fifty times larger integrated luminosity. Using much more abundant data set of  $e^+e^- \rightarrow B\bar{B}$ ,  $e^+e^- \rightarrow \tau^+\tau^-$ ,  $e^+e^- \rightarrow c\bar{c}$ , etc, further precision tests of the SM will become available. Most notably, improvements of analyses whose uncertainties are statistical dominant will be main goals of this project. The measurement of  $\bar{\eta}$  and  $\xi\kappa$  is truly a part of this subject. In Table 10.1, we summarize the information of the upgrade.\*

Considering the improvement of the gain of statistics by a factor of 50, we can roughly expect seven times better statistical uncertainty than this analysis, accordingly the measurement of the  $\bar{\eta}$  and  $\xi\kappa$  will be systematic dominant. Here, we discuss possible solutions to maintain the sensitivity.

First of all, it is worth noting that many sources of the systematic uncertainties, which are listed in Table 7.1, are evaluated by fitting the Michel parameters with and without the effect of original sources of uncertainties. The variation of fitted  $\bar{\eta}$  and  $\xi\kappa$  values is taken as their effects on the Michel parameters. For this reason, the magnitude of such uncertainties largely depend on the sensitivity of fitted Michel parameters to the spectra of MC distribution, where amount of statistics of experimental events has a notable contribution to the precision. However, it will not be so straightforward to

\*For more details, see *e.g.* [82] (physics) and [83] (accelerator and detector).

Table 10.1: Upgrade of the Belle experiment

Item	Belle	Belle II
<b>Accelerator</b>	KEKB	Super KEKB
Beam Energy ( $E_{e^-}, E_{e^+}$ ) (GeV)	(8.0, 3.5)	(7.0, 4.0)
Current ( $I_{e^-}, I_{e^+}$ ) (A)	(1.6, 1.2)	(3.6, 2.6)
Instantaneous lumi. ( $\text{cm}^{-2}\text{s}^{-1}$ )	$2.1 \times 10^{34}$	$8.0 \times 10^{35}$
Integrated lumi. ( $\text{ab}^{-1}$ )	1.0	50
<b>Detector</b>	Belle	Belle II
Vertex detector	Four layers of SVD	Pixel [84] & strip [85] (2 + 4 lays.)
Tracking	CDC	Increase granularity of CDC [86]
PID	TOF & ACC	TOP [87] & ARICH [88]
Calorimeter	ECL	Improve readout electronics [89]
Computing	KEK main	International grid computing [90]

increase the statistics of MC events because a correct evaluation/validation of the procedure requires the generic  $\tau\tau$  MC sample, where various background modes are required to be simulated as well. In general, both detector simulation and store of data for generic  $\tau\tau$  MC events are very heavy and tend to be substantial problem.<sup>†</sup> In fact, in this analysis, we use generic MC sample that is only five times as large amount as that of real experiment. To maintain sensitivity for the Belle II analysis, it will be necessary to prepare at least several times (order of 5-10) larger amount of MC data sample than the statistics of real Belle II experiment.<sup>‡</sup> Moreover, even in the situation of Belle analysis, we need approximately ten hours to calculate the PDFs using fifty CPUs. To accommodate 50 times larger processing, new breakthrough in the handling of computation would be required. At the time of writing, a use of graphical processing unit (GPU) receives more and more people's attention. GPU was originally developed to calculate huge amount of simple data for the graphics of computer games but nowadays they are made use of in many science fields like a neural network, an economics, a liquid simulation and so on. Their excellent cost performance may realize the huge amount of calculation.

Second, the 50 times larger data set may enable us to adopt more stringent selection criteria so as to increase the purity of signal within a realistic statistical uncertainty. In this analysis, we are required to retain both selection efficiency and purity then resulting statistical and systematic errors are almost compatible. However, it is not impossible to apply more strong selection criteria. For example, the contamination from the extra bremsstrahlung for  $\tau \rightarrow e\nu\bar{\nu}\gamma$  candidates can be reduced by applying a selection criteria for the invariant mass of lepton and photon  $m_{e\gamma}$ . As shown in Fig. 10.1, the extra bremsstrahlung can be excluded once we require  $m_{e\gamma} > 0.1 - 0.2$  GeV though this drastically degrades the efficiency. Similarly, for muon mode, a stringent cut on the  $\cos\theta_{\mu\gamma}$  (*e.g.*  $\cos\theta_{\mu\gamma} > 0.99$ ) may be reasonable. Nevertheless, as described in Sec. 5.6.2, the sensitivity of the Michel parameters generally depends on a specific selection cut even if statistics is same. Therefore, cautious study of the sensitivity may be important. In fact, as mentioned in Ref. [91], the sensitivity of effect BSM would be maximum around  $\theta_{\mu\gamma} \sim 180^\circ$ . Therefore, it will be reasonable to allow events like  $|\cos\theta_{\mu\gamma}| > 0.98$  to enhance sensitivity. However, it is worth to mention that this indicates a contamination from background in this region also highly affects the fitted Michel parameters.

Third, as the method described in Sec. 5.4.3 and mentioned in Sec. 5.6.3, dedicated treatment of backgrounds which is currently classified as *others* are necessarily to achieve further precision. The simplification of the  $T = B_{\text{sel}}/S_{\text{sel}}$  into products of subsets of  $T$ s generally discards the high-dimension correlations in the phase space and delivers a systematic bias. There are some possible strategies to overcome this situation. Using more abundant data, it is possible to tabulate the subset of  $T$ s in larger dimension of phase space. In this analysis, we tabulate the subset as a function of three variables at maximum. We may be able to extend up to four variables. Another possibility is to find more precise way of the reduction of  $T$ . Although the dimension of phase space is fixed to be twelve, the possible definition of  $T$  is almost infinity, hence trial and error are inevitable. Modern computer technologies like *deep learning* may help this discovery.

Finally, to realize precise analyses of radiative decays (not only  $\tau \rightarrow \ell\nu\bar{\nu}\gamma$  but also other processes like  $\tau \rightarrow \mu\gamma$ ,  $b \rightarrow s\gamma$ ) in the environment of forty times as large instantaneous luminosity as Belle, the suppression of beam background plays a crucial role in their successes. Since physics processes such as radiative Bhabha scattering  $ee \rightarrow ee\gamma$  and ISR emission are proportional to luminosity, their existence does not cause a substantial increase of the systematic effects while the beam background may be much stronger than the factor of forty. To overcome the (possibly) severe situation of the beam background, the readout electronics of the Belle II ECL will be upgraded, where waveform signals from the PIN photo diodes attached on the CsI crystal are fitted to detect the hit timing precisely. The requirement of the correspondence of the hit and collision timing using this new

<sup>†</sup>The amount of data for  $703 \text{ fb}^{-1}$  (whole available  $\Upsilon(4S)$  data) of generic MC is approximately 5 TB.

<sup>‡</sup>This corresponds to  $\sim 2$  PB when Belle MC is assumed.

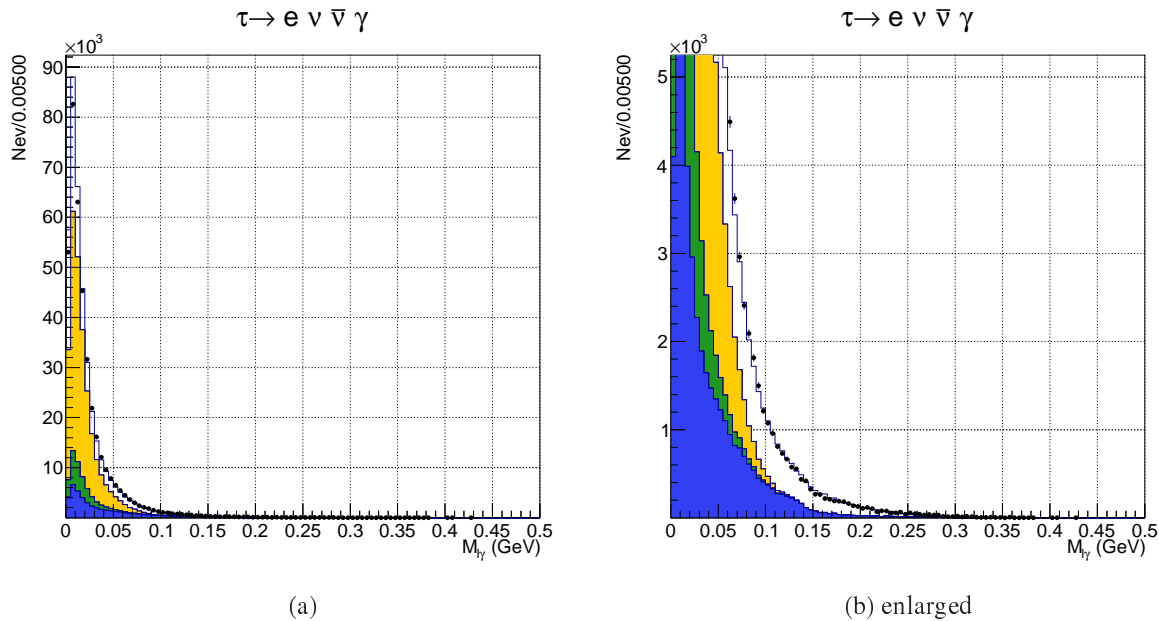


Figure 10.1: Distribution of the invariant mass of electron and photon  $m_{e\gamma}$  for  $\tau^- \rightarrow e^- \nu \bar{\nu} \gamma$  candidate: (a) overall view (b) enlarged view. As explained in Chapter 4, yellow and green histogram represent the extra bremsstrahlung.

technique may give a significant improvement in the purity. Even at Belle, in some latter period, it is not impossible to access the hit time information but we did not use them.

Taking into account all facts listed above, it is not far from realistic to expect an improvement of systematic uncertainty by the same gain as statistical, *i.e.*, a gain of the factor of  $\sqrt{50} \sim 7$ .

## 10.2 Conclusion

We present a measurement of the Michel parameters  $\bar{\eta}$  and  $\xi\kappa$  of the  $\tau$  lepton using  $703 \text{ fb}^{-1}$  of  $\Upsilon(4S)$  beam energy data collected with the Belle detector at the KEKB  $e^+e^-$  collider. The Michel parameters are fundamental nature of  $\mu$  and  $\tau$  leptons, which characterize the spectra of daughter particles from their leptonic decays. The generalized amplitude of leptonic decays is written as a superposition of ten contributions, in which the scalar, vector and tensor interactions are summed for each configuration of chiralities of mother and daughter charged leptons. The Michel parameters are defined as bilinear combinations of the dimensionless coupling constants of ten amplitudes. The comparison of experimentally measured Michel parameters vs the Standard Model prediction is thus the model independent verification of physics beyond the Standard Model.

The *ordinary* Michel parameters  $\rho$ ,  $\eta$ ,  $\xi$  and  $\xi\delta$  have been precisely measured in  $\tau^- \rightarrow \ell^- \nu \bar{\nu}$  ( $\ell = e$  or  $\mu$ ) and their previous measured values are consistent with the Standard Model predictions. Whereas,  $\bar{\eta}$  and  $\xi\kappa$  parameters can be measured only if we observe a photon from leptonic decay, or *radiative decay*,  $\tau^- \rightarrow \ell^- \nu \bar{\nu} \gamma$ . The angular distribution of photon with respect to the daughter lepton movement indirectly exposes the polarization of daughter lepton and this enables us to understand another aspect of internal structure of the weak interaction.

$\bar{\eta}$  and  $\xi\kappa$  parameters are extracted from the radiative leptonic decay  $\tau^- \rightarrow \ell^- \nu \bar{\nu} \gamma$  and the tagging  $\rho$  decay  $\tau^+ \rightarrow \rho^+ (\rightarrow \pi^+ \pi^0) \bar{\nu}$  of the partner  $\tau^+$  to exploit the spin-spin correlation in  $e^+e^- \rightarrow \tau^+ \tau^-$ . Because of the suppression of sensitivity from the small mass of electron,  $\bar{\eta}$  parameter is extracted

only from  $\tau^- \rightarrow \mu^- \nu \bar{\nu} \gamma$  mode.  $\bar{\eta}$  and  $\xi\kappa$  are simultaneously fitted to the kinematic distribution to be

$$\bar{\eta}^\mu = -1.3 \pm 1.5 \pm 0.8 \quad (10.1)$$

$$(\xi\kappa)^\mu = 0.8 \pm 0.5 \pm 0.3. \quad (10.2)$$

In the electron mode,  $\xi\kappa$  is fitted by fixing  $\bar{\eta}$  value to the Standard Model prediction of  $\bar{\eta} = 0$  and the optimal value is

$$(\xi\kappa)^e = -0.4 \pm 0.8 \pm 0.9. \quad (10.3)$$

The first errors are statistical and the second are systematic. This is the first measurement of both parameters for the  $\tau$  lepton. These values are consistent with the SM expectation within the errors.

Based on the measured values of  $\bar{\eta}$  and  $\xi\kappa$ , we obtained the upper limit of the coupling constant on  $g_{ij}^N$ s. Combining linear combination of  $\rho$  and  $\xi\kappa$  values we obtain

$$|g_{RL}^T| < 0.55 \quad (95\% \text{ C.L.}) \quad (10.4)$$

From observed  $\xi\kappa$  value, we also tried to obtain upper limit of the normalized probability that  $\tau$  lepton couples with a right-handed daughter lepton as

$$Q_R^\tau < 2.4 \quad (95\% \text{ C.L.}) \quad (10.5)$$

This is the first experimental constraint for the tau lepton.

To make the measurement of  $\bar{\eta}$  and  $\xi\kappa$  have further significant impacts on the theories BSM, it is desired to perform more precise measurement using next generation experiments. In the improvements of the accuracy of these measurements, it is necessary to reduce systematic uncertainties, which is already competitive to statistical uncertainties of Belle data sample. The key of the improvements will be treatment huge amount of data of the MC as well as the real experiment using modern technologies of the computing.

Further optimizing the selection criteria, we also measured the branching ratio of radiative decays  $\tau^- \rightarrow \ell^- \nu \bar{\nu} \gamma$ . The results are

$$\mathcal{B}(\tau^\pm \rightarrow e^\pm \nu \bar{\nu} \gamma)_{E_\gamma^* > 10 \text{ MeV}} = (1.82 \pm 0.02 \pm 0.10) \times 10^{-2}, \quad (10.6)$$

$$\mathcal{B}(\tau^\pm \rightarrow \mu^\pm \nu \bar{\nu} \gamma)_{E_\gamma^* > 10 \text{ MeV}} = (3.68 \pm 0.02 \pm 0.15) \times 10^{-3}, \quad (10.7)$$

where the first error is statistic and second is systematic. These values are consistent with the results by BaBar experiment.

To reduce various systematic effects, in particular from  $\pi^0$  reconstruction efficiency, we obtained a ratio of the branching ratio

$$Q = \frac{\mathcal{B}(\tau^- \rightarrow e^- \nu \bar{\nu} \gamma)_{E_\gamma^* > 10 \text{ MeV}}}{\mathcal{B}(\tau^- \rightarrow \mu^- \nu \bar{\nu} \gamma)_{E_\gamma^* > 10 \text{ MeV}}} = 4.95 \pm 0.06 \pm 0.20, \quad (10.8)$$

where the first error is statistic and second is systematic. The magnitude of systematic uncertainty slightly improves to give  $\Delta Q/Q = 4.0\%$ . This result does not change the conclusion described above.

The results are consistent with the leading order theoretical calculation, whereas, similarly to the result of BaBar experiment, in the electron mode the measured branching ratio does not prefer the exclusive branching ratio that is predicted by taking into account the NLO contribution. Though we veto the multiple photon candidates by the selection criteria, due to the photon energy threshold, the experimentally measured value should not be regarded as an ideal exclusive mode and indeed, it is

more plausible to think it of the middle between the exclusive and inclusive modes. This arises from the ignorance of the multiple photon emissions at the stage of event generation and the implementation of NLO formalism in the TAUOLA generator is required to do further analysis.

Based on the agreement of observed branching ratio of radiative decay, we attempt to constrain the coupling constants of anomalous four-point scalar and tensor interactions. Integrating the differential decay width due to interference between the anomalous and the SM amplitudes, we evaluate the expected shift of branching ratio and obtained upper limits are  $|\kappa_\tau^S| < 4.9$  (68% C.L) and  $|\kappa_\tau^T| < 1.3$  (68% C.L). This is the first attempt to constrain the four-point interactions.



# Bibliography

- [1] ATLAS Collaboration, Phys. Lett. **B716**, 1 (2012).
- [2] CMS Collaboration, Phys. Lett. **B716**, 30 (2012).
- [3] Y. Fukuda, *et al.*, Phys. Rev. Lett. **81**, 1562 (1998).
- [4] K. Abe, *et al.*, Phys. Rev. **D88**, 032002 (2013).
- [5] K. G. Wilson, Phys. Rev. **D3**, 15 (1971).
- [6] G. W. Bennett, *et al.*, Phys. Rev. Lett. **92**, 161802 (2004).
- [7] K. A. Olive, *et al.*, (Particle Data Group), Chin. Phys. **C38**, 090001 (2014).
- [8] (German) E. Fermi, Z. Physik, **88**, 161 (1934).
- [9] (English) F. L. Wilson, Am. J. Phys. **36**, 1150 (1968).
- [10] C. S. Wu, *et al.*, Phys. Rev. **105**, 1413 (1957).
- [11] M. Ruderman and R. Finkelstein, Phys. Rev. **76**, 1458 (1949).
- [12] T. Fazzini, *et al.*, Phys. Rev. Lett. **1**, 247 (1958).
- [13] G. Czappek, *et al.*, Phys. Rev. Lett. **70**, 17 (1993).
- [14] W. J. Marciano and A. Sirlin, Phys. Rev. Lett. **36**, 1425 (1976).
- [15] S. Weinberg. Phys. Rev. Lett. **19**, 1264 (1967).
- [16] G. Abbiendi, *et al.*, Eur. Phys. J. **C19**, 587 (2001).
- [17] W. Fetscher, H. J. Gerber, K. F. Johnson, Phys. Lett. **B173**, 102 (1986).
- [18] W. Fetscher, H. J. Gerber, Adv. Ser, Direct. High Energy Phys. 14 657 (1995).
- [19] N. Danneberg, *et al.*, Phys. Rev. Lett. **94**, 021802 (2005).
- [20] R. Bayes *et al.*, (TWIST Collaboration), Phys. Rev. Lett. **106**, 041804 (2011).
- [21] J. F. Bueno *et al.*, (TWIST Collaboration), Phys. Rev. **D84**, 032005, (2011).
- [22] W. Eichenberger *et al.*, Nucl. Phys. **A412**, 523, (1984).
- [23] H. Burkard *et al.*, Phys. Lett. **B160**, 343, (1985).
- [24] A. Heister, S. Schael, *et al.*, Eur. Phys. J. **C22**, 217 (2001).

- [25] J. P. Alexander, *et al.*, Phys. Rev. D**56**, 5320 (1997).
- [26] M. L. Perl, arXiv:9812400 (1998).
- [27] C. Fronsdal, H. Uberall, Phys. Rev. **113**, 654 (1939).
- [28] A. B. Arbuzov, *et al.*, arXiv:1605.06612 (2016).
- [29] N. Shimizu *et al.*, Nucl. Instrum. Meth. A**824**, 11, 237 (2016).
- [30] W. Fetscher and H. J. Gerber, ETHZ IMP PR-93-1 (1993).
- [31] A. Stahl and H. Voss, Z. Phys. C**74**, 73 (1997).
- [32] J. Polak and M. Zralek, Phys. Rev. D**46**, 3871 (1992).
- [33] A. Stahl, Nucl. Phys. B**76**, 173 (1999).
- [34] R. Prieelset *et al.*, Phys. Rev. D**90**, 112003, (2014).
- [35] A. Rougé "Tau Decays as Polarization Analysers" Proceedings of Tau Lepton Physics (1990).
- [36] T. Bergfeld, *et al.*, Phys. Rev. Lett. **84**, 830 (2000).
- [37] J. P. Lees, *et al.* Phys. Rev. D **91**, 051103.
- [38] T. Kinoshita and A. Sirlin, Phys. Rev. **113**, 6 (1958).
- [39] T. Kinoshita and A. Sirlin, Phys. Rev. Lett. **2**, 177 (1959).
- [40] M. Fael, *et al.*, JHEP. 07. 153 J (2015).
- [41] R. Barate, *et al.*, Eur. Phys. J. C**3** **2**, 395.
- [42] S. Kurokawa and E. Kikutani, Nucl. Instrum. Meth. A**499**, 1 (2003).
- [43] A. Abashian, *et al.*, Nucl. Instrum. Meth. A**479**, 117 (2002).
- [44] H. Aihara, *et al.*, Nucl. Instrum. Meth. A**568**, 269 (2006).
- [45] H. Hirano, Nucl. Instrum. Meth. A**455**, 294 (2000).
- [46] Radeka, Veljko. Annu. Rev. Nucl. Part. Sci. **38.1**, 217 (1988).
- [47] Y. Ohshima, *et al.*, Nucl. Instrum. Meth. A**380**, 517 (1996).
- [48] T. Iijima, *et al.*, Nucl. Instrum. Meth. A**379**, 457 (1996).
- [49] T. Sumiyoshi, *et al.*, Nucl. Instrum. Meth. A**433**, 385 (1999).
- [50] H. Kichimi, *et al.*, Nucl. Instrum. Meth. A**453**, 315 (2000).
- [51] A. Abashian, *et al.*, Nucl. Instrum. Meth. A**449**, 112 (2000).
- [52] H. J. Kim, *et al.*, Nucl. Instrum. Meth. A**457**, 634 (2001).
- [53] A. J. Bevan, *et al.*, Eur. Phys. J. C**74**, 3026 (2014).
- [54] K. Hanagaki *et al.*, Nucl. Instrum. Meth. A**485**, 490 (2002).

- [55] A. Abashian *et al.*, Nucl. Instrum. Meth. **A491**, 69 (2002).
- [56] S. Jadach, *et al.*, Comput. Phys. Commun. **130**, 260 (1993).
- [57] S. Jadach, *et al.*, Comput. Phys. Commun. **64**, 275 (1993).
- [58] S. Jadach, *et al.*, Comput. Phys. Commun. **70**, 69 (1992).
- [59] S. Jadach, *et al.*, Comput. Phys. Commun. **76**, 361 (1993).
- [60] E. Barberio and Z. Waş, Comput. Phys. Commun. **79**, 291 (1994).
- [61] S. Uehara, KEK Report 96-11 (1996).
- [62] R. Brun, *et al.*, CERN-DD-78-2 (1978).
- [63] Y. S. Tsai, *et al.*, Phys. Rev. **D4** 2821 (1971).
- [64] S. Anderson *et al.* (CLEO Collaboration), Phys. Rev. **D61**, 112002 (2000).
- [65] S. Jadach, J. H. Kühn and Z. Waş, Comput. Phys. Commun. **64**, 275 (1991).
- [66] H. W. Koch and J. W. Motz Rev. Mod. Phys. **31**, 4 (1959).
- [67] S. Jadach and Z. Waş, Acta. Phys. Pol. **B15** No. 12 (1984).
- [68] A. B. Arbuzov, *et al.*, JHEP. **10**, 1 (1997).
- [69] A. B. Arbuzov, *et al.*, Eur. Phys. J. **C46**, 689 (2006).
- [70] D. M. Schmidt, *et al.*, Nucl. Instrum. Meth. **A328**, 547 (1993).
- [71] E. A. Kuraev, V. S. Fadin, Sov. J. Nucl. Phys. **41**, 466 (1985).
- [72] B. A. Shwartz *Calorimetry in particle physics*, 182 (2002).
- [73] M. Davier, *et al.*, Phys. Let. **B306**, 411 (1993).
- [74] J. Heinrich eConf **C030908**, MOCT001 (2003).
- [75] M. Williams, JINST**5**, P09004 12010 (2010).
- [76] B. Aslan and G. Zech, Stat. Comp. Simul. **75**, 109 (2004).
- [77] S. Banerjee, *et al.*, Phys. Rev. **D77**, 054012 (2008).
- [78] M. L. Perl, arXiv:1605.06612 (2016).
- [79] P. Abreu, *et al.*, Eur. Phys. J. **C16**, 229 (2000).
- [80] R. N. Mohapatra and J. C. Pati, Phys. Rev. **D11**, 2558 (1975).
- [81] J. C. Pati and A. Salam. Phys. Rev. **D10**, 275 (1974).
- [82] T. Aushev, *et al.*, arXiv:1002.5012 (2009).
- [83] T. Abe, *et al.*, arXiv:1011.0352 (2010).
- [84] M. Boronat, Nucl. Part. Phys. Proc. **273-275**, 982 (2016).

- [85] C. Irmeler, *et al.*, JINST **8**, C01014 (2013).
- [86] N. Taniguchi, *et al.*, Nucl. Instrum. Meth. A**732**, 540 (2013).
- [87] Y. Horii, PoS, EPS-HEP, 500 (2013).
- [88] S. Iwata, *et al.*, Prog. Theor. Exp. Phys. 033H01 (2016).
- [89] V. Aulchenko, *et al.*, J. Phys. Conf. Ser. **587**, 012045 (2015).
- [90] S. Pardi, *et al.*, Nucl. Part. Phys. Proc. **273-275**, 950 (2016).
- [91] M. L. Laursen, *et al.* Phys. Rev. D**29**, 2652 (1984).
- [92] M. Yokoyama, Ph.D thesis (2002).
- [93] D. M. Asner, *et al.*, Phys. Rev. D**61**, 012002 (2000).
- [94] S. Jadach and J. H. Kühn, Comput. Phys. Commun. **76**, 361 (1993).
- [95] K. Tamai, KEK Preprint 2003-14 (2003).
- [96] M. Fael, *et al.*, publication under preparation.
- [97] J. Polak and M. Zral'ek, Nucl. Phys. B**363**, 385 (1991).

# Acknowledgments

In completing my Ph.D. thesis, I have been supported by various people and a wonderful environment in many ways. First of all, I would like to extend my greatest gratitude to the lucky destiny that led to me meeting my beloved cat. As Figure Ack.1 shows, she happily chose to be a new member of my family rather than remaining in her life as a stray cat. Her existence always makes us calm and inspires us to remember the importance of our lives. This gives us the patience and persistence to overcome various challenges including, of course, physics research.

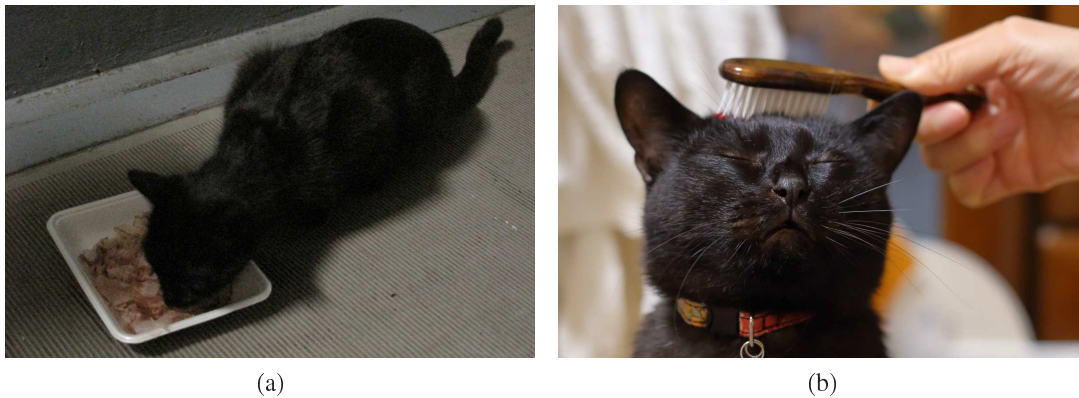


Figure Ack.1: My beloved cat: (a) A homeless cat came to our house in the summer of 2011. (b) She is usually happy just on her own but brushing her seems to be an exception.

I also want to thank all the staff of the Aihara/Yokoyama laboratory group for their daily education and support. H. Aihara gave me a precious environment for research and much constructive advice. It was his many gifts that enabled me to complete my Ph.D. work. The enormous educational effort of my supervisor M. Yokoyama also helped me to grow up from an egg of a physicist. In writing this thesis, he kindly checked my draft and gave me many useful suggestions and comments in spite of the heavy burden of his office work as well as his research (this analysis is not directly related to his main research subject). I chose this laboratory mainly because I was fond of his personality and now I deeply realize that this was not the wrong decision. It is an honor for me to be one of the first Ph.D. students to graduate from his laboratory. Y. Onuki also helped and sustained me for a long time. In particular, to receive my master diploma, his educational advice about the development of the silicon vertex detector for Belle II were essential. I strongly believe that it would have been impossible to understand the basics of mechanics (which are necessary for detector construction) without his support.

I would like to show my special and deepest thanks to D. Epifanov, who was a former staff member of the Aihara group before moving to BINP (Budker Institute of Nuclear Physics) in the Autumn of 2015. Although he was also very busy with his own research (the measurement of Michel parameters  $\rho$ ,  $\eta$ ,  $\xi$  and  $\xi\delta$ ), he kindly spared his precious time and allowed me to share in his enormous ideas, techniques and even his passion for physics. In particular, the huge number of lines of the calculation of the differential decay width reminds me of the importance of concentration and effort in achieving a precious result. I have never seen such a gentle and patient person as him.

I am grateful for efforts of not only the present but also the former collaborators who participated in the Belle group. All of their hard work helped realize such a precious analysis. In particular, I would like to express my respect to S. I. Eidelman, T. Browder, K. Hayasaka, Y. Kwon, M. Nakao, S. Nishida, L. Piilonen, Y. Sakai and S. Uehara. They gave me numerous advice and suggestions for my study.

I also would like to appreciate my colleagues of our laboratory, IPMU and so on: M. Alejandro, J. Changwoo, N. Chikuma, T. Higuchi, F. Hosomi, T. Horiguch, Y. Jin, Y. Kakichi, R. Kameswara, T. Koga, K. Kono, T. Lou, H. Madokoro, S. Mineo, H. Miyatake, S. Mochida, T. Morii, H. Niikura, T. Ose, J. Sasaki, N. Sato, Y. Seino, Y. Suda, R. Tamura, T. Yoshinobu, H. Wakana, K. Wan and I. Watson. All of them encouraged me at every moment in a variety of ways, from serious physics discussions to a daily chat. The step-by-step piling up of these experiences and their cooperation certainly strengthened me. In particular, discussions with N. Chikuma, T. Koga and J. Sasaki were sometimes really exciting and fruitful for my growth. Moreover, I. Watson kindly helped me revise English phrases for several publications, which turned out to be valuable chance for me to receive corrections from a native speaker.

I owe an important debt to the research fellows of the Japan Society for the Promotion of Science, which kindly supported my life as a doctoral student and funded me for the advancement of our research. Thanks to the valuable financial support, I was able to concentrate on extending the wisdom of human beings. I am proud to be a fellow of this institution.

In the diploma defense, the committee members kindly checked my thesis and gave me many essential suggestions and comments. I would like to express my greatest appreciation for Y. Hayato (chair), K. Hamaguchi, T. Mori, H. Sakurai and J. Tanaka.

Finally, I want to express my gratitude to Canon and Sigma corporations for their excellent cameras and lenses. The Canon EOS 6D, which is the cheapest and lightest full-frame format single-lens reflex camera at the time of writing, delivered a huge number of wonderful pictures with a lot of memories of my doctoral course. Sigma has been producing numerous remarkable lenses with amazing cost performance like, the 50mm F1.4 DG HSM and the 24mm F1.4 DG HSM, which are very helpful for students who are not economically privileged. These gadgets indirectly supported my research by inspiring my curiosity and passion.

Now, it's over. Thank you all!<sup>§</sup>

---

<sup>§</sup>I borrowed this phrase from Ref. [92]

# Appendix A

## Measurement of the branching ratio

### $\mathcal{B}(\tau^- \rightarrow \ell^- \nu \bar{\nu} \gamma)$ (validation)

As one of a validation of our procedures, we measure the branching ratio of  $\tau^- \rightarrow \ell^- \nu \bar{\nu} \gamma$  decay for  $\ell = e$  or  $\mu$ . The agreement of the branching ratio with previous measurements tells us the additional consistency for the estimation of  $R$  as well as an evaluation of backgrounds contamination for  $\tau^- \rightarrow \ell^- \nu \bar{\nu} \gamma$  decays.

#### A.1 Method and evaluation of systematic uncertainties

Taking into account the confirmation purpose of this measurement, we must use completely same selection criteria as that of the measurement of Michel parameters. The method of the measurement of the branching ratio and its systematic uncertainty are same as presented in Chapter 9. Since it is difficult to define the sideband region, we use same value as a difference of background amount described in Chapter 9. Taking into account a fraction of backgrounds, estimated systematic effect on the purity  $f_{\text{bg}}$  is 2.9% and 2.1% for electron and muon modes, respectively. In Table A.1, we summarize the contributions of the systematic uncertainties for each item.

#### A.2 Result

Table A.2 shows information of extracted values. Based on these information, we obtain that  $\mathcal{B}(\tau^- \rightarrow e^- \nu \bar{\nu} \gamma) = (1.83 \pm 0.00 \pm 0.11)\%$  and  $\mathcal{B}(\tau^- \rightarrow \mu^- \nu \bar{\nu} \gamma) = (0.348 \pm 0.001 \pm 0.019)\%$ . This result agrees with the measurement by BaBar experiment.

#### A.3 Discussion and conclusions

##### A.3.1 $E_{\text{extray}}^{\text{LAB}}$ dependence

The inconsistency of the experimental result with the NLO theoretical prediction may come from double emission of photons. The stability of the measurement towards the extra gamma energy  $E_{\text{extray}}^{\text{LAB}}$  cut is useful prove of the verification of this effect because the additional emission of photons is suppressed by this cut. We measure the branching ratio for samples separately selected by different extra gamma energy cut from 0.00 GeV to 0.45 GeV with 0.05 GeV step. Since  $E_{\text{extray}}^{\text{LAB}}$  is defined as a sum of energy of separate photon clusters which exceeds 40 MeV in laboratory frame, the selection with  $E_{\text{extray}}^{\text{LAB}} = 0$  GeV means we do not allow any photon clusters in the event occurrence. Figure A.1 shows the dependence of the branching ratio on the extra gamma energy cut. Since the statistics

Table A.1: Summary of systematic contributions (%)

item	$(e^- \gamma, \pi^+ \pi^0)$	$(e^+ \gamma, \pi^- \pi^0)$	$(\mu^- \gamma, \pi^+ \pi^0)$	$(\mu^+ \gamma, \pi^- \pi^0)$
$R_{\text{trg}}$	2.8	2.8	1.8	1.8
$R_{\gamma\text{ID}}$	0.6	0.6	1.7	1.7
$R_{\ell\text{ID}}$	3.0	3.0	2.8	2.8
$R_{\pi\text{ID}}$	0.7	0.7	0.6	0.6
$R_{\pi^0\text{ID}}$	3.5	3.5	3.5	3.5
$R_{\text{rec}}$	0.7	0.7	0.7	0.7
Luminosity	1.4	1.4	1.4	1.4
$\mathcal{B}(\tau^+ \rightarrow \pi^+ \pi^0 \bar{\nu})$	0.4	0.4	0.4	0.4
$\sigma(e^+ e^- \rightarrow \tau^+ \tau^-)$	0.3	0.3	0.3	0.3
$f_{\text{bg}}$	2.9	2.9	2.1	2.1
Total	6.4	6.4	5.8	5.8

Table A.2: Summary of result

item	$(e^- \gamma, \pi^+ \pi^0)$	$(e^+ \gamma, \pi^- \pi^0)$	$(\mu^- \gamma, \pi^+ \pi^0)$	$(\mu^+ \gamma, \pi^- \pi^0)$
$N_{\text{obs}}$	$391954 \pm 626$	$384880 \pm 620$	$35198 \pm 188$	$35973 \pm 190$
$1 - f_{\text{bg}}^\dagger$ (%)	$33.0 \pm 1.1$	$33.0 \pm 1.1$	$57.4 \pm 1.3$	$57.4 \pm 1.3$
$\bar{\epsilon}^{\text{MC}}$ (%)	4.825	4.786	3.880	3.859
$\bar{R}$	$0.89 \pm 0.05$	$0.89 \pm 0.05$	$0.92 \pm 0.05$	$0.92 \pm 0.05$
$\bar{\epsilon}^{\text{EX}}$ (%)	$4.28 \pm 0.24$	$4.25 \pm 0.23$	$3.58 \pm 0.19$	$3.56 \pm 0.18$
$\mathcal{B}$ (%)	$1.84 \pm 0.00 \pm 0.12$	$1.82 \pm 0.00 \pm 0.12$	$0.344 \pm 0.002 \pm 0.020$	$0.353 \pm 0.002 \pm 0.020$

<sup>†</sup> The definition of signal is different from the main analysis. In the measurement of the branching ratio, events generated as radiative leptonic decay and whose photon energy exceeds  $E_\gamma^* = 10$  MeV are inclusively treated as signal. Therefore, for instance, even if the external bremsstrahlung of electron in  $\tau \rightarrow e \nu \bar{\nu} \gamma$  is reconstructed as signal photon, it is still categorized as a signal.

have overlaps, they are systematically correlated each other. The variation of the branching ratios towards the different extra gamma energy cut are within the range of uncertainties. These stabilities of the branching ratio imply that the measurements are more or less strong for the contaminations from backgrounds because different cut value generally changes the fractions of various background modes. Here, we can see a good agreement with the theoretical leading order calculation while it is difficult to judge which next-leading order calculation is more preferable, namely, an inclusive or an exclusive branching ratio.\* Our result is consistent with measurement by BaBar experiment [37] within its uncertainty.

### A.3.2 Conclusions

As one of a validation of the procedures of the measurement of the Michel parameters, we measure branching ratio of  $\tau^- \rightarrow \ell^- \nu \bar{\nu} \gamma$  decay using tagged  $\tau^+ \rightarrow \pi^+ \pi^0 \bar{\nu}$  decay. The observed results are  $\mathcal{B}(\tau^- \rightarrow e^- \nu \bar{\nu} \gamma) = (1.83 \pm 0.00 \pm 0.10)\%$  and  $\mathcal{B}(\tau^- \rightarrow \mu^- \nu \bar{\nu} \gamma) = (0.348 \pm 0.001 \pm 0.019)\%$ . Since the selection criteria is not optimized for the branching ratio measurement, the systematic effects turn

\*For these definitions, see Sec. 2.3 or Sec. 9.5



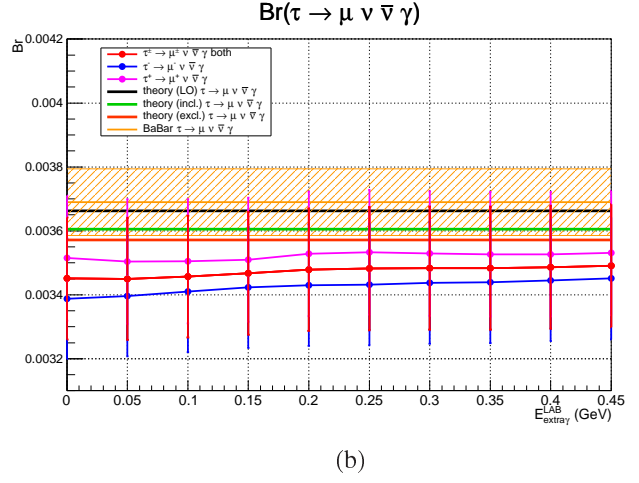
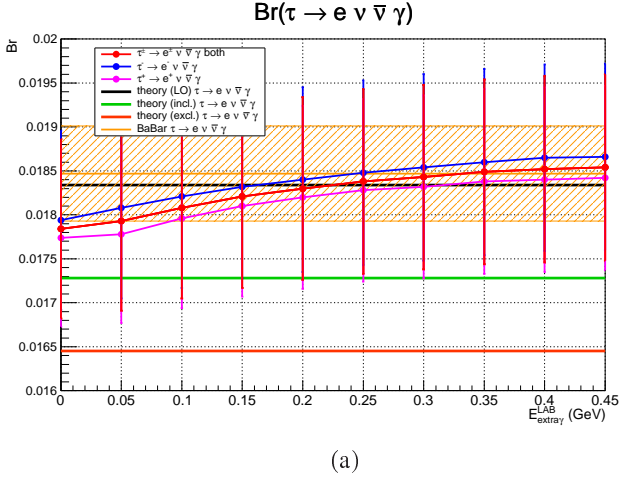


Figure A.1: Branching ratio of  $\tau^- \rightarrow \ell^- \nu \bar{\nu} \gamma$  decay as a function of  $E_{\text{extray}}^{\text{LAB}}$  cut: (a)  $\ell = e$  and (b)  $\ell = \mu$ . Red, blue and magenta lines respectively represent branching ratio of  $\tau^\pm \rightarrow \ell^\pm \nu \bar{\nu} \gamma$ ,  $\tau^- \rightarrow \ell^- \nu \bar{\nu} \gamma$  and  $\tau^+ \rightarrow \ell^+ \nu \bar{\nu} \gamma$ . Orange region shows result of the measurement by BaBar [37]. Black, green and red lines are theoretical predictions for LO, inclusive and exclusive modes, respectively [40]. The error includes both statistical and systematic uncertainties.

out to be approximately six percent and difficult to give a conclusive decision. However, the result well supports our Michel parameter measurement as one of consistency check.

# Appendix B

## Description of background PDFs

### B.1 Ordinary leptonic decay + beam background

As explained in Sec. 5.4.2, the contribution from beam background is finally given by

$$\lambda \cdot \frac{P_{\text{sel}}(\mathbf{z}) \cdot B^{\text{ord}}(\mathbf{y})}{\tilde{\varepsilon}(\mathbf{z})}, \quad (\text{B.1})$$

where as defined before,  $\mathbf{y} = \{P_\ell, \Omega_\ell, P_\rho, \Omega_\rho, m_{\pi\pi}^2, \tilde{\Omega}_\pi\}$  and  $\mathbf{z} = \{P_\gamma, \Omega_\gamma\}$  are, respectively variables for the ordinary leptonic decay and beam background,  $B^{\text{ord}}(\mathbf{y})$  is an intrinsic PDF of the ordinary leptonic decay  $\tau^- \rightarrow \ell^- \nu \bar{\nu} \gamma$  and  $\tilde{\varepsilon}(\mathbf{z})$  is an average efficiency of the beam background with respect to selected  $\mathbf{y}$  distribution, which is explicitly given by

$$\tilde{\varepsilon}(\mathbf{z}) = \int d\mathbf{y} \varepsilon(\mathbf{y}) \varepsilon(\mathbf{z}|\mathbf{y}) B^{\text{ord}}(\mathbf{y}). \quad (\text{B.2})$$

The tabulation of  $\tilde{\varepsilon}(\mathbf{z})$  for a certain cell of  $\mathbf{z}$  (denoted as  $\Delta\mathbf{z}^{(i)}$ ) is obtained by using selected MC signal sample with a factor of weight  $B^{\text{ord}}(\mathbf{y})/P^{\text{signal}}(\mathbf{y}, \mathbf{z})$ :

$$\tilde{\varepsilon}(\mathbf{z}^{(i)}) = \int d\mathbf{y} \varepsilon(\mathbf{y}) \varepsilon(\mathbf{z}^{(i)}|\mathbf{y}) B^{\text{ord}}(\mathbf{y}) \quad (\text{B.3})$$

$$= \frac{\int_{\mathbf{z} \in \Delta\mathbf{z}^{(i)}} d\mathbf{z} \int d\mathbf{y} \varepsilon(\mathbf{y}) \varepsilon(\mathbf{z}|\mathbf{y}) B^{\text{ord}}(\mathbf{y})}{\Delta\mathbf{z}^{(i)}} \quad (\text{B.4})$$

$$= \frac{\int_{\mathbf{z} \in \Delta\mathbf{z}^{(i)}} d\mathbf{z} \int d\mathbf{y} P^{\text{signal}}(\mathbf{y}, \mathbf{z}) \times \frac{B^{\text{ord}}(\mathbf{y})}{P^{\text{signal}}(\mathbf{y}, \mathbf{z})} \varepsilon(\mathbf{y}) \varepsilon(\mathbf{z}|\mathbf{y})}{\Delta\mathbf{z}^{(i)}} \quad (\text{B.5})$$

$$\sim \frac{\frac{1}{N_{\text{gen}}^{(i)}} \sum_{\substack{\mathbf{y}^k \in \mathcal{E} P^{\text{signal}} \\ \mathbf{z}^k \in \Delta\mathbf{z}^{(i)}}} \frac{B^{\text{ord}}(\mathbf{y}^k)}{P^{\text{signal}}(\mathbf{y}^k, \mathbf{z}^k)}}{\Delta\mathbf{z}^{(i)}}. \quad (\text{B.6})$$

The probability density function of the ordinary leptonic decay  $B^{\text{ord}}(\mathbf{y})$  is similarly formulated as signal. First, we construct the intrinsic PDF of  $\tau^+ \tau^- \rightarrow (\pi^+ \pi^0 \bar{\nu})(\mu^- \nu \bar{\nu} \gamma)$ :

$$\tilde{B}_{\text{int}}^{\text{ord}}(\mathbf{y}) \equiv \frac{d\sigma(\mu^- \nu \bar{\nu}, \pi^+ \pi^0)}{dE_\ell^* d\Omega_\ell^* d\Omega_\rho dm_{\pi\pi}^2 d\tilde{\Omega}_\pi} \propto \frac{\beta_\tau}{E_\tau^2} \left[ D_0 A^+ A^-(x) + D_{ij} B_i^+ \cdot B_j^-(x) \right], \quad (\text{B.7})$$

where tilde means a constant factor is ignored, *i.e.*, the right hand side of Eq. (B.7) is not normalized. The spin-independent and spin-dependent terms for  $\tau^+ \rightarrow \pi^+\pi^0\bar{\nu}$  sides ( $A^+$ ,  $B^+$ ) are common as signal and the ordinary leptonic decay parts are written using dimensionless kinematic variable  $x = E_\ell^*/E_{\ell\max}^*$ :

$$A^-(x) = A_0(x) + \rho A_1(x) + \eta A_2(x), \quad (\text{B.8})$$

$$B^-(x) = [\xi B_1(x) + \xi\delta B_2(x)] \mathbf{n}_i^*, \quad (\text{B.9})$$

$$A_0(x) = x(1-x)\sqrt{x^2-x_0^2}, \quad A_1(x) = \frac{2}{9}(4x^2-3x-x_0^2)\sqrt{x^2-x_0^2}, \quad (\text{B.10})$$

$$A_2(x) = x_0(1-x)\sqrt{x^2-x_0^2}, \quad B_1(x) = \frac{1}{3}(x^2-x_0^2)(1-x), \quad (\text{B.11})$$

$$B_2(x) = \frac{2}{9}(x^2-x_0^2)(4x-4-\sqrt{1-x_0}), \quad (\text{B.12})$$

$$x_0 = \frac{m_\ell}{E_{\ell\max}^*}, \quad E_{\ell\max}^* = \frac{m_\tau^2 + m_\ell^2}{2m_\tau}, \quad (\text{B.13})$$

$$(\text{B.14})$$

The differential variables are converted into CMS frame with Jacobians ( $dE_\ell^*d\Omega_\ell^*d\Omega_\rho^*d\Omega_\tau \rightarrow d\Phi dP_\ell d\Omega_\ell dP_\rho d\Omega_\rho$  and  $dE_\gamma^{\text{LAB}}d\Omega_\gamma^{\text{LAB}} \rightarrow dE_\gamma d\Omega_\gamma$ )

$$J_1 = \left| \frac{\partial(E_\ell^*, \Omega_\ell^*)}{\partial(P_\ell, \Omega_\ell)} \right| = \frac{P_\ell^2}{E_\ell P_\ell^*}, \quad (\text{B.15})$$

$$J_2 = \left| \frac{\partial(\Omega_\rho^*, \Omega_\tau)}{\partial(P_\rho, \Omega_\rho, \Phi)} \right| = \frac{m_\tau P_\rho}{E_\rho P_\rho^* P_\tau}, \quad (\text{B.16})$$

$$J_3 = \left| \frac{\partial(E_\gamma^{\text{LAB}}, \Omega_\gamma^{\text{LAB}})}{\partial(P_\gamma, \Omega_\gamma)} \right| = \frac{E_\gamma}{E_\gamma^{\text{LAB}}}. \quad (\text{B.17})$$

Thus we finally obtain

$$\lambda \cdot \frac{P_{\text{sel}}(\mathbf{z}) \cdot B^{\text{ord}}(\mathbf{y})}{\tilde{\mathcal{E}}(\mathbf{z})} = \lambda \cdot \frac{P_{\text{sel}}(\mathbf{z})}{\tilde{\mathcal{E}}(\mathbf{z})\sigma_{\text{ord}}} J_3 \int_{\Phi_1}^{\Phi_2} d\Phi \frac{\beta_\tau}{E_\tau^2} [D_0 A^+ A^- + D_{ij} B_i^+ \cdot B_j^-] J_1 J_2, \quad (\text{B.18})$$

where  $\sigma_{\text{ord}}$  is a normalization of  $B^{\text{ord}}(\mathbf{y})$ .

## B.2 Description of PDF for $3\pi$ events

When either of two  $\pi^0$ s from  $\tau^+ \rightarrow a_1^+\bar{\nu} \rightarrow \pi^+\pi^0\pi^0\bar{\nu}$  decay is lost, this is reconstructed as  $\rho^+ \rightarrow \pi^+\pi^0$  decay. For example, if  $\gamma$  from  $\pi^0 \rightarrow \gamma\gamma$  process is produced outside an acceptance of detector, the reconstruction fails. Furthermore, even if both  $\gamma$ s are inside detector, their scattering with materials leads misreconstruction of  $\pi^0$ . In order to describe the possibility of the loss of  $\pi^0$ , we define effective probability density of  $3\pi$  events:

$$\tilde{B}^{3\pi}(\mathbf{x}) \equiv \int d\mathbf{y} 2 \cdot [1 - \varepsilon_{\pi_{\text{lost}}^0}(\mathbf{y})] \frac{\varepsilon_{\text{extray}}^{3\pi}}{\varepsilon_{\text{extray}}^{\text{sig}}} \cdot B_{\text{int}}^{3\pi}(\mathbf{x}, \mathbf{y}). \quad (\text{B.19})$$

Here,  $\mathbf{x}$  represent the visible twelve-dimension observables and  $\mathbf{y}$  is a set of parameters for the lost  $\pi^0$  defined as  $\mathbf{y} = \{P_{\pi_{\text{lost}}^0}^0, \Omega_{\pi_{\text{lost}}^0}^0\}$ . The factor inside bracket  $1 - \varepsilon_{\pi_{\text{lost}}^0}(\mathbf{y})$  represents a probability that

$\pi^0$  is not reconstructed or *inefficiency*,  $\varepsilon_{\text{extray}}^{3\pi}/\varepsilon_{\text{extray}}^{\text{sig}}$  means a ratio of an efficiency from the extra gamma energy cut relative to signal distribution.  $B^{3\pi}(\mathbf{x}, \mathbf{y})$  is an intrinsic PDF for the  $3\pi$  events  $\tau^+\tau^- \rightarrow (\pi^+\pi^0\pi^0\bar{\nu})(\ell^-\nu\bar{\nu}\gamma)$ . The factor of 2 in the equation comes from number of counting for two  $\pi^0$ s.

The differential decay width of  $\tau^+(P) \rightarrow \pi^0(p_1)\pi^0(p_2)\pi^+(p_3)\bar{\nu}(q)$  can be expressed as sum of two terms depending on the correlation to spin of  $\tau$ :

$$\frac{d\Gamma(\tau^+ \rightarrow \pi^+\pi^0\pi^0\bar{\nu})}{d\Phi_4} = A^+ + \mathbf{B}^+ \cdot \mathbf{S}_\tau^*, \quad (\text{B.20})$$

where  $A^+$  and  $\mathbf{B}^+$  are spin independent and dependent form factors, respectively. These factors are obtained by  $3\pi$  hadronic four-vector current  $J^\mu$  with following relation:

$$A^+ = (P \cdot J^*)(q \cdot J) + (P \cdot J)(q \cdot J^*) - (J \cdot J^*)(P \cdot q) + i\varepsilon^{\mu\nu\rho\sigma} J_\mu J_\nu^* P_\rho q_\sigma. \quad (\text{B.21})$$

$$\mathbf{B}^{+\mu} = im_\tau \varepsilon^{\mu\nu\rho\sigma} J_\nu J_\rho^* q_\sigma + m_\tau [(J \cdot J^*)q^\mu - (q \cdot J)J^{*\mu} - (q \cdot J^*)J^\mu]. \quad (\text{B.22})$$

$d\Phi_4$  is well-known Lorentz-invariant four-body phase space and can be explicitly decomposed into

$$d\Phi_4 \propto d\Omega_{a_1}^* dm_{a_1}^2 d\hat{\Omega}_\rho dm_\rho^2 d\tilde{\Omega}_\pi \cdot \frac{2P_{a_1}^*}{m_\tau} \frac{2\hat{P}_\rho}{m_{a_1}} \frac{2\tilde{P}_\pi}{m_\rho}, \quad (\text{B.23})$$

where the asterisk marks it is defined on  $\tau^+$  rest frame. Similarly the hat means value on  $a_1^+$  and tilde on  $\rho^+.$  As  $J^\mu$ , CLEO model is used where structure of  $\tau^+ \rightarrow \pi^+\pi^0\pi^0\bar{\nu}$  is considered to be a superposition of seven amplitudes with respect to their partial waves [93]:

$$J^\mu = B_{a_1}(s) \sum_{i=1,2,..,7} \beta_i j_i^\mu, \quad (\text{B.24})$$

$$\begin{aligned} \beta_1 = 1.00e^{0.00i} & : j_1^\mu = T^{\mu\nu} \left[ q_{1\nu} B_\rho^P(s_1) - q_{2\nu} B_\rho^P(s_2) \right], \\ \beta_2 = 0.12e^{0.99i} & : j_2^\mu = T^{\mu\nu} \left[ q_{1\nu} B_{\rho'}^P(s_1) - q_{2\nu} B_{\rho'}^P(s_2) \right], \\ \beta_3 = 0.37e^{-0.15i} & : j_3^\mu = T^{\mu\nu} \left[ Q_{1\nu}(a \cdot q_1) B_\rho^P(s_1) - Q_{2\nu}(a \cdot q_2) B_\rho^P(s_2) \right], \\ \beta_4 = 0.87e^{0.53i} & : j_4^\mu = T^{\mu\nu} \left[ Q_{1\nu}(a \cdot q_1) B_{\rho'}^P(s_1) - Q_{2\nu}(a \cdot q_2) B_{\rho'}^P(s_2) \right], \\ \beta_5 = 0.71e^{0.56i} & : j_5^\mu = T^{\mu\nu} \left[ q_{3\nu}(a \cdot q_3) - \frac{q_3^2}{3} \left( a_\nu - h_{3\nu} \frac{h_3 \cdot a}{s_3} \right) \right] B_{f_2}^D(s_3), \\ \beta_6 = 2.1e^{0.23i} & : j_6^\mu = T^{\mu\nu} \left[ Q_{3\nu} B_\sigma^S(s_3) \right], \\ \beta_7 = 0.77e^{-0.54i} & : j_7^\mu = T^{\mu\nu} \left[ Q_{3\nu} B_{f_0}^S(s_3) \right], \end{aligned}$$

where  $\beta_i$  are complex coefficients of  $j_i^\mu$ ,  $h_i = p_j + p_k$  with ( $i \neq j$ ,  $i \neq k$ ),  $q_1 = p_2 - p_3$ ,  $q_2 = p_3 - p_1$ ,  $q_3 = p_1 - p_2$ ,  $a = p_1 + p_2 + p_3$ ,  $Q_i = h_i - p_i$ ,  $s_i = h_i^2$  and  $s = a^2$ .  $B_{a_1}$  and  $B_L^Y(s_i)$  are

\* Generally  $d\Phi_n(p_1, p_2, \dots, p_n) \propto dm_{1,2,..,(n-1)}^2 d\Phi_2(p_{12(n-1)}, p_n) \cdot d\Phi_{n-1}(p_1, p_2, \dots, p_{n-1})$  with  $d\Phi_2(\mathbf{p}, \mathbf{q}) = \frac{\tilde{p}}{16\pi^2 m_{pq}} d\Omega_{\tilde{p}}$ . Here,  $\tilde{p}$  means that it is defined on the CMS frame of  $\mathbf{p}$  and  $\mathbf{q}$ .

Breit-Wigner functions of  $a_1$  and  $Y$ . The latter is defined as

$$B_L^Y(s_i) = \frac{m_{0Y}^2}{m_{0Y}^2 - s_i - im_{0Y}\Gamma^{Y,L}(s_i)}, \quad (\text{B.25})$$

$$\Gamma^{Y,L}(s_i) = \Gamma_0^Y \left( \frac{k'_i}{k_{0i}^{Y'}} \right)^{2L+1} \frac{m_{0Y}}{\sqrt{s_i}}, \quad (\text{B.26})$$

$$k'_i = \frac{\sqrt{[s_i - (m_j + m_k)^2][s_i - (m_j - m_k)^2]}}{2\sqrt{s_i}} \quad (\text{B.27})$$

$$k_{0i}^{Y'} = \frac{\sqrt{[m_{0Y}^2 - (m_j + m_k)^2][m_{0Y}^2 - (m_j - m_k)^2]}}{2m_{0Y}} \quad \text{with } (i \neq j, i \neq k) \quad (\text{B.28})$$

$$Y = \rho, \rho', f_2, \sigma, f_0, \quad L = 0, 1, 2 \quad (\text{which corresponds to } S, P \text{ or } D).$$

$B_{a_1}$  is numerically approximated as Eqs. (B.29) to (B.35) which is same implementation as TAUOLA [94].

$$B_{a_1}(s) = \frac{m_{a_1}^2}{m_{a_1}^2 - s - im_{a_1}\Gamma_{a_1}(s)} \quad (\text{B.29})$$

$$\Gamma_{a_1}(s) = \Gamma_0^{a_1} w_{a_1}(s) / (1.3281 * 0.806) \quad (\text{B.30})$$

$$w_{a_1}(s) = c_{3\pi}(g_{\pi\pi\pi} + g_{\pi\pi^0\pi^0}) + \Theta(s - (m_K + m_{K^*})^2) c_{K^*} \Gamma_{K^*} \quad (\text{B.31})$$

$$c_{3\pi} = 0.2384^2, \quad c_{K^*} = 4.7621^2 c_{3\pi} \quad (\text{B.32})$$

$$\Gamma_{K^*} = \frac{\sqrt{s - (m_K + m_{K^*})^2} \sqrt{s - (m_K - m_{K^*}^*)^2}}{2s} \quad (\text{B.33})$$

$$g_{\pi\pi\pi} = \begin{cases} 0 & (s < 0.823) \\ 5.809(s - s_{\text{th}})^3 [1.0 - 3.0098(s - s_{\text{th}}) + 4.5792(s - s_{\text{th}})^2] & (0.1753 = s_{\text{th}} < s < 0.823) \\ -13.914 + 27.679s - 13.393s^2 + 3.1924s^3 - 0.10487s^4 & (0.823 < s) \end{cases} \quad (\text{B.34})$$

$$g_{\pi\pi^0\pi^0} = \begin{cases} 0 & (s < 0.823) \\ 6.2845(s - s_{\text{th}})^3 [1.0 - 2.9595(s - s_{\text{th}}) + 4.3355(s - s_{\text{th}})^2] & (0.1676 = s_{\text{th}} < s < 0.823) \\ -15.411 + 32.088s - 17.666s^2 + 4.9355s^3 - 0.37498s^4 & (0.823 < s) \end{cases} \quad (\text{B.35})$$

$m_{0Y}$  and  $\Gamma_0^Y$  are nominal mass and decay width of  $Y$ . These decay parameters are summarized in Table B.1.

The kinematic variables in Eq. (B.23) are converted with Jacobians.

$$\begin{aligned} d\Omega_\tau d\Omega_{a_1}^* dm_{a_1}^2 dm_\rho^2 d\hat{\Omega}_\rho d\tilde{\Omega}_\pi &= d\Phi_\tau dP_{a_1} d\Omega_{a_1} dm_{a_1}^2 dm_\rho^2 \hat{\Omega}_\rho d\tilde{\Omega}_\pi \times \left| \frac{\partial(\Omega_\tau, \Omega_{a_1}^*)}{\partial(\Phi_\tau, P_{a_1}, \Omega_{a_1})} \right| \\ &= d\Phi_\tau dP_{\pi_{\text{lost}}^0} d\Omega_{\pi_{\text{lost}}^0} dP_\rho d\Omega_\rho dm_\rho^2 d\tilde{\Omega}_\pi \times \left| \frac{\partial(\Omega_\tau, \Omega_{a_1}^*)}{\partial(\Phi_\tau, P_{a_1}, \Omega_{a_1})} \right| \cdot \left| \frac{\partial(P_{a_1}, \Omega_{a_1}, m_{a_1}^2, \hat{\Omega}_\rho)}{\partial(P_{\pi_{\text{lost}}^0}, \Omega_{\pi_{\text{lost}}^0}, P_\rho, \Omega_\rho)} \right|. \end{aligned} \quad (\text{B.36})$$

Thus the intrinsic PDF of  $\tau^+\tau^- \rightarrow (\pi^+\pi^0\pi^0\bar{\nu})(\ell^- \nu\bar{\nu}\gamma)$  process is given by

$$\begin{aligned} \tilde{B}_{\text{int}}^{3\pi}(\mathbf{x}, \mathbf{y}) &\equiv \frac{d\sigma(\tau^+\tau^- \rightarrow (\pi^+\pi^0\pi^0\bar{\nu})(\ell^- \nu\bar{\nu}\gamma))}{dP_\ell d\Omega_\ell dP_\gamma d\Omega_\gamma dP_{\pi_{\text{lost}}^0} d\Omega_{\pi_{\text{lost}}^0} dP_\rho d\Omega_\rho dm_\rho^2 d\tilde{\Omega}_\pi} \\ &= \int d\Phi_\tau \frac{d\sigma}{dP_\ell d\Omega_\ell dP_\gamma d\Omega_\gamma dP_{\pi_{\text{lost}}^0} d\Omega_{\pi_{\text{lost}}^0} dP_\rho d\Omega_\rho dm_\rho^2 d\tilde{\Omega}_\pi d\Phi_\tau} \\ &= \int d\Phi_\tau \frac{d\sigma}{d\Omega_\tau dE_\ell^* d\Omega_\ell^* dE_\gamma^* d\Omega_\gamma^* d\Omega_{a_1}^* dm_{a_1}^2 dm_\rho^2 d\hat{\Omega}_\rho d\tilde{\Omega}_\pi} \end{aligned} \quad (\text{B.37})$$

Table B.1: Decay parameters for  $\tau^+ \rightarrow a_1^+ \bar{\nu}$  decay [93].

Y	$\rho$	$\rho'$	$f_2$	$f_0$	$\sigma$	$a_1$
$m_{0Y}$ (GeV/ $c^2$ )	0.7743	1.370	1.275	1.186	0.860	1.275
$\Gamma_0^Y$ (GeV)	0.1491	0.386	0.185	0.350	0.880	0.700

$$\begin{aligned}
 & \times \left| \frac{\partial(E_\ell^*, \Omega_\ell^*)}{\partial(P_\ell, \Omega_\ell)} \right| \cdot \left| \frac{\partial(E_\gamma^*, \Omega_\gamma^*)}{\partial(P_\gamma, \Omega_\gamma)} \right| \cdot \left| \frac{\partial(\Omega_\tau, \Omega_{a_1}^*)}{\partial(\Phi_\tau, P_{a_1}, \Omega_{a_1})} \right| \cdot \left| \frac{\partial(P_{a_1}, \Omega_{a_1}, m_{a_1}^2, \hat{\Omega}_\rho)}{\partial(P_{\pi_{\text{lost}}^0}, \Omega_{\pi_{\text{lost}}^0}, P_\rho, \Omega_\rho)} \right| \\
 \propto & \int_{\Phi_1}^{\Phi_2} d\Phi_\tau \frac{\beta_\tau}{E_\tau^2} [D_0 A A' - D_{ij} B^i B'^j] \cdot \frac{2P_{a_1}^*}{m_\tau} \frac{2\hat{P}_\rho}{m_{a_1}} \frac{2\tilde{P}_\pi}{m_\rho} \cdot J_1 J_2 J_3 J_4
 \end{aligned} \tag{B.38}$$

$$J_1 = \left| \frac{\partial(E_\ell^*, \Omega_\ell^*)}{\partial(P_\ell, \Omega_\ell)} \right| = \frac{P_\ell^2}{E_\ell P_\ell^*}, \tag{B.39}$$

$$J_2 = \left| \frac{\partial(E_\gamma^*, \Omega_\gamma^*)}{\partial(P_\gamma, \Omega_\gamma)} \right| = \frac{E_\gamma}{E_\gamma^*}, \tag{B.40}$$

$$J_3 = \left| \frac{\partial(\Omega_\tau, \Omega_{a_1}^*)}{\partial(\Phi_\tau, P_{a_1}, \Omega_{a_1})} \right| = \frac{m_\tau P_{a_1}}{E_{a_1} P_{a_1}^* P_\tau}, \tag{B.41}$$

$$J_4 = \left| \frac{\partial(P_{a_1}, \Omega_{a_1}, m_{a_1}^2, \hat{\Omega}_\rho)}{\partial(P_{\pi_{\text{lost}}^0}, \Omega_{\pi_{\text{lost}}^0}, P_\rho, \Omega_\rho)} \right| = \frac{m_{a_1}}{\hat{P}_\rho} \cdot \left( \frac{P_\rho^2 P_{\pi_{\text{lost}}^0}^2}{P_{a_1}^2} \right)^2 \cdot \frac{E_{a_1}}{E_\rho E_{\pi_{\text{lost}}^0}}. \tag{B.42}$$

## B.2.1 Extraction of the inefficiencies

The product of the additional efficiencies  $2[1 - \epsilon_{\pi_{\text{lost}}^0}] \epsilon_{\text{extray}}^{3\pi} / \epsilon_{\text{extray}}^{\text{sig}}$  is simultaneously tabulated from MC events.  $\tau^+ \tau^- \rightarrow (\pi^+ \pi^0 \pi^0 \bar{\nu})(\ell^- \nu \bar{\nu} \gamma)$  events are selected with same criteria except two requirements: number of photons in the cone around lepton and the extra gamma energy. The fraction of events which are further selected with the additional requirement is taken as the desired inefficiency. Figures B.1 and B.2 show the obtained inefficiencies as a function of an energy and a cosine of polar angle for lost  $\pi^0$ .

## B.3 Description of $\rho\rho$ background

$\tau^+ \rightarrow \rho^+ \bar{\nu} \rightarrow \pi^+ \pi^0 (\rightarrow \gamma\gamma) \bar{\nu}$  process is also selected as signal provided that  $\pi^+$  is mis-reconstructed as  $\mu^+$  and either of two photons from  $\pi^0$  enters inside aforementioned cone around lepton. The formulation of  $\rho\rho$  background is quite similar to that of  $3\pi$  events except that an additional mis-identification factor appears:

$$\tilde{B}^{\rho\rho}(\mathbf{x}) \equiv \int d\mathbf{y} 2 [1 - \epsilon_{\gamma'}(\mathbf{P}_{\gamma'})] \frac{\mathcal{E}_{\text{extray}}^{\rho\rho}}{\mathcal{E}_{\text{extray}}^{\text{sig}}} \frac{\mathcal{E}_{\pi \rightarrow \mu}^{\text{PID}}}{\mathcal{E}_{\mu \rightarrow \mu}^{\text{PID}}} B_{\text{int}}^{\rho\rho}(\mathbf{x}, \mathbf{y}), \tag{B.43}$$

where  $\mathbf{x}$  is a set of visible variables in twelve-dimension phase space defined as  $\mathbf{x} = \{P_{\pi_{\text{mis}}}, \Omega_{\pi_{\text{mis}}}, P_\gamma, \Omega_\gamma, P_{\rho_2}, \Omega_{\rho_2}, m_{\rho_2}^2, \tilde{\Omega}_{\pi_2}\}$  (subscript 2 is attached for a later purpose) and  $\mathbf{y} = \{\Omega_{\gamma'}\}$  corresponds to a phase space of lost  $\gamma$ . Because there is a mass constraint between two photons from  $\pi^0$ :  $m_{\pi^0}^2 = (p_\gamma + p_{\gamma'})^2 = 2E_\gamma E_{\gamma'} (1 - \cos \theta_{\gamma\gamma'})$ , an energy of lost  $\gamma$  is not independent variable. A factor

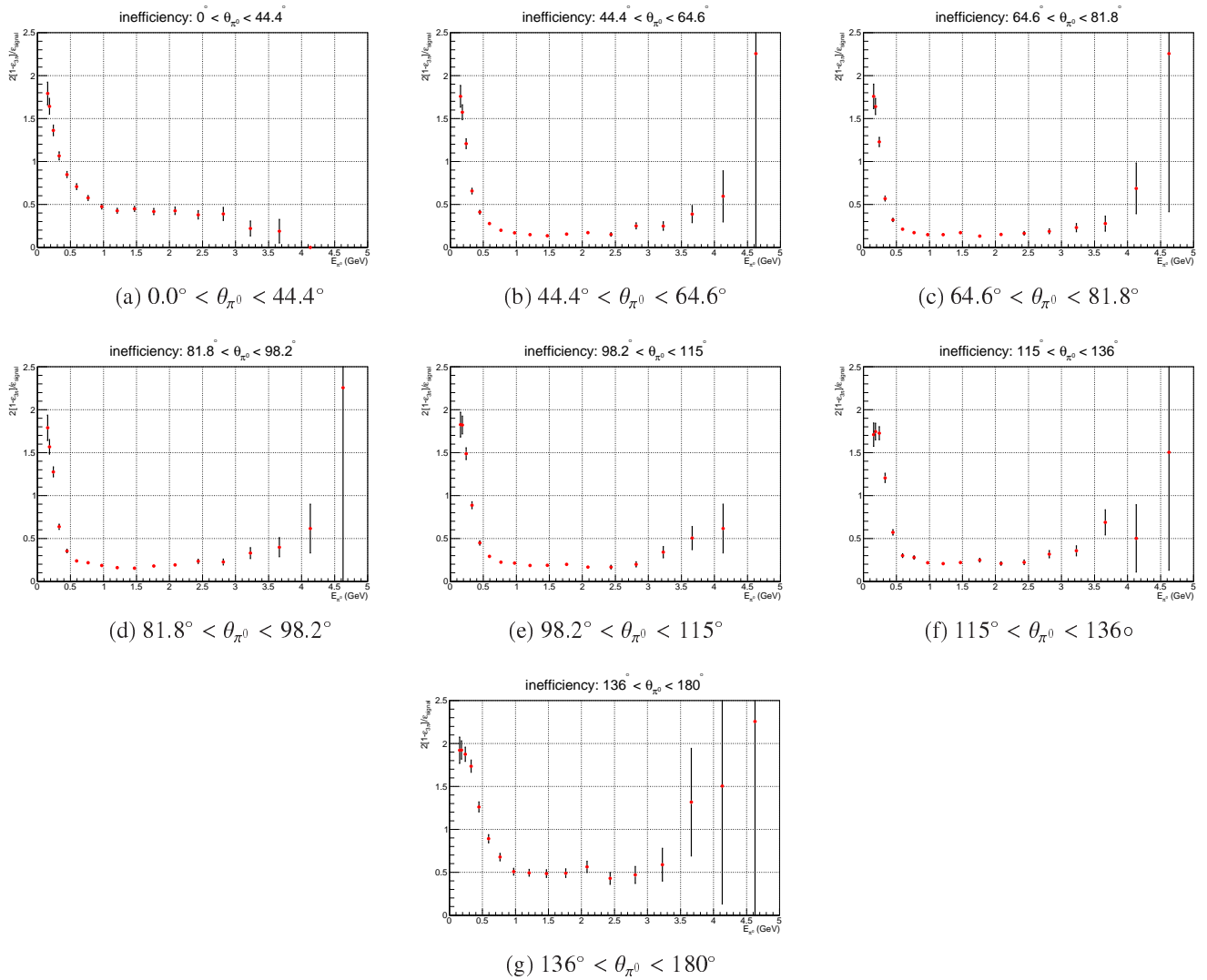


Figure B.1: Inefficiency of  $\pi^0$  as a function of energy for each bin of  $\theta_{\pi^0}$  ( $E_{\text{extray}} < 0.3$  GeV). Horizontal axis represents energy of  $\pi^0$ .

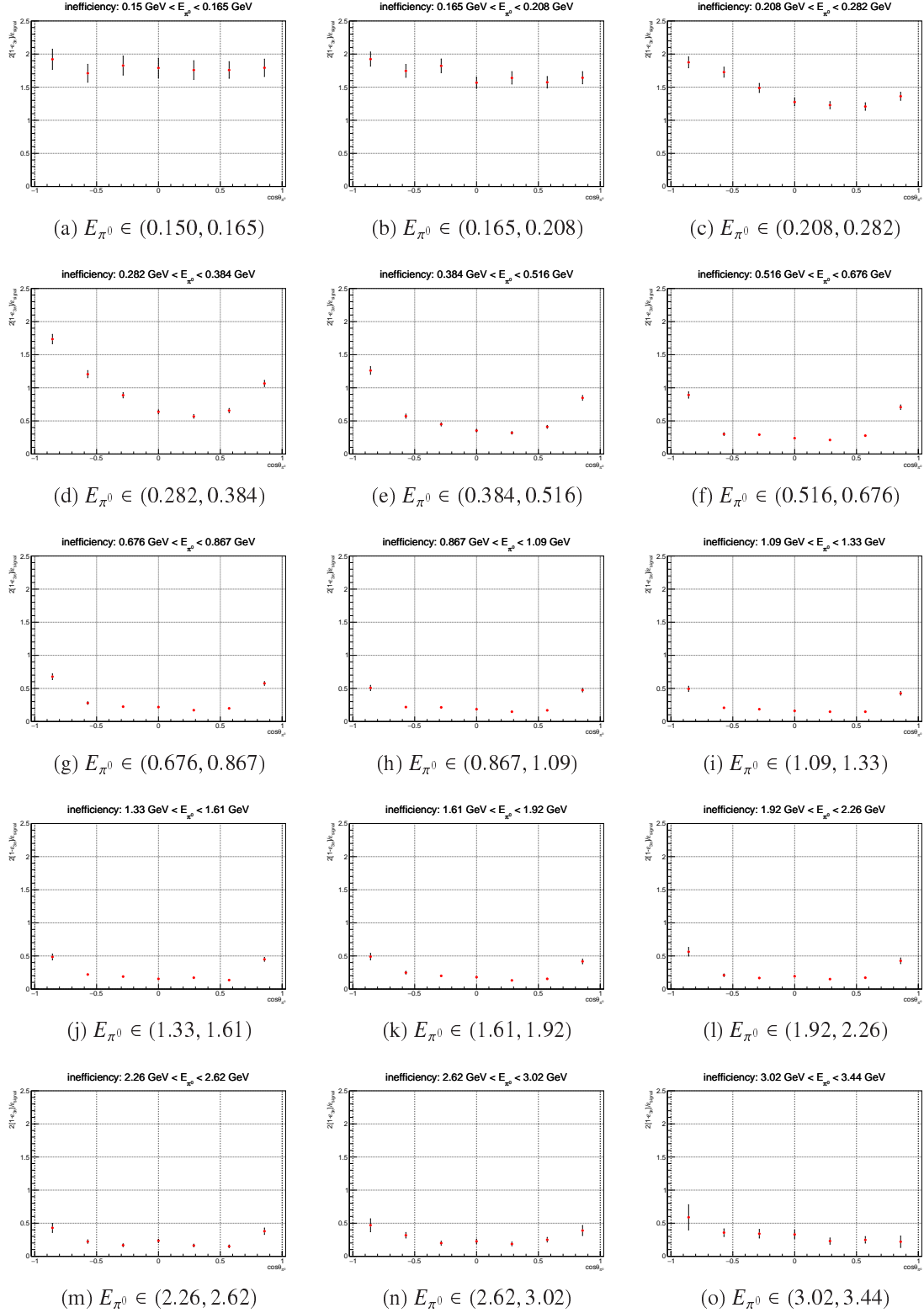


Figure B.2: Inefficiency of  $\pi^0$  as a function of cosine of zenith angle of  $\pi^0$  for each bin of energy. The unit of energy is GeV. Horizontal axis represents energy of  $\pi^0$ .



inside bracket  $1 - \varepsilon(\mathbf{y})$  is an inefficiency of photon,  $\varepsilon_{\text{extray}}^{\rho\rho}/\varepsilon_{\text{extray}}^{\text{sig}}$  is an efficiency of extra  $\gamma$  energy cut relative to signal and  $\varepsilon_{\pi \rightarrow \mu}^{\text{PID}}/\varepsilon_{\mu \rightarrow \mu}^{\text{PID}}$  is a ratio of lepton mis-identification efficiency.

The construction of an intrinsic PDF of the  $\tau^+ \tau^- \rightarrow (\pi^+ \pi^0 \bar{\nu})(\pi^- \pi^0 \nu)$  process  $B_{\text{int}}^{\rho\rho}(\mathbf{x}, \mathbf{y})$  begins by the differential cross section in the  $\tau$  rest frame:

$$\frac{d\sigma(\tau^+ \tau^- \rightarrow \rho_1^+ \rho_2^- \nu \bar{\nu})}{d\Omega_{\rho_1}^* dm_{\rho_1}^2 d\tilde{\Omega}_{\pi_1} d\Omega_{\rho_2}^* d\Omega_{\rho_2} dm_{\rho_2}^2 d\tilde{\Omega}_{\pi_2} d\Omega_{\tau}} \propto \frac{\beta_{\tau}}{E_{\tau}^2} (D_0 AA' - D_{ij} B^i B^{j'}), \quad (\text{B.44})$$

where  $A, A', \mathbf{B}$  and  $\mathbf{B}'$  are same form factors defined in the construction of signal PDF. To obtain visible differential cross section at CMS frame, the differential variables are converted with three Jacobians.

$$\begin{aligned} & \frac{d\sigma}{dP_{\rho_1} d\Omega_{\rho_1} dm_{\rho_1}^2 d\tilde{\Omega}_{\pi_1} dP_{\rho_2} d\Omega_{\rho_2} dm_{\rho_2}^2 d\tilde{\Omega}_{\pi_2}} \\ &= \frac{d\sigma}{d\Omega_{\rho_1}^* dm_{\rho_1}^2 d\tilde{\Omega}_{\pi_1} d\Omega_{\rho_2}^* dm_{\rho_2}^2 d\tilde{\Omega}_{\pi_2} d\Omega_{\tau}} \times \left| \frac{\partial(\Omega_{\rho_1}^*, \Omega_{\rho_2}^*, \Omega_{\tau})}{\partial(P_{\rho_1}, \Omega_{\rho_1}, P_{\rho_2}, \Omega_{\rho_2})} \right| \end{aligned} \quad (\text{B.45})$$

$$\begin{aligned} & \frac{d\sigma}{dP_{\pi_{\text{mis}}} d\Omega_{\pi_{\text{mis}}} dP_{\pi^0} d\Omega_{\pi^0} dP_{\rho_2} d\Omega_{\rho_2} dm_{\rho_2}^2 d\tilde{\Omega}_{\pi_2}} \\ &= \frac{d\sigma}{dP_{\rho_1} d\Omega_{\rho_1} dm_{\rho_1}^2 d\tilde{\Omega}_{\pi_1} dP_{\rho_2} d\Omega_{\rho_2} dm_{\rho_2}^2 d\tilde{\Omega}_{\pi_2}} \times \left| \frac{\partial(P_{\rho_1}, \Omega_{\rho_1}, m_{\rho_1}^2, \tilde{\Omega}_{\pi_1})}{\partial(P_{\pi_{\text{mis}}}, \Omega_{\pi_{\text{mis}}}, P_{\pi^0}, \Omega_{\pi^0})} \right|. \end{aligned} \quad (\text{B.46})$$

$$\begin{aligned} & \frac{d\sigma}{dP_{\pi_{\text{mis}}} d\Omega_{\pi_{\text{mis}}} dP_{\pi^0} d\Omega_{\pi^0} d\Omega_{\gamma}^{**} dP_{\rho_2} d\Omega_{\rho_2} dm_{\rho_2}^2 d\tilde{\Omega}_{\pi_2}} \\ &= \frac{1}{4\pi} \frac{d\sigma}{dP_{\pi_{\text{mis}}} d\Omega_{\pi_{\text{mis}}} dP_{\pi^0} d\Omega_{\pi^0} dP_{\rho_2} d\Omega_{\rho_2} dm_{\rho_2}^2 d\tilde{\Omega}_{\pi_2}} \end{aligned} \quad (\text{B.47})$$

$$\begin{aligned} & \frac{d\sigma}{dP_{\pi_{\text{mis}}} d\Omega_{\pi_{\text{mis}}} dP_{\gamma} d\Omega_{\gamma} d\Omega_{\gamma'} dP_{\rho_2} d\Omega_{\rho_2} dm_{\rho_2}^2 d\tilde{\Omega}_{\pi_2}} \\ &= \frac{d\sigma}{dP_{\pi_{\text{mis}}} d\Omega_{\pi_{\text{mis}}} dP_{\pi^0} d\Omega_{\pi^0} d\Omega_{\gamma}^{**} dP_{\rho_2} d\Omega_{\rho_2} dm_{\rho_2}^2 d\tilde{\Omega}_{\pi_2}} \times \left| \frac{\partial(P_{\pi^0}, \Omega_{\pi^0}, \Omega_{\gamma}^{**})}{\partial(P_{\gamma}, \Omega_{\gamma}, \Omega_{\gamma'})} \right|. \end{aligned} \quad (\text{B.48})$$

$$\frac{d\sigma}{dP_{\pi_{\text{mis}}} d\Omega_{\pi_{\text{mis}}} dP_{\gamma} d\Omega_{\gamma} d\Omega_{\gamma'} dP_{\rho_2} d\Omega_{\rho_2} dm_{\rho_2}^2 d\tilde{\Omega}_{\pi_2}} \quad (\text{B.49})$$

$$\propto \frac{\beta_{\tau}}{E_{\tau}^2} (D_0 AA' - D_{ij} B^i B^{j'}) J_1 J_2 J_3 \equiv B_{\text{int}}^{\rho\rho}(\mathbf{x}, \mathbf{y}) \quad (\text{B.50})$$

$$J_1 = \left| \frac{\partial(\Omega_{\rho_1}^*, \Omega_{\rho_2}^*, \Omega_{\tau})}{\partial(P_{\rho_1}, \Omega_{\rho_1}, P_{\rho_2}, \Omega_{\rho_2})} \right| = \frac{\beta_{\rho_1} \beta_{\rho_2}}{\beta_{\tau}^2 \gamma_{\tau}^2 P_{\rho_1}^* P_{\rho_2}^* |\mathbf{n}_{\tau} \cdot (\mathbf{n}_{\rho_1} \times \mathbf{n}_{\rho_2})|} \quad (\text{B.51})$$

$$J_2 = \left| \frac{\partial(P_{\rho_1}, \Omega_{\rho_1}, m_{\rho_1}^2, \tilde{\Omega}_{\pi_1})}{\partial(P_{\pi_{\text{mis}}}, \Omega_{\pi_{\text{mis}}}, P_{\pi^0}, \Omega_{\pi^0})} \right| = \left( \frac{P_{\pi_{\text{mis}}} P_{\pi^0}}{P_{\rho_1}} \right)^2 \frac{E_{\rho_1}}{E_{\pi_{\text{mis}}} E_{\pi^0}} \frac{2m_{\rho_1}}{\tilde{P}_{\pi_1}} \quad (\text{B.52})$$

$$J_3 = \left| \frac{\partial(P_{\pi^0}, \Omega_{\pi^0}, \Omega_{\gamma}^{**})}{\partial(P_{\gamma}, \Omega_{\gamma}, \Omega_{\gamma'})} \right| = \frac{4E_{\gamma}^2 E_{\gamma} E_{\pi^0}}{P_{\pi^0}^2 m_{\pi^0}^2} \quad (\text{B.53})$$

where  $\beta_{\rho_1}$ ,  $\beta_{\rho_2}$  and  $\beta_\tau$  are, respectively velocities of  $\rho_1$ ,  $\rho_2$  and  $\tau$  in the CMS frame and  $\mathbf{n}_\tau$ ,  $\mathbf{n}_{\rho_1}$  and  $\mathbf{n}_{\rho_2}$  are normalized direction and  $\gamma_\tau = E_\tau/m_\tau$ . The tilde and double-asterisk mark that variables are defined in  $\rho$  and  $\pi^0$  rest frames, respectively. In the conversion from Eq. (B.46) into Eq. (B.47), we use the fact that decay direction of  $\gamma$  is isotropic in the  $\pi^0$  rest frame (because  $\pi^0$  is pseudo scalar particle). In general, after the step from Eq. (B.46), the solution of the  $\tau$  direction ( $\Omega_\tau$ ) is not uniquely determined from a set of visible variables  $\{P_{\rho_1}, \Omega_{\rho_1}, P_{\rho_2}, \Omega_{\rho_2}\}$ . As introduced in Sec. 2.5, there are generally two solutions for  $\Omega_\tau$  candidates. Therefore, we use a sum of Eq. (B.49) for both cases to give an accessible differential cross section:  $d\sigma = d\sigma_1 + d\sigma_2$ , where 1 and 2 indicate indexes of the two solutions.

### B.3.1 Extraction of inefficiency

The product of an inefficiency of photon and a selection efficiency of extra  $\gamma$  energy  $[1 - \epsilon(\mathbf{P}_\gamma)]\epsilon_{\rho\rho}^{\text{extray}}/\epsilon_{\text{sig}}^{\text{extray}}$  is simultaneously obtained by selected MC  $\tau^+\tau^- \rightarrow (\pi^+\pi^0\bar{\nu})(\pi^-\pi^0\nu)$  process, to which all selection criteria are applied except the extra  $\gamma$  energy cut and a number of photon in the cone around lepton. The fraction of events which are further selected with this additional cut is estimated as the inefficiency. Since we do not allow any  $\gamma$  in the cone, we separate the conditions depending on whether the  $\gamma$  is generated in the cone or not.

The lepton mis-identification probability is extracted using  $\tau^- \rightarrow \pi^-\nu$  and  $\tau^- \rightarrow \mu^-\nu\bar{\nu}$  decays:

$$\frac{\epsilon_{\pi\rightarrow\mu}^{\text{PID}}}{\epsilon_{\mu\rightarrow\mu}^{\text{PID}}}(\mathbf{P}_\ell) = \frac{N_{\text{sel}}(\tau \rightarrow \pi\nu)|_{\mathbf{P}_\pi=\mathbf{P}_\ell}}{N_{\text{sel}}(\tau \rightarrow \mu\nu\bar{\nu})|_{\mathbf{P}_\mu=\mathbf{P}_\ell}} \cdot \frac{N_{\text{gen}}(\tau \rightarrow \mu\nu\bar{\nu})|_{\mathbf{P}_\mu=\mathbf{P}_\ell}}{N_{\text{gen}}(\tau \rightarrow \pi\nu)|_{\mathbf{P}_\pi=\mathbf{P}_\ell}}. \quad (\text{B.54})$$

## B.4 Description of ISR photon + ordinary leptonic decay events

The formulation of the differential cross section of ISR process  $e^+e^- \rightarrow \tau^+\tau^-\gamma_{\text{ISR}} \rightarrow (\pi^+\pi^0\bar{\nu})(\mu^-\nu\bar{\nu})\gamma_{\text{ISR}}$  is obtained according to a cross section of the production  $e^+e^- \rightarrow \tau^+\tau^-\gamma$  instead of Eq. (5.27).

$$\frac{d\sigma(e^+e^- \rightarrow \tau^+\tau^-\gamma)}{dP_\gamma d\Omega_\gamma d\Omega'_\tau} = \frac{\alpha^3 \tilde{\beta}_\tau}{16\pi^2 E_0^2} [D'_0 + D'_{ij} S_{\tau^+}^{*i} S_{\tau^-}^{*j}]. \quad (\text{B.55})$$

Here, prime means the direction of  $\tau^-$  ( $\Omega'_\tau$ ) is defined in the  $\tau^+\tau^-$  rest frame. The explicit formula of  $D'_0$  and  $D'_{ij}$  are given in Ref. [67]. Similarly to a construction of the PDF of beam background described in Appendix B.1, the differential decay widths of  $\tau^+ \rightarrow \pi^+\pi^-\bar{\nu}$  and  $\tau^- \rightarrow \ell^-\nu\bar{\nu}$  are given by

$$\frac{d\Gamma(\tau^- \rightarrow \mu^-\nu\bar{\nu})}{dE_\ell^* d\Omega_\ell^*} = A + \mathbf{B} \cdot \mathbf{S}_{\tau^-}^*, \quad (\text{B.56})$$

and

$$\frac{d\Gamma(\tau^+ \rightarrow \pi^+\pi^0\bar{\nu})}{d\Omega_\rho^* dm_{\pi\pi}^2 d\tilde{\Omega}_\pi} = A' + \mathbf{B}' \cdot \mathbf{S}_{\tau^+}^*, \quad (\text{B.57})$$

then total differential cross section is constructed as

$$\frac{d\sigma(e^+e^- \rightarrow \tau^+\tau^-\gamma \rightarrow (\pi^+\pi^0\bar{\nu})(\mu^-\nu\bar{\nu})\gamma)}{dP_\gamma d\Omega_\gamma dE_\ell^* d\Omega_\ell^* d\Omega_\rho^* dm_{\pi\pi}^2 d\tilde{\Omega}_\pi d\Omega'_\tau} = \frac{\alpha^3 \tilde{\beta}_\tau}{16\pi^2 E_0^2} [D'_0 A A' + D'_{ij} B_i B'_j]. \quad (\text{B.58})$$

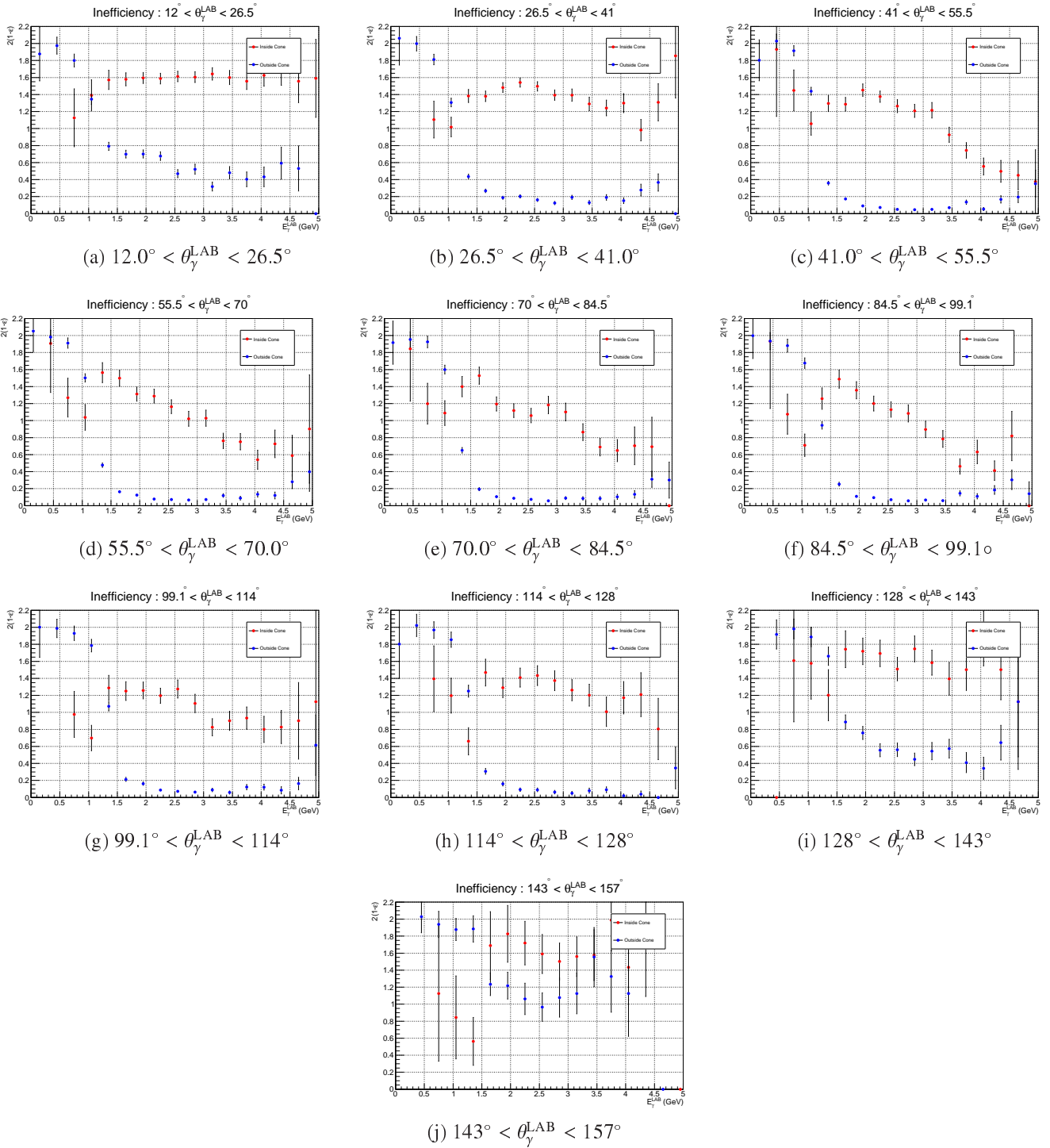


Figure B.3: The inefficiency of  $\gamma$  as a function of energy  $E_\gamma^{\text{LAB}}$  in each range of angle  $\theta_\gamma^{\text{LAB}}$ . The blue and red points represent the inefficiency when the  $\gamma$  is generated inside and outside cone around  $\pi$  respectively.

The visible PDF in CMS is obtained by change of variables with four Jacobians:

$$\begin{aligned} \tilde{B}^{\text{ISR+ord}}(\mathbf{x}) &\equiv \frac{d\sigma}{dP_\gamma d\Omega_\gamma dP'_\ell d\Omega'_\ell dP'_\rho d\Omega'_\rho dm_{\pi\pi}^2 d\tilde{\Omega}_\pi} \\ &= \int_{\Phi'_1}^{\Phi'_2} d\Phi'_\tau \frac{d\sigma}{dP_\gamma d\Omega_\gamma dP'_\ell d\Omega'_\ell dP'_\rho d\Omega'_\rho dm_{\pi\pi}^2 d\tilde{\Omega}_\pi d\Phi'_\tau} \left| \frac{\partial(P'_\ell, \Omega'_\ell)}{\partial(P_\ell, \Omega_\ell)} \right| \cdot \left| \frac{\partial(P'_\rho, \Omega'_\rho)}{\partial(P_\rho, \Omega_\rho)} \right| \end{aligned} \quad (\text{B.59})$$

$$= \int_{\Phi'_1}^{\Phi'_2} d\Phi'_\tau \frac{d\sigma}{dP_\gamma d\Omega_\gamma dE'_\ell d\Omega'^*_\ell d\Omega'^*_\rho dm_{\pi\pi}^2 d\tilde{\Omega}_\pi d\Omega'_\tau} \left| \frac{\partial(E'_\ell, \Omega'^*_\ell)}{\partial(P'_\ell, \Omega'_\ell)} \right| \left| \frac{\partial(\Omega'^*_\rho, \Omega'_\tau)}{\partial(P'_\rho, \Omega'_\rho, \Phi'_\tau)} \right| \left| \frac{\partial(P'_\ell, \Omega'_\ell)}{\partial(P_\ell, \Omega_\ell)} \right| \left| \frac{\partial(P'_\rho, \Omega'_\rho)}{\partial(P_\rho, \Omega_\rho)} \right| \quad (\text{B.60})$$

$$= \int_{\Phi'_1}^{\Phi'_2} d\Phi'_\tau \frac{\alpha^3 \tilde{\beta}_\tau}{16\pi^2 E_0^2} [D'_0 AA' + D'_{ij} B_i B'_j] J_1 J_2 J_3 J_4. \quad (\text{B.61})$$

$$J_1 = \left| \frac{\partial(E'_\ell, \Omega'^*_\ell)}{\partial(P'_\ell, \Omega'_\ell)} \right| = \frac{P'^2_\ell}{E'_\ell P'^*_\ell}, \quad (\text{B.62})$$

$$J_2 = \left| \frac{\partial(\Omega'^*_\rho, \Omega'_\tau)}{\partial(P'_\rho, \Omega'_\rho, \Phi'_\tau)} \right| = \frac{m_\tau P'_\rho}{E'_\rho P'^*_\rho P'_\tau}, \quad (\text{B.63})$$

$$J_3 = \left| \frac{\partial(P'_\ell, \Omega'_\ell)}{\partial(P_\ell, \Omega_\ell)} \right| = \frac{P'^2_\ell E'_\ell}{P'^2_\ell E_\ell}, \quad (\text{B.64})$$

$$J_4 = \left| \frac{\partial(P'_\rho, \Omega'_\rho)}{\partial(P_\rho, \Omega_\rho)} \right| = \frac{P'^2_\rho E'_\rho}{P'^2_\rho E_\rho}. \quad (\text{B.65})$$

## B.5 Description of $3\pi$ - $2\pi$ decay events

The  $3\pi$ - $2\pi$  process  $e^+e^- \rightarrow \tau^+\tau^- \rightarrow (\pi^+\pi^0\bar{\nu})(\pi^-\pi^0\pi^0\nu)$  has a large impact for the fitted Michel Parameters (especially  $\xi\kappa$ ) and we analytically describe this distribution. This process is reconstructed when a charged pion from  $\tau^- \rightarrow \pi^-\pi^0\pi^0\nu$  decay is mis-identified as a muon and one photon from either of  $\pi^0$  is reconstructed as a signal photon.

The description of PDF is similar to the  $3\pi$  and  $\rho$ - $\rho$  cases explained in Sec. B.2 and B.3. The start point of formulation is

$$\frac{d\Gamma(\tau^- \rightarrow \pi^-\pi^0\pi^0\nu)}{d\Omega_{a_1}^* dm_{a_1}^2 d\hat{\Omega}_\rho dm_\rho^2 d\tilde{\Omega}_\pi} = [A^- - \mathbf{B}^- \cdot \mathbf{S}_\tau^*] \frac{2P_{a_1}^*}{m_\tau} \frac{2\hat{P}_\rho}{m_{a_1}} \frac{2\tilde{P}_\pi}{m_\rho}, \quad (\text{B.66})$$

and

$$\frac{d\Gamma(\tau^+ \rightarrow \pi^+\pi^0\bar{\nu})}{d\Omega_{\rho'}^* dm_{\rho'}^2 d\tilde{\Omega}_{\pi'}} = A^+ + \mathbf{B}^+ \cdot \mathbf{S}_\tau^*, \quad (\text{B.67})$$

where  $A^-$  and  $\mathbf{B}^-$  are the form factors of the  $\tau^- \rightarrow \pi^-\pi^0\pi^0\nu$  events and  $A^+$  and  $\mathbf{B}^+$  are those of  $\tau^+ \rightarrow \pi^+\pi^0\bar{\nu}$ . In the same manner as signal PDF construction, using  $D_0$  and  $D_{ij}$ , we obtain

$$\frac{d\sigma(e^+e^- \rightarrow \tau^+\tau^- \rightarrow (\pi^+\pi^0\pi^0\bar{\nu})(\pi^-\pi^0\nu))}{d\Omega_{a_1}^* dm_{a_1}^2 d\hat{\Omega}_\rho dm_\rho^2 d\tilde{\Omega}_\pi d\Omega_{\rho'}^* dm_{\rho'}^2 d\tilde{\Omega}_{\pi'} d\Omega_\tau} \propto \frac{\beta_\tau}{E_\tau^2} (A^- A^+ D_0 - D_{ij} B_i^- B_j^+) \frac{2P_{a_1}^*}{m_\tau} \frac{2\hat{P}_\rho}{m_{a_1}} \frac{2\tilde{P}_\pi}{m_\rho}. \quad (\text{B.68})$$

The differential variables are changed to those of CMS by Jacobians:

$$\frac{d\sigma}{dP_{\rho'} d\Omega_{\rho'} dm_{\rho'}^2 d\tilde{\Omega}_{\pi'} dP_{\pi} d\Omega_{\pi} dP_{\pi^0} d\Omega_{\pi^0} dP_{\pi^0} d\Omega_{\pi^0}} \quad (\text{B.69})$$

$$= \frac{d\sigma}{d\Omega_{a_1}^* dm_{a_1}^2 d\hat{\Omega}_{\rho} dm_{\rho}^2 d\tilde{\Omega}_{\pi} d\Omega_{\rho'}^* dm_{\rho'}^2 d\tilde{\Omega}_{\pi'} d\Omega_{\tau}} J_1 J_2 J_3, \quad (\text{B.70})$$

$$J_1 = \left| \frac{\partial(\Omega_{\tau}, \Omega_{\rho'}, \Omega_{a_1}^*)}{\partial(P_{\rho'}, \Omega_{\rho'}, P_{a_1}, \Omega_{a_1})} \right| = \frac{\beta_{\rho'} \beta_{a_1}}{\beta_{\tau}^2 \gamma_{\tau}^2 P_{\rho'}^* P_{a_1}^* |\mathbf{n}_{\tau} \cdot (\mathbf{n}_{\rho'} \times \mathbf{n}_{a_1})|} \quad (\text{B.71})$$

$$J_2 = \left| \frac{\partial(P_{a_1}, \Omega_{a_1}, m_{a_1}^2, \hat{\Omega}_{\rho})}{\partial(P_{\rho}, \Omega_{\rho}, P_{\pi^0}, \Omega_{\pi^0})} \right| = \left( \frac{P_{\rho} P_{\pi^0}}{P_{a_1}} \right)^2 \frac{E_{a_1}}{E_{\pi^0} E_{\rho}} \frac{2m_{a_1}}{\hat{P}_{\rho}} \quad (\text{B.72})$$

$$J_3 = \left| \frac{\partial(P_{\rho}, \Omega_{\rho}, m_{\rho}^2, \tilde{\Omega}_{\pi})}{\partial(P_{\pi}, \Omega_{\pi}, P_{\pi^0}, \Omega_{\pi^0})} \right| = \left( \frac{P_{\pi} P_{\pi^0}}{P_{\rho}} \right)^2 \frac{E_{\rho}}{E_{\pi} E_{\pi^0}} \frac{2m_{\rho}}{\tilde{P}_{\pi}} \quad (\text{B.73})$$

Furthermore, using the isotropic nature of  $d\Gamma(\pi^0 \rightarrow \gamma\gamma) = d\Omega_{\gamma}^{**}/4\pi$ , the intrinsic PDF is given by:

$$B_{\text{int}}^{(3\pi, 2\pi)} \equiv \frac{d\sigma}{dP_{\rho'} d\Omega_{\rho'} dm_{\rho'}^2 d\tilde{\Omega}_{\pi'} dP_{\pi} d\Omega_{\pi} dP_{\pi^0} d\Omega_{\pi^0} dP_{\gamma} d\Omega_{\gamma} d\Omega_{\gamma'}} \quad (\text{B.74})$$

$$= \frac{d\sigma}{d\Omega_{a_1}^* dm_{a_1}^2 d\hat{\Omega}_{\rho} dm_{\rho}^2 d\tilde{\Omega}_{\pi} d\Omega_{\rho'}^* dm_{\rho'}^2 d\tilde{\Omega}_{\pi'} d\Omega_{\tau}} J_1 J_2 J_3 J_4, \quad (\text{B.75})$$

$$J_4 = \left| \frac{\partial(P_{\pi^0}, \Omega_{\pi^0}, \Omega_{\gamma}^{**})}{\partial(P_{\gamma}, \Omega_{\gamma}, \Omega_{\gamma'})} \right| = \frac{4E_{\gamma}^2 E_{\gamma} E_{\pi^0}}{P_{\pi^0}^2 m_{\pi^0}^2} \quad (\text{B.76})$$

Thus the visible PDF is

$$\tilde{B}_{\text{int}}^{(3\pi, 2\pi)} = \frac{d\sigma}{dP_{\rho'} d\Omega_{\rho'} dm_{\rho'}^2 d\tilde{\Omega}_{\pi'} dP_{\pi} d\Omega_{\pi} dP_{\gamma} d\Omega_{\gamma}} \quad (\text{B.77})$$

$$= \int dP_{\pi^0} d\Omega_{\pi^0} d\Omega_{\gamma'} B_{\text{int}}^{(3\pi, 2\pi)} 4 \frac{\mathcal{E}_{\pi \rightarrow \mu}^{\text{PID}}}{\mathcal{E}_{\mu \rightarrow \mu}^{\text{PID}}} \mathcal{E}^{\text{inef.}} \quad (\text{B.78})$$

### B.5.1 extraction of inefficiency

Due to the small statistics of the  $3\pi-2\pi$  events, an ideal tabulation of inefficiency is difficult when we use the generic MC. In fact, if the explained selection criteria is applied, the efficiency is approximately  $3 \times 10^{-5}$ , which finally gives only  $\sim 5000$  events with five times as large statistics as real experiment. This small efficiency mainly comes from requirement of the likelihood of muon,  $P(\mu/\pi) > 0.9$ , hence it is possible to recover the efficiency with relax of the cut. The inefficiency can be obtained by following formula:

$$\mathcal{E}_{\text{inef.}} = N_{\text{numerator}}/N_{\text{denominator}}, \quad (\text{B.79})$$

where the denominator is number of selected events which passed all selection criteria except the extra gamma energy cut and number of gamma in the cone and the numerator is number of selected events which passes the excluded selection criteria. The tabulation of the inefficiency is obtained depending on the topology of the events, which are categorized into eighteen groups. See the Fig B.4. The gamma  $A$  is divided into three groups: it is outside the acceptance, or it is inside the acceptance but is in the cone around lepton or not. This situation is shown in Fig. B.5. Due to the small statistics, we tabulated the factor as a constant for each categorization. The obtained values are summarized in Table B.2.

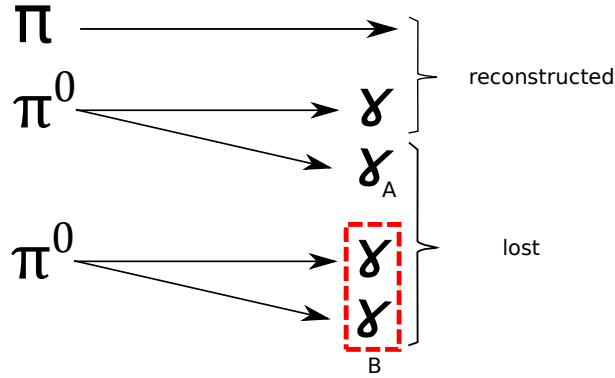


Figure B.4: Notation of gamma. The lost gamma whose mother is same as reconstructed one is tagged as  $A$ . The other gammas are tagged  $B$ .

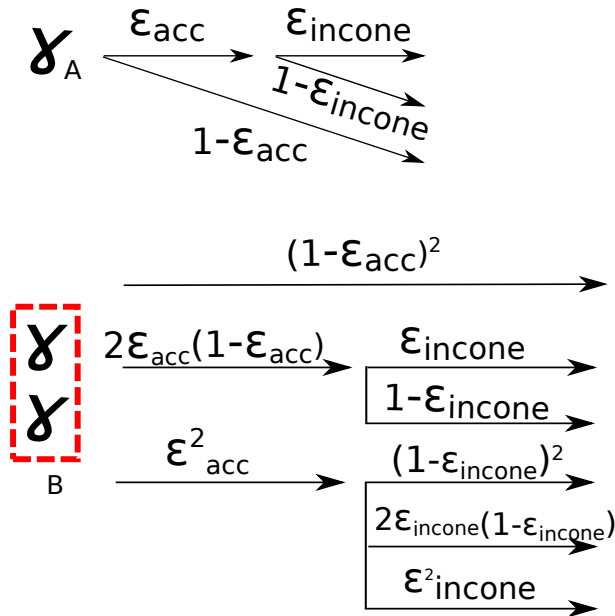


Figure B.5: The gamma  $A$  is categorized into three groups, while two gamma  $B$  are into six groups. The  $\epsilon_{acc}$  is an efficiency that gamma is in the acceptance of detector. The  $\epsilon_{incone}$  is an efficiency that gamma is inside cone around lepton. In total, three lost gammas are categorized into  $3 \times 6 = 18$  groups.

Table B.2: Obtained inefficiency and efficiency of extra gamma energy cut

ID	A type	B type	$\epsilon_{\text{inef}} / \epsilon_{\text{extray}}^{\text{sig}}$	error
0	$1 - \epsilon_{\text{acc}}$	$(1 - \epsilon_{\text{acc}})^2$	0.98	0.05
1	$1 - \epsilon_{\text{acc}}$	$2\epsilon_{\text{acc}}(1 - \epsilon_{\text{acc}})\epsilon_{\text{incone}}$	0.75	0.10
2	$1 - \epsilon_{\text{acc}}$	$2\epsilon_{\text{acc}}(1 - \epsilon_{\text{acc}})(1 - \epsilon_{\text{incone}})$	0.66	0.02
3	$1 - \epsilon_{\text{acc}}$	$\epsilon_{\text{acc}}^2 2\epsilon_{\text{incone}}(1 - \epsilon_{\text{incone}})$	0.24	0.14
4	$1 - \epsilon_{\text{acc}}$	$\epsilon_{\text{acc}}^2 \epsilon_{\text{incone}}^2$	0.193	0.003
5	$1 - \epsilon_{\text{acc}}$	$\epsilon_{\text{acc}}^2 (1 - \epsilon_{\text{incone}})^2$	0.17	0.05
6	$\epsilon_{\text{acc}}(1 - \epsilon_{\text{incone}})$	$(1 - \epsilon_{\text{acc}})^2$	0.54	0.01
7	$\epsilon_{\text{acc}}(1 - \epsilon_{\text{incone}})$	$2\epsilon_{\text{acc}}(1 - \epsilon_{\text{acc}})\epsilon_{\text{incone}}$	0.32	0.01
8	$\epsilon_{\text{acc}}(1 - \epsilon_{\text{incone}})$	$2\epsilon_{\text{acc}}(1 - \epsilon_{\text{acc}})(1 - \epsilon_{\text{incone}})$	0.279	0.002
9	$\epsilon_{\text{acc}}(1 - \epsilon_{\text{incone}})$	$\epsilon_{\text{acc}}^2 2\epsilon_{\text{incone}}(1 - \epsilon_{\text{incone}})$	0.099	0.002
10	$\epsilon_{\text{acc}}(1 - \epsilon_{\text{incone}})$	$\epsilon_{\text{acc}}^2 \epsilon_{\text{incone}}^2$	0.0957	0.0004
11	$\epsilon_{\text{acc}}(1 - \epsilon_{\text{incone}})$	$\epsilon_{\text{acc}}^2 (1 - \epsilon_{\text{incone}})^2$	0.129	0.01
12	$\epsilon_{\text{acc}} \epsilon_{\text{incone}}$	$(1 - \epsilon_{\text{acc}})^2$	0.41	0.02
13	$\epsilon_{\text{acc}} \epsilon_{\text{incone}}$	$2\epsilon_{\text{acc}}(1 - \epsilon_{\text{acc}})\epsilon_{\text{incone}}$	0.36	0.03
14	$\epsilon_{\text{acc}} \epsilon_{\text{incone}}$	$2\epsilon_{\text{acc}}(1 - \epsilon_{\text{acc}})(1 - \epsilon_{\text{incone}})$	0.278	0.003
15	$\epsilon_{\text{acc}} \epsilon_{\text{incone}}$	$\epsilon_{\text{acc}}^2 2\epsilon_{\text{incone}}(1 - \epsilon_{\text{incone}})$	0.141	0.004
16	$\epsilon_{\text{acc}} \epsilon_{\text{incone}}$	$\epsilon_{\text{acc}}^2 \epsilon_{\text{incone}}^2$	0.145	0.001
17	$\epsilon_{\text{acc}} \epsilon_{\text{incone}}$	$\epsilon_{\text{acc}}^2 (1 - \epsilon_{\text{incone}})^2$	0.077	0.02

## B.6 Description of an ordinary leptonic decay + bremsstrahlung events

The ordinary leptonic decay  $\tau^- \rightarrow e^- \nu \bar{\nu}$  is reconstructed as signal when the electron produces a photon accelerated by an electric field of atoms in the material of detector. To clarify the notation, we divide all observables into three parts: we use  $\mathbf{x} = \{P_\rho, \Omega_\rho, m_\rho^2, \tilde{\Omega}_\pi\}$ , which is not relevant to bremsstrahlung,  $\mathbf{y} = \{P_\ell, \Omega_\ell\}$  and  $\mathbf{z} = \{P_\gamma, \Omega_\gamma\}$ . Moreover, we further define generated momentum of electron as  $\mathbf{y}' = \{P'_\ell, \Omega'_\ell\}$ . Hereafter in this section,  $\mathbf{y}$ ,  $\mathbf{y}'$  and  $\mathbf{z}$ , are evaluated in the laboratory frame even if letters do not have LAB in the superscript. Based on the above notation, the PDF is formulated as:

$$B_{\text{ini}}^{(\text{ord}+\text{brems})}(\mathbf{x}, \mathbf{y}, \mathbf{y}', \mathbf{z}) = f(\mathbf{y}') B^{\text{ord.}}(\mathbf{x}, \mathbf{y}') B^{\text{brems}}(\mathbf{y}, \mathbf{y}', \mathbf{z}) \quad (\text{B.80})$$

$$f(\mathbf{y}') = \frac{L(\theta_\ell)}{1 - \frac{E_{\gamma\text{min}}}{E_\ell^{\text{LAB}}} \log\left(\frac{E_{\gamma\text{min}}}{E_\ell^{\text{LAB}}}\right)}, \quad (\text{B.81})$$

where function  $f$  represents probability that electron ( $P'_\ell, \Omega'_\ell$ ) emits bremsstrahlung whose energy is larger than energy threshold  $E_{\gamma\text{min}}$ .<sup>†</sup>  $L(\theta_\ell)$  is an amount of material per unit of radiation length. The  $L(\theta_\ell)$  can be simplified as  $L(\theta_\ell) = L(\theta_\ell = 90^\circ) / \sin\theta_\ell$ . For SVD1, we use  $L = 0.19\% X_0$  and  $0.27\% X_0$  for SVD2. The energy threshold  $E_{\gamma\text{min}} = 1 \text{ MeV}$  is chosen to satisfy the condition  $E_{\gamma\text{min}}/E_\ell \ll \sigma_{P_e}/P_e$ . The  $B^{\text{brems.}}(\mathbf{y}, \mathbf{y}', \mathbf{z})$  is a differential decay width of bremsstrahlung as a function of photon and scattered electron and represented as

<sup>†</sup>The decrease of electron energy inside material follows well known equation  $dE/dx = -E/X_0$ . Assuming that the flight length in material is small, we can approximate the energy loss of electron as  $\epsilon = E_0 x/X_0$ . Using simplified PDF of energy of bremsstrahlung,  $\text{PDF}(E_\gamma) = (1 - f)\Theta(E_\gamma - E_{\gamma\text{min}}) + f/E_\gamma \log(E_\gamma/E_\ell)$ , we can formulate a equation  $\epsilon = \int \text{PDF}(E_\gamma) E_\gamma dE_\gamma$ , which accordingly gives analytical fraction  $f$ .

$$B_{\text{ini}}^{\text{brems}}(\mathbf{y}, \mathbf{y}', \mathbf{z}) = \frac{d\Gamma}{dP_\gamma d\Omega_\ell d\Omega_\gamma} \quad (\text{B.82})$$

$$\begin{aligned} &\propto \frac{1}{E} \frac{P}{P_0} \left[ \frac{P^2 \sin^2 \theta}{(E - P \cos \theta)^2} (4E_0^2 - Q^2) + \frac{P_0^2 \sin^2 \theta_0}{(E_0 - P_0 \cos \theta)^2} (4E^2 - Q^2) \right. \\ &\quad \left. - \frac{2PP_0 \sin \theta \sin \theta_0 \cos \phi (4EE_0 - Q^2)}{(E - P \cos \theta)(E_0 - P_0 \cos \theta_0)} + \frac{2K^2 (P^2 \sin \theta + P_0^2 \sin \theta_0 - 2PP_0 \sin \theta \sin \theta_0 \cos \phi)}{(E - P \cos \theta)(E_0 - P_0 \cos \theta_0)} \right] \end{aligned} \quad (\text{B.83})$$

$$Q^2 = P^2 + P_0^2 + K^2 - 2P_0 K \cos \theta_0 + 2PK \cos \theta - 2P_0 P (\cos \theta \cos \theta_0 + \sin \theta \sin \theta_0 \cos \phi), \quad (\text{B.84})$$

where capital letters  $K$ ,  $P$  and  $P_0$  are momenta of gamma, electron and scattered electron, which are normalized in a unit of mass of electron.  $\theta_0$ ,  $\theta$  and  $\phi$  are directions of them illustrated in Fig B.6. The visible differential cross section is obtained by integrating  $\mathbf{y}'$  as

$$\tilde{B}_{\text{vis}}^{(\text{ord+brems})}(\mathbf{x}, \mathbf{y}, \mathbf{z}) = \frac{d\sigma}{dP_\ell d\Omega_\ell dP_\gamma d\Omega_\gamma dP_\rho d\Omega_\rho dm_\rho^2 d\tilde{\Omega}_\pi} \quad (\text{B.85})$$

$$= \int d\mathbf{y}' \tilde{B}_{\text{ini}}^{(\text{ord+brems})}(\mathbf{x}, \mathbf{y}, \mathbf{y}', \mathbf{z}) \frac{E_\gamma^{\text{CMS}}}{E_\gamma^{\text{LAB}}} \frac{P_\ell^{2\text{CMS}} E_\ell^{\text{LAB}}}{E_\ell^{\text{CMS}} P_\ell^{2\text{LAB}}}. \quad (\text{B.86})$$

The last two factors in Eq. (B.86) are Jacobians which convert differential variables of photon and electron momenta from the laboratory frame to CMS frame.



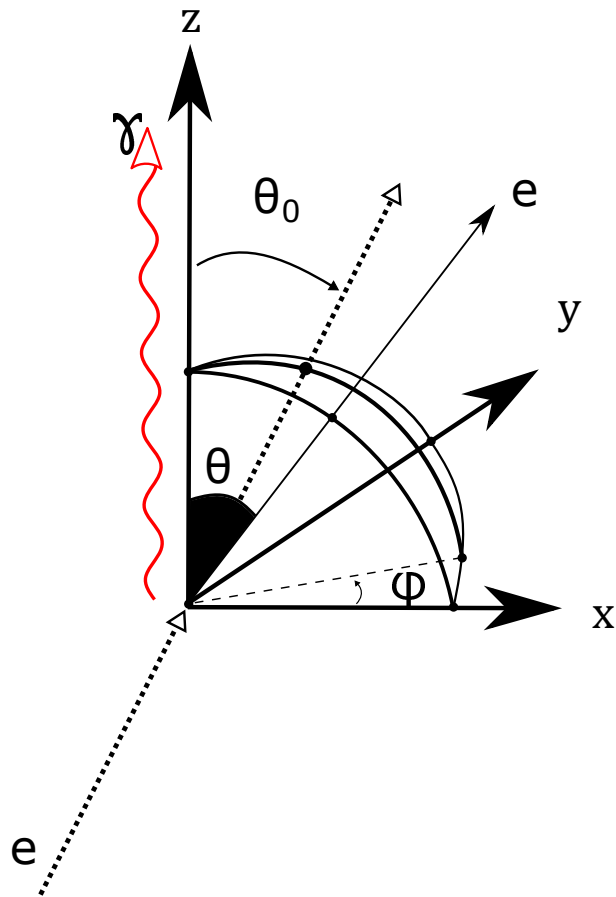


Figure B.6: Definition of the variable of bremsstrahlung of electron. The direction of the bremsstrahlung photon is  $z$ -axis, and scattered electron is in the  $xz$ -plane.

# Appendix C

## Calculation of Jacobians

Here, the calculations of some of Jacobians appearing in the main text are described. In this analysis, we use many Jacobians to change variables from ones defined in tau rest frame into those of the CMS frame. Because an intrinsic differential decay width is usually defined in the  $\tau$  rest frame, it is required to convert variables so that all differential variables are within a common coordinate system. In principle, any Jacobians can be directly calculated by differentiations of variables in numerators with those of denominators and a calculation of determinant of the matrix. Although the calculation itself is straightforward, it sometimes takes pains to perform the simple calculation because the number of terms tends to be very large. On the other hand, for a certain set of Jacobians related to the Lorentz transformation, there is a more simple and easier method utilizing the nature of Lorentz-invariance.

Normally, the Lorentz-invariant phase space of one particle is defined as  $d^3p/(2\pi)^3 2E_p$ . However, the  $(2\pi)^3$  is a common factor and not important for the derivation of Jacobians. Therefore, in this appendix, we forget this factor and adopt an unusual Lorentz-invariant phase space as  $d^3p/2E_p$ . Apparently, the Lorentz-invariance is not broken at all. To denote the magnitude of spatial component of four vector  $p$ , we use a capital letter  $P$ . The differential variables  $d^3p$  and  $d^4p$  mean  $dp_x dp_y dp_z$  and  $dEdp_x dp_y dp_z$ , respectively. Moreover, we abbreviate the explicit notation of the integration sign  $\int$ .

### C.1 Jacobian for Lorentz-transformation

By definition, Lorentz-invariant phase space should not change when Lorentz transformation is applied to a certain four momentum  $p \rightarrow p'$ . Therefore, the following equation holds:

$$\begin{aligned} \frac{d^3p}{2E_p} &= \frac{d^3p'}{2E'_p} \\ \Leftrightarrow \frac{P^2 dP d\Omega_p}{2E_p} &= \frac{P'^2 dP' d\Omega'_p}{2E'_p} = \frac{P'^2 dP d\Omega_p}{2E'_p} \times \left| \frac{\partial(P', \Omega'_p)}{\partial(P, \Omega_p)} \right| \\ \left| \frac{\partial(P', \Omega'_p)}{\partial(P, \Omega_p)} \right| &= \frac{P^2 E'_p}{P'^2 E_p}. \end{aligned} \tag{C.1}$$

### C.2 2-body decay

For massive particle  $a$ , we can consider the frame in which  $a$  is at rest. In this system, the phase space of two body decay can be simplified. Hereafter, the result is often quoted. We consider following two body decay:

$$a(p) \rightarrow b(q)c(r).$$

Since the four-vector conservation holds, the delta function  $\delta(p - q - r)$  is multiplied for the Lorentz-invariant phase space. If we apply integration for four vector  $r$  in the  $a$ -rest frame, the Lorentz invariant phase space can be expressed as:

$$\frac{d^3q}{2E_q} \frac{d^3r}{2E_r} \delta(p - q - r) = \frac{d^3q}{2E_q} \frac{d^3\tilde{r}}{2\tilde{E}_r} \delta(p - q - r) = \frac{d^3q}{4E_q\tilde{E}_r} \delta^{(0)}(m_a - \tilde{E}_q - \tilde{E}_r), \quad (\text{C.2})$$

where tilde means variables are defined in the  $a$ -rest frame and  $m_a$  is a mass of  $a$ . Furthermore,  $d^3q/2E_q$  is also evaluated in  $a$ -rest frame and Eq. (C.2) becomes

$$\begin{aligned} & \frac{d^3\tilde{q}}{4\tilde{E}_q\tilde{E}_r} \delta^{(0)}(m_a - \tilde{E}_q - \tilde{E}_r) \\ &= \frac{\tilde{Q}^2 d\tilde{Q} d\tilde{\Omega}_q}{4\tilde{E}_q\tilde{E}_r} \delta^{(0)}\left(m_a - \tilde{E}_q - \sqrt{m_c^2 + \tilde{Q}^2}\right) \\ &= \frac{\tilde{Q}^2 d\tilde{\Omega}_q}{4\tilde{E}_q\tilde{E}_r} \left[ \frac{\tilde{Q}}{\tilde{E}_q} + \frac{\tilde{Q}}{\tilde{E}_r} \right]^{-1} \\ &= \frac{\tilde{Q} d\tilde{\Omega}_q}{4\tilde{E}_p} = \frac{\tilde{Q} d\tilde{\Omega}_q}{4m_a}. \end{aligned} \quad (\text{C.3})$$

From second to third line, an equation of the delta function

$$\delta(f(x)) = \frac{1}{|f'(x_0)|} \delta(x - x_0) \quad (f(x_0) = 0) \quad (\text{C.4})$$

is used. Thus the two-body phase space is simplified

$$\frac{d^3q}{2E_q} \frac{d^3r}{2E_r} \delta(p - q - r) = \frac{\tilde{Q} d\tilde{\Omega}_q}{4m_a} \quad (\text{C.5})$$

### C.2.1 $\left| \frac{\partial(P_{\pi_0}, \Omega_{\pi_0}, \Omega_{\gamma}^{**})}{\partial(P_{\gamma}, \Omega_{\gamma}, \Omega_{\gamma'})} \right|$

The Jacobian which appears in the decay of pion

$$\pi^0(p) \rightarrow \gamma(k)\gamma'(q)$$

is also calculated by a manipulation of the Lorentz-invariant phase space.

$$\begin{aligned} \text{dLIPS} &= \frac{d^3p}{2E_p} \frac{d^3k}{2E_k} \frac{d^3q}{2E_q} \delta(p - k - q) \\ &= \frac{d^3k d^3q}{8E_p E_k E_q} \delta^{(0)}(E_p - E_k - E_q) \quad (\mathbf{p} = \mathbf{k} + \mathbf{q}) \\ &= \frac{K^2 dk d\Omega_k Q^2 dQ d\Omega_q}{8E_p E_k E_q} \delta^{(0)}\left(\sqrt{m_{\pi_0}^2 + (\mathbf{k} + \mathbf{q})^2} - E_k - E_q\right) \\ &= \frac{K dK d\Omega_k Q dQ d\Omega_q}{8E_p} \delta^{(0)}\left(\sqrt{K^2 + 2KQ \cos \psi_{\gamma\gamma'} + Q^2 + m_{\pi_0}^2} - K - Q\right) \end{aligned}$$

$$\begin{aligned}
&= \frac{KdKd\Omega_k Qd\Omega_q}{8E_p} \frac{1}{\left| \frac{K \cos \psi_{\gamma\gamma'} + Q}{E_p} - 1 \right|} \\
&= \frac{KdKd\Omega_k Q^2 d\Omega_q}{4m_{\pi^0}^2}. \quad \left( Q = \frac{m_{\pi^0}^2}{2K(1 - \cos \psi_{\gamma\gamma'})} \right)
\end{aligned} \tag{C.6}$$

Applying Eq. (C.5) for the Lorentz-invariant phase space of three particles for two photons in  $\pi^0$  rest frame, we obtain another expression:

$$\begin{aligned}
d\text{LIPS} &= \frac{d^3 p}{2E_p} \frac{K^{**} d\Omega_k^{**}}{4E_p^{**}} = \frac{P^2 d\Omega_p dP \frac{m_{\pi^0}}{2} d\Omega_k^{**}}{8E_p m_{\pi^0}} = \frac{P^2 d\Omega_p dP d\Omega_k^{**}}{16E_p} \\
&\equiv \frac{P^2}{16E_p} dK d\Omega_k d\Omega_q \times \left| \frac{\partial(P_{\pi_0}, \Omega_{\pi_0}, \Omega_{\gamma}^{**})}{\partial(P_{\gamma}, \Omega_{\gamma}, \Omega_{\gamma'})} \right| \\
&\Rightarrow \left| \frac{\partial(P_{\pi_0}, \Omega_{\pi_0}, \Omega_{\gamma}^{**})}{\partial(P_{\gamma}, \Omega_{\gamma}, \Omega_{\gamma'})} \right| = \frac{4E_p K Q^2}{P^2 m_{\pi^0}^2}
\end{aligned} \tag{C.7}$$

$$\mathbf{C.3} \quad \left| \frac{\partial(P_{a_1}, \Omega_{a_1}, m_{a_1}^2, \hat{\Omega}_\rho)}{\partial(P_{\pi_0^{\text{lost}}}, \Omega_{\pi_0^{\text{lost}}}, P_\rho, \Omega_\rho)} \right|$$

$$a_1(p) \rightarrow \rho(q)\pi(r)$$

Since  $a_1$  is not on-shell particle, Lorentz-invariant phase space becomes  $\frac{d^3 p}{2E_p} \rightarrow d^4 p = \frac{dm^2 d^3 p}{2E_p}$ .

$$\begin{aligned}
d\text{LIPS} &= \frac{d^3 p}{2E_p} \frac{dm_{a_1}^2}{2E_q} \frac{d^3 q}{2E_r} \delta(p - q - r) \\
&= \frac{dm_{a_1}^2 d^3 q d^3 r}{8E_p E_q E_r} \delta^{(0)}(E_p - E_q - E_r) \\
&= \frac{dm_{a_1}^2 d^3 q d^3 r}{8E_p E_q E_r} \delta^{(0)}\left(\sqrt{m_{a_1}^2 + (\mathbf{q} + \mathbf{r})^2} - E_q - E_r\right) = \frac{Q^2 R^2 dQ d\Omega_q dR d\Omega_r}{4E_q E_r} \\
d\text{LIPS} &= \frac{d^3 p}{2E_p} \frac{dm_{a_1}^2}{2E_q} \frac{d^3 q}{2E_r} \delta(p - q - r) \\
&= \frac{d^3 p}{2E_p} \frac{dm_{a_1}^2}{4m_{a_1}} \tilde{Q} d\tilde{\Omega}_q \quad (\text{we use Eq. (C.5)}) \\
&= \frac{P^2 \tilde{Q} dP d\Omega_p dm_{a_1}^2 d\tilde{\Omega}_q}{8E_p m_{a_1}} = \frac{P^2 \tilde{Q} dQ d\Omega_q dR d\Omega_r}{8E_p m_{a_1}} \times \left| \frac{\partial(P, \Omega_p, m_{a_1}^2, \tilde{\Omega}_q)}{\partial(Q, \Omega_q, r, \Omega_r)} \right| \\
&\quad \left| \frac{\partial(P, \Omega_p, m_{a_1}^2, \tilde{\Omega}_q)}{\partial(Q, \Omega_q, r, \Omega_r)} \right| = \frac{2Q^2 R^2 E_p m_{a_1}}{P^2 \tilde{Q} E_q E_r}
\end{aligned} \tag{C.8}$$

This formula also holds when  $p$  is a on-shell particle.

$$\mathbf{C.4} \quad \left| \frac{\partial(\Omega_{\rho_1}^*, \Omega_{\rho_2}^*, \Omega_\tau)}{\partial(P_{\rho_1}, \Omega_{\rho_1}, P_{\rho_2}, \Omega_{\rho_2})} \right|$$

$$e^+ e^-(r) \rightarrow \tau^+(q_1) \tau^-(q_2) \rightarrow \rho^+(p_1) \bar{\nu}(k_1) \rho^-(p_2) \nu(k_2)$$

$$\begin{aligned} \text{dLIPS} &= \frac{d^3 p_1}{2E_{p_1}} \frac{d^3 p_2}{2E_{p_2}} \frac{d^3 k_1}{2E_{k_1}} \frac{d^3 k_2}{2E_{k_2}} \frac{d^3 q_2}{2E_{q_2}} \frac{d^3 q_1}{2E_{q_1}} \delta(r - q_2 - q_1) \delta(q_1 - p_1 - k_1) \delta(q_2 - p_2 - k_2) \\ &= \frac{d^3 p_1 d^3 p_2 d^3 k_1 d^3 k_2}{16E_{p_1} E_{p_2} K_1 K_2} \frac{Q_2 d\Omega_{q_2}}{8E_\tau} \delta(q_1 - p_1 - k_1) \delta(q_2 - p_2 - k_2) \quad (\mathbf{q}_2 = -\mathbf{p}) \quad (\text{Eq. (C.2) for } \mathbf{q}_2 \text{ and } \mathbf{q}_1) \\ &= \frac{P_1^* d\Omega_{p_1}^*}{4E_{q_1}^*} \frac{P_2^* d\Omega_{p_2}^*}{4E_{q_2}^*} \frac{Q_2 d\Omega_{q_2}}{8E_\tau} = \frac{P_1^* P_2^* d\Omega_{p_1}^* d\Omega_{p_2}^*}{16m_\tau^2} \frac{Q_2 d\Omega_{q_2}}{8E_\tau} \quad (\text{Eq. (C.2) for } (\mathbf{k}_1, \mathbf{p}_1) \text{ and } (\mathbf{k}_2, \mathbf{p}_2)) \\ \text{dLIPS} &= \frac{d^3 p_1 d^3 p_2 d^3 k_1 d^3 k_2}{16E_{p_1} E_{p_2} K_1 K_2} \frac{Q_2 d\Omega_{q_2}}{8E_\tau} \delta(q_1 - p_1 - k_1) \delta(q_2 - p_2 - k_2) \\ &= \frac{d^3 p_1 d^3 p_2}{16E_{p_1} E_{p_2} K_1 K_2} \frac{Q_2 d\Omega_{q_2}}{8E_\tau} \delta^{(0)}(E_q - E_{p_1} - k_1) \delta^{(0)}(E_{q_2} - E_{p_2} - k_2) \quad (\mathbf{k}_1 = \mathbf{q}_1 - \mathbf{p}_1, \mathbf{k}_2 = \mathbf{q}_2 - \mathbf{p}_2) \\ &= \frac{Q_2 P_1^2 P_2^2 dP_1 d\Omega_{p_1} dP_2 d\Omega_{p_2}}{16E_{p_1} E_{p_2} K_1 K_2} \frac{d\Omega_{q_2}}{8E_\tau} \delta^{(0)}(E_\tau - E_{p_1} - |\mathbf{p}_1 + \mathbf{q}_2|) \delta^{(0)}(E_q - E_{p_2} - |\mathbf{q}_2 - \mathbf{p}_2|) \end{aligned} \quad (\text{C.9})$$

$$= \frac{Q_2 P_1^2 P_2^2 dP_1 d\Omega_{p_1} dP_2 d\Omega_{p_2}}{16E_{p_1} E_{p_2} K_1 K_2} \frac{d\Omega_{q_2}}{8E_\tau} \delta^{(0)}(K_1) \delta^{(0)}(K_2) \quad (\text{C.10})$$

$$K_1^2 = |\mathbf{p}_1 + \mathbf{q}_2|^2 = P_1^2 + Q_2^2 + 2Q_2(p_{1x} \sin \theta_{p_2} \cos \phi_{q_2} + p_{1y} \sin \theta_{q_2} \sin \phi_{q_2} + p_{1z} \cos \theta_{q_2})$$

$$K_2^2 = |\mathbf{p}_1 - \mathbf{q}_2|^2 = P_2^2 + Q_2^2 - 2Q_2(p_{2x} \sin \theta_{p_2} \cos \phi_{q_2} + p_{2y} \sin \theta_{q_2} \sin \phi_{q_2} + p_{2z} \cos \theta_{q_2})$$

$$\rightarrow \left| \frac{\partial(K_1, K_2)}{\partial\Omega_{q_2}} \right| = \frac{|\mathbf{q}_2 \cdot (\mathbf{p}_1 \times \mathbf{p}_2)|}{K_1 K_2}$$

$$\begin{aligned} \text{Eq. (C.9)} &= \frac{Q_2 P_1^2 P_2^2 dP_1 d\Omega_{p_1} dP_2 d\Omega_{p_2}}{16E_{p_1} E_{p_2} K_1 K_2} \frac{dK_1 dK_2}{8E_\tau} \cdot \frac{K_1 K_2}{|\mathbf{q}_2 \cdot (\mathbf{p}_1 \times \mathbf{p}_2)|} \\ &\quad \times \delta^{(0)}(E_\tau - E_{p_1} - K_1) \delta^{(0)}(E_{q_1} - E_{p_2} - K_2) \\ &= \frac{Q_2 P_1^2 P_2^2 dP_1 d\Omega_{p_1} dP_2 d\Omega_{p_2}}{16E_{p_1} E_{p_2}} \frac{1}{8E_\tau |\mathbf{q}_2 \cdot (\mathbf{p}_1 \times \mathbf{p}_2)|} \\ &= \frac{Q_2 P_1^2 P_2^2 d\Omega_{p_1}^* d\Omega_{p_2}^* d\Omega_{q_2}}{16E_{p_1} E_{p_2}} \frac{1}{8E_\tau |\mathbf{q}_2 \cdot (\mathbf{p}_1 \times \mathbf{p}_2)|} \times \left| \frac{\partial(P_1, \Omega_{p_1}, P_2, \Omega_{p_2})}{\partial(\Omega_{p_1}^*, \Omega_{p_2}^*, \Omega_{q_2})} \right| \\ &\rightarrow \left| \frac{\partial(\Omega_{p_1}^*, \Omega_{p_2}^*, \Omega_{q_2})}{\partial(P_1, \Omega_{p_1}, P_2, \Omega_{p_2})} \right| = \frac{P_1^2 P_2^2 m_\tau^2}{P_1^* P_2^* E_{p_1} E_{p_2} P_\tau |\mathbf{q}_2 \cdot (\mathbf{p}_1 \times \mathbf{p}_2)|} = \frac{\beta_1 \beta_2 m_\tau^2}{P_1^* P_2^* P_\tau^2 |\mathbf{n}_\tau \cdot (\mathbf{n}_{p_1} \times \mathbf{n}_{p_2})|} \end{aligned} \quad (\text{C.11})$$

$$\mathbf{C.4.1} \quad \left| \frac{\partial(\Omega_\rho^*, \Omega_\tau)}{\partial(P_\rho, \Omega_\rho, \Phi_\tau)} \right|$$

So far, we have not received simple derivation of this Jacobian based on the Lorentz-invariance approach. The steady calculation can be seen Ref. [95]. In the original reference, the author gives

$$\left| \frac{\partial(\Omega_\rho^*, \Omega_\tau)}{\partial(P_\rho, \Omega_\rho, \Phi_\tau)} \right| = \frac{m_\tau}{P_\tau} \left[ \frac{P_\rho}{E_\rho P_\rho^*} \frac{\cos^2 \phi_\rho^*}{A_\rho^2} \sin^2 \theta_\tau \right]$$

$$\text{with } A_\rho = \cos(\phi_i - \phi_\tau) \sin \theta_i \cos \theta_\tau - \cos \theta_i \sin \theta_\tau, \quad (\text{C.12})$$

but the explicit dependence of angles should disappear\*and in fact this identically equals to

$$\left| \frac{\partial(\Omega_\rho^*, \Omega_\tau)}{\partial(P_\rho, \Omega_\rho, \Phi_\tau)} \right| = \frac{m_\tau P_\rho}{E_\rho P_\rho^* P_\tau}. \quad (\text{C.13})$$

$$\mathbf{C.5} \quad \left| \frac{\partial(P_\gamma, \Omega_\gamma)}{\partial(\tilde{\Omega}_\gamma, \beta)} \right|$$

Though this Jacobian does not appear in the main text, we describe the deviation because the method used here is worthy to note for many application of tau physics. Suppose a  $\pi^0$  is moving to  $+z$  direction and decays into two photons.

$$\pi^0(p_0) \rightarrow \gamma(p_1)\gamma(p_2). \quad (\text{C.14})$$

A Jacobian related to this decay

$$\left| \frac{\partial(P_\gamma, \Omega_\gamma)}{\partial(\tilde{\Omega}_\gamma, \beta)} \right| \quad (\text{C.15})$$

is calculated by a comparison of the Lorentz-invariant phase space, where  $\beta$  is a velocity of  $\pi^0$  in the CMS frame and  $\tilde{\Omega}_\gamma$  is an angular component of the photon in the  $\pi^0$  rest frame (the decision of photon is arbitrary). The characteristic feature of this system is that  $\beta$  is not a parameter but rather an independent variable. If we fix the direction of  $\pi^0$  movement, the internal variable  $\tilde{\Omega}_\gamma$  and velocity of  $\pi^0$  is determined by observables measured in the system outside. The dependence of boost from  $\beta$  is taken into account by the Lorentz-invariant phase space of  $\pi^0$ .

$$d\text{LIPS} = \frac{d^3 P_0}{2E_0} \frac{d^3 P_1}{2E_1} \frac{d^3 P_2}{2E_2} \delta(p_0 - p_1 - p_2) \delta^{(2)}(p_{0\perp}) \quad (\text{C.16})$$

$$= \frac{dp_{z0}}{E_0} \frac{d\tilde{P}_1 d\tilde{\Omega}_1 \tilde{P}_1^2}{8\tilde{E}_2 \tilde{E}_2} \delta(\tilde{E}_0 - \tilde{E}_1 - \tilde{E}_1) \quad (\text{C.17})$$

$$= \frac{E_0^2 d\beta d\tilde{\Omega}_1 \tilde{P}_1^2}{m_{\pi^0}^2 8\tilde{E}_2 \tilde{E}_2} \frac{1}{2} \quad (\text{C.18})$$

$$= \frac{E_0^2 d\beta d\tilde{\Omega}_1}{16m_{\pi^0}^2}. \quad (\text{C.19})$$

Here, we used a formula

$$dp_{0z} = d(\beta\gamma m_{\pi^0}) = m_{\pi^0}(\gamma d\beta + \beta d(\gamma)) = m_{\pi^0}(\gamma + \beta^2 \gamma^3) d\beta = m_{\pi^0} \gamma^3 d\beta = \frac{E_0^3}{m_{\pi^0}^2}. \quad (\text{C.20})$$

---

\*Generally, Jacobians should not have such an explicit dependence on the angle of coordinates, *i.e.*, this kind of dependence should be written as inner (or external) product of particle four-vectors. Otherwise, the Jacobian depends on a specific decision of coordinate but this apparently violates the isotropic nature of space.

The delta function in Eq. (C.16) represents  $\delta^{(2)}(p_{\perp}) = \delta(p_x)\delta(p_y)$  and constrains the movement of  $\pi^0$  onto  $+z$  axis. The Lorentz-invariant phase space is calculated in a different way as

$$d\text{LIPS} = \frac{d^3P_0}{2E_0} \frac{d^3P_1}{2E_1} \frac{d^3P_2}{2E_2} \delta(p_0 - p_1 - p_2) \delta^{(2)}(p_{0\perp}) \quad (\text{C.21})$$

$$= \frac{dp_{0z}}{E_0} \frac{P_1^2 dP_1 d\Omega_1}{8E_0 E_1 E_2} \delta(E_0 - E_1 - E_2) \quad (\text{C.22})$$

$$= \frac{dp_{0z}}{E_0} \frac{P_1^2 dP_1 d\Omega_1}{8E_0 E_1 E_2} \delta\left(\sqrt{m_{\pi^0}^2 + p_{0z}^2} - P_1 - |\mathbf{p}_0 - \mathbf{p}_1|\right) \quad (\text{C.23})$$

$$= \frac{dp_{0z}}{E_0} \frac{P_1^2 dP_1 d\Omega_1}{8E_0 E_1 E_2} \delta\left(\sqrt{m_{\pi^0}^2 + p_{0z}^2} - P_1 - \sqrt{(p_{0z} - p_{1z})^2 + p_{1x}^2 + p_{1y}^2}\right) \quad (\text{C.24})$$

$$= \frac{1}{E_0} \frac{P_1^2 dP_1 d\Omega_1}{8E_0 E_1 E_2} \frac{1}{\left|\frac{p_{0z}}{E_0} - \frac{p_{0z} - p_{1z}}{E_2}\right|} \quad (\text{C.25})$$

$$= \frac{1}{E_0} \frac{P_1^2 dP_1 d\Omega_1}{8E_0 E_1 E_2} \frac{1}{|\beta - \beta_{2z}|} \quad (\text{C.26})$$

$$\equiv \frac{P_1^2}{8E_0^2 E_1 E_2 |\beta - \beta_{2z}|} d\beta d\tilde{\Omega}_1 \left| \frac{\partial(P_1, \Omega_1)}{\partial(\tilde{\Omega}_\gamma, \beta)} \right| \quad (\text{C.27})$$

Comparing Eqs. (C.19) and (C.27), we obtain

$$\left| \frac{\partial(P_\gamma, \Omega_\gamma)}{\partial(\tilde{\Omega}_\gamma, \beta)} \right| = \frac{E_0^3 E_1 E_2 |\beta - \beta_{2z}|}{2P_1^2 m_{\pi^0}^2} = \frac{E_0^2 \tilde{\beta}_{1z}}{4E_1} = \frac{E_0^2}{4E_1} (\tilde{\mathbf{n}}_1 \cdot \mathbf{n}_0). \quad (\text{C.28})$$

The direct calculation of this Jacobian is not impossible at all, but in the similar way more complex Jacobians can be easily extracted. For example, another Jacobian

$$\left| \frac{\partial(P_1, \Omega_1, P_2, \Omega_2)}{\partial(m_{\pi\pi}^2, \Omega_{\pi\pi}^*, \tilde{\Omega}_\pi, \beta)} \right| \quad (\text{C.29})$$

related to the decay from a moving  $K_L$  ( $+z$  direction)

$$K_L(p_0) \rightarrow \pi^0(p_1)\pi^0(p_2)\pi^0(p_3), \quad (\text{C.30})$$

is calculated by applying this method to give

$$\left| \frac{\partial(P_1, \Omega_1, P_2, \Omega_2)}{\partial(m_{\pi\pi}^2, \Omega_{\pi\pi}^*, \tilde{\Omega}_\pi, \beta)} \right| = \frac{E_{K_L}^3 \tilde{\beta}_\pi P_{\pi\pi}^* E_1 E_2 E_3 |\beta - \beta_{3z}|}{4m_{K_L}^3 P_1^2 P_2^2} = \frac{\tilde{\beta}_\pi P_{\pi\pi}^{*2} E_{K_L}^2 E_1 E_2}{4m_{K_L}^2 P_1^2 P_2^2} (\mathbf{n}_3^* \cdot \mathbf{n}_{K_L}). \quad (\text{C.31})$$

where the asterisk and tilde indicate that variables are defined in  $K_L$  and  $\pi\pi$  rest frame, respectively. The  $\pi\pi$  means  $\pi^0(p_1)$  and  $\pi^0(p_2)$ . If we use the strategy of direct calculation, we must differentiate the left hand side of

$$p_{\pi_{1,2}} = L(\beta \mathbf{n}_z) L(\beta_{\pi\pi}^* (m_{\pi\pi}) \mathbf{n}_{\pi\pi}^*) \left( \begin{array}{c} \frac{m_{\pi\pi}}{2} \\ \pm \sqrt{\frac{m_{\pi\pi}^2}{4} - m_\pi^2} \tilde{\mathbf{n}} \end{array} \right) \quad (\text{C.32})$$

by  $\beta$ ,  $m_{\pi\pi}$ ,  $\mathbf{n}_{\pi\pi}^*$  and  $\tilde{\mathbf{n}}$ , but this may be beyond the level of hand calculation.<sup>†</sup>

<sup>†</sup> $L(\beta)$  is a matrix of the Lorentz-transformation for general boost  $\beta$ , which is represented as

$$L(\beta) = \begin{pmatrix} \gamma & \gamma\boldsymbol{\beta} \\ \gamma\boldsymbol{\beta} & \mathbf{1} + \boldsymbol{\beta} \frac{\gamma-1}{\beta^2} \boldsymbol{\beta} \end{pmatrix}. \quad (\text{C.33})$$

## C.6 Recursive relation of the Lorentz-invariant phase space

In this section, we use conventional definition of phase space  $d^3p/(2\pi^3)2E_p$ . Suppose a particle  $a$  decays into  $n$ -particles  $b_1, b_2, \dots, b_n$ .

$$a(p) \rightarrow b_1(q_1) + b_2(q_2) + \dots + b_n(q_n). \quad (\text{C.34})$$

The  $n$ -body Lorentz-invariant phase space is reduced into that of  $(n-1)$ -body as bellow:

$$d\text{LIPS}_n = \left( \prod_{i=1\dots n} \frac{d^3q_i}{(2\pi)^3 2E_{q_i}} \right) (2\pi)^4 \delta \left( p - \sum_{i=1\dots n} q_i \right) \quad (\text{C.35})$$

$$= d^4k \delta \left( k - \sum_{i=2\dots n} q_i \right) \left( \prod_{i=1\dots n} \frac{d^3q_i}{(2\pi)^3 2E_{q_i}} \right) (2\pi)^4 \delta \left( p - \sum_{i=1\dots n} q_i \right) \quad (\text{C.36})$$

$$= d^4k \delta \left( k - \sum_{i=2\dots n} q_i \right) \frac{d^3q_1}{(2\pi)^3 2E_{q_1}} \left( \prod_{i=2\dots n} \frac{d^3q_i}{(2\pi)^3 2E_{q_i}} \right) (2\pi)^4 \delta \left( p - \sum_{i=1\dots n} q_i \right) \quad (\text{C.37})$$

$$= K^{*2} dK^* d\Omega_k^* \frac{dm_k^2}{2E_k^*} (2\pi) \delta^{(0)} \left( m_p - \sqrt{m_1^2 + \left| \sum_{i=2\dots n} \mathbf{q}_i^* \right|^2} - \sum_{i=2\dots n} E_{q_i}^* \right) \times \delta \left( k - \sum_{i=2\dots n} q_i \right) \frac{1}{2E_{q_1}^*} \left( \prod_{i=2\dots n} \frac{d^3q_i}{(2\pi)^3 2E_{q_i}^*} \right) \quad (\text{C.38})$$

$$= K^{*2} dK^* d\Omega_k^* \frac{dm_k^2}{2E_k^*} (2\pi) \delta^{(0)} \left( m_p - \sqrt{m_1^2 + K^{*2}} - E_k^* \right) \times \delta \left( k - \sum_{i=2\dots n} q_i \right) \frac{1}{2E_{q_1}^*} \left( \prod_{i=2\dots n} \frac{d^3q_i}{(2\pi)^3 2E_{q_i}^*} \right) \quad (\text{C.39})$$

$$= K^{*2} d\Omega_k^* \frac{dm_k^2}{2E_k^*} \frac{2\pi}{\frac{K^*}{E_{q_1}^*} + \frac{K^*}{E_k^*}} \delta \left( k - \sum_{i=2\dots n} q_i \right) \frac{1}{2E_{q_1}^*} \left( \prod_{i=2\dots n} \frac{d^3q_i}{(2\pi)^3 2E_{q_i}^*} \right) \quad (\text{C.40})$$

$$= (2\pi) K^* \frac{E_{q_1}^* E_k^*}{m_p} d\Omega_k^* \frac{dm_k^2}{2E_k^*} \delta \left( k - \sum_{i=2\dots n} q_i \right) \frac{1}{2E_{q_1}^*} \left( \prod_{i=2\dots n} \frac{d^3q_i}{(2\pi)^3 2E_{q_i}^*} \right) \quad (\text{C.41})$$

$$= \frac{K^*}{4m_p} d\Omega_k^* \frac{dm_k^2}{(2\pi)^3} \left( \prod_{i=2\dots n} \frac{d^3q_i}{(2\pi)^3 2E_{q_i}^*} \right) (2\pi)^4 \delta \left( k - \sum_{i=2\dots n} q_i \right) \quad (\text{C.42})$$

$$= \frac{K^*}{4(2\pi)^3 m_p} d\Omega_k^* dm_k^2 d\text{LIPS}_{n-1}, \quad (\text{C.43})$$

where asterisk means variables are defined in  $a$ -rest frame.



# Appendix D

## Doubly radiative leptonic decay $\tau^- \rightarrow \ell^- \nu \bar{\nu} \gamma \gamma$

In this appendix, we summarize characteristics of the doubly radiative leptonic decay  $\tau^- \rightarrow \ell^- \nu \bar{\nu} \gamma \gamma$ . The number of final-state particles are five and this has a seven-dimension phase space when we do not see the angular distribution of neutrinos in the  $\nu \bar{\nu}$  rest frame. The differential decay width in the tree level calculation is given by

$$\frac{d\Gamma(\tau^- \rightarrow \ell \nu \bar{\nu} \gamma \gamma)}{dm_{\gamma\gamma}^2 dm_{\ell\nu\bar{\nu}}^2 dm_{\nu\bar{\nu}}^2 d\tilde{\Omega}_\gamma d\Omega_\ell^{**}} = \frac{G_F^2 \alpha^2}{2^{11} \cdot 3\pi^8 m_\tau} \left[ G - (x\beta_\ell^* J \mathbf{n}_\ell^* + y_1 K_1 \mathbf{n}_{\gamma_1}^* + y_2 K_2 \mathbf{n}_{\gamma_2}^*) \cdot \mathbf{S}_\tau^* \right] \cdot \frac{P_{\gamma\gamma}^* \tilde{P}_\gamma P_\ell^{**}}{m_\tau m_{\gamma\gamma} m_{\ell\nu\bar{\nu}}}, \quad (\text{D.1})$$

where  $m_{\gamma\gamma}$ ,  $m_{\ell\nu\bar{\nu}}$ ,  $m_{\nu\bar{\nu}}$  are masses defined by combined four momenta  $m_{\gamma\gamma}^2 = (p_{\gamma_1} + p_{\gamma_2})^2$ ,  $m_{\ell\nu\bar{\nu}}^2 = (p_\ell + p_\nu + p_{\bar{\nu}})^2$  and  $m_{\nu\bar{\nu}} = (p_\nu + p_{\bar{\nu}})^2$ , tilde and double asterisk, respectively mean that variables are defined in  $p_{\gamma_1} + p_{\gamma_2}$  and  $p_\ell + p_\nu + p_{\bar{\nu}}$  rest frame,  $x = 2E_\ell^*/m_\tau$  and  $y_{1,2} = 2E_{\gamma_{1,2}}^*/m_\tau$ . The form factors— $G$ ,  $J$ ,  $K_1$  and  $K_2$ —are functions of  $x$ ,  $y_1$ ,  $y_2$ ,  $w = 2p_{\gamma_1} \cdot p_{\gamma_2}/m_\tau^2$  and  $z_{1,2} = 2p_\ell \cdot p_{\gamma_{1,2}}/m_\tau^2$  and their explicit (lengthy) formulae are given in Ref. [96].

Figure D.1 shows the distributions of kinematic variables for the doubly radiative leptonic decay  $\tau^- \rightarrow \ell^- \nu \bar{\nu} \gamma \gamma$  in the  $\tau^-$  rest frame calculated according to Eq. (D.1). To obtain the distributions, we apply the energy threshold for both photons, *i.e.*,  $E_\gamma^* > 10$  MeV. From these figures, we can observe that (similarly to the single radiative decay) the electron mode shows narrower distribution at  $\theta_{\ell\gamma} \rightarrow 0$  than muon case. However, it deserves to be mentioned that in the doubly radiative decay,  $\theta_{\mu\gamma}$  has a broader distribution than that of the single decay. The shift of the momentum of lepton compared to the single decay may be explained by the additional energy loss from two photon emission.

To consider possibilities to observe the doubly radiative decays, we simulate an angular distribution of an opening angle of photons and the energy distribution of photons both in the laboratory frame as shown in Fig. D.3. In this calculation, we assume a boost factor of the beam energy of KEKB accelerator. As seen from figure, the most probable magnitude of the opening angle is approximately  $10^\circ - 20^\circ$  and this is sufficiently large to distinguish both clusters each other. Moreover, there is a region in which both energies of photons are reasonably observable ( $E_\gamma^{\text{LAB}}$  is more than  $\sim 0.1$  GeV). Taking into account the tree level theoretical prediction of the branching ratio.\*

$$\mathcal{B}(\tau^- \rightarrow e^- \nu \bar{\nu} \gamma \gamma) = (8.327 \pm 0.008) \times 10^{-4}, \quad (\text{D.2})$$

$$\mathcal{B}(\tau^- \rightarrow \mu^- \nu \bar{\nu} \gamma \gamma) = (3.347 \pm 0.003) \times 10^{-5}, \quad (\text{D.3})$$

it may not be impossible to experimentally measure the branching ratio.

---

\*This value is calculated by a software provided by the author of Ref. [96]. The error includes only uncertainties from mathematical calculation.

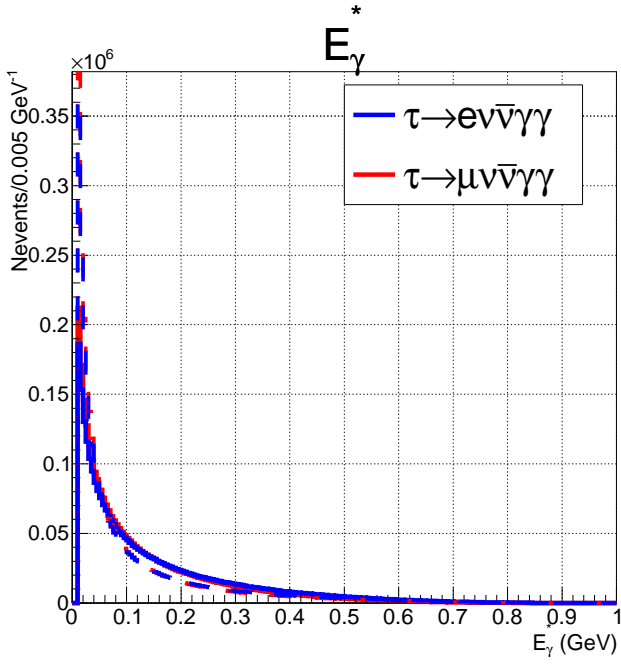
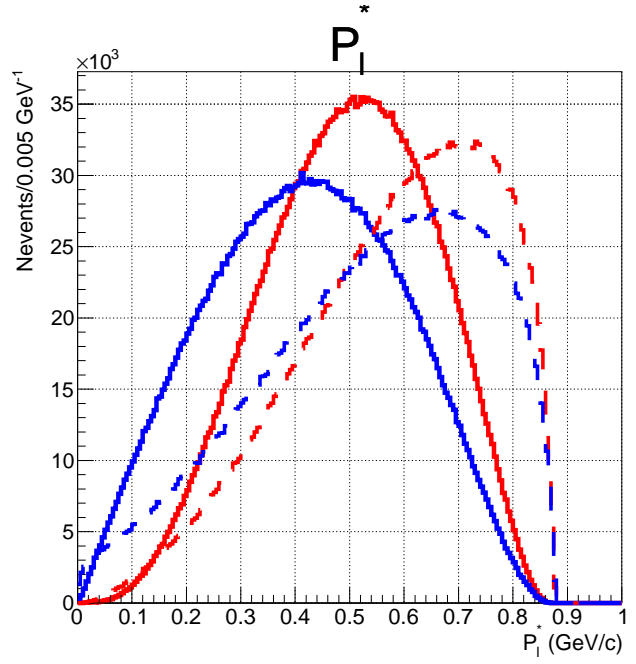
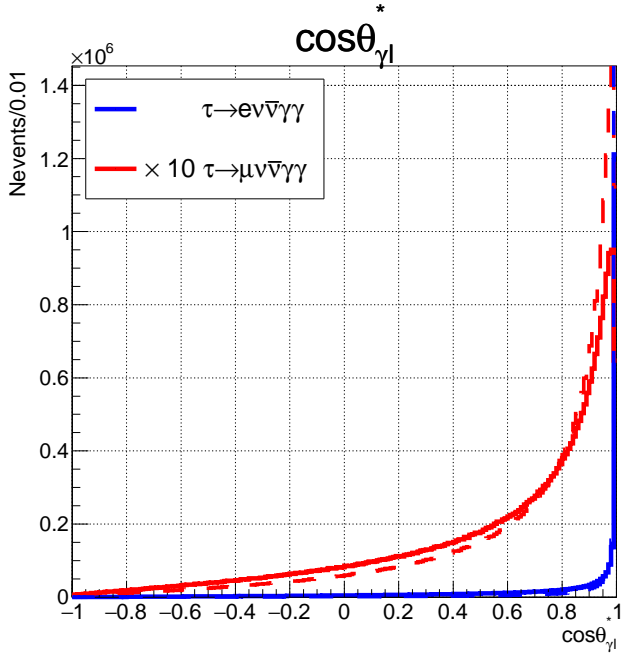
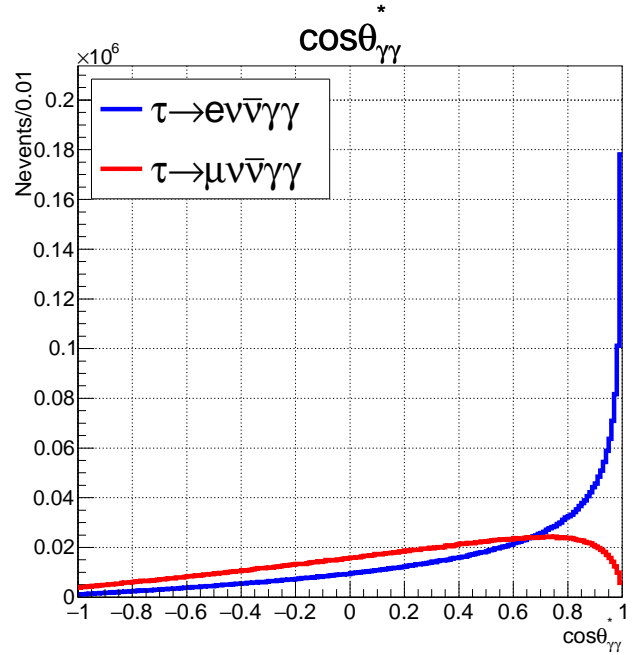
(a)  $E_\gamma^*$ (b)  $P_\ell^*$ (c)  $\cos\theta_{\ell\gamma}^*$ (d)  $\cos\theta_{\gamma\gamma}^*$ 

Figure D.1: Distribution of variables from doubly radiative leptonic decay  $\tau^- \rightarrow \ell \nu \gamma \gamma$ . Blue and red lines indicate electron and muon modes, respectively: (a)  $E_\gamma^*$  (b)  $E_\ell^*$  (c)  $\cos\theta_{\ell\gamma}^*$  and (d)  $\cos\theta_{\gamma\gamma}^*$ . For comparison, distribution of the single radiative decay is drawn for (a)(b)(c) with dashed lines. The distribution of  $\cos\theta_{\mu\gamma}$  in (c) is enlarged by a factor of ten.

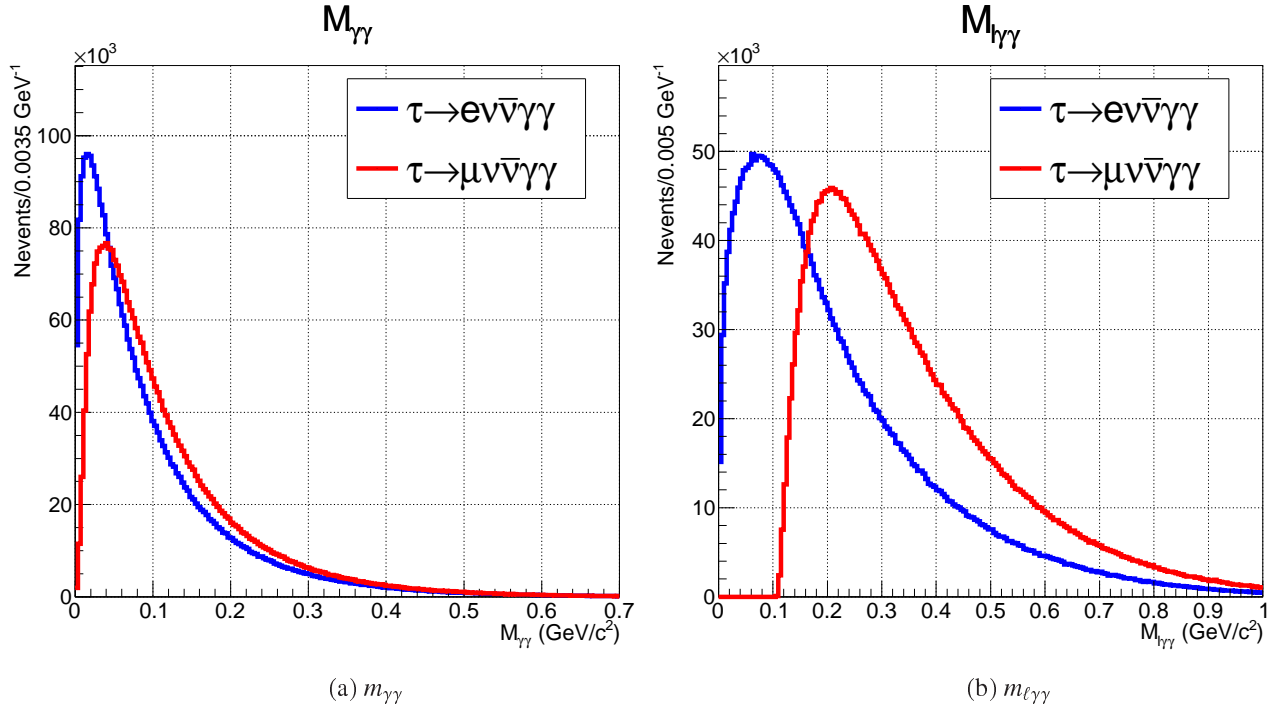


Figure D.2: Distribution of invariant masses. Blue and red lines indicate electron and muon modes, respectively: (a)  $m_{\gamma\gamma}$  (b)  $m_{\ell\gamma\gamma}$ .

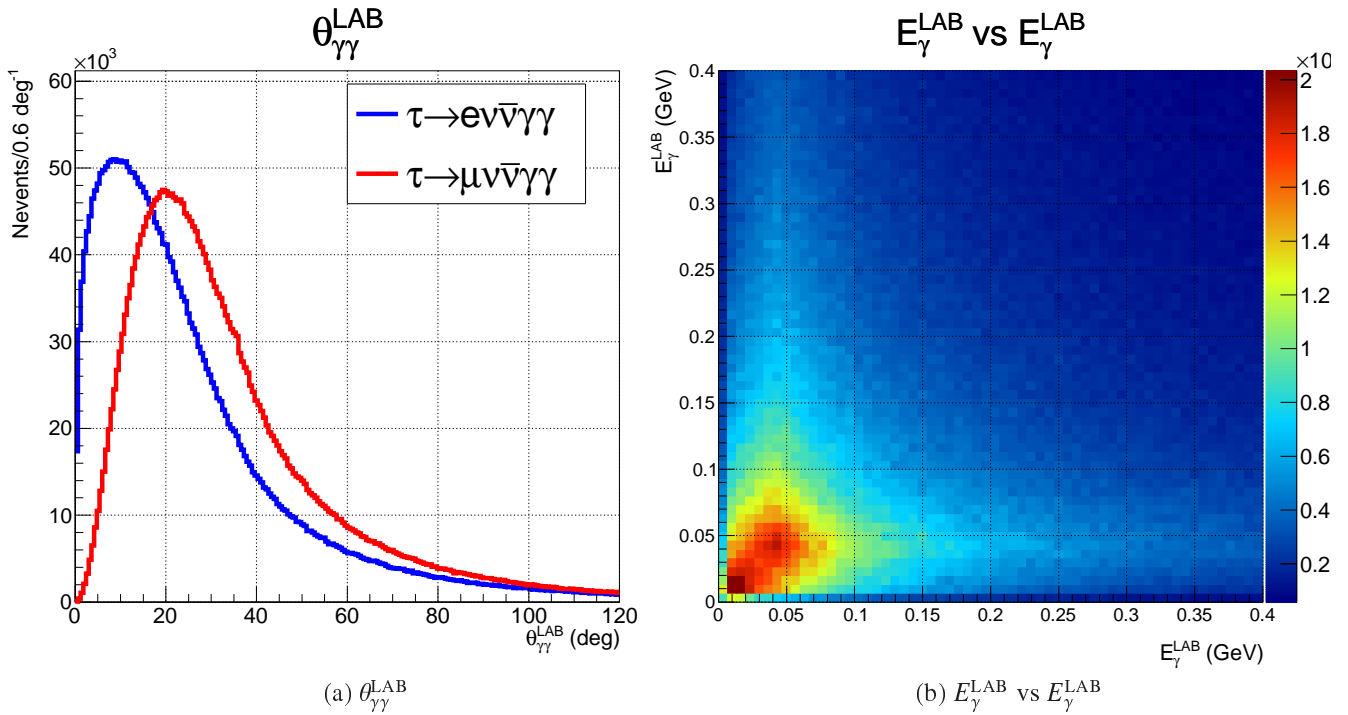


Figure D.3: Distribution of variables in the laboratory frame: (a) opening angle of photons (b)  $E_{\gamma}^{\text{LAB}}$  vs  $E_{\gamma}^{\text{LAB}}$  map distribution for  $\tau^- \rightarrow e^- \nu\bar{\nu}\gamma\gamma$ .

# Appendix E

## Detector resolution

### E.1 description of energy response

As roughly explained in Section 5.4.5, the response of detector is described by the logarithmic Gaussian. Here, the details are explained. The PDF of variable  $x$ , which follows Gaussian distribution is written as

$$\frac{dP}{dx} = \frac{1}{\sqrt{2\pi}\sigma} e^{-\frac{(x-x_0)^2}{2\sigma^2}}. \quad (\text{E.1})$$

Based on this  $x$ , we change  $x$  into  $E$  with relation  $x = \log(\epsilon - E)$ , where  $\epsilon$  is a constant which determines maximum energy. Therefore, the new variable  $E$  follows new PDF

$$\frac{dP}{dE} = \frac{1}{\epsilon - E} \frac{1}{\sqrt{2\pi}\sigma} e^{-\frac{(\log(\frac{\epsilon-E}{\epsilon-E_0}))^2}{2\sigma^2}}, \quad (\text{E.2})$$

where  $E_0$  corresponds nominal energy which satisfies  $x_0 = \log(\epsilon - E_0)$ . The most probable energy  $E_p$  is not generally same as  $E_0$  and given by  $E_p = \epsilon - (\epsilon - E_0)e^{-\sigma^2}$ . The degree of asymmetry is represented by  $\eta = \frac{\sigma_E}{\epsilon - E_p}$ , where  $\sigma_E$  is defined as FWHM of  $E$ . These variables follow equations  $\sigma = \frac{2}{\xi} \sinh^{-1}\left(\frac{\eta\xi}{2}\right)$  and  $\epsilon = E_p + \frac{\sigma_E}{\eta}$  ( $\xi = 2\sqrt{2\log 2}$ ), hence original constants  $\sigma$ ,  $x_0$  and  $\epsilon$  are obtained by assuming  $E_p$ ,  $\sigma_E$  and  $\eta$ . As these values, given energy resolution is substituted for  $\sigma_E$ ,  $E_p$  is taken from the reconstructed energy and  $\eta = 0.2$ .

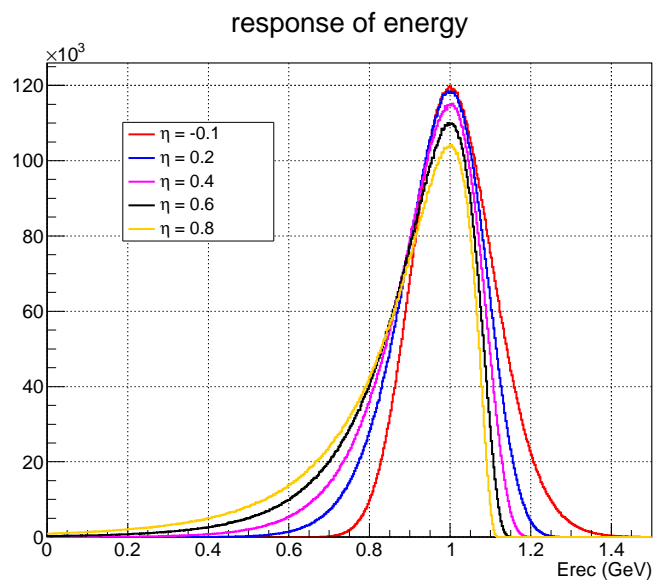


Figure E.1: Distribution of logarithmic Gaussian function in various  $\eta$  values.  $E_p = 1$  GeV,  $\sigma_E = 0.1$  GeV are assumed.

# Appendix F

## The right-left symmetric model

The right-left symmetric model [80, 81] is one of the natural extensions of the SM, in which  $SU(2)_L \otimes SU(2)_R \otimes U(1)$  gauge couplings  $g_L$  and  $g_R$  of  $SU(2)_L$  and  $SU(2)_R$  subgroup are equal:  $g_L = g_R$ . The symmetry spontaneously breaks into  $SU(2)_L \otimes U(1)$ , predicting not only the SM  $W^\pm$  and  $Z$  bosons but also additional gauge bosons  $W_2^\pm$  and  $Z_2$ . The mass spectrum of charged bosons are obtained by a diagonalization of real symmetric mass matrix of  $SU(2)_L \otimes SU(2)_R$  bosons  $W_L^\pm$  and  $W_R^\pm$

$$M_W^2 = \begin{pmatrix} M_L^2 & M_{LR}^2 \\ M_{LR}^2 & M_R^2 \end{pmatrix} \quad (\text{F.1})$$

by

$$\begin{pmatrix} W_1^\pm \\ W_2^\pm \end{pmatrix} = \begin{pmatrix} \cos \zeta & \sin \zeta \\ -\sin \zeta & \cos \zeta \end{pmatrix} \begin{pmatrix} W_L^\pm \\ W_R^\pm \end{pmatrix}, \quad (\text{F.2})$$

where  $\zeta$  is a mixing angle, which satisfies

$$\tan 2\zeta = \frac{2M_{LR}^2}{M_R^2 - M_L^2}. \quad (\text{F.3})$$

The mass eigenvalues of  $W_{1,2}$  are given by

$$M_{W_{1,2}}^2 = \frac{M_L^2 + M_R^2 \mp \sqrt{(M_R^2 - M_L^2)^2 + 4M_{LR}^4}}{2} = \frac{M_R^2}{2} \left[ \beta + 1 \mp \frac{1 - \beta}{\cos 2\zeta} \right], \quad (\text{F.4})$$

where  $\beta = M_L^2/M_R^2$  is a ratio of mass squared and observed fact implies it is small  $\beta \ll 1$ . Consequently, the mass relation of charged boson is described in terms of  $M_R$ ,  $\beta$  and  $\zeta$ . According to Ref. [97], the Michel parameters  $\rho$ ,  $\xi$ ,  $\xi' = -\xi - 4\xi\kappa + 8\xi\delta/3$  and  $\xi'' = 16\rho/3 - 4\bar{\eta} - 3$  are related with  $\beta$  and  $\zeta$  as:

$$\rho = \frac{3}{4} \cos^4 \zeta \left( 1 + \tan^4 \zeta + \frac{4\beta}{1 + \beta^2} \right), \quad (\text{F.5})$$

$$\xi = \xi' = \cos^2 \zeta (1 - \tan^2 \zeta) \frac{1 - \beta^2}{1 + \beta^2}, \quad (\text{F.6})$$

$$\xi'' = \cos^4 \zeta \left( 1 + \tan^4 \zeta + 2 \tan^2 \zeta \frac{3 - 4\beta + 3\beta^2}{1 + \beta^2} \right). \quad (\text{F.7})$$

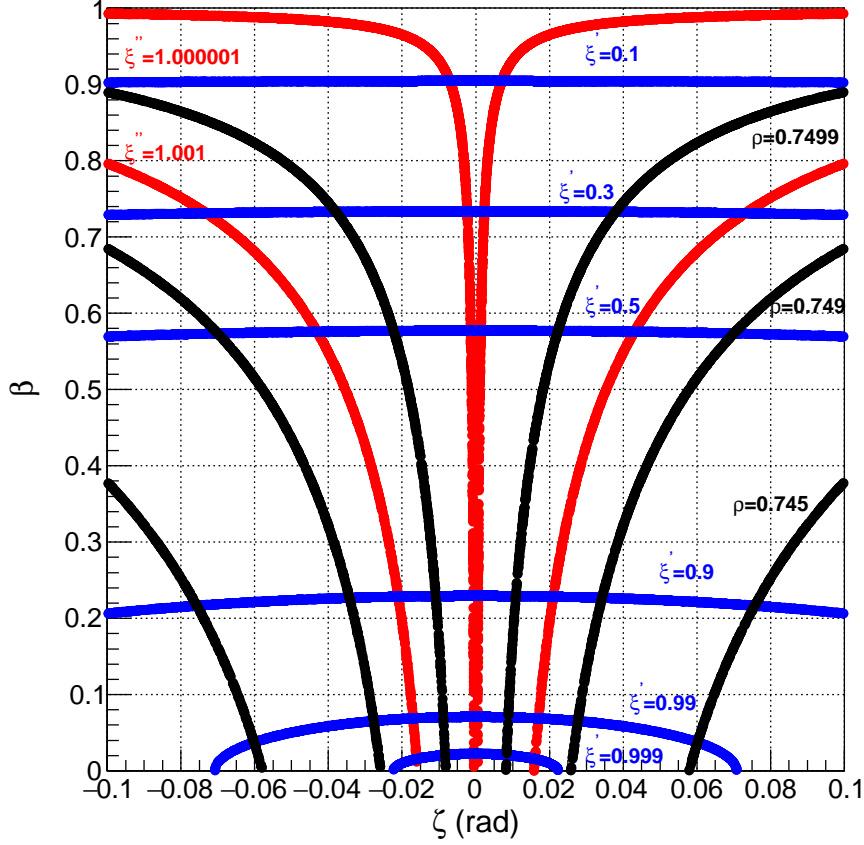


Figure F.1: Contour of  $\zeta$  and  $\beta$  determined by  $\rho$ ,  $\xi'$  and  $\xi''$ . Black, blue and red lines represent contours of Eqs. (F.5), (F.6) and (F.7), respectively.  $\rho = 0.745, 0.749, 0.7499$ ,  $\xi = \xi' = 0.1, 0.3, 0.5, 0.9, 0.99, 0.999$  and  $\xi'' = 1.001, 1.000001$  are drawn.

Figure F.1 shows the contours of  $\zeta$  vs  $\beta$  determined by Eqs. (F.5), (F.6) and (F.7). Note that  $\rho = 3/4 + \epsilon$  and  $\xi'' = 1 - \epsilon$  do not have proper solutions for infinitesimal value  $\epsilon > 0$  and they converge  $\beta \rightarrow 0, \zeta \rightarrow 0$  when  $\epsilon \rightarrow 0$ , *i.e.*, a large mass limit of the new charged boson for  $\rho = 3/4$ ,  $\xi = \xi' = \xi'' = 1$ . From the figure, we can observe that  $\xi$  and  $\xi'$  have large sensitivities on  $\beta$  parameter, accordingly it is used to determine the scale of  $M_R$  (for example,  $\beta = 0.1$  corresponds to  $M_R \sim 250 \text{ GeV}/c^2$ ).  $\xi'$  is induced by the measurement of  $\xi\kappa$  parameter, it is, however, more reasonable to use  $\xi$  parameter to constrain  $\beta$  in terms of resulting experimental sensitivity. In fact, with current sensitivity, we cannot give any conclusive remark. Similarly, from  $\xi''$  parameter, which is induced from  $\bar{\eta}$ , it is not possible to constrain  $\beta$  and  $\zeta$  due to its large uncertainty.

As three equations suggest, the lepton universality predicts the equal coupling structure between charged leptons and the  $W_2^\pm$  boson, it is thus much straightforward to measure  $\xi$  parameter by means of  $\mu \rightarrow e\nu\bar{\nu}$  decay. Current measured value of  $\xi_\mu$  parameter, which is approximately 0.2%, constrains mass  $M_R > 450 \text{ GeV}/c^2$ .





